Uniwersytet Warszawski

Wydział Biologii

Julian David Janna Olmos

Nr albumu: 331075

Engineering efficient energy and electron transfer in the all-solid-state biophotovoltaic and solar-to-fuel nanodevices containing photosystem I and cytochrome c_{553} from a red extremophilic microalga *Cyanidioschyzon merolae*

Rozprawa doktorska
w zakresie nauk biologicznych
dyscyplinie biologii

Praca wykonana pod kierunkiem
dr hab. Joanny Kargul, prof. UW
Centrum Nowych Technologii UW

Warszawa, maj 2017

Oświadczenie kierującego pracą

Oświadczam, że niniejsza praca została przygotowana pod moim kierunkiem i stwierdzam, że spełnia ona warunki do przedstawienia jej w postępowaniu o nadanie stopnia doktora nauk biologicznych w zakresie biologii.

12.05.2017 r.
Data

Podpis kierującego pracą

Oświadczenie autora pracy

Świadom odpowiedzialności prawnej oświadczam, że niniejsza rozprawa doktorska została napisana przeze mnie samodzielnie i nie zawiera treści uzyskanych w sposób niezgodny z obowiązującymi przepisami.

Oświadczam również, że przedstawiona praca nie była wcześniej przedmiotem procedur związanych z uzyskaniem stopnia doktora w innej jednostce.

Oświadczam ponadto, że niniejsza wersja pracy jest identyczna z załączoną wersją elektroniczną.

12.05.2017 r.
Data

Podpis autora pracy

Keywords

artificial leaf; biophotovoltaics; *Cyanidioschyzon merolae*; cytochrome *c*; hydrogen; plasmonic enhancement of fluorescence; photosystem I; photosynthesis; silicon; solar-to-fuel devices

Słowa kluczowe

biofotowoltaika; *Cyanidioschyzon merolae*; cytochrom *c*; fotoogniwa paliwowe; fotosystem I; fotosynteza; krzem; plazmonowe wzbudzenie fluorescencji; sztuczny liść; wodór

Tytuł pracy

Optymalizacja procesów transferu energii i transferu elektronowego w biofotowoltaicznych nanourządzeniach zawierających fotosystem I oraz cytochrom c_{553} z ekstremofilnego krasnorostu *Cyanidioschyzon merolae*

Abstract

One of the biggest challenges of modern-day solar technologies is to develop carbon-neutral, efficient and sustainable systems for solar energy conversion into electricity and fuel. Over the last two decades there has been a growing impact of 'green' solar conversion technologies based on the natural solar energy converters, such as the robust extremophilic photosystem I (PSI) and its associated protein cofactors. The main bottleneck of the currently available biophotovoltaic and solar-to-fuel technologies is the low power conversion efficiency of the available devices due to wasteful charge recombination reactions at the interfaces between the working modules, as well as instability of the organic and inorganic components.

This thesis describes the development of three novel approaches to improve energy and electron transfer in PSI-based biophotoelectrodes and plasmonic nanostructures: *(1)* construction of all-solid-state mediatorless biophotovoltaic devices incorporating *p*-doped silicon substrate, extremophilic robust PSI complex and its associated light harvesting antenna (PSI-LHCI) in conjunction with its natural electron donor cytochrome c_{553} (cyt c_{553}) from a red microalga *Cyanidioschyzon merolae* and *(2)*, biofunctionalization of the silver nanowires (AgNWs) with a highly organised architecture of the cyt c_{553}/PSI-LHCI assembly for the significant improvement of absorption cross-section of the *C. merolae* PSI-LHCI complex due to plasmonic interactions between the distinct subpool of chlorophylls (Chls) and AgNWs nanoconstructs. The third (*3*) approach was based on development of the photo-driven *in vitro* hydrogen production system following hybridisation of the robust extremophilic PSI-LHCI complex with the novel and established proton reducing catalysts (PRC). The last approach has led to generation of molecular hydrogen with TOF of 521 mol H_2 (mol PSI)$^{-1}$ min^{-1} and 729 mol H_2 (mol PSI)$^{-1}$ min^{-1} for the hybrid systems of PSI-LHCI with cobaloxime and the DuBois-type mononuclear nickel proton reduction catalysts, respectively. The TOF values for biophotocatalytic H_2 production obtained in this study were 3-fold and 16.6-fold higher than those published for cyanobacterial PSI/PRC hybrid systems employing cobaloxime and a similar Ni mononuclear PRC, respectively.

Construction of all-solid-state mediatorless PSI-based nanodevices was facilitated by biopassivation of the *p*-doped Si substrate with His_6-tagged cyt c_{553}, as evidenced by significant lowering of the inherent dark saturation current (J_0), a well-known semiconductor surface recombination parameter. Five distinct variants of cyt c_{553} were obtained by genetically engineering the specific linker peptides of 0-19 amino acids in length between the cyt c_{553} holoprotein and a *C*-terminal His_6-tag, the latter being the affinity 'anchor' used for specific immobilisation of this protein on the semiconductor surface. The calculated 2D Gibbs free energy maps for all the five cyt c_{553} variants and the protein lacking any peptide linker showed a much higher number of thermodynamically feasible conformations for the cyt *c* variants containing longer linker peptides upon their specific immobilisation on the Si surface. The bioinformatic calculations were verified by constructing the respective cyt c_{553}/Si bioelectrodes and measuring their dark current-voltage (*J-V*) characteristics to determine the degree of *p*-doped Si surface passivation, measured by minimisation of the J_0 recombination parameter. The combined bioinformatic and *J-V* analyses indicated that the cyt c_{553} variants with longer linker peptides, up to 19AA in length, allowed for more structural flexibility of immobilised cyt c_{553} in terms of both, orientation and distance of the haem group with respect to the Si surface, resulting in efficient biopassivation of this semiconductor substrate. This molecular approach has allowed for the developing of an alternative, cheap and facile route

for significant reduction of the inherent minority charge recombination at the *p*-doped Si surface.

To improve direct electron transfer within all-solid state PSI-based nanodevices, the specific His_6-tagged cyt c_{553} variants, generated in this study, were attached to the Ni-NTA-functionalised *p*-doped Si surface prior to incorporation of the PSI-LHCI photoactive layer. Such nanoarchitecture resulted in an open-circuit potential increment of 333 μV for the specific PSI-LHCI/cyt c_{553}/Si nanodevice compared to the control device devoid of cyt c_{553}. Moreover, the all-solid state mediatorless PSI-LHCI-based devices produced photocurrents in the range of 104-234 $\mu A/cm^2$ when a bias of -0.25 V was applied, demonstrating one of the highest photocurrents for this type of solid-state devices reported to date. The power conversion efficiency of the PSI-LHCI/*p*-doped Si devices was 20-fold higher when 19AA variant of cyt c_{553} was incorporated as the biological conductive interface between the PSI-LHCI photoactive module and the substrate, demonstrating the significant role of this cyt variant for improving direct electron transfer within the PSI-based all-solid-state mediatorless biophotovoltaic device.

In a complementary line of research, it was demonstrated that the highly controlled assembly of *C. merolae* PSI-LHCI complex on plasmon-generating AgNWs substantially improved the optical functionality of such a novel biohybrid nanostructure. By comparing fluorescence intensities measured for PSI-LHCI complex randomly oriented on AgNWs and the results obtained for the PSI-LHCI/cyt c_{553} bioconjugate with AgNWs it was concluded that the specific binding of PSI-LHCI complex with the defined uniform orientation yields selective excitation of a pool of Chls that are otherwise almost non-absorbing. This is remarkable, as this work shows for the first time that plasmonic excitations in metallic nanostructures not only can be used to enhance native absorption of photosynthetic pigments, but also, by employing cyt c_{553} as the conjugation cofactor, to activate the specific Chl pools as the absorbing sites, only when the uniform and well-defined orientation of PSI-LHCI complex with respect to plasmonic nanostructures is achieved. This innovative approach paves the way for the next generation solar energy-converting technologies to outperform the reported-to-date biohybrid devices with respect to power conversion efficiency.

Streszczenie

Jednym z głównych wyzwań technologicznych jest opracowanie wydajnych i odnawialnych systemów konwersji energii słonecznej w elektryczność i paliwo, stosując zerowy bilans emisji związków węgla. W ciągu ostatnich dwóch dekad nastąpił znaczący postęp w zastosowaniu "zielonych" technologii biofotowoltaicznych, opartych na naturalnych białkach absorbujących energię słoneczną, takich jak fotosystem I (PSI) wraz ze związanymi z nim kompleksami antenowymi i kofaktorami transportu elektronowego. Głównym ograniczeniem obecnych urządzeń fotowoltaicznych jest ich niska wydajność kwantowa, związana z procesami rekombinacji ładunku w interfejsach pomiędzy modułami tych urządzeń, jak również ograniczona stabilność zastosowanych jak dotąd biologicznych i syntetycznych komponentów.

W ramach niniejszej rozprawy doktorskiej opracowano nowatorską technologię, polegającą na zastosowaniu wysokostabilnego PSI oraz naturalnego donora elektronów dla tego kompleksu, cytochromu c_{553} (cyt c_{553}), wyizolowanych z ekstremofilnego krasnorostu *Cyanidioschyzon merolae*, do konstrukcji trzech typów nanourządzeń biofotowoltaicznych: (*1*), biofotoogniw w stałej konfiguracji (*ang.*, all-solid-state), zawierających domieszkowany pozytywnie półprzewodnikowy substrat krzemowy (ang., *p*-doped Si, *p*-Si) wraz z warstwami fotoaktywnego kompleksu PSI i cyt c_{553}; *(2)*, plazmonowych srebrnych bionanodrutów (AgNWs), funkcjonalizowanych wysokouporządkowaną nanoarchitekturą monowarstw PSI i cyt c_{553}, oraz (*3*), systemu fotokatalitycznej produkcji wodoru cząsteczkowego *in vitro* z zastosowaniem kompleksów hybrydowych PSI wraz z syntetycznymi katalizatorami redukcji protonów (*ang.*, proton reducing catalysts, PRC). W przypadku ostatniego z powyższych systemów, optymalizacja biofotokatalitycznej produkcji wodoru cząsteczkowego z zastosowaniem systemów hybrydowych z PSI i PRC, opartych na kobaloksymie i niklowym katalizatorze mononuklearnym typu DuBois, precypitowanych na powierzchni PSI w roztworze wodnym, pozwoliła na osiągnięcie aktywności wydzielania wodoru odpowiednio, 521 moli H_2 (mol PSI)$^{-1}$ min^{-1} oraz 729 moli H_2 (mol PSI)$^{-1}$ min^{-1}, przewyższając tym samym 3-17-krotnie aktywność wydzielania wodoru w podobnych systemach biohybrydowych i warunkach pomiarowych.

Poraz pierwszy zastosowano cyt c_{553} z *C*-terminalną metką His_6 do biopasywacji półprzewodnikowego substratu *p*-Si, mierzonej minimalizacją parametru rekombinacji powierzchniowej J_0. Poprzez inżynierię genetyczną sklonowano i wyrażono w *E. coli* 5 różnych wariantów cyt c_{553}, z których 4 zawierały w swej strukturze sekwencje peptydowe o długości 5-19 aminokwasów (AA), aby zbadać ich wpływ na procesy rekombinacji ładunku w obrębie elektrody krzemowej. Peptydy te zostawy wstawione pomiędzy holobiałkiem a metką His_6, którą zastosowano do unieruchomienia każdego z wariantów cyt c_{553} na powierzchni elektrody. Obliczenie energii swobodnej Gibbsa pozwoliło na utworzenie konformacyjnych map 2D dla każdego z wariantów, w których pokazano, iż warianty z semi-helikalnym peptydem 19AA przyjmują znacząco większą liczbę termodynamicznie możliwych konformacji na powierzchni elektrody pod względem odległości i kąta nachylenia grupy hemowej w stosunku do powierzchni elektrody. Bioinformatyczna analiza została potwierdzona poprzez ciemniową charakterystykę prądowo-napięciową (*J-V*) utworzonych odpowiednio bioelektrod krzemowo-cytochromowych. Stwierdzono, że warianty cyt c_{553} z dłuższymi peptydami pomiędzy metką His_6 a holobiałkiem efektywnie minimalizują prądy ciemniowe krzemowego substratu, najprawdopodobniej dzięki istnieniu większej ilości

termodynamicznie zoptymalizowanych konformacji cytochromu, pozwalających na minimalizację rekombinacji ładunku powierzchniowego substratu.

Funkcjonalizacja elektrody *p*-Si wariantem cyt c_{553}, charakteryzującym się największym stopniem swobody orientacji grupy hemowej w stosunku powierzchni elektrody krzemowej, pozwoliła na efektywną biopasywację tego półprzewodnikowego substratu poprzez minimalizację parametru J_0, co z kolei pozwoliło na zwiększenie parametru V_{oc} o 333 µV w biofotoogniwach typu PSI/cyt c_{553}/*p*-Si, w porównaniu do kontroli zawierającej jedynie PSI/*p*-Si. Uzyskano fotoprądy w stałych biofotoogniwach PSI/*p*-Si w zakresie 104-234 µA cm^{-2} (przy nadpotencjale -0.25 V), co należy do jednych z najwyższych wartości fotoprądów wygenerowanych przez stałe biofotoogniwa z PSI, w podobnych warunkach pomiarowych. Jednocześnie wydajność konwersji energii słonecznej w fotoogniwach typu PSI-LHCI/cyt c_{553}/*p*-Si była 20-krotnie wyższa, w obecności wariantu cyt c_{553} 19AA, zastosowanego w tych urządzeniach jako biologiczna warstwa biopasywacji substratu krzemowego oraz warstwa kondukcyjna pomiędzy substratem a PSI. Tym samym wykazano, że ów wariant może być zastosowany w urządzeniach biofotowoltaicznych do zwiększenia transferu elektronowego pomiędzy substratem a PSI.

W równoległym i komplementarnym kierunku badań, zastosowanie równomiernej i specyficznie ukierunkowanej nanoarchitektury fotoaktywnej warstwy PSI na plazmonowych nanostrukturach metalicznych AgNWs, sfunkcjonalizowanych uprzednio cyt c_{553}, pozwoliło na znaczące zwiększenie efektywnej absorpcji PSI, w zakresie spektralnym, w którym PSI jest nieaktywny *in vivo*, poprzez aktywację specyficznej puli tzw. czerwonych cząsteczek chlorofilu w obrębie fluoroforów PSI. Tym samym pokazano, że oddziaływania plazmonowe mogą być efektywnie zastosowane nie tylko do zwiększenia całkowitej absorpcji fotoaktywnych kompleksów białkowych, ale również do aktywacji spektralnej specyficznych pigmentów, wyłącznie w obrębie wysokouporządkowanej i zorientowanej nanoarchitektury tych fotokompleksów na nanokonstruktach plazmonowych. Powyższe nowatorskie podejście badawcze może być w przyszłości zastosowane do konstrukcji nowej generacji urządzeń biofotowoltaicznych o zwiększonej wydajności konwersji energii słonecznej.

Engineering efficient energy and electron transfer in the all-solid-state biophotovoltaic and solar-to-fuel nanodevices containing photosystem I and cytochrome c_{553} from a red extremophilic microalga *Cyanidioschyzon merolae*

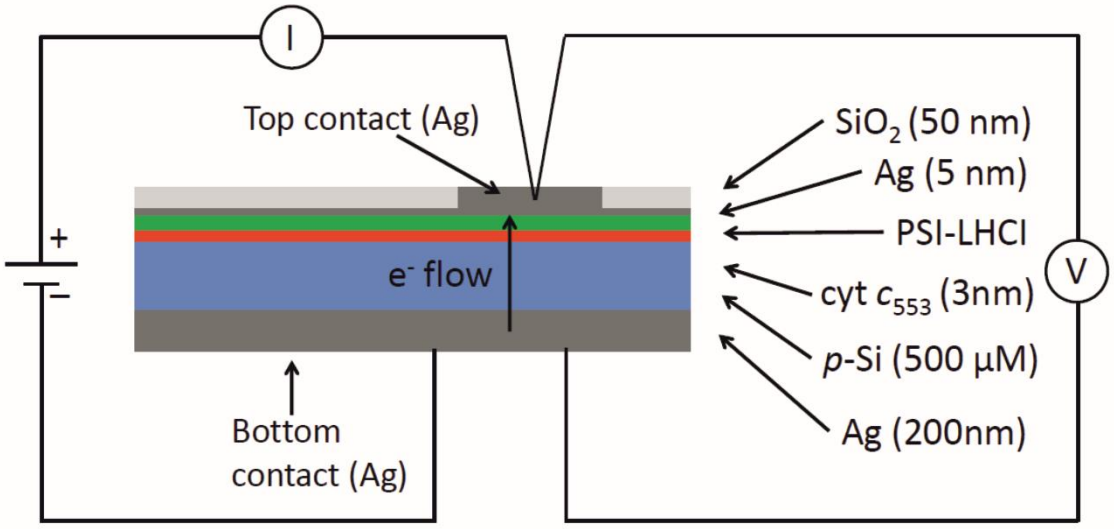

Julian David Janna Olmos

This PhD study was conducted in the Faculty of Biology and Centre for New Technologies, the University of Warsaw, Poland


WYDZIAŁ BIOLOGII
UNIWERSYTET WARSZAWSKI


C·NT
CENTRUM
NOWYCH
TECHNOLOGII


UNIVERSITAS
VARSOVIENSIS

Engineering efficient energy and electron transfer in the all-solid-state biophotovoltaic and solar-to-fuel nanodevices containing photosystem I and cytochrome c_{553} from a red extremophilic microalga *Cyanidioschyzon merolae*

PhD thesis

To obtain the degree of PhD at the University of Warsaw on the authority of the committee of the Faculty of Biology, the Dean of the Faculty of Biology, Prof. dr hab. Agnieszka Mostowska and Rector Magnificus, Dr hab. Marcin Pałys, Prof. UW, and in accordance with all the rules and regulations as stipulated by the Faculty of Biology and the Senate of the University of Warsaw

This thesis will be defended in public on

by

Julian David Janna Olmos

Born on 20th January 1987 in Corozal, Sucre, Colombia

Supervisor

Dr hab. Joanna Kargul, Prof. UW

Assessment committee

Prof. dr hab. Wiesław Gruszecki

Dr hab. Krzysztof Gibasiewicz, Prof. UAM

Table of Contents

List of Tables

List of Figures

Preface

Exploring the molecular interaction between cytochrome c_{553} and photosystem I with its associated light-harvesting antenna complex for an improved energy and electron transfer in three distinct configurations of artificial photosynthetic devices

We can learn a great deal from nature. Over the course of 3.5 billion years, nature has optimised the pathways of energy conversion from sunlight directly into sugars and other biomass building molecules that ultimately power the existence and development of humankind. Plants, and other photoautotrophic photosynthetic organisms, are ultimately responsible for powering our society. The logarithmic growth of the global population over the last century has increased dramatically the consumption of the natural energy resources, including fossil fuels which can be considered as energy equivalents accumulated since the onset of photosynthesis. Due to our indiscriminate consumption of fossil fuels, we will run out of them, sooner rather than later. Moreover, the current political agendas aim at consuming these finite sources of fuel even more aggressively than it has been envisaged in the last decade. Therefore, it is imperative to urgently find ways of developing sustainable forms of clean energy in the not-too-distant future.

We do not have to look very far to get inspired on how to develop technologies for sustainable solar energy conversion. The primary reactions of photosynthesis have been evolutionary optimised at a spectacular efficiency of the primary conversion events. Overall, photosynthesis is rather inefficient (0.2% solar-to-biomass efficiency on average), yet it powers life on our Planet in a cyclic manner, providing at the same time the sole source of atmospheric oxygen. Photosystem I (PSI) and photosystem II (PSII) are the macromolecular pigment-protein complexes embedded in the light-converting sub-cellular membranes of oxygenic phototrophs. These nanomolecular machines are responsible for converting the energy of sunlight into reducing equivalents through a complex, yet conserved, chain of electron transfer pathways, ultimately leading to the production of adenosine triphosphate (ATP), an energy-rich molecule which powers carbon dioxide conversion into sugars and ultimately, fossil fuels. As the Sun is a practically an infinite source of energy, the modes in which these two macromolecular machines operate provide a blueprint for developing alternative, innovative technologies for sustainable solar energy conversion.

Over the last decade, the scientific community has witnessed a plethora of approaches to incorporate the photosynthetic complexes into the specialised nanodevices capable of either

exploiting the abilities of these proteins to convert solar energy into electricity or fuel. Throughout my doctorate and with the help of a very talented interdisciplinary team, I have managed to construct a new class of energy-converting devices which in some cases enhanced PSI's ability to capture solar light. This is remarkable, as for the first time we have exploited the natural interaction between PSI and its natural electron donor, cytochrome c_{553}, to specifically orient this complex on the surface of plasmonic nanostructures. Importantly, we now have the strong evidence suggesting that by employing the specific orientation of PSI on plasmon-emitting nanomaterial, a distinct group of chlorophylls is activated to absorb certain wavelengths of light which are normally not captured. Thus, we have exploited the interaction between inorganic material and the natural PSI complex to improve functionality of the latter.

Moreover, I have also constructed all-solid-state silicon-based biophotoelectrodes, functionalised with PSI and cytochrome c_{553}, either individually, or together. Silicon is a very attractive solar energy conversion material as it is cheap and it is the second most abundant and evenly distributed element in the Earth's crust. The absorption spectrum of silicon complements that of PSI. By exploiting the evolutionary optimised intermolecular interaction between PSI and cytochrome c_{553}, and by minimising the distance between all the modules of the bioelectrode (that is, silicon, cytochrome c_{553} and PSI) I have managed to construct the biohybrid electrodes which serve as the prototype for the development of cost-effective, scalable biophotovoltaic devices, as evidenced by some of the highest current density values reported for this type of devices to date.

Nature has a great deal to teach us, and as this thesis shows, we do not need to circumvent nature to improve it. On the contrary, we need to learn, use and exploit nature for the service of the society. If we want to improve nature, we should understand how it works. Most importantly, we should understand the intricate molecular processes that exist in natural photosynthetic systems to be able to exploit the newly discovered or improved functionalities of photosynthetic complexes upon their integration with plasmonic nanomaterials within cheap and scalable solar energy-converting devices.

My favourite quotes:

“Science requires sacrifice” Maria Skłodowska-Curie

“Duty first, self second” HM (HRH) Queen Elizabeth II of the United Kingdom of Great Britain and Northern Ireland

“If you can't explain it simply, you don't understand it well enough” Albert Einstein

Dedicatoria

Dedico los contenidos enteros de esta tesis doctoral solo a una persona, a mi queridísima y amada Abuela Graciela. Querida Abuela, te quiero agradecer sinceramente, desde el fondo de mi corazón, por nunca perder tu fe en mí, y siempre creer en mí, a pesar de la distancia y todas las circunstancias difíciles que he tenido que enfrentar durante estos últimos seis años. Las enseñanzas más importantes y duraderas que me has inculcado desde joven son los valores de la fe, la perseverancia, y lo más importante de todo, me has dado un ejemplo de fortaleza monumental. Sin tu ejemplo de fortaleza todos estos años no creo que actualmente seria la persona que soy hoy en día, fuerte, lleno de fe y de energía positiva, y siempre con una sonrisa y una actitud tranquila y positiva ante todos los obstáculos que llegan día a día. Estoy seguro que sin tu ejemplo de fuerza y perseverancia nunca lo hubiera encontrado en mí levantarme para lograr mis sueños, convertirme en un doctor de ciencia, en el campo científico que siempre ha sido mi pasión y mi sueño. Hoy, te dedico mis talentos, mi inteligencia, y lo más importante, mi industria, mi trabajo y mis méritos. Hoy, estoy orgulloso de proclamar que soy tu nieto, y por eso te dedico mis últimos seis años de vida, los cuales le he dedicado exclusivamente a la ciencia. Hoy es un día, cuando puedo decir con orgullo y gran estrepito que soy el nieto mayor de Graciela Toro de Olmos.

Dedicatory

I would like to dedicate the entire contents of this PhD thesis to one person only, my dearest and most beloved Grandmother. Dearest Grandma, I would like to thank you sincerely, from the bottom of my heart, for never losing your faith in me, and for always believing in me, despite the distance and the difficult personal circumstances that I had over the last six years. The most valuable and enduring lessons that you have instilled in me are faith, perseverance and most importantly, strength. Without your example of strength throughout all these years I would have never grown to be as strong as I am today, but most importantly, I doubt I would have found it in me to stand up for the daunting task of becoming a doctor of science. Today, I dedicate to you my talents, my intelligence, and most importantly, my industry, my work and my merits. Today, I am proud to proclaim that I am your grandson, and I dedicate to you my last six years of life, which I have devoted solely and exclusively to science. Today, is a day, when I can proudly and loudly say to everyone, that I am the eldest grandson of Graciela Toro de Olmos.

Acknowledgements and financial support

First and foremost, I would like to give a very, very special thanks to my supervisor, Joanna (Joasia) Kargul. Joasia, thank you so much for being my rock all these years, but most importantly, I would like thank you sincerely, for being so demanding. As a PhD student perhaps one doesn't realise immediately the importance of having a demanding supervisor, but I wouldn't be so demanding on myself today if it wasn't for Joasia's education and example. Thank you, Joasia, for being so unfaltering, and for always expecting nothing but the highest quality work from me. Thank you for being so understanding, and for being such a fantastic 'opiekun naukowy' (scientific supervisor). Without your constant stimulation, it would have been even more difficult for me to complete my PhD, so I would like to reiterate my most sincere gratitude for stimulating me, knowing from personal experience that stimulating a student is by no means a trivial task. Thank you, for being there from the first day until the last, and for being so understanding. Thank you for being strict but fair. Thank you for making me an independent researcher, and thank you for taking my education so seriously. Thank you for being so caring.

I would like to thank chronologically all the people that have helped me at the University of Warsaw since my arrival in the autumn of 2011. Principally, I would like to thank my three best friends, Alicja Buczyńska, Ana and Agnes Podgórski, for being my support since the beginning. Most importantly, I would like to thank you sincerely for your relentless loyalty. Thank you for always having a shoulder for me to cry on, for being there for me in the most difficult times, and thank you for stimulating me to carry on. And thanks for all the amazing parties and trips! Weehoo!

I would like to thank the people at the Faculty of Biology that received me, Ms. Emilia Kurowska and Prof. dr hab. Agnieszka Mostowska, the Dean of the Faculty, for helping me with all the paperwork from the beginning. Prof. Siński and Dr hab. Ewa Borsuk, Prof. UW for guiding me to meet all the formalities of the Faculty and the University, Prof. dr hab. Maciej Garstka, Ms Monika Jankowska and all the people in the Financial Section of the Faculty for helping me with the complicated matters of managing a Polish grant. I would like to thank the Faculty members that were so amazingly helpful to me, a very, very special thanks to Prof. Eugeniusz Parys for always greeting me with a smile and always feeding me with cakes and sweets, Prof. dr hab. Maria Ciemerych-Litwinienko for her support and motivating

words, Prof. dr hab. Małgorzata Wierzbicka, for infinite generosity and understanding, and Prof. dr hab. Dariusz Bartosik for helping me out tremendously with the molecular biology aspects of my PhD research. From his group I would like to thank Kuba, Magda, Łukasz, Robert and Marcin. I would like to thank other members of the Faculty of Biology, like Ms. Kasia Zapaśnik, for the media preparation and sterilisation; this was such an amazing help. I would like to thank the members of ZMFR, including Maks, Wiola, Ilona, Ania and Alusia, thank you so much for all the help, despite the circumstances, and for all the assistance you provided me with when you could.

I would like to give a very special thanks to all the members of the Centre of New Technologies of the University of Warsaw (CeNT UW) who assisted me with the challenging and time-consuming transition to the new laboratory. A very special thanks to Ms Ewa Jastrzębska, and Prof. dr hab. Piotr Węgleński for providing us with such a fantastic work environment. I would like to thank everyone in the administration, Mariusz, Kuba, Sławek, Ludka, Bartek, Aleksandra, Bogdan, Ewa Jabłonka-Gronowska, and the amazing ladies in the Financial Section. I would like to give a very special thanks to all of you for helping me settle at CeNT, and for always helping me and greeting me with a smile. Thank you for making me feel so comfortable and great at CeNT, where I completed the experimental section of my PhD and where I truly feel and always will feel at home.

Very importantly, I would like to thank members of our international and national consortia, which also helped me out tremendously with their superb advice and brilliant scientific input. I would like to thank Prof. A. R. Holzwarth, Prof. Dr. Lubitz, Prof. Dr. Huub de Groot, Doç. Dr. Kasim Ocakoğlu, Dr. Andrea Barbieri, Prof. Tom Moore, Prof. Richard Cogdell, Prof. Barry Bruce, Prof. Kane Jennings, Prof. Dr. rer. nat. habil. Fred Lisdat, Dr. Nicolas Plumeré and Dr. Mike Jones.

A very special thanks to the principal investigators that hosted me in their labs, Prof. Joost Reek, Dr. Raoul Frese and Dr. Olaf Ruediger, thank you so much! Thanks to all the people that worked with me closely, Remko and Andrea in Joost's lab, Vincent of course, and Olaf, thank you for being so patient and understanding with me. ¡Muchas gracias!

I would like to express also my gratitude to our Polish collaborators, a very, very warm thanks to Prof. Sebastian Maćkowski, for seeing my deep and root-seated interest in photonics and biophysics, I would like to thank Dr. Dorota Kowalska, for being so amazing, Dorota Buczyńska and Marcin Szalkowski for their hard work, understanding and dedication, and all

the other members of this amazing optical physics lab that helped me out so tremendously during my Toruń visits.

I would like to thank Prof. dr hab. Andrzej Szczepaniak for his pEC86 vector gift, and once again to Prof. dr hab. Dariusz Bartosik for providing pET28b-(+) and pBAD/HisA expression vectors, as well as TOP10, BL21 and DH5α *E. coli* strains.

Very significantly, I would like to thank the current members of the Solar Fuels Laboratory. Pacza, Grzesiek, Mateusz and Gleb, thank you so, so much for putting up with me. Please forgive me if I caused you any inconvenience. A very special thanks to Grzesiek Bubak for being so incredibly patient and understanding with me, thank you so, so much for your help at the end of my PhD work, for teaching me how to use Origin and for spending so much time teaching me electrochemistry and photovoltaics. I cannot deny that I consider you all like my family now, and that I will always do. I will never forget the times I spent with you all in the lab, the times I spent with you out of the lab, and the amazing stories we shared together. I wish you all nothing but the best of luck, and I am sure that you will have nothing but success in life. Cheers and Godspeed!

I would also like to thank the members of my current research lab, where I am currently working and where I hope to expand my scientific horizons vastly. Thank you all for being so, so caring and so, so understanding, but mostly, thank you for your patience. Thank you, Marcin, Koksu, Sebastian, the two Rafałs, Łukasz, Roberto, Arek, and, most importantly, Prof. dr hab. Artur Osyczka. Artur, I am sincerely grateful for your patience and endless understanding. I will never forget it, and I will remember this level of patience and understanding forever.

Once again I would like to thank Joasia for taking me to all the amazing EuroSolarFuels consortium conferences, and paving the way for me to visit all these internationally renowned labs. It has been such an amazing PhD, truly European, and I can't thank you enough for giving me this amazing opportunity to learn so much from so many different fields, I truly feel like a real interdisciplinary researcher, and it is all thanks to you, Joanna. Thank you for all the travels, and all the opportunities to attend such prestigious conferences, and from giving me the once-in-a-life-time opportunity to learn from the best experts in the field. I must admit that you now make a part of my personal affections and I will always hold you very dear to my heart.

Financial support was provided by:

- 844/N-ESF EuroSolarFuels/10/2011/0 to **JK** (I am grateful for the very generous 3-year stipend)

- UMO-2013/11/N/NZ1/02390 to **JDJO** (I am grateful to NCN for giving me the opportunity to learn grant management skills and expand my scientific horizons)

- UMO-2014/15/B/NZ1/00975 to **JK** (I am grateful for the help at the end of the PhD)

- Faculty of Biology (I am grateful for the stipend from 2014 to 2015)

Abbreviations (in alphabetical order)

AA	Amino acid
ADP	Adenosine diphosphate
AEC	Anion exchange chromatography
AgNW	Silver nanowires
AM 1.5	Air mass coefficient
APS	Ammonium persulphate
Asc	Ascorbate or ascorbic acid
atm	Atmosphere
ATP	Adenosine tri-phosphate
Au	Gold
BCR	*β*-carotene
BSA	Bovine serum albumin
Cars	Carotenoids
Chl*a*/Chl*b*	Chlorophyll *a*/Chlorophyll *b*
CPCD	Confined-plume chemical deposition
CRC	Carbon dioxide reducing catalyst
CV	Cyclic voltammogram
Cyt b_6f	Cytochrome b_6f complex (plastoquinol-plastocyanin reductase)
Cyt c_{553}/cyt c_6	Cytochrome c_{553} / cytochrome c_6
DCPIP	2,6-Dichlorophenolindophenol
DDM	β-Dodecylmaltopyranoside
DET	Direct electron transfer
DGDG	Digalactosyldiacylglycerol
DITC	1,4-phenylene diisothiocyanate
DMSO	Dimethyl sulfoxide
DNA	Deoxyribonucleic acid
DSPEC	Dye-sensitised photoelectrochemical cell
DSSC	Dye-sensitised solar cell
DTT	1,4-Dithiothreitol
E	Elution
EDTA	Ethylene diamine tetra-acetic acid
EM	Electron microscopy
ETC	Electron transfer cofactors
eV	Electronvolt
EXAFS	Extended X-ray absorption fine structure
Fd	Ferredoxin
FF	Fill factor
FNR	Ferredoxin-NADP-reductase
FPLC/HPLC	Fast protein liquid chromatography/High performance liquid chromatography
FT	Flowthrough
F-T	Fischer-Tropsch
GC	Gas chromatography
H_2ase	Hydrogenase
HEC	Hydrogen evolving catalyst
HEPES	4-(2-hydroxyethyl)-1-piperazineethanesulfonic acid

HER	Hydrogen evolving reaction
HisProbe-HRP	Nickel (Ni^{2+}) conjugate of horseradish peroxidase
HL	High light illumination (150 µmoles photons m^{-2} s^{-1})
HVP	High value product
I	Induced
ICP-GFAAS	Inductively coupled plasma–Graphite furnace atomic absorption spectroscopy
ICP-MS	Inductively coupled plasma mass spectrometry
IEM	Inner envelope membrane
IMAC	Immobilised Metal Affinity Chromatography
IR	Infrared
IRF	Internal reflective factor
ITME	Instytut Technologii Materiałów Electronicznych/ Institute of Electronic Materials Technology
J_0	Recombination parameter/dark saturation current
J_{sc}	Short circuit current of a solar cell
LB	Lysogeny Broth, also known and Luria-Bertani madium
Lhc/Lhcr/Lhca/LHCI	Light harvesting complex/Light harvesting complex subunit r/Light harvesting complex subunit a/Light harvesting complex I
LL	Low light illumination (30 µmoles photons m^{-2} s^{-1})
Lut	Lutein
M	Protein size marker
MA	Mercaptoacetic acid
MCS	Multiple cloning site
MES	2-(N-morpholino)ethanesulphonic acid
MET	Mediated electron transfer
MGDG	Monogalactosyldiacyl glycerol
ML	Medium light illumination (90 µmoles photons m^{-2} s^{-1})
MOPS	3-morpholinopropane-1-sulfonic acid
MSA	Mercaptosuccinic acid
MWCO	Molecular weight cut-off
MV	Methyl viologen
MW	Molecular weight
η	External quantum efficiency of a solar cell
NaAsc	Sodium ascorbate
$NADP^+$/ NADP/NADPH	Nicotinamide adenine dinucleotide phosphate/reduced
NHE	Normal hydrogen electrode
Ni-NTA	Nickel–nitrilo acetic acid
NPQ	Non-photochemical quenching
OCP	Open circuit potential
OEC	Oxygen evolving complex
OEM	Outer envelope membrane
ORF	Open reading frame
P	Primary electron donor
P_{in}	power input of a solar cell
P680	Photosystem II primary donor
P700	Photosystem I primary donor
PAni	Polyaniline

PAR	Photosynthetically active radiation
PBS	Phosphate buffered saline
PBSs	Phycobilisomes
PC	Plastocyanin
PCR	Polymerase chain reaction
PEC	Photoelectrochemical cell
PG	Phosphatidylglycerol
Pheo	Phaeophytin
PhQ	Phylloquinone
P_i	Inorganic phosphate
PMF	Proton-motive force
PMS	Phenyl methyl sulphonate
PMSF	Phenyl methyl sulphonyl fluoride
PQ/PQH_2	Plastoquinone/Plastoquinol
PRC	Proton reducing catalyst
PSI	Photosystem I
PSII	Photosystem II
PSI-LHCI	Photosystem I with its associated light harvesting antenna
PV	Photovoltaic
PVA	Polyvinyl alcohol
PVDF	Polyvinylidene fluoride
PVP	polyvinylpyrrolidone
qE	energy-dependent quenching component of NPQ
RC	Reaction centre
RCF	Relative centrifugal force
RPM	Rotations per minutes
RT	Room temperature
SACLA	SPring-8 Ångstrom compact free-electron laser
SAM	Self-assembled monolayer
SDS-PAGE	Sodium dodecyl sulphate–Polyacrylamide gel electrophoresis
SEA	Sacrificial electron acceptor
SEC	Size exclusion chromatography
SED	Sacrificial electron donor
SEM	Scanning electron microscopy
SHE	Standard hydrogen electrode
Si/*p*-Si	Silicon/ *p*-doped silicon
SOEC	Solid oxide electrolysis cell
SPB	Standard phosphate buffer
SPCEC	Solid proton conducing electrolysis cell
SPR	Surface plasmon resonance
STPV	Solar thermophotovoltaic
TAE	Tris-acetate EDTA
TBST	Tris-buffered saline supplemented with 0.05% Tween-20
TCSPC	Time-correlated single photon counting
TEMED	Tetramethylethylenediamine
TOF	Turnover frequency
TON	Turnover number
U	Unbound
UV	Ultraviolet

Vio	Violaxanthine
VIS	Visible
V_{oc}	Open circuit potential of a solar cell
W	Wash
WOC	Water oxidation catalyst
WT	Wild type
XRD	X-ray diffraction
λ-NAD	Nicotinamide adenine dinucleotide

Abstract

One of the biggest challenges of modern-day solar technologies is to develop carbon-neutral, efficient and sustainable systems for solar energy conversion into electricity and fuel. Over the last two decades there has been a growing impact of 'green' solar conversion technologies based on the natural solar energy converters, such as the robust extremophilic photosystem I (PSI) and its associated protein cofactors. The main bottleneck of the currently available biophotovoltaic and solar-to-fuel technologies is the low power conversion efficiency of the available devices due to wasteful charge recombination reactions at the interfaces between the working modules, as well as instability of the organic and inorganic components.

This thesis describes the development of three novel approaches to improve energy and electron transfer in PSI-based biophotoelectrodes and plasmonic nanostructures: *(1)* construction of all-solid-state mediatorless biophotovoltaic devices incorporating *p*-doped silicon substrate, extremophilic robust PSI complex and its associated light harvesting antenna (PSI-LHCI) in conjunction with its natural electron donor cytochrome c_{553} (cyt c_{553}) from a red microalga *Cyanidioschyzon merolae* and *(2)*, biofunctionalization of the silver nanowires (AgNWs) with a highly organised architecture of the cyt c_{553}/PSI-LHCI assembly for the significant improvement of absorption cross-section of the *C. merolae* PSI-LHCI complex due to plasmonic interactions between the distinct subpool of chlorophylls (Chls) and AgNWs nanoconstructs. The third (*3*) approach was based on development of the photo-driven *in vitro* hydrogen production system following hybridisation of the robust extremophilic PSI-LHCI complex with the novel and established proton reducing catalysts (PRC). The last approach has led to generation of molecular hydrogen with TOF of 521 mol H_2 (mol PSI)$^{-1}$ min^{-1} and 729 mol H_2 (mol PSI)$^{-1}$ min^{-1} for the hybrid systems of PSI-LHCI with cobaloxime and the DuBois-type mononuclear nickel proton reduction catalysts, respectively. The TOF values for biophotocatalytic H_2 production obtained in this study were 3-fold and 16.6-fold higher than those published for cyanobacterial PSI/PRC hybrid systems employing cobaloxime and a similar Ni mononuclear PRC, respectively.

Construction of all-solid-state mediatorless PSI-based nanodevices was facilitated by biopassivation of the *p*-doped Si substrate with His_6-tagged cyt c_{553}, as evidenced by significant lowering of the inherent dark saturation current (J_0), a well-known semiconductor surface recombination parameter. Five distinct variants of cyt c_{553} were obtained by genetically engineering the specific linker peptides of 0-19 amino acids in length between the

cyt c_{553} holoprotein and a *C*-terminal His_6-tag, the latter being the affinity 'anchor' used for specific immobilisation of this protein on the semiconductor surface. The calculated 2D Gibbs free energy maps for all the five cyt c_{553} variants and the protein lacking any peptide linker showed a much higher number of thermodynamically feasible conformations for the cyt *c* variants containing longer linker peptides upon their specific immobilisation on the Si surface. The bioinformatic calculations were verified by constructing the respective cyt c_{553}/Si bioelectrodes and measuring their dark current-voltage (*J-V*) characteristics to determine the degree of *p*-doped Si surface passivation, measured by minimisation of the J_0 recombination parameter. The combined bioinformatic and *J-V* analyses indicated that the cyt c_{553} variants with longer linker peptides, up to 19AA in length, allowed for more structural flexibility of immobilised cyt c_{553} in terms of both, orientation and distance of the haem group with respect to the Si surface, resulting in efficient biopassivation of this semiconductor substrate. This molecular approach has allowed for the developing of an alternative, cheap and facile route for significant reduction of the inherent minority charge recombination at the *p*-doped Si surface.

To improve direct electron transfer within all-solid state PSI-based nanodevices, the specific His_6-tagged cyt c_{553} variants, generated in this study, were attached to the Ni-NTA-functionalised *p*-doped Si surface prior to incorporation of the PSI-LHCI photoactive layer. Such nanoarchitecture resulted in an open-circuit potential increment of 333 µV for the specific PSI-LHCI/cyt c_{553}/Si nanodevice compared to the control device devoid of cyt c_{553}. Moreover, the all-solid state mediatorless PSI-LHCI-based devices produced photocurrents in the range of 104-234 µA/cm^2 when a bias of -0.25 V was applied, demonstrating one of the highest photocurrents for this type of solid-state devices reported to date. The power conversion efficiency of the PSI-LHCI/*p*-doped Si devices was 20-fold higher when 19AA variant of cyt c_{553} was incorporated as the biological conductive interface between the PSI-LHCI photoactive module and the substrate, demonstrating the significant role of this cyt variant for improving direct electron transfer within the PSI-based all-solid-state mediatorless biophotovoltaic device.

In a complementary line of research, it was demonstrated that the highly controlled assembly of *C. merolae* PSI-LHCI complex on plasmon-generating AgNWs substantially improved the optical functionality of such a novel biohybrid nanostructure. By comparing fluorescence intensities measured for PSI-LHCI complex randomly oriented on AgNWs and the results obtained for the PSI-LHCI/cyt c_{553} bioconjugate with AgNWs it was concluded

that the specific binding of PSI-LHCI complex with the defined uniform orientation yields selective excitation of a pool of Chls that are otherwise almost non-absorbing. This is remarkable, as this work shows for the first time that plasmonic excitations in metallic nanostructures not only can be used to enhance native absorption of photosynthetic pigments, but also, by employing cyt c_{553} as the conjugation cofactor, to activate the specific Chl pools as the absorbing sites, only when the uniform and well-defined orientation of PSI-LHCI complex with respect to plasmonic nanostructures is achieved. This innovative approach paves the way for the next generation solar energy-converting technologies to outperform the reported-to-date biohybrid devices with respect to power conversion efficiency.

Chapter 1 Introduction

1.1 The fundamental processes of oxygenic photosynthesis

The simple resources of water, sunlight and carbon dioxide power so much motion and activity in the world. The photosynthetic apparatus that enables the fundamental process of natural photosynthesis consists of components that operate in an extremely sophisticated orchestration of steps. A more thorough and comprehensive understanding of the fundamental aspects of photosynthesis not only has revealed an indispensably applicable plethora of knowledge, but has indisputably been of importance in trying to meet the rapidly increasing energy demand of humankind.

The evolution of oxygenic photosynthesis resulted in an explosive change in the biosphere of our planet as the atmosphere then became capable of sustaining aerobic respiration and ultimately, higher complexity of life. Most organisms – including oxygenic photoautotrophs – use oxygen for cellular respiration. Interestingly, oxygen is considered as the by-product of the photosynthetic water splitting reaction. Our current biosphere functions in a way which requires continuous oxygen consumption for essential respiratory biological processes to take place.

Photoautotrophs are not limited to oxygenic photosynthesis, as anaerobic photoautotrophy can also take place in some organisms, e.g., non-sulphur purple bacteria or green-sulphur bacteria. In oxygenic photosynthesis water is normally employed as the source of reducing equivalents, but some organisms have the capability of using other compounds as electron donors. Examples include small organic molecules and hydrogen gas, formate, acetate, or methanol, and hydrogen sulfide in the case of green-sulphur bacteria.

The introduction of this PhD thesis will encompass the most recent advances in dissecting the mechanisms of natural oxygenic photosynthesis at the molecular level. With organic thin-film arrays and solid-state solar cells already surpassing the efficiency of phototrophs in terms of power conversion efficiency, it may seem perhaps that little could be gained from elucidating nature's approach in photosynthesis, but further understanding of this rather complex and fundamental process may in fact continue to improve the efficiency of conversion of sunlight into electricity and perhaps more practically, into storable high-density liquid or gaseous fuels.

1.1.1 Overview of products and chemical reactions of oxygenic photosynthesis

All chemical reactions occur due to the flow of electrons, so understanding their movement is critical to understanding chemical processes. In photosynthesis, excited electrons are transferred in a series. This is core to the conversion of sunlight to energy equivalents stored in chemical bonds of organic molecules. Oxidation and reduction reactions are the terms used to describe this movement of electrons. The term 'oxidising' refers to accepting a compound's electrons, and 'reducing' refers to donating of electrons.

In cells, energy equivalents are ultimately stored as chemical bonds. Formation of bonds is achieved through electron movement. The reaction below summarizes photosynthesis and shows the formation of carbohydrates (**Eq. 1**); it does not show additional products that can be made and only conveys mass balance stoichiometric aspects:

$$CO_2 + H_2O \rightarrow (CH_2O)_x + O_2 \qquad \textbf{(Eq. 1)}$$

During photosynthesis, cellular energy equivalents are stored temporarily in two molecules, chiefly NADPH and ATP. In subsequent reactions, these two compounds are utilised to achieve long-term energy storage by synthesising carbohydrates. The energy from photons is employed to form the 'high energy bond' between ADP and P_i (inorganic phosphate) during the formation of ATP. One could think of ATP as the "energy currency" of photosynthesis (and the whole cellular metabolism), as it serves as an energy investment for later reactions that otherwise would not occur. Specifically, photosynthesis can reverse the equilibrium of key reactions by coupling the chemical reactions with ATP hydrolysis (**Eq. 2**). As an illustration, the equilibrium of the reaction adding phosphate to glucose is shifted to the product, glucose-6-P (**Eq. 3** and **4**).

$$ATP + H_2O \rightarrow ADP + P_i \ (-31 \text{ kJ mol}^{-1}) \qquad \textbf{(Eq. 2)}$$

$$P_i + \text{glucose} \rightarrow \text{glucose-6-P} + H_2O \ (+ 14 \text{ kJ mol}^{-1}) \qquad \textbf{(Eq. 3)}$$

$$\text{glucose} + \text{phosphate} \rightarrow \text{glucose-6-P} \ (-17 \text{ kJ mol}^{-1}) \qquad \textbf{(Eq. 4)}$$

The transfer of electrons to reduce $NADP^+$ also enables the transfer of protons across the photosynthetic membrane (so-called thylakoid). This results in generation of the proton gradient across the membrane, which in turn produces a proton motive force (pmf). The movement of protons through membrane-bound cytochrome *b_6f* (cyt *b_6f*) from the side of high proton concentration to low concentration generates sufficient mechanical force to produce a conformational change (a rotation to be more specific) in the enzyme ATPase (also bound

within the same photosynthetic membrane), which in turn enables it to catalyse the production of ATP.

Conventionally, the light reactions (known as the photosynthetic primary reactions) are the light-driven redox reactions that are responsible for production of ATP and NADPH. The overall light reaction is summarised below:

$$2H_2O + 2NADP^+ + 3ADP \rightarrow 3P_i + O_2 + 2NADPH + 3ATP \qquad \textbf{(Eq. 5)}$$

where P_i is a free phosphate ion that is negatively charged

The movability of NADP and ATP allows for the series of dark reactions to occur in a separate soluble compartment, the stroma, from where energy from photons is collected in the form of chemical bonds of carbohydrates. Analogously, one can envisage how electricity generated in one place may be stored in fuel or batteries elsewhere.

In conclusion, the production of carbohydrates by photosynthesis occurs in two sets of reactions: (1) those yielding NADPH and ATP (light reactions, also known as the primary reactions of photosynthesis) and (2) light-independent reactions that utilise these high-energy molecules for reductive synthesis of organic products from CO_2 (dark reaction, also known as the secondary reactions of photosynthesis).

1.1.2 Primary reactions of oxygenic photosynthesis: energy and electron transfer

Charge separation results from an electron leaving its location within a bond in a molecule, leaving behind a positive charge (a hole). As opposite charges attract, their separation requires an input of energy, which in photosynthesis comes from the energy of photons. The captured solar energy expels electrons from the pigment molecules of the so-called primary donors to higher energy levels, or in terms of molecular orbital theory, it promotes electrons from lower molecular orbitals to higher molecular orbitals.

It is known that 8-10 photons must be captured to fix each molecule of CO_2 [1]. The photons travel all the way from the Sun before participating in photosynthesis, but then they are very quickly utilised. Photons produced by our solar system's nuclear reactor travel 10,000 years from the Sun, and cover a distance of 150,000,000 km in about 8 min. to reach our atmosphere, and within a time frame of 100 ps they are captured and channelled in the reaction centres of photosystem I (PSI) and photosystem II (PSII) that are present in the thylakoid membranes of oxygenic photoautotrophs [2].

The light-harvesting modules in photosynthesis absorb photons of certain wavelength very efficiently, then tunnel them to the photochemical reaction centres containing a specialised chlorophyll (Chl) *a* pair, known as the primary donor. As a matter of fact, the primary donor operates almost perfectly – one electron is excited every time a photon is absorbed within the proper wavelength range of red light. This miracle of nature is accomplished in PSI by a very complex system – in higher plant PSI there are 190 pigments incorporated in the protein scaffold in addition to several other cofactors and lipids. Excited electrons routinely pass through these light-absorbing pigments before reaching their destination, the primary donor [3].

The efficiency of photosynthesis, is limited, as it utilises only a subset of visible light within the red and blue regions of solar light. Moreover, the visible spectrum of photosynthetically active radiation (PAR), 400-800 nm, represents merely half of the solar spectrum that reaches the Earth. The wavelength range available to use in each photoautotroph is dictated by the composition of the pigment molecules within and/or surrounding the reaction centres (**Figure 1**).

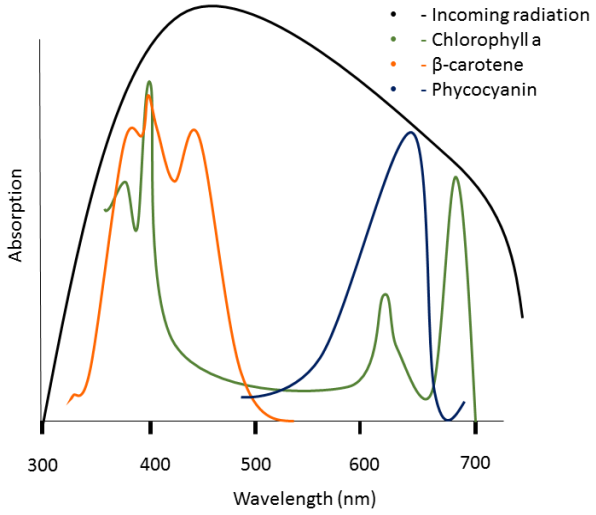

Figure 1

Spectrum of sunlight in the visible region and absorption of various pigment molecules.

Most of the photons utilised are in the blue and red regions. Adapted from [4].

1.1.3 Primary donor excitation and electron transfer pathways

In natural photosynthesis, PSII complex present in oxygenic phototrophs (plants, algae and cyanobacteria) catalyses the light-driven water splitting reaction, while PSI generates highly reducing potential (E_m of −1.3 eV) to power electrons derived from water for generation of a biological "hydrogen storage" molecule, NADPH. Both photosystems act concomitantly as their Chl*a*-containing reaction centres (termed P680 and P700 for PSII and PSI, repectively) absorb quanta of red light to drive a unidirectional electron flow through intricately organised branches of redox-active cofactors (see **Figure 2**). As briefly introduced, with the aid of a third redox-active protein complex, cyt b_6f, which in the thylakoid membrane is localised between PSII and PSI, an electrochemical potential gradient of protons is also formed, driving the activity of the thylakoid-bound ATP synthase to chemiosmotically produce ATP. ATP and NADPH are subsequently used for reduction of CO_2 into sugars in the dark reactions of oxygenic photosynthesis, as well as several other biomass components [5].

Natural photosystems operate as nearly perfect photoelectrical devices, exhibiting a quantum efficiency close to 100%. The spatial organisation of light absorbing pigments, redox-active cofactors and metals of the water-oxidation complex (WOC) of PSII are optimised to facilitate and maximize forward electron transfer and minimise wasteful back reactions. As a matter of fact, structural analysis of various photosynthetic reaction centres (including those from anoxygenic photosynthetic bacteria) revealed that these centres all share a common structural blueprint: they all contain a charge-separator cofactor assembly embedded with a protein dimer composed of 5-transmembrane spanning domains, as well as the light harvesting system [6]. The photosynthetic unit rapidly harnesses solar energy across the whole PAR spectrum and rapidly tunnels it efficiently to the associated reaction centres, with minimal energy losses at relatively low light intensities. This is possible through the presence of various pigments with different and varying spectral properties and their discrete interactions with the protein scaffold to which they bind. The overall transfer times of energy migration from the light harvesting system to the reaction centre occurs on a sub-nanosecond timescale [6–8].

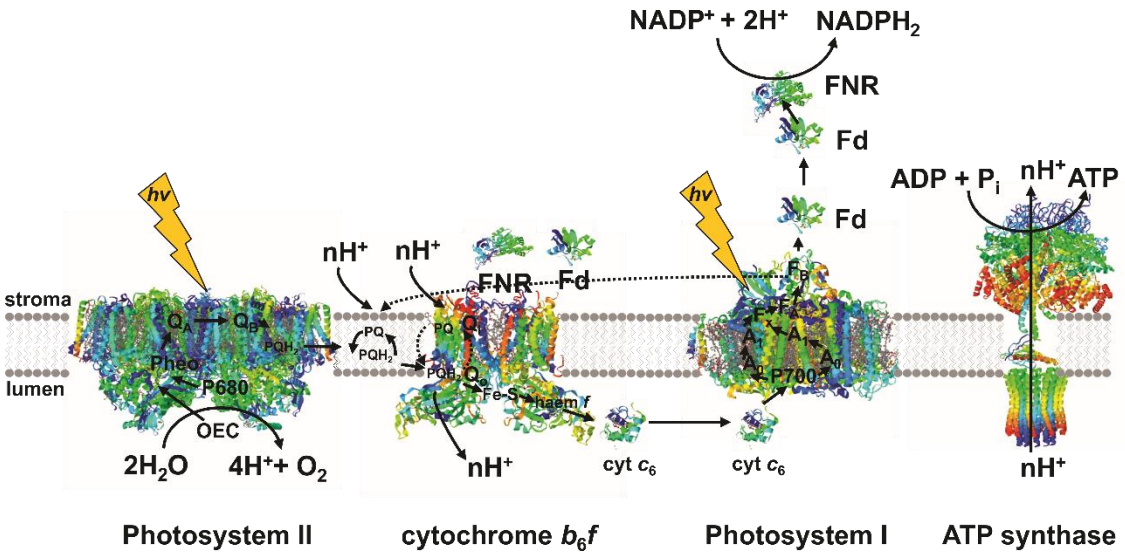

Figure 2

Linear and cyclic electron transfer pathways in oxygenic photosynthesis. Reproduced from [9] with updated crystal structures from photosystem II (PSII), cytochrome *b*$_6$*f* (cyt *b*$_6$*f*) and photosystem I (PSI) (see below for PDB accession numbers and respective references). Linear and cyclic electron transport and regeneration of reducing equivalents along with NAPDH and ATP is performed by the concerted action of PSII (4UB6 [10]), cyt *b*$_6$*f* (4PV1, [11]) and PSI (4XK8 [3]), aided by the mobile electron carriers: plastocyanin in higher plants and green algae (PC) or cytochrome *c*$_6$ (cyt *c*$_6$, 1CYI [12]) in cyanobacteria and green algae; ferredoxin (Fd, 3AB5 [13]) and ferredoxin:NADP$^+$ reductase (FNR, 1FNB [14]). The ATP synthase powers the formation of ATP thanks to the proton motive force generated by photo-oxidation of water and the subsequent electron transport across the thylakoid membrane. NADPH and ATP generated during the light reactions are subsequently employed for fixation and reduction of CO_2 into carbohydrates (not shown). When ATP is consumed under certain metabolic circumstances, cyclic electron flow is induced (dotted arrow) which produces ATP without production of NADPH. The Mn_4CaO_5 which comprises the oxygen evolving complex (OEC) is buried within he donor side of PSII. F_X, F_A, F_B – [4Fe – 4S] clusters; A_1 – phylloquinone; A_0 – Chl*a*; PQ/PQH_2 – plastoquinone/plastoquinol: oxidised and reduced plastoquinone; Q_A, Q_B – primary and secondary quinone electron acceptors; Pheo – pheophytin: a primary electron acceptor in PSII.

As shown in **Figure 2,** the continuous demand of the photosynthetic apparatus for electrons requires a substrate to sustain the supply; in the case of oxygenic photosynthesis, that source is water. During evolution, the ability of the protoautotroph to oxidise water – and hence generate protons, electrons and molecular oxygen – ultimately resulted in the evolution of oxygenic photosynthesis, and ultimately highly efficient aerobic respiration.

$$2H_2O \rightarrow O_2 + 4H^+ + 4e^- \quad \textbf{(Eq. 6)}$$

The redox power of photosynthesis is remarkable. The reaction centres of PSII and PSI are the strongest oxidant and strongest reductant known in biology, respectively. The reaction centre of PSII, P680 is a strong oxidant (E_m +1.25 eV) that is responsible for water oxidation and formation of molecular oxygen as the by-product of this reaction.

Regulation of photosynthetic electron transport in the thylakoid membrane is a fundamental feature for coping with dynamic fluctuations in light intensity and variable demand for ATP and NADPH. The abovementioned process, known as linear electron transport, generates a proton gradient across the thylakoid membrane (ΔpH) through the combination of protons generated by the water-splitting complex associated with PSII and proton translocation associated with electrons passing through the cyt b_6f complex [15]. The ΔpH together with a membrane potential formed across the thylakoid membrane (Δψ) drives ATP production by ATP synthase. In addition, the water-water cycle (Mehler reaction), in which electrons, through linear electron transport, reduce O_2 to O_2^- in the chloroplast, are coupled to the generation of ΔpH, which drives ATP synthesis without accumulating NADPH [16].

In contrast to linear electron transport, cyclic electron transport requires only cooperation of PSI with the cyt b_6f complex to generate the ΔpH. This gradient is able to drive ATP synthesis without producing NADPH in chloroplasts [17]. Importantly, an additional consequence of the trans-thylakoid ΔpH is that it alters energy dissipation from the light-harvesting complexes *via* induction of the energy-dependent quenching component (qE) of nonphotochemical quenching (NPQ) of absorbed light [18]. Notably, several studies have indicated that cyclic electron transport around PSI requires only PSI photochemical reactions to efficiently operate under excess-light conditions [19–21], although its physiological relevance and precise molecular mechanisms still remain an open question.

Each of the two charge-separation transmembrane complexes (PSI and PSII) in the thylakoid membrane have distinct pigment composition with unique absorption

characteristics. Therefore, an imbalance of energy distribution between the two photosystems tends to occur in natural habitats, where light quantity and quality fluctuate at different time intervals [22]. Because these two photosystems are functionally connected in series under natural conditions, plants and algae must constantly have to balance their excitation levels to ensure perfect efficiency of electron flow. State transitions happen under such conditions to equilibrate the light-harvesting capacities of the two photosystems, thereby minimising the unequal distribution of light energy. Classically, State 1 occurs when PSI is favourably excited and the light-harvesting capacities of PSII and PSI are increased and decreased, respectively, to compensate for the excitation imbalance between both photosystems; this state is indicated by pointedly higher Chl fluorescence yield at room temperature. On the other hand, State 2 occurs when PSII is favourably excited and the light harvesting capacities of PSII and PSI are decreased and increased, respectively, to readjust the excitation imbalance; this state may be monitored as a lower Chl fluorescence yield at room temperature [22].

One of the major discoveries in this field occurred with the isolation of the megasupercomplex conducting cyclic electron flow in the green alga *Chlamydomonas reindhardtii*, upon chemical induction of State 2 [23]. The isolated megasupercomplex was composed of PSI with its associated light-harvesting complex (LHCI), the PSII light-harvesting complex (LHCII), the cyt b_6f complex, Fd-NADPH oxidoreductase (FNR), and the trans-membrane protein PGRL1 [23]. Spectroscopic analyses indicated that upon illumination, reducing equivalents from downstream PSI were transferred to cyt b_6f, whereas oxidised PSI was re-reduced by electrons from cyt b_6f, indicating that this megasupercomplex is engaged in the cyclic electron flow [23]. Thus, the authors claim that formation and dissociation of the PSI–LHCI/LHCII/FNR/cyt b_6f/PGRL1 supercomplex not only switched the mode of photosynthetic electron flow (from linear to cyclic), but also controlled the energy balance between the two photosystems [23].

More recently, State 1 and State 2 PSI and PSII supercomplexes from *Chlamydomonas reindhardtii* have been purified and analysed [24]. It was shown that PSI was capable of binding two LHCII trimers that contained all four major Lhcb isoforms in State 2, and one minor Lhcb monomer, most probably CP29, in addition to the nine Lhca subunits of the LHCI complex [24]. This structure was the largest PSI complex ever observed, having an antenna size of 340 Chls/P700. Furthermore, it was demonstrated that all Lhcas bound to PSI were able to transfer energy efficiently to the PSI reaction centre [24]. A 20Å EM projection map of the supercomplex was obtained which revealed the structural organisation of this complex

(see [24]). Moreover, the authors claimed that only LHCII type I, II and IV, are in fact phosphorylated when associated with PSI, in contrast to LHCII type III and CP29 subunits which are not phosphorylated upon their association with PSI. Interestingly, CP29 was shown to be phosphorylated when associated with PSII in State 2, confirming the crucial role of this post-translational modification in inducing conformational changes of this subunit during state transitions [24].

Figures 3 and **4** display the *Z*-scheme of photosynthesis, with different times of reactions and energy in eV associated with every step of the photosynthetic electron transfer pathway.

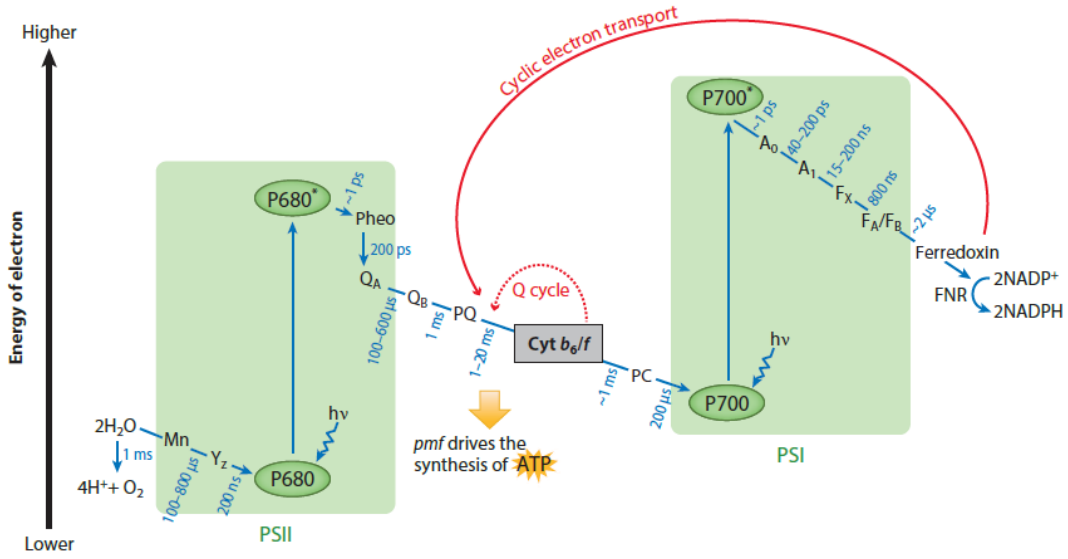

Figure 3

***Z*-scheme of photosynthetic electron transfer from H_2O to $NADP^+$, including estimated times for the various steps.** Reproduced from [18]. The solid blue arrows display linear electron flow, the solid red arrow shows cyclic electron flow around PSI, and the dotted red arrow shows the Q cycle of the cyt b_6f complex. Electrons transported in series produce pmf, which ultimately drives ATP production catalysed by the chloroplast ATP synthase. Abbreviations (left to right): PSI/II, photosystem I/II; Mn, manganese cluster; Y_z, tyrosine 161 in the D1 protein; P680, reaction centre of PSII; P680*, excited P680; Pheo, primary electron acceptor of PSII; PQ, plastoquinone pool; pmf, proton motif force; cyt b_6f, cytochrome b_6f complex; PC, plastocyanin; P700, reaction centre of PSI; hγ, photon energy; P700*, excited P700; A_0, primary electron acceptor of PSI; F_X, F_A, and F_B, three different iron-sulphur centres; FNR, ferredoxin-NADP reductase.

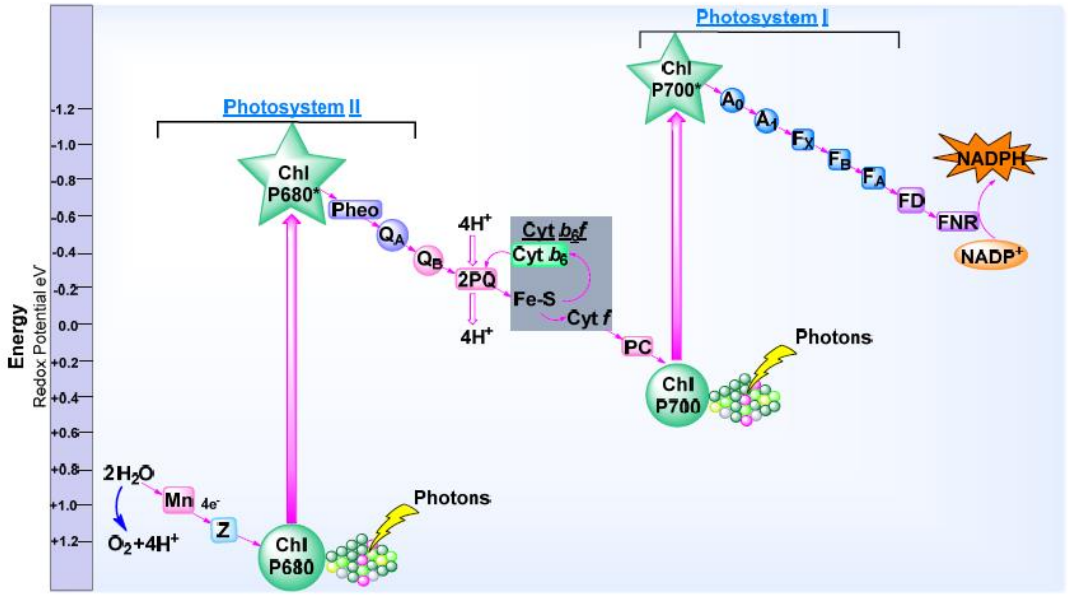

Figure 4

***Z*-scheme of photosynthesis displaying different energy levels (in eV).** Reproduced from [25]. The primary reactions of photosynthesis have a very large energetic spread, ranging from almost +1.25 eV to -1.3 eV, which is bioenergetically impressive.

1.2 Structure and function of the oxygenic photosynthetic apparatus

In order to fully understand the design intricacies of the oxygenic photosynthetic machinery, a comprehensive and thorough understanding of each component's structure is essential. Extensive structural investigations have enlightened us over the last two decades with the near-atomic or medium resolution X-ray structures of these complexes, particularly those of PSII and PSI, which are exclusively responsible for solar energy capture and ultimate photo-electrical conversion.

Below are subchapters referring to structural characterisation of the components of oxygenic photosynthetic apparatus, including cytochrome c_{553} (cyt c_{553}), which plays a crucial role in mediating electron transfer between cyt b_6f and PSI in a model organism used in this PhD study, an extremophilic red microalga *Cyanioschyzon merolae*.

1.2.1 Photosystem II as H_2O-plastoquinone oxidoreductase

The structure of PSII was solved by X-ray diffraction (XRD) at 1.9 Å resolution, and showed, as in all the previous X-ray structures of this complex [26–32], that the oxygen-evolving complex (OEC) is a Mn_4CaO_5-cluster coordinated by a properly defined protein environment [33]. Extended X-ray absorption fine structures (EXAFS) studies have shown that the manganese cations in the OEC are easily reduced by X-ray radiation and therefore, the distance between the Mn-Mn atoms differs between XRD studies and EXAFS [27–29,34–36].

For the first time, a 'radiation-damage-free' structure of PSII from *Thermosynechococcus vulcanus* has been reported at a resolution of 1.95 Å in the S_1 (dark) state employing the most advanced state-of-the art femtosecond X-ray pulses of the SPring-8 Ångstrom compact free-electron laser (SACLA) using hundreds of large, highly isomorphous PSII crystals [10]. This achievement is revolutionary, as for the first time the entire, intact, operational oxygen-evolving complex (OEC) has been elucidated in its entirety, contributing invaluably to our understanding of the complete mechanism of biological water oxidation in oxygenic phototrophs.

The PSII complex is a multimeric pigment-protein complex embedded in the thylakoid membranes of cyanobacteria, green algae and higher plants. It is the only multimeric macromolecular protein complex capable of oxidising water using visible light. Biological water oxidation results in the release of electrons, oxygen molecules and protons at the catalytic centre of PSII, specifically, the OEC. The process encompasses four consecutive electron and/or proton removing steps within the S_i-state cycle (with i = 0-4, where i indicates

the number of oxidative equivalents accumulated) [10]. Because of its ability to perform biological photolysis rather efficiently [10], the OEC is considered a potential, very promising template for the synthesis of artificial catalysts for water-splitting, with the ultimate purpose of obtaining clean and renewable energy from sunlight, as will be explained in the subsequent chapters of this PhD thesis.

The PSII complex occurs as a dimer and each monomer contains 20 subunits with a total molecular mass of 350 kDa [28,31,33,34,36,37] for each monomer (see **Figure 5**, **Panel A**) The latest X-ray structure of the cyanobacterial dimeric PSII complex revealed that in addition to the protein subunits, there are 35 Chls, 11 β-carotenes, two pheophytins, more than 20 lipids, 2 haem irons, 2 plastoquinones, 1 non-haem iron, 4 manganese atoms, 3-4 calcium atoms (one of which is in the Mn_4Ca cluster), 3 Cl^- ions (two of which are in the vicinity of the Mn_4Ca cluster), 1 bicarbonate ion and more than 15 detergents per monomer [33]. Each monomer contains more than 1,300 water molecules, yielding a total of 2,795 water molecules in the dimer (see **Figure 5**, **Panel B**). As shown, the water molecules are organised in two layers located on the surfaces of the lumenal and stromal sides, with the former having more water molecules than the latter. Some water molecules have been found within the membrane region, most of them serving as ligands to Chls [33]. **Figure 6** displays the organisation of the OEC and its protein environment [10]. **Figure 7** presents the possible mechanisms for biological water oxidation based on the assumption that when the S_2 state is reached, one electron may be removed from Mn4A, leading to a dextro-open structure ('R-type'), or from Mn1D, leading to a levo-open structure ('L-type') [10].

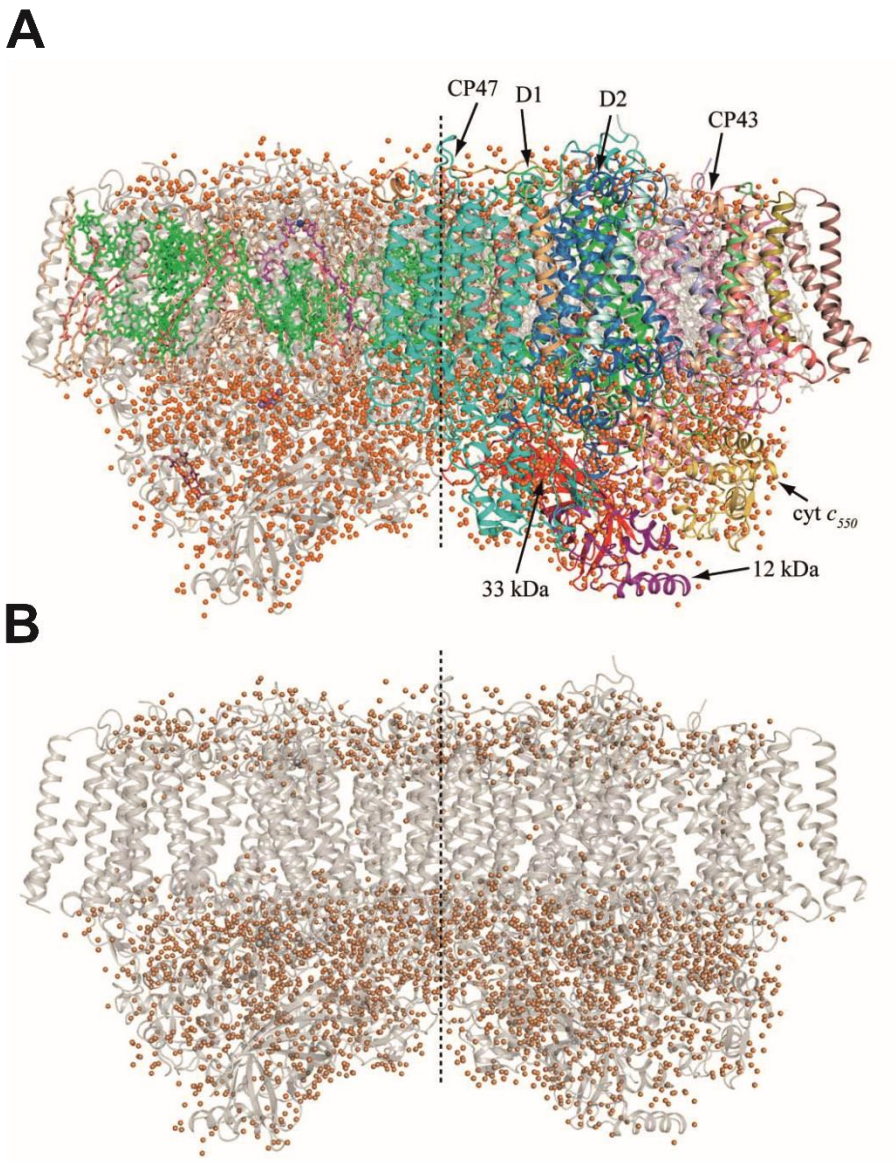

Figure 5

PSII overall structure from *T. vulcanus* at a resolution of 1.9 Å. Reproduced from [33]. Plane view is perpendicular to the membrane normal. A: Overall structure of the monomer complex. The protein subunits are coloured individually in the right-side monomer and in light-grey of the left-side monomer. The OEC is embedded close to the 33-kDa protein and can be distinguished by a considerable cluster of water molecules. Water molecules are represented by orange balls. B: Water molecule arrangement in the PSII dimer. Protein subunits are coloured in light grey and all other cofactors are omitted for simplicity. Central dotted lines are non-crystallographic and indicate monomer-monomer interaction. PDB code: 3ARC.

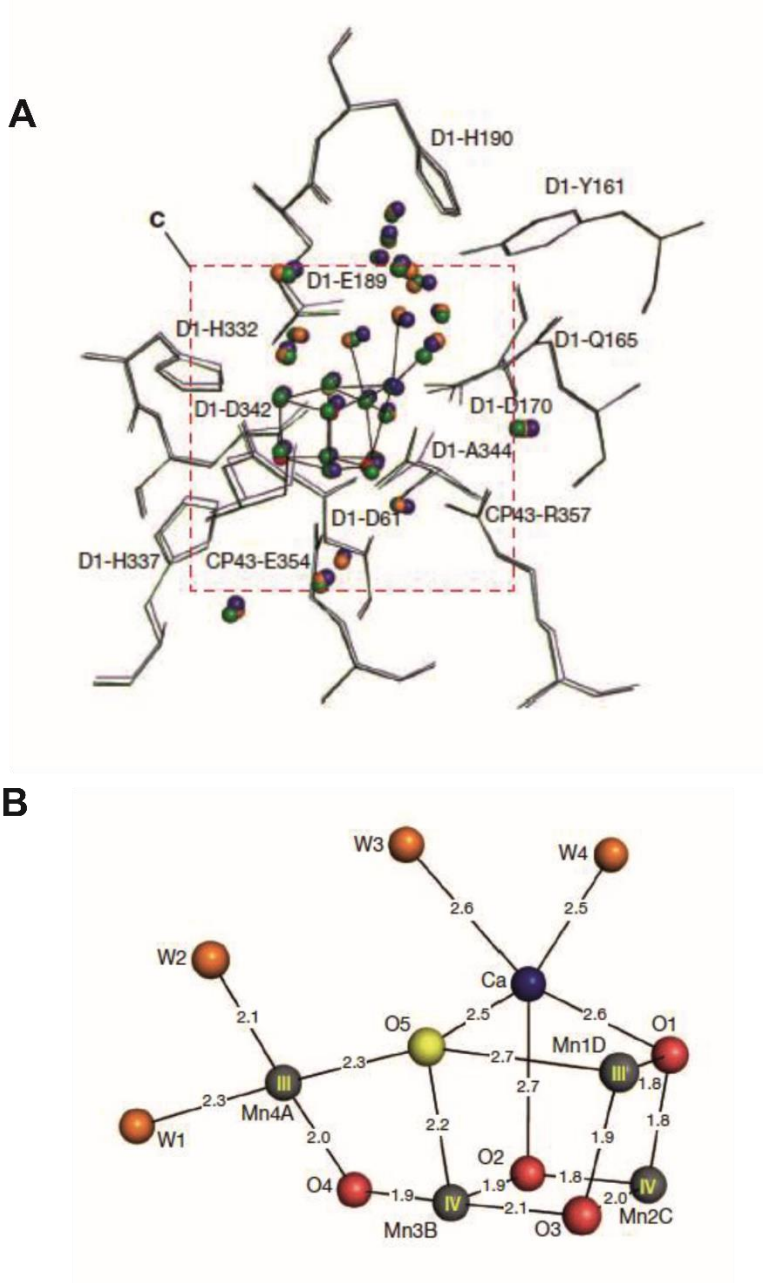

Figure 6

X-ray structure of the OEC and its ligand environment at 1.9 Å. Reproduced with identical labelling from [10]. A: Superposition of the OEC and its ligand environment from the three structures available. For clarity, the structures and protein environment are labelled. B: Overall structure of the chair comprising the OEC. Orange spheres; water molecules, grey spheres; manganese atoms, red spheres, oxygen atoms; blue sphere, calcium atom. Distances between atoms are displayed in Angstroms. Labelling of atoms is as specified in [10].

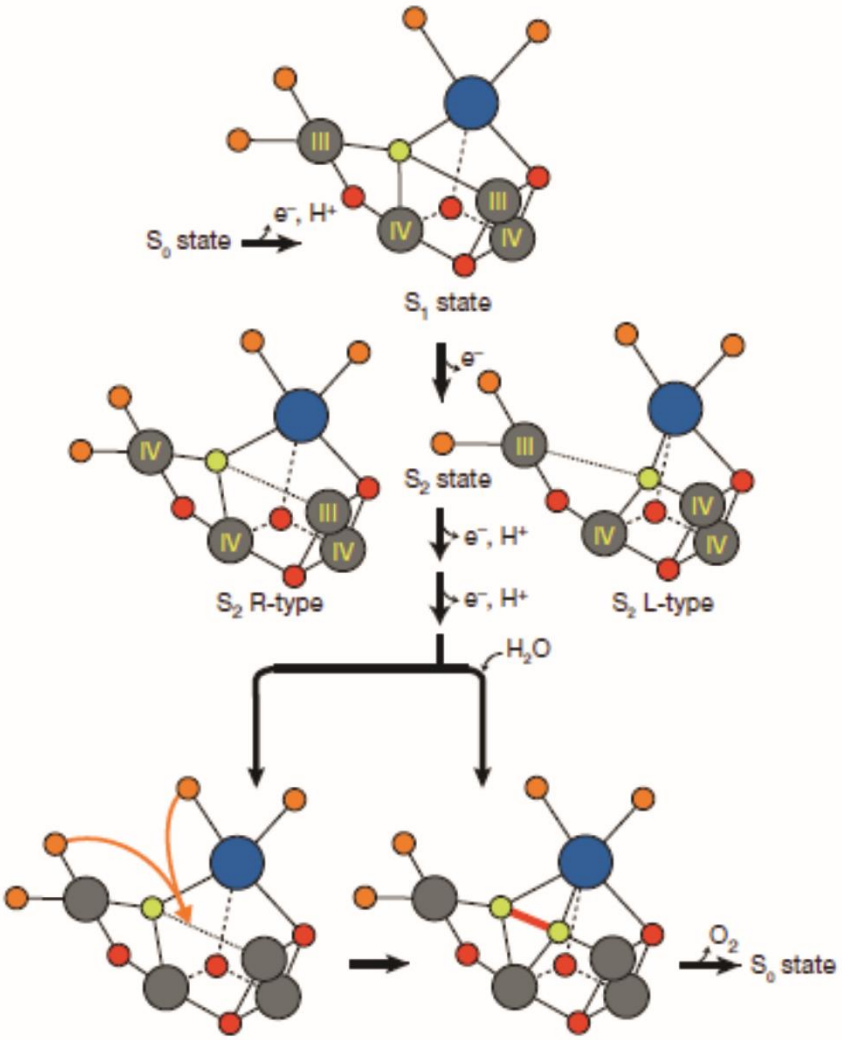

Figure 7

Possible mechanisms for photosynthetic water oxidation. Reproduced from [10]. In the S_1 state O5 is connected to both Mn1D (III) and M4A (III). When the S_2 state is reached, one electron may be removed from Mn4A, leading to a dextro-open structure ('R-type'), or from Mn1D, leading to a levo-open structure ('L-type'). Both structures will allow insertion of a new water molecule from the nearby microenvironment during the following S-state transition, in preparation for the transition state immediately before O=O bond formation (this is indicated by a red bond in the right-hand structure of the bottom row). In contrast, the transition state preparing for O=O bond formation may be formed by moving either W2 or W3 towards O5 (this is indicated in the left-hand structure from the bottom row).

The precise mechanism of the water-splitting reaction is still a matter of heated debates and its intricacies are beyond the scope of this PhD thesis. Nonetheless, the PSII complex is responsible for all oxygenic life on Earth, and its ability to perform photon-powered biological water oxidation is unique and awe-provoking. Therefore, understanding the complete mechanism of photosynthetic water photooxidation will not only elucidate the chemical nature of this energetically demanding reaction, but it has inspired chemists to build the artificial water-splitting catalysts [38–40] that could match or even hopefully outperform PSII in the not-too-distant future.

Recently, the first X-ray structure of the eukaryotic (red algal) PSII dimer has been revealed, showing the structural similarities and differences with its cyanobacterial counterpart [41]. The X-ray structure of the PSII dimer of *Cyanidium caldarium* has been reported at a 2.76 Å resolution, where the presence of the lumenal PsbQ' subunit and its interaction sites are revealed. This protein subunit functions as a fourth extrinsic protein required for stabilising the OEC on the lumenal surface of PSII [41]. Significantly, the X-ray structure confirmed the earlier electron microscopy/single particle analysis study [42] that PsbQ' is present right under the lumenal domain of the CP43 inner light harvesting subunit, close to PsbV extrinsic subunit. Moreover, it reveals four up-to-down helices arranged in a similar fashion to those of cyanobacterial and higher plant PsbQ homologues, although helices I and II of PsbQ' were kinked compared to its higher plant counterpart due to its interactions with CP43 [41]. Furthermore, the structure revealed two previously unknown transmembrane helices which are not present in the cyanobacterial PSII dimer. The authors propose that one of them may correspond to PsbW which is exclusively present in eukaryotic PSII.

1.2.2 Cytochrome b_6f as plastoquinol-oxidised-plastocyanin oxidoreductase

Integral membrane cytochrome *bc* lipoprotein complexes (namely cyt *bc* complexes) b_6f and bc_1 play critical roles in photosynthetic and respiratory electron transport chains, respectively, where they regulate electron transfer by coupling transmembrane proton translocation to membrane electron transfer through redox reactions of plastoquinone/plastoquinol and ubiquinone/ubiquinol, respectively [11,43–47]. Plastoquinone in photosynthetic membranes, contains a redox active ring that is attached to a 45-50 carbonyl prenyl tail (See **Figure 8, Panel A**). On the electro-positive side of *bc* complexes (known as p-side), quinol deprotonation-oxidation occurs within the Q_p domain and it involves quinol entry into an 11 Å portal that connects the Q_p site to the quinone pool in the lipid-full intermonomer cavity of *bc* complexes, as clearly shown in detail for the X-ray structure of the cyt b_6f complex [48] (See **Figure 8, Panel B**).

The main function of cyt b_6f is to: (i), couple electron transfer from plastoquinol on the stromal side of the membrane to a soluble cyt c_6 or plastocyanin on the lumenal side of thylakoids and (ii), generate a transmembrane electrochemical proton gradient [49]. This happens *via* a two-electron oxidation of hydroplastoquinone coupled with the release of two protons at the Q_o on the lumenal side of thylakoids. One electron is transferred through a high-potential chain constituting a [2Fe-2S] cluster (also known as "Rieske cluster" or the "Rieske iron-sulphur protein") and a haem *f*, similar to c_1 in cytochrome bc_1, in contrast to the other electron which travels through haems b_L and b_H to reduce quinone at the Q_i site on the other side of the membrane, the stromal side. Upon two sequential reduction events at the Q_i site, two protons are taken up from the stroma. This way, a proton electrochemical gradient is generated through the release and uptake of protons on either side of the membrane [49].

Three dimensional structures of the cyt b_6f complex have been obtained at a resolution of 3.0-3.1 Å from the thermophilic filamentous cyanobacterium, *Mastigocladus laminosus* (PDB code: 1VF5) [50] and the green alga, *Chlamydomonas reinhardtii* (PDB code: 1Q90) [49] in the presence of the quinone analogue inhibitor, tri-decyl-stigmatellin. These structures display that the b_6f complex contains eight polypeptide subunits with 13 transmembrane helices in each monomer of a functional dimer [50]. Four of the eight subunits, PetA, B, C and D, comprise considerably sized redox cofactors (16–31 kDa: cyt *f*, cyt b_6, the Rieske iron-sulfur protein, and subunit IV). The four small (3.3–4.1 kDa) hydrophobic subunits, PetG, L, M, and N (see **Figure 9, Panel A**) form a "ring" at the outside periphery of each monomer, with each small subunit containing one transmembrane helix.

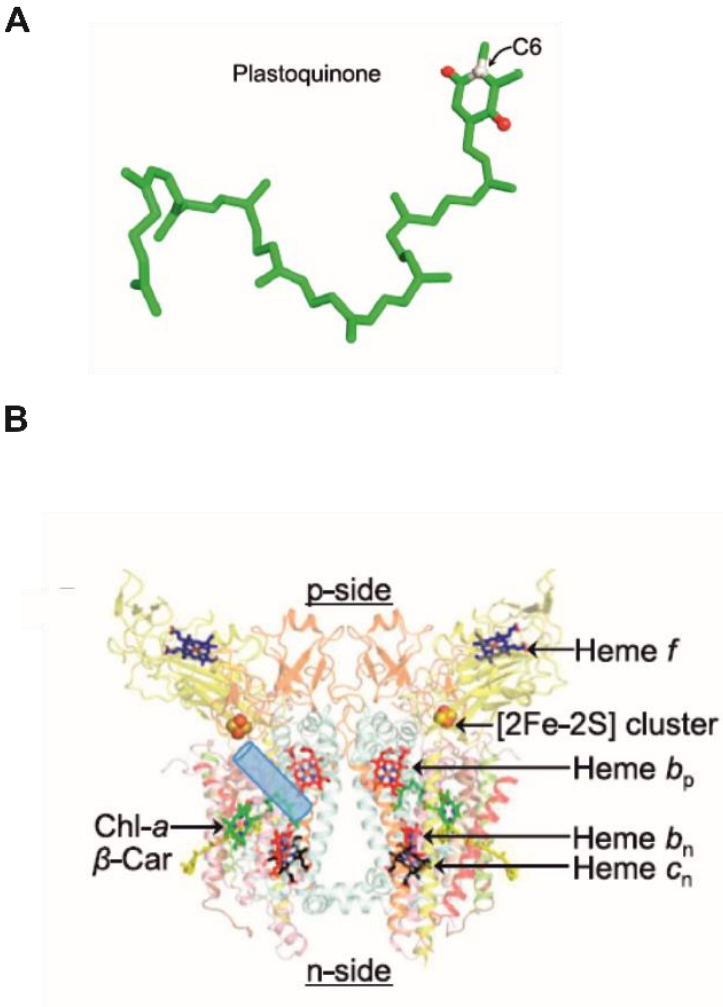

Figure 8

Structure of plastoquinone and spatial arrangement of cytochrome *b_6f* electron transfer cofactors. Reproduced from [11]. A: The plastoquinone molecule, the main substrate of cytochrome *b_6f* redox catalysis. B: Electron transfer cofactors are shown as sticks, the Q_p portal is displayed as a blue cylinder. PDB code: 2E74.

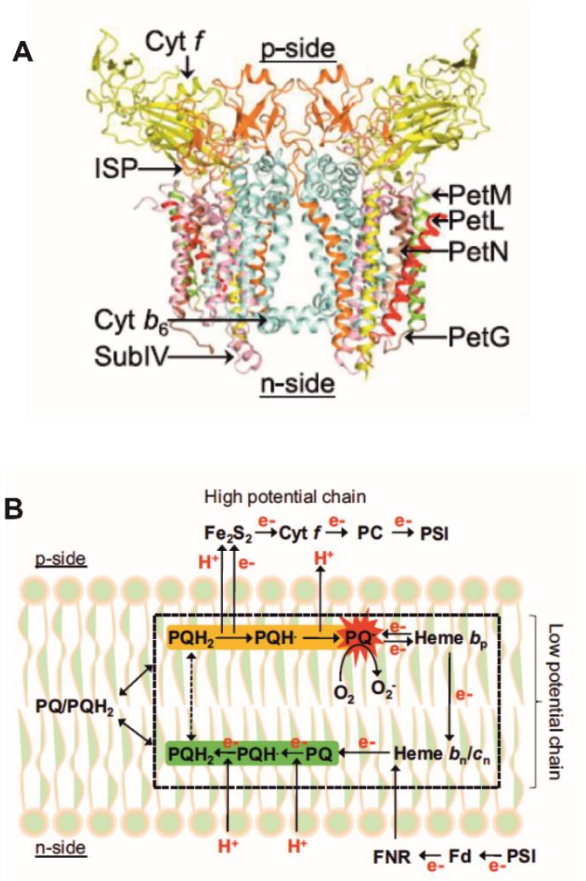

Figure 9

Polypeptide composition of the cyt *b*$_6$*f* complex and a schematic representation of electron-proton transfer pathways in the complex. Reproduced from [11]. A: Dimeric cytochrome *b*$_6$*f* complex of oxygenic photosynthesis from M. laminosus (PDB code: 2E74, [50]). The colour code displays the eight known subunits of the complex, cyt *b*$_6$, cyan; subunit IV, pink; cyt *f*, yellow; ISP, orange; PetL, red; PetM, green; PetG, brown; PetN, wheat. B: Electron-proton transfer processes in cyt *b*$_6$*f* complex in higher oxygenic phototrophs. The dashed fence represents the complex's transmembrane core. On the p-side, deprotonation-oxidation of the reduced plastoquinol (PQH_2) results in production of anionic semiquinone ($PQ^{\cdot -}$) (highlighted in red). This highly reactive subspecies can also be produced by back-transfer of an electron to the oxidized PQ from the reduced haem b_p (more commonly known as b_L). This anionic semiquinone has been associated with the reduction of molecular oxygen to superoxide ($O_2^{\bullet -}$) which could serve as the "master switch" of global homeostasis in photosynthesis and similarly in respiration. FNR, ferredoxin-$NADP^+$-oxidoreductase; Fd, ferredoxin; PC, plastocyanin; F_2S_2 iron-sulphur protein or Rieske cluster.

Despite the mechanistic and structural similarities between cyt b_6f and cyt bc_1 complexes, fundamental differences also exist. As explained above, in oxygenic photosynthesis the electron transfer chain can switch from a linear mode, which starts with water and ends with NADPH, to a cyclic electron flow, whereby electrons are transferred from cyt b_6f to PSI, on the lumenal side of the membrane, then are fed back to cyt b_6f on the stromal side, boosting ATP synthesis at the expense of reducing equivalents [49]. Despite considerable and substantial advances in the field, this cyclic electron flow mechanism remains largely unknown. Interestingly, isolation of cyt b_6f from spinach thylakoids suggested some association with FNR protein, although this has not been investigated further [51]. It has been postulated that this pathway may involve an NADH-plastoquinone reductase, the PGR5/PGRL1 [52] or perhaps it may be mediated directly by ferredoxin, the ferredoxin:$NADP^+$ reductase [51], or by a biochemically unidentified G cytochrome [53,54]. Moreover, cyt b_6f has been thought to regulate state transitions by activating a protein kinase(s) [55,56].

Interestingly, two cofactors of unknown function per monomer, Chl*a* and β-carotene, are part of the cyt b_6f complex [11] and although they are believed to play structural roles in anionic semiquinone production [11], their functions are still not fully understood. It is speculated that these pigments may play a role in response to excessive illumination, which could explain for instance why haem *f* has different kinetic properties than the six haems in the cyt bc_1 complex [57]. **Figure 10** compares the main structural features of the cyt b_6f and cyt bc_1 monomers.

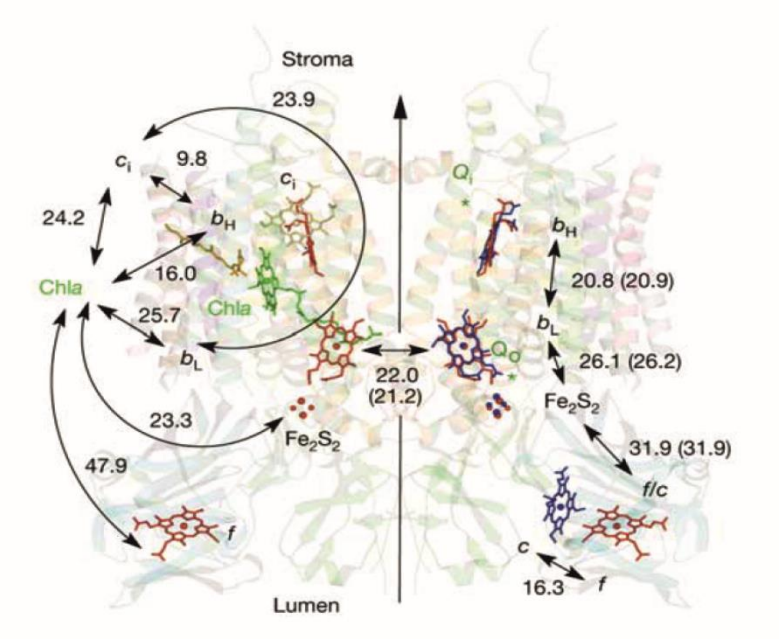

Figure 10

Comparison between cyt *b*$_6$*f* and cyt *bc*$_1$ monomer. Reproduced from [49]. Left: cyt *b*$_6$*f*. Right: cyt *bc*$_1$. Cyt *b*$_6$*f*'s haems red, haem c_i in yellow), [2Fe-2S] (red) and chlorophyll (green) are represented as viewed along the membrane plane. Distances between metal centres (in Å) are indicated (parenthesis indicate the distances from *b*$_6$*f* structure) (PDB code: 1Q90 [49]). On the right, the cofactors of cyt *bc*$_1$ (blue) are superimposed on the monomer structure of *b*$_6$*f* (*bc*$_1$ structure from PDB code 1KB9, [58]). The angle between the planes of haem c_i and b_H is 74º; the iron of haem c_i is 3.9 Å closer to the stroma than that of b_H.

1.2.3 Photosystem I as plastocyanin-ferredoxin oxidoreductase

In higher plants and algae, the PSI supercomplex comprises the core complex that is surrounded by a crescent-like light-harvesting complex (LHCI) that captures sunlight and transfers the excitation energy to the reaction centre [3]. In fact, PSI-LHCI supercomplex is the most efficient 'photoelectric device' that is known in biology [59,60] (and all references therein). The quantum yield of the PSI complex is almost unity, which means that for every photon absorbed one electron is ejected from the reaction centre. This is remarkable as no man-made device can operate with such photophysical efficiency.

Recently, the structure of the PSI-LHCI supercomplex from *Pisum sativum* has been solved at a 2.8 Å resolution [3,61]. The structure reveals a 600-kDa supercomplex with detailed arrangement of pigments and other cofactors, particularly within the LHCI complex, as well as numerous specific interactions between the reaction centre and the LHCI complex. At last, these structural intricacies have enlightended our understanding of the precise energy transfer pathways and significantly, photoprotection mechanisms within the PSI-LHCI supercomplex.

The PSI complex exists predominantly as a homotrimer in cyanobacteria and its X-ray structure has been determined at a 2.5 Å resolution [62]. Each reaction centre monomer contains 12 protein subunits, 128 cofactors (comprising 96 Chls, 2 phylloquinones, 3 [4Fe-4S] clusters, 22 carotenoids, 4 lipids and a Ca^{2+} ion). In contrast, the higher plant PSI-LHCI supercomplex occurs strictly as a monomer in the thylakoid membranes. It contains four unique eukaryotic subunits, PsaG, PsaH, PsaN and PsaO in the core complex, in addition to the subunits homologous to cyanobacterial counterpart [63] and four Lhca subunits (Lhca1 to Lhca4) of the LHCI complex.

The latest X-ray structure of PSI-LHCI reveals a semi-spherical shape similar to what has been observed for previous structures [62,64], with a dimension of 140 Å x 40 Å (**Figure 11, Panels A** and **B**). The supercomplex comprises 16 subunits, but the X-ray structure does not include PsaN and PsaO [3]. These subunits are thought to be lost during purification and/or crystallisation most likely due to their weak association with the core complex. Four LHCI subunits, Lhca1 to Lhca4, are arranged in as the functional dimers of two heterodimers (Lhca1-Lhca4 and Lhca2-Lhca3) and are attached to one side of the PSI core where PsaG, PsaF, PsaJ, and PsaK are located, in the shape of a semi-crescent moon (**Figure 11, Panels A** and **C**).

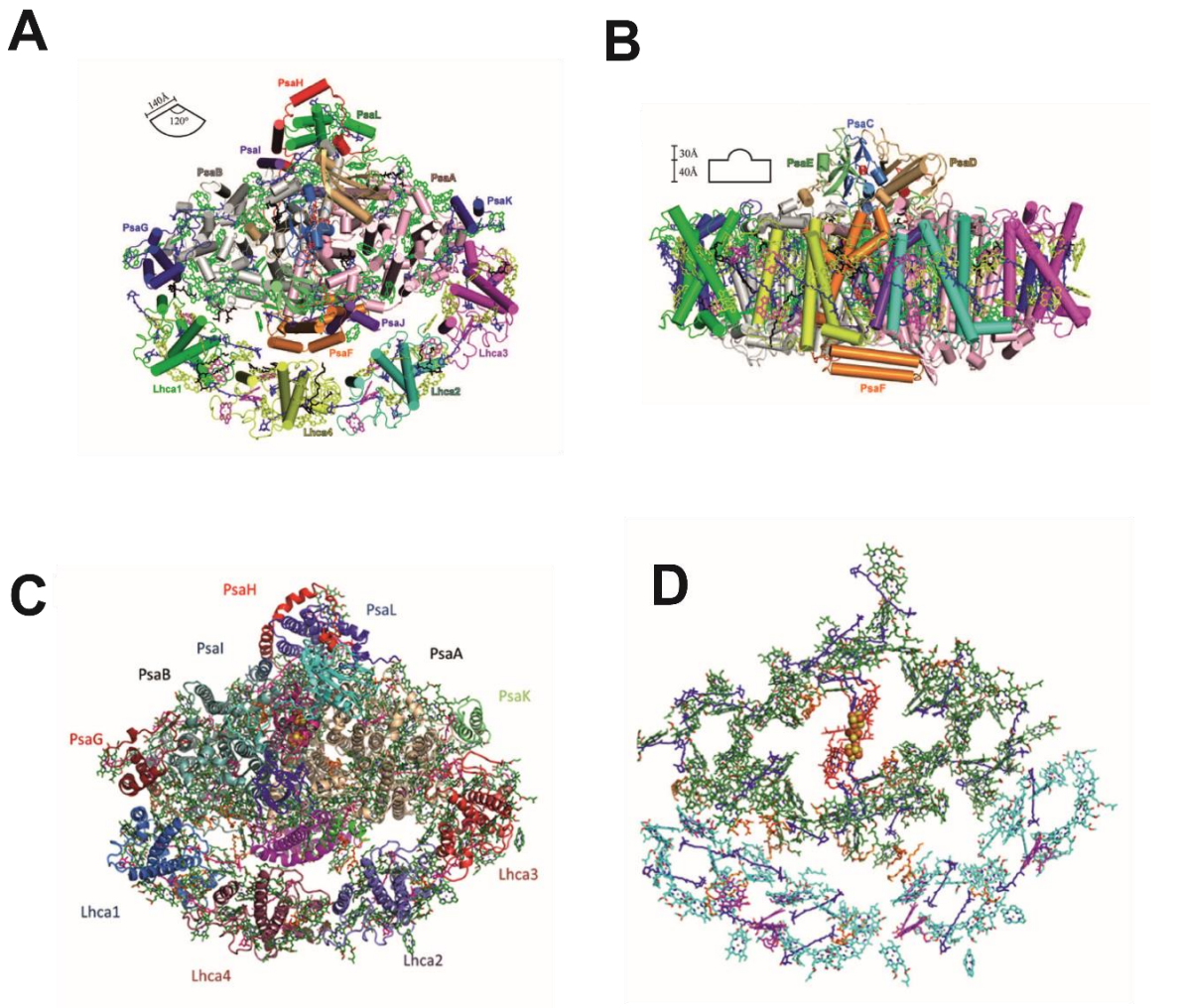

Figure 11

Overall structure of the PSI-LHCI supercomplex from *Pisum sativum* at a 2.8 Å resolution. Panels A and B are reproduced from [3]. Panels C and D are reproduced from [61]. A: View along the membrane normal from the stromal side. B: Side view of the PSI-LHCI complex from the peripheral antenna (LHCI) side, with the phytol tails of Chls omitted. Colour codes for A and B: Core subunits: pink, PsaA; grey, PsaB; light blue, PsaC; khaki, PsaD; light green, PsaE; orange, PsaF; blue, PsaG and PsaK; red, PsaH; purple, PsaI and PsaJ; green, PsaL as in [3]. Lhca subunits: green, Lhca1; cyan, Lhca2; magenta, Lhca3; yellow, Lhca4. C: Overall structure of the supercomplex with ribbons replacing cylinders in A. The PsaJ and PsaF subunits connecting in the middle of LHCI belt are coloured in green and magenta, respectively. The three subunits of the stromal ridge, PsaC, PsaD, and PsaE, are distinguished in the middle of the complex, coloured cyan, pink, and blue, respectively. The two iron-sulphur clusters of PsaC can be distinguished as yellow and orange clusters in the

middle of the complex. D: Pigment organisation in the supercomplex. The electron-transfer cofactors of the core are depicted in red, Chls of the core antenna green, Chl*a* in the LHCI belt in cyan, and Chl*b* in magenta. Carotenoids which are distributed throughout the complex, are coloured in blue and lipids in key connecting points and conserved positions in the core, in orange. PDB code: 4XK8.

In addition to the protein subunits, the latest structure [3] revealed 155 Chls (143 Chls *a* and 12 Chls *b*), 35 carotenoids [26 *β*-carotenes (BCRs), 5 luteins (Luts) and 4 violaxanthins (Vios)], 10 lipids [six phosphatidylglycerols (PGs), 3 monogalactosyldiacylglycerols (MGDGs)], and 1 digalactosyldiacylglycerol (DGDG), 3 [4Fe-4S] clusters, 2 phylloquinones, and several water molecules (**Figure 11, Panel B**). In total, these molecules amount to 226 cofactors. In contrast, Nelson and colleagues [61] identified 156 Chls (147 Chls *a* and 9 Chls *b*), 32 carotenoids and 14 lipids in their 2.8 Å X-ray structure published in parallel to the structure of the complex from Shen and colleagues [3], many of them located at key contact points of the core complex and the LHCI antenna. They amount to the total of 202 cofactors, in contrast to the 226 cofactors identified by Shen and co-workers [3].

1.2.3.1 The electron transfer cofactors

A crystallographic comparison of the cyanobacterial and higher plant PSI X-ray structures reveals an almost identical organisation and ligating sites for the electron transfer cofactors (ETC). This part of PSI comprises six Chl*a* molecules, two phylloquinones and three [4Fe-4S] clusters, as shown in **Figure 12, Panel A**. The Chls and phylloquinones are arranged along two branches, A and B, as pairs of pseudo-dimers related by the pseudo-symmetry C_2 axis and coordinated by the side chains of the PsaA/PsaB reaction centre heterodimer [62,65]. Branch A is composed of Chls eC-A1, eC-B2, eC-B3 and a phylloquionone Q_K-A, whereas branch B contains Chls eC-B1, eC-A2, eC-B3 and a phylloquinone Q_K-B (nomenclature from [62]). The two branches join once again at the [4Fe-4S] cluster F_x which is followed by the two additional [4Fe-4S] clusters, termed F_A and F_B, both of which are coordinated by the side chains of the stromal extrinsic subunit, PsaC [66].

It is now well established that both branches of the ETC are active in electron transfer. [67,68]. The rate constants are 35×10^6 s^{-1} and 4.4×10^6 s^{-1} for the electron transfer steps from each phylloquinone to F_X [54,69]. The latest data indicates that the fastest phase is considered to be dominated by the phylloquinone (PhQ) molecule oxidation coordinated by

the PsaB subunit (PhQ_B), and the slowest phase is dominated by the oxidation of the PhQ coordinated by the PsaA subunit (PhQ_A) [70] (see **Figure 12, Panel B**). The reaction centre of PSI is comprised by a cluster of 6 Chl*a* molecules that function as the primary electron donors (eC-A1-3 and eC-B1-3, according to nomenclature from [62]) and primary electron acceptors (A_0, eC-A3 and eC-B3). Secondary electron acceptors are formed by 2 phylloquinones (A_1: Q_K-A and Q_K-B) [62]. The primary electron donor of PSI reaction centre is the P700 pair, ($E_m \sim 0.5$ eV), which is formed by the 'special' pair of the eC-A1/eC-B1 Chls that are excitonically tightly coupled with a Mg–Mg distance of 6.6 Å [62]. The planes of chlorins of P700 Chls are oriented perpendicular to the membrane plane and form a stacked dimer with a 3.6 Å interplanar distance. This arrangement contrasts with the special pair in purple-bacteria reaction centres where the Mg-Mg distance is larger than 7.6 Å [71,72]. Moreover, in contrast to purple bacterial RCs, P700 Chls form a heterodimer, with eC-A1 being Chl *a*' 13'-epimer [62,73]. The characteristically heterodimeric nature of P700 primary electron donor is also reflected by the presence of hydrogen bonds within the binding pocket of eC-A1 and lack of those in the binding site of eC-B1 [62].

The other two Chl*a* pairs are composed of the eC-B2/eC-A2 and eC-A3/eC-B3 [62]. These eC-A/B-2 Chls represent the 'accessory' Chls. The eC-A/B-3 Chls are commonly referred to as A_0 (E_m of −1.0 eV), which represents the primary electron acceptor from the primary donor. The A_0 Chls are adjacent to a pair of phylloquinone molecules (often referred to as A_1). They are called Q_K-A and Q_K-B according to [62]. The A_1 phylloquinones (E_m of −0.8 eV) act as secondary electron acceptors that are rapidly reduced to the phyllosemiquinone by a minimum of two exponential phases, characterised by lifetimes in the 10–30 ns and 150–300 ns ranges [70]. Unsurprisingly, all the amino acid ligands coordinating the eC-2 and eC-3 Chl*a* pairs are highly conserved within PsaA and PsaB subunits from cyanobacteria to higher oxygenic phototrophs, indicating that throughout evolution these interactions are in fact essential for fine-tuning the redox potentials of the ETC cofactors [66]. The electron acceptor from A_1 is the [4Fe-4S] cluster, well known as F_x [66], which, similar to P700, is located at the interface of the PsaA/B heterodimer. The F_x cluster, (E_m of −0.7 eV) is ligated by four strictly conserved Cys residues present in the loop segments A/B-hi of the PsaA/B heterodimer [62]. The two terminal [4Fe-4S] iron-sulphur clusters F_A and F_B, which operate in tandem, are coordinated by Cys residues present within the conserved regions of the stromal extrinsic PsaC subunit [62].

Recently, electron transfer processes within the ETC of cyanobacterial PSI particles from *Synechocystis* sp. PCC 6803 with a high potential naphthoquinone (2,3-dichloro-1,4-naphthoquinone) incorporated into the A_1 quinone binding site have been investigated at 298 and 77 K using state-of-the-art time-resolved visible and infrared difference spectroscopy [74]. This high potential naphthoquinone inhibits electron transfer past $A_{1,}$ and biphasic $P700^+A_1^-$ radical pair recombination is observed. The two phases were assigned to $P700^+A_{1B}^-$ and $P700^+A_{1A}^-$ recombination, respectively. Analyses of the transient absorption changes illustrate that the ratio of A- and B-branch electron transfer is 95:5 at 77 K and 77:23 at 298 K [74].

For a summary of approximate standard free energy levels and kinetics of charge separation of PSI principal ETCs please refer to **Figure 13**. For snapshots of the electronic density at different time illustrating the different charge transfer steps across the ETC please refer to **Figure 14**. The aspects of quantum interference and advanced physics go beyond the scope of this PhD thesis, but the interested reader is invited to consult the pertinent literature on the matter (see [75,76] and all references therein).

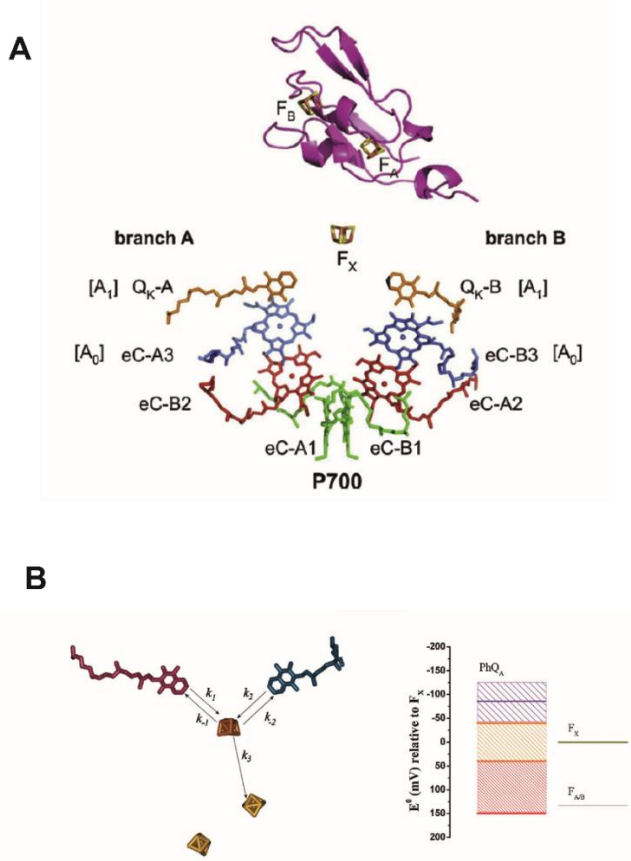

Figure 12

Electron transfer cofactors of PSI and a relative standard redox potential for PhQ_A^- /PhQ_A with respect to F_X/$F_{A/B}$. A: Electron transfer cofactors for PSI. Organisation of the electron transfer confactors (ETCs) in cyanobacterial PSI from *T. elongatus* viewed along the membrane plane. The cofactors of the ETC are related by the pseudo-symmetry C_2 axis passing through F_x, and oriented perpendicular to the paper plane. eC-A1/B1: a primary electron donor; eC-A2/B2, accessory Chls; eC-A3/B3 Chls, A_0 primary electron acceptor in P700; Q_K-A and Q_K-B, A_1 phylloquinones which are secondary electron acceptors in P700; F_X, F_A, F_B: [4Fe–4S] clusters, the latter two are shown embedded in the backbone of PsaC (pink). B: Schematic illustration of the cofactors involved in secondary electron transfer reactions in photosystem I. PhQ_A (red), PhQ_B (blue), F_X (gold) and $F_{A/B}$ (yellow). Schematic illustration of the spread of standard redox potential for PhQ_A^-/PhQ_A with respect to F_X/$F_{A/B}$, according to comparative kinetic and energetic modelling of phyllosemiquinone oxidation in PSI [70]. The dashed box indicates energetic circumstances in which the reaction can be considered as largely uphill (red), coupled to a weak driving force (orange) or coupled to a large driving force (violet). A reproduced from [66] and B reproduced from [70]. PDB code: 1JB0.

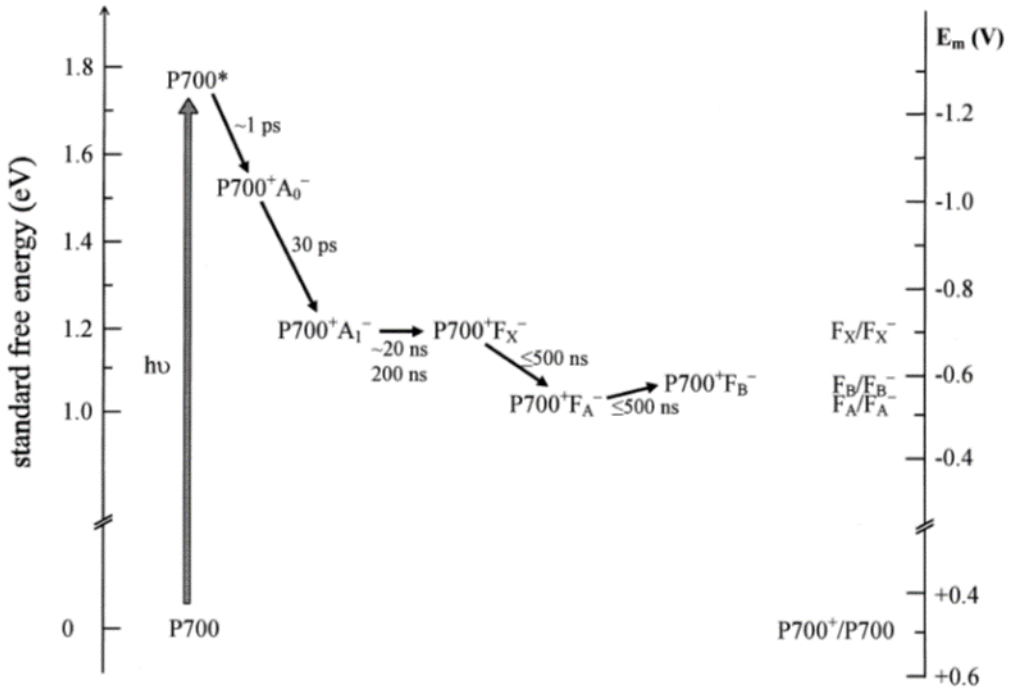

Figure 13

Approximate free energy levels and kinetics of charge separation within the PSI electron transfer chain. Reproduced from [75]. The standard free energy of the dark state (P700) was arbitrarily set to zero for clarity. Reduction midpoint potentials (*vs.* NHE) obtained by redox titrations of intact PSI and indicated on the right-hand side scale (data displayed is from [75]). If interactions between the cofactors are negligible, the standard reaction free energy ΔG^0 (per molecule) for the formation of a pair P^+A^- from PA is related to the reduction potentials by:

$$\Delta G^0 (PA \blacktriangleright P^+A^-) = q_e [E_m (P^+/P) - E_m (A/A^-)] \qquad \textbf{(Eq. 7)}$$

where q_e is the elementary charge.

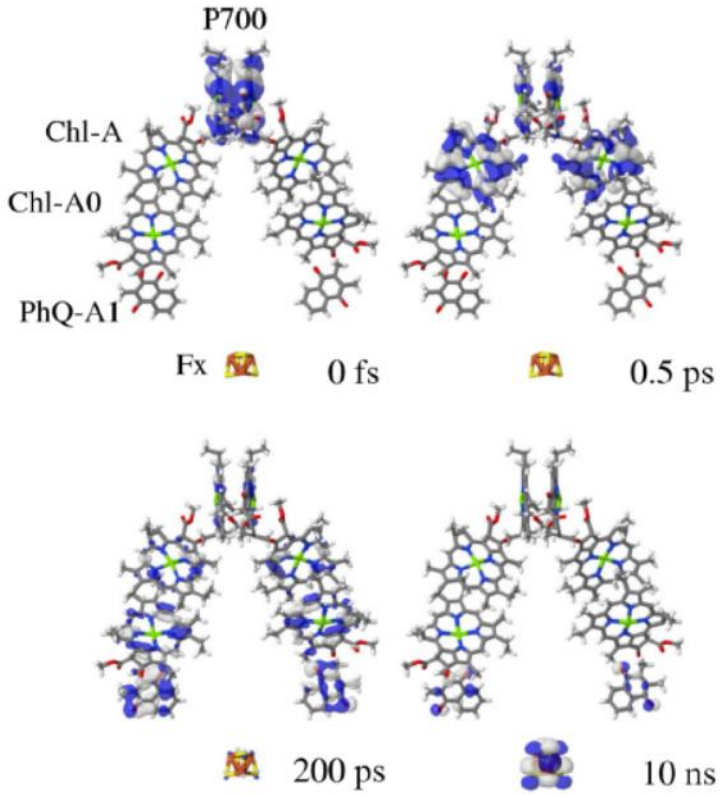

Figure 14

Changes of the electronic density during charge transfer within the electron transfer chain. Reproduced from [76]. Note the efficiency of the primary steps, taking only 0.5 ps to transfer charge density to Chl-A molecules in the ETC, the cofactors in the immediate vicinity of the P700 primary electron donor.

1.2.3.2 Light harvesting antenna complexes and energy transfer pathways in photosystem I

The latest crystal structure of the PSI-LHCI supercomplex identified 75 cofactors within the four Lhca subunits: 45 Chls *a*, 12 Chls *b*, 5 Luts, 4 BCRs, 4 Vios, 2 MGDGs and 3 PGs (**Figure 15**). The Chl *a/b* ratio was determined to be 3.75, which is in agreement to the value determined previously by [77]. The distribution of Chls in the LHCI is divided in two layers; one is close to the stromal and the other one is close to the lumenal surface (see **Figure 15, Panel A**). The stromal-side contains 36 Chls (29 Chls *a* and 7 Chls *b*) with an average Mg-Mg distance of 11.3 Å (see **Figure 15, Panel A**). On the lumenal side the Chls are less densely packed and the layer is comprised of 16 Chls *a* and 5 Chls *b*, which are separated into two different clusters or subgroups in each Lhca with an average Mg-Mg distance of 10.6 Å and a

total distance of 19.7 Å between the two sub-groups. The smallest distance between the stromal- and lumenal-side layers is 11.6 Å, in Lhca3, from Chl a607 to Chl a619 [3].

An important and striking feature of Lhcas is the presence of red forms of several Chls that are important for energy trapping and transfer in the entire PSI complex [78]. It has been shown that these 'red forms' of Chl play critical roles in harvesting of energy and transfer to the reaction centre with exceptionally high efficiency [79–81]. The Chl603-609 dimers in each Lhca (**Figure 15, Panel B**) have a close distance and some overlap between their E and C rings, displaying their nature as red Chls [3]. All four Chl603-609 dimers are trapped at the inside of LHCI, with their phytol tails bulging into the gap region between LHCI and the PSI core, in excellent agreement with their function as energy mediators responsible for energy transfer from LHCI to the PSI core. It is believed that the interactions between LHCI and the PSI core may affect the conformation of the red Chl dimers, particularly through interactions involving the hydrophobic phytol chains [82], which correlates with the emission enhancement of red Chls in LHCI upon its binding to the core complex [79]. There are marked structural differences between the Lhca subunits, like for instance, in the Lhca1 and Lcha2, the central ligand of Chl a603 is a histidine (**Figure 15, Panel B**), whereas in Lhca3 and Lhca4 it is an asparagine. Chl a603 is hydrogen-bonded to Chl a609 by the His or Asn residue, and Chl a609 is further hydrogen-bonded with an arginine residue (**Figure 15, Panel B**). Interestingly, the multiple interactions of Chl*a* a609 suggest that its porphyrin head is more stable geometrically than Chl a603, implying that Chl a603 is more likely to undergo conformational modulation. This suggests a functional difference between the individual Chl molecules in the red dimer [3].

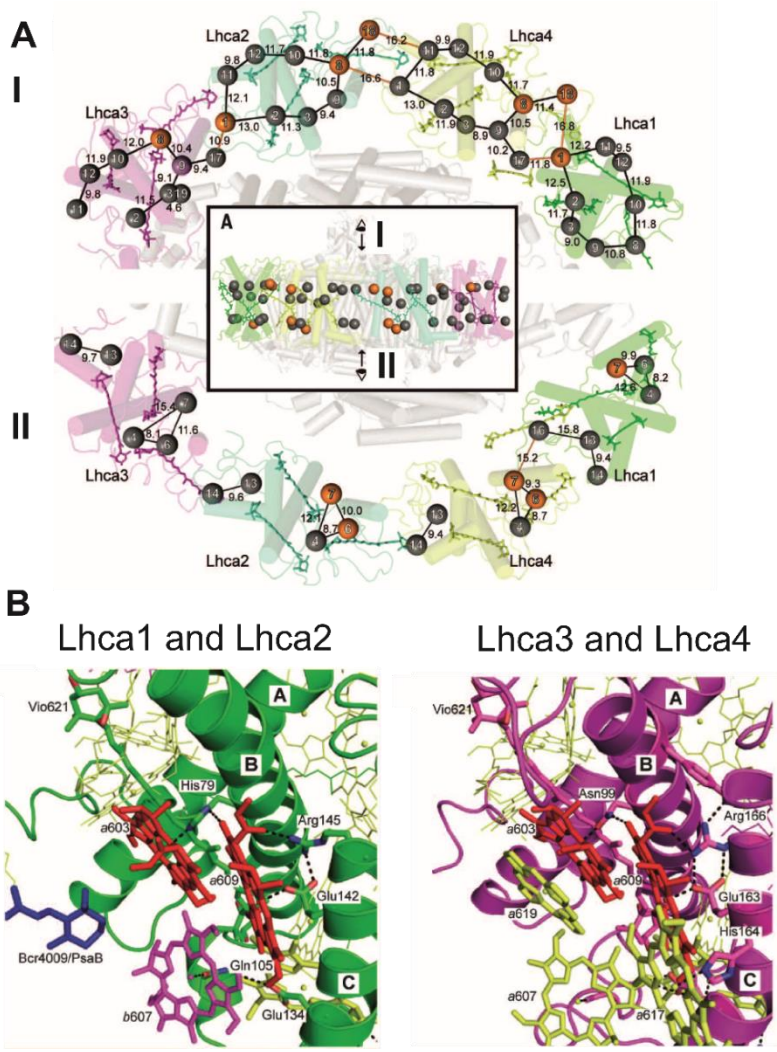

Figure 15

Detailed structural analysis of Chl organisation, distribution and red dimer coordination within the Lhcr belt of PSI-LHCI supercomplex. Reproduced from [3]. A: View of the Chl organisation from the membrane normal from the stromal and lumenal sides, respectively (I; stroma and II; lumen, as indicated in A, inset). Chls *a* and *b* are represented by grey and orange spheres, respectively. The distance in Å of the Mg-Mg centres are indicated. The numbering of Chls is as per [3]. B: Local environments of the red Chl a603-a609 dimers in LHCI. The view is perpendicular to the membrane from the stromal side of the complex. Bonds to the central Mg^{2+} ligands, hydrogen bonds, and ionic bonds are portrayed as dashed lines. Lhcr colour coding is as per **Figure 11, Panel A**. Red, Chl a603-a609 dimers; yellow, other Chls *a*; magenta, Chls *b*; pink, MGDG molecules; red spheres, water molecules. PDB code: 4XK8

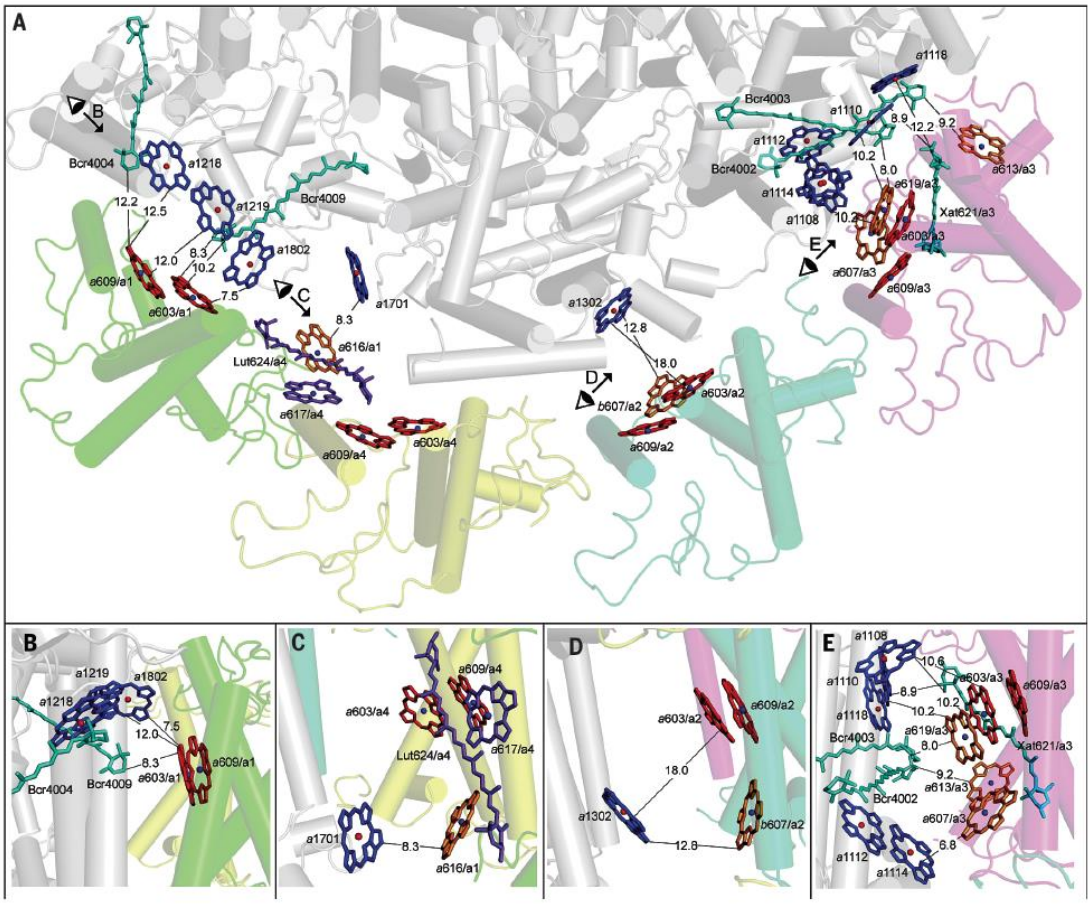

Figure 16

Plausible energy transfer pathways from LHCI to the PSI core. Reproduced from [3]. A: Overall location of pigments involved in energy transfer from LHCI to the PSI core, with cone symbols and arrowheads representing view directions shown in the lower panels. B: Stromal-side energy transfer pathway 1Bs from Lhca1 to PSI core. C: Lumenal-side pathway 1Fl from Lhca1 to PSI core. D: Pathways 2Js and 2Jl from Lhca2 to PSI core. E: Pathways 3As and 3AI from Lhca3 to PSI core. Visual geometries are from the stromal side for (A) and perpendicular to the membrane normal for (B) to (E), respectively. The terminology of the core subunits follows the cyanobacterial one. Colour codes as in [3]: blue, Chls a in PSI core; red, Chl a603-a609 dimers; purple, Chl a617 and Lut624 in Lhca4; orange, other Chls close to PSI core; cyan, carotenoids. PDB code: 4XK8.

A detailed structural analysis of near-neighbour associations between pigments revealed a number of possible energy transfer pathways from Lhcas to the PSI reaction centre, of which four appear to be more likely; these were designated 1Bs, 1Fl, 2Js, and 3As/3Al (according to nomenclature from [3]). The 1Bs pathway suggests possible energy transfer from the a603-a609 of Lhca1 to three Chls (a1218, a1219, and a1802) of PsaB at the stromal side with the shortest edge-to-edge distance of 7.5 Å. Chl a616 of Lhca1 may also direct energy to Chl a1701 of PsaF at the lumenal side, providing the 1Fl pathway (**Figure 16, Panels A** and **C**). Because of the considerable gap between Lhca4 and the PSI core, an unswerving energy transfer from Lhca4 to the PSI core would be quite unlikely, and Lhca4 may guide its energy to the PSI core *via* its red forms Chl a603-a609 through the 1Fl pathway [3]. Chl a603 of Lhca2 is somewhat distant to accomplish a direct energy transfer to Chl a1302 of PsaJ. This suggests that the 2Js pathway may not be very efficient. The Chl trimer (a603-a609-a619) of Lhca3 is close enough to Chl a1108 and the a1110-a1118 dimer of PsaA at the stromal side, forming the 3As pathway. Due to the considerably strong coupling between Chl a1110-a1118, this pathway suggests energy transfer from the red forms of Lhca3 to this Chl pair in the PSI core. At the lumenal side, Chl a607 of Lhca3 is in proximity to another Chl a1112-a1114 dimer of PsaA, providing the 3Al pathway. Furthermore, Chls a613 and a614 of Lhca3 are close to Chl a1002 of PsaK (3Kl pathway), which may also facilitate to some extent energy transfer from Lhca3 to the PSI core [3].

1.2.4 *Cyanidioschyzon merolae* as the model photoautotroph with the efficient and robust photosynthetic apparatus

As discussed in **Chapter 1.1.3** and **Figure 2**, compulsory oxygenic phototrophs are distinguished by a well-known chain of linear electron transfer, comprising the transmembrane components of PSII, cyt b_6f complex, PSI and ATPase. Soluble electron carriers include cyt c_6, and for the extremophilic red microalga *C. merolae* used in this PhD project, a close homologue, cyt c_{553}. Other mobile electron carriers include ferredoxin and ferredoxin-NADPH reductase (FNR) operating on the stromal side of the thylakoid membrane. As explained above, the whole purpose of this electron transfer chain is to generate a *pmf* across the thylakoid membrane, with the ultimate purpose of generating ATP *via* a transmembrane ATPase.

A red extremophilic unicellular red alga *Cyanidioschyzon merolae* is an ideal organism to study the photosynthetic machinery of compulsory oxygenic phototrophs as it is capable of sustaining a strong chemiosmotic balance between the lumen and stroma of thylakoids inside the chloroplasts while thriving in an extremely acidic environment at a pH range of 0.4-4.0 and moderately high temperatures of 40-56 ºC [83,84]. The *pmf* needs to be approximately 50 $kJ \cdot mol^{-1}$ for the ATP synthase to be able to synthesise ATP [85].

C. merolae is an ultrasmall (2 µm in diameter), club-shaped, unicellular haploid red alga adapted to high sulphur acid hot spring environments. The cellular architecture of *C. merolae* is exquisitely simple, containing merely a single chloroplast and a single mitochondrion, lacking a vacuole and a cell wall [83]. Moreover, the cellular and organelle divisions may be synchronised. For the abovementioned reasons, *C. merolae* is an excellent model system for study of cellular and organelle division processes, as well as structural biology and biochemistry [86,87]. *C. merolae's* genome was fully sequenced in 2004 [88]. Its plastid sequence was sequenced in 2000 and 2003, and its mitochondrial sequence in 1998 [89]. The organism is considered the simplest eukaryotic organism that exists due to the simplicity of its intracellular architecture [90].

Because *C. merolae* thrives in such extreme conditions, its photosynthetic machinery must function well under such severe environmental pressure, and the molecular mechanisms behind this phenomenon have been studied by Kargul and colleagues [42,91]. The transmembrane complexes of this organism must function with a sufficient efficiency, most likely with the need for additional ATP to drive the active extrusion of protons from the cytoplasm [92] in the presence of low external pH. It has been shown that the dimeric PSII

complex isolated from *C. merolae* is very stable across a range of extreme light, temperature, and pH conditions [42]. By measuring the fluorescence quenching properties of the isolated *C. merolae* PSII complex, the first direct evidence was provided of the pH-dependent non-photochemical quenching in the red algal PSII reaction centre [42]. This type of quenching, along with accumulation of zeaxanthin, appears to delineate photoprotection mechanisms that are rather resourcefully utilised by this robust water-splitting complex under excess illumination [42].

In order to reveal the structural details of this red algal (eukaryotic) PSII, electron microscopy was employed in conjunction with single particle analysis to obtain a 17-Å map of the *C. merolae* PSII dimer where the position of PsbQ' was identified [42]. It was concluded that this lumenal subunit is present in the vicinity of the CP43 protein, close to the membrane plane [42]. The assignment of the PsbQ' position is supported by previous EM studies of cyanobacterial PSII [37,93], whereby the side view dimer projection lacks the additional mass identified in the *C. merolae* PSII dimer particles [42].

The red algal PSI-LHCI complex is redolent of the green algal and higher plant counterparts as it is composed of the monomeric reaction centre core complex composed of 13 subunits, (PsaA-PsaF and PsaI-PsaO) [94,95] and is associated with a non-symmetrically located, crescent-like peripheral LHCI complex composed of an adjustable number of Chl*a*-binding Lhcr subunits depending on the species and environmental conditions [96–98]. Analysis of the *Galdieria sulphuraria* plastid genome suggests that the red algal PSI complex may have evolved earlier than the present-day cyanobacterial, green algal and higher plant counterparts [94]. The interesting features of the red algal PSI-LHCI supercomplex is the retention of the cyanobacterial PsaM subunit and lack of higher plant and green algal PsaH and PsaG subunits implied in docking of the LHCII antenna and formation of the LHCI belt, respectively [66]. The chimeric nature of the two core subunits PsaF and PsaL accommodating both cyanobacterial and higher-plant like structural domains further supports the notion of the evolutionary intermediate character of the red algal PSI-LHCI supercomplex [66,99].

1.2.5 Cytochrome c_{553}: structure and function

Cytochrome c_{553} (cyt c_{553}) is an analogue of cyanobacterial and algal cyt c_6 whose function is to carry electrons between cyt b_6f complex and the P700 reaction centre of PSI. In higher oxygenic phototrophs, plastocyanin, a copper metal-centre protein, is a functional analogue of cyt c_{553}. Interestingly, genes encoding for both proteins are present in certain species of green algae, including *Chlamydomonas reinhardtii*, and these genes are regulated by growth

conditions and copper availability in the medium [100,101]. Although red algal cyt c_{553} and plastocyanin have very similar sizes (~10 kDa), similar redox potential (~ +370 mV) and isoelectric points (~4.5), these two proteins have no sequence similarity, contain different metal centres and are structurally discrepant [102]. Although plastocyanin is a β-sheet protein with copper as the central metal centre, [103] cyt c_6 is a highly α-helical haem-containing protein [104,105]and references therein].

Cyt c_{553} is a class I *c*-type cytochrome, where the haem iron has methionine-histidine axial coordination [102] (see **Figure 17, Panel A**). Class I cytochromes encompass mainly low-spin bacterial and mitochondrial soluble cyts *c* [106]. Classically, the haem attachment site sits towards the N-terminus, with the sixth ligand provided by a methionine residue approximately 40 residues further down, towards the *C*-terminus [106]. Although chloroplasts are believed to have risen evolutionarily from cyanobacteria [107], there are marked differences in the expression and genome coding of cyt c_6 between green and red algae. In *C. reinhardtii*, the gene for cyt c_6 exists in the genomic DNA and its coding region is interrupted by two introns [108]. On the other hand, in red algal species such as *Cyanidioschyzon merolae*, the *petJ* gene encoding cyt c_{553} is present in the chloroplast genome and is intronless [87]. Cyt c_{553} from *C. merolae* is highly homologous to other red algal counterparts, including those from *Cyanidiaceae* sp. MX-AZ01, *Cyanidium caldarium*, *Porphyridium purpureum* and *Galdieria sulphuraria* (see **Figure 17, Panel C**).

As established by Howe and Merchant [109], maturation of thylakoid lumen proteins proceeds post-translationally through an intermediate *in vivo*. In *C. merolae*, pre-holo-cytochrome c_{553} is synthesised in the chloroplast as a larger molecular weight precursor and subsequently it is processed to its mature size during transport into the thylakoid lumen [109–111]. In contrast, in *Chlamydomonas reinhardtii*, the green algal nuclear-encoded cyt c_6 is synthesised outside the chloroplast as a larger molecular weight precursor and subsequently it is processed to its mature size during its transport into chloroplasts and thylakoid lumen [109–111]. Import of soluble proteins into chloroplasts encompass an extremely sophisticated and highly-redox regulated system. Nuclear genetically encoded proteins are translated in the cytosol and must be subsequently imported to the chloroplast [111]. The process involves three main steps; (I) cytosolic sorting procedures, (II) binding to the appropriate receptor-equipped target organelle and (III) the successive translocation process [111]. During the import, proteins must overcome two main barriers of the chloroplast envelope, chiefly the outer envelope membrane (OEM), and inner envelope membrane (IEM) [111]. In most cases,

this process is facilitated by two distinct multiprotein complexes, located in the OEM and IEM respectively, classically known as TOC and TIC [111].

Phototrophs, and particularly extremophilic acidophiles such as *C. merolae*, are constantly exposed to fluctuating environmental conditions such as temperature, light and pH, and must therefore regulate protein composition within the chloroplast very quickly and efficiently in order to ensure optimal functioning of essential ATP production processes [111]. In the case of cyt c_{553}, the pre-pro-protein is translated within the chloroplast ribosomal machinery and subsequently transported to the thylakoid lumen, with the involvement of a signalling peptide termed "an N-terminal cTP" [110–112]. The processes of pre-pro-protein processing and complete maturation of the redox-active haem group in the chloroplast (more specifically the thylakoid lumen) are extremely sophisticated and go beyond the scope of this PhD thesis. The interested reader is referred to an excellent recent review on the subject [111] and on the topic of post-transcriptional control of chloroplast gene expression [110].

For a detailed 1.57-Å X-ray structure and coordination of the red algal cyt *c* haem group, please refer to **Figure 17** (**Panels A** and **B**) below, which displays in detail the haem environment, as observed in the crystal structure of the red algal cyt c_6 from a red alga *Porphyra yezoensis* [102].

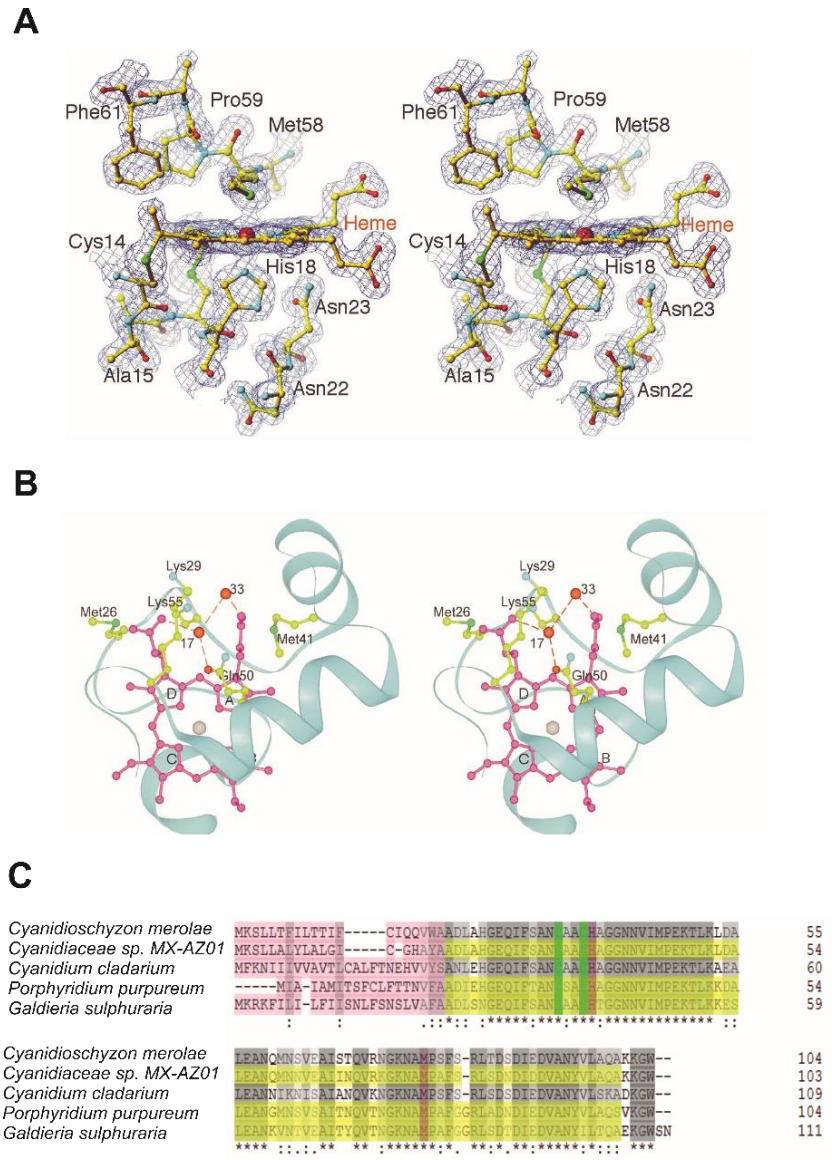

Figure 17

Structural analysis of haem environment from the crystal structure of red algal cyt c_6 at a 1.57 Å resolution. Structures in A and B obtained from *Porphyra yezoensis* [102] (PDB code: 1GDV). A: Parallel view to the haem planes of the final electron-density map ($2F_o$ - F_c) around the haem of the cyt c_6 from *Porphyra yezoensis*. This map was calculated with amplitudes of reflections in the resolution range 20.0-1.57 Å and is contoured at 1.3σ where σ is the standard deviation of the electron-density map. Haems and neighbouring residues are represented by ball-and-stick models with atom specific colours: yellow, carbon, cerulean, nitrogen; red, oxygen; green, sulphur; dark red, iron. B: The structure around the exposed haem edge of the cyt c_6 from *P. yezoensis*. The ribbon model displays the protein region (residues 14 to 59). The haem is represented in pink and the haem iron by a grey sphere. Lys29, Met26, Gln50, Met41, and Lys55 are symbolised by ball-and stick models in the same

colouring scheme as in A. Water molecules are represented as red spheres. Possible hydrogen bonds are represented by red dashed lines. C: Sequence homology blast between the most related sequences of cyt c_6 from the red algal lineage. The sequences are ordered from top to bottom in order of homology; *Cyanidiaceae sp.* MX-AZ01 has a 90.5% alignment, *Cyanidium caldarium* has an 80% alignment, *Porphyridium purpureum* has an 79.8% alignment and *Galdieria sulphuraria* a 76.5% alignment. Notice the identical residues involved in haem group binding/chelation (marked in green and red for clarity).

1.3 Artificial and biohybrid solar cells and solar-to-fuel devices

Over the last several decades, significant research effort has been put into developing the efficient technologies capable of harnessing solar energy for generation of electricity and heat using widely available materials such as silicon. Nevertheless, the main challenge remains to efficiently store solar energy in the form of high energy density fuels to alleviate the environmental burden associated with burning fossil fuels. As explained in previous chapters, phototrophs perform conversion of solar energy into chemical bonds stored in biomass through the fundamental process of photosynthesis. For years, scientists worldwide have been trying to imitate the early events of photosynthesis to construct the so-called "artificial leaf," using both the natural and synthetic light-converting components in order to produce storable solar fuels for use when sunlight is not available.

1.3.1 The energy crisis: current status and perspectives for the transition of the global energy economy

At present, fossil fuels provide 87% (a percentage which is deemed to increase this year) of the global primary supply of energy, and renewables merely reach 9% of the overall share (mainly hydroelectricity) [113] (**Figure 18**). The global demand for fossil fuels amounts to 1,066 barrels of oil, 108,000 cubic metres of natural gas and 250 tonnes of coal per second [113]. Data from 2015 indicate that coal reserves might cover the current total world energy demand for over 110 years, compared to oil and natural gas, which will be depleted at the current rate of consumption in 52.5 and 54.1 years' time, respectively, in the best case scenario [113]. These periods are expected to decrease by the time the next BP Statistical Review of World Energy is published in June of 2017.

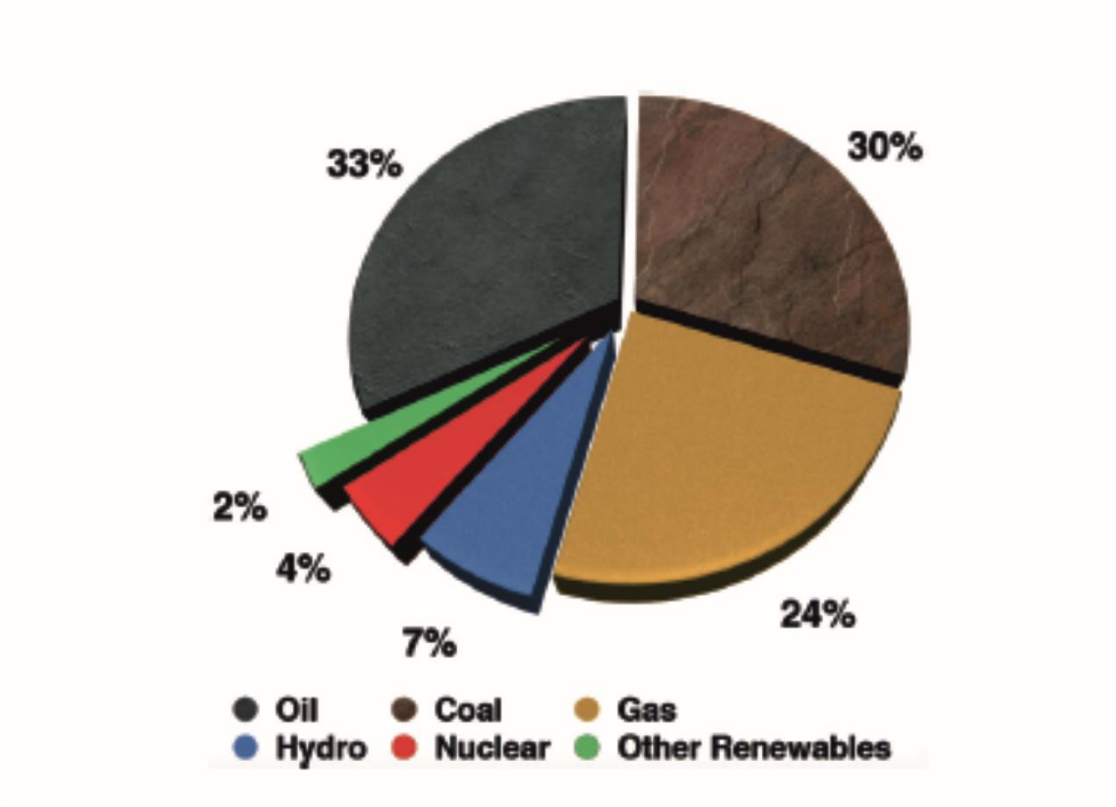

Figure 18

Global supply of commercially traded primary energy. Data reproduced from [113].

1.3.2 Recent advances in silicon-based photovolotaics

It is now a matter of urgency to find a scalable, cost-effective, and viable technology that will ensure a smooth transition from the fossil fuel-based economy to a renewable energy-based one where global energy sustainability will be attained. A gargantuan plethora of approaches have emerged over the last fifteen years or so that have attempted to address this issue; however, they are mostly limited to the laboratory scale. So far, only one attempt has succeeded in realising the upscaling of a concept which, originally by design, is scalable to large areas and is compatible with multiple thin-film photovoltaic (PV) technologies [114]. The recent study introduces the design and realisation of monolithically integrated solar-driven water-splitting modules based on silicon thin-film module technology [114]. The current device fulfils the basic requirements for a future large-scale technology, as it is wireless and scalable to arbitrary device areas [114]. The scalability of the device has been achieved by a continuous and multipliable reproduction of a base unit, which in itself combines a PV device with two electrodes of an electrolyser [114].

The authors of this study took advantage of the pre-existing laser-patterning processes used for the series connection of thin-film solar cells [115–117] and the versatility of design options in line with this type of processing. Importantly, the authors feature a large-area module (device area of 64 cm^2) encompassing thirteen base units. The latter represents one of the few practical demonstrations of the first generation of scalable monolithic water-splitting macrodevices reported to date (**Figure 19**). The authors postulate that the base unit of the PV-driven water-splitting device described in their study may be employed either in a series connection of three Si:H single-junction cells or two a-Si:H/µc-Si:H tandem cells connected in a series [114].

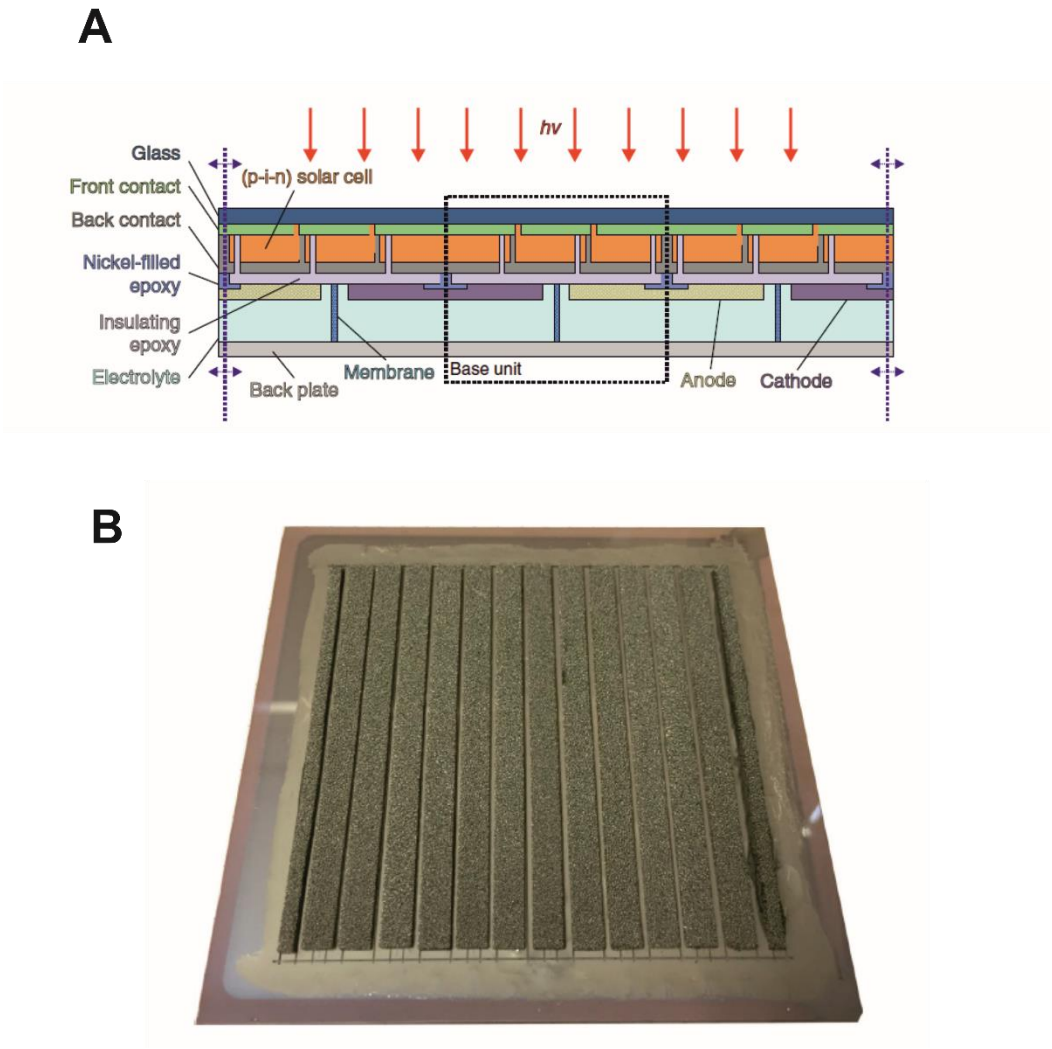

Figure 19

Schematic representation of the solar-driven water splitting device and a photograph of a scaled-up device with an area of 64 cm^2. Reproduced from [114]. A: The sketch illustrates the cross-section of the device structure of a scalable, completely integrated water-splitting device in the superstrate (monolithic) configuration. The number of cell stripes in series may

be adjusted easily or added in series as desired (here three are presented). Note, dimensions are not to scale. The schematic representation only displays an excerpt from the device. The configuration may be extended in either direction, as shown by the dashed blue arrows, the base unit that defines the area of periodic repetition is illustrated by a dashed box. B: The total device area reported is 64 cm^2 with an active area of 52.8 cm^2. Each base unit is comprised of two series-connected a-Si:H/µc-Si:H tandem solar cells with a cell stripe length and width of 80 and 2.5 mm, respectively. In this configuration, thirteen base units were neighbouring on a 10 x 10 cm^2 substrate. The back part was made of laser-cut nickel-foam elements for both cathodes and anodes.

The device features a solar-to-hydrogen efficiency of 3.9%, one of the highest reported in the scientific literature for scalable water-splitting devices [114]. The concept and its successful operation and realisation gives birth to the latest generation of scalable, Si-based devices that contribute towards the large-scale application of artificial photosynthesis technology.

Silicon is the second most abundant and evenly distributed element in the Earth's crust and there is no risk of its shortage for the time being [113]. In the hypothetical scenario where Si-based PV technologies provide 100% of the world's electricity supply by 2030, the Si production growth rate required would fall within the range of the historical range recorded over the last four decades, as argued by Armaroli and Balzani [113]. This is excellent news as not only is Si reasonably priced, but its absorption spectrum overlaps the visible region (see **Figure 20**).

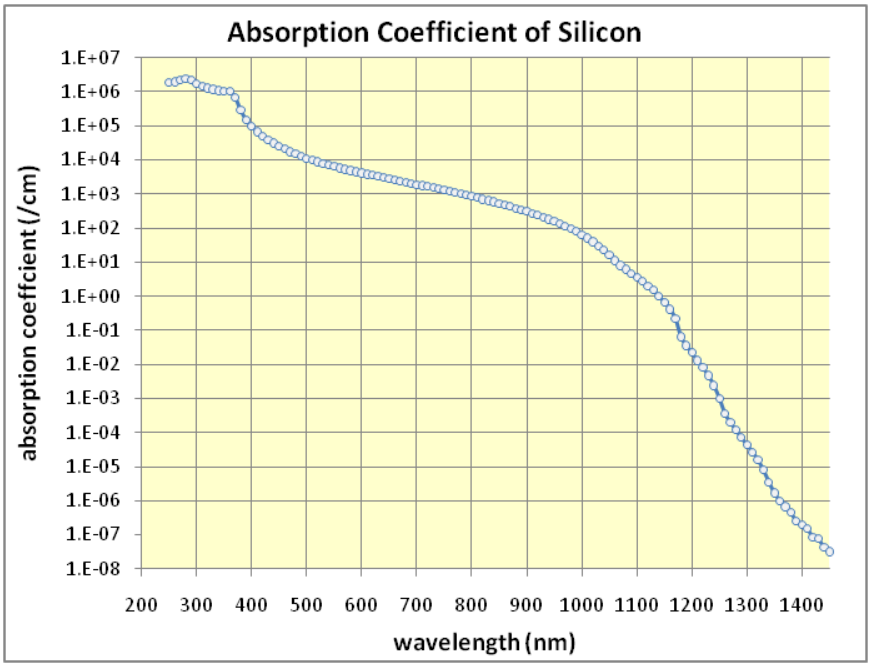

Figure 20

Absorption coefficient of silicon as a function of wavelength. Absorption coefficient of Si in cm^{-1}. Silicon is known to be an indirect bandgap semiconductor so there is a long tail in absorption out to long wavelengths, which is characteristic for this type of materials. This data is graphed and presented conventionally on a log scale. Reproduced from http://www.pveducation.org/pvcdrom/materials/optical-properties-of-silicon.

Moreover, Si-based PV is the most mature solar-to-electric technology to date which carries great potential for generation of cheap renewable energy from sunlight. With over 80% of the current solar energy market and a growth rate exceeding 40% p.a., Si solar cells have the potential to make a substantial contribution towards meeting the globally increasing energy demand [113,118]. Furthermore, the global share of Si-based technologies in PV has increased from about 80% in 2009 to more than 90% in 2014 [113]. Recently, the third most efficient solar cell was reported, a black Si-based solar cell, with an efficiency of 27.6 ± 1.2% [119].

Over the last 55 years, experts in the field have believed that it was impossible to break the Shockley-Queisser limit. This has been established to be the maximum theoretical efficiency of a solar cell employing a single *p-n* junction to collect power from the cell [120]. This limit is understood to be one of the most fundamental to solar energy production, and as a matter of fact, it is one of the most important discoveries in the PV field. The limit dictates a maximum solar conversion efficiency of approximately 33.7% assuming a single *p-n* junction with a band gap of 1.34 eV (using a standard 1.5 AM solar spectrum) [121]. This

means, that of all the power of incident sunlight falling onto an ideal solar cell, (approximately 1000 W m^{-2}) only 33.7% could ever be turned into electricity (337 W m^{-2}). Silicon, has a less favourable band gap of 1.1 eV, resulting in a maximum efficiency of about 32% [120]. It is important to note that the Schockley-Queisser limit only applies to cells with a single p-n junction; cells with multiple layers may out-perform this limit. Theoretically, with an infinite number of layers, the corresponding limit is 86.8% using concentrated sunlight [122].

The most recent developments in the field indicate that very soon this limit will be surpassed. Last year, thermally based spectral shaping has emerged as a potential technology for the ultimate purpose of enhancing PV energy conversion [123]. Specifically, in this approach the absorption of sunlight and subsequent re-emission of electromagnetic radiation is achieved from tuned thermal emission from nanophotonic structures [123]. The entire incident photon spectrum is yoked through a "broadband index-matched thermalisation process by a high-temperature (>1,000 ºC) absorber" [123]. This results in thermal excitations within the emitter structure, generating a thermal emission spectrum that culminate in the generation of free electrons that are localised to the conduction band edge in the PV (**Figure 21**). In conjunction with strong suppressors of sub-bandgap photon emission, high efficiency is retained by means of the spectral shift, while absorbed photon thermalisation in the PV cell is diminished and excessive heat generation rates can be eradicated [123]. This effect could in principle allow for cooling of the PV despite the device typically being under high solar concentration (>100 suns). Moreover, this technology could also allow for the integration of auxiliary heating [124] and thermal energy storage [125] for continuous operation, perhaps the most appealing aspects of this technology compared to other spectral converters. Therefore, these qualities render this technology as the most attractive technology to date for enhancement of PV energy conversion as it addresses the issues of efficiency, waste heat issues, and dispatchability, which are the main bottlenecks of achieving less than 30% solar conversion efficiency.

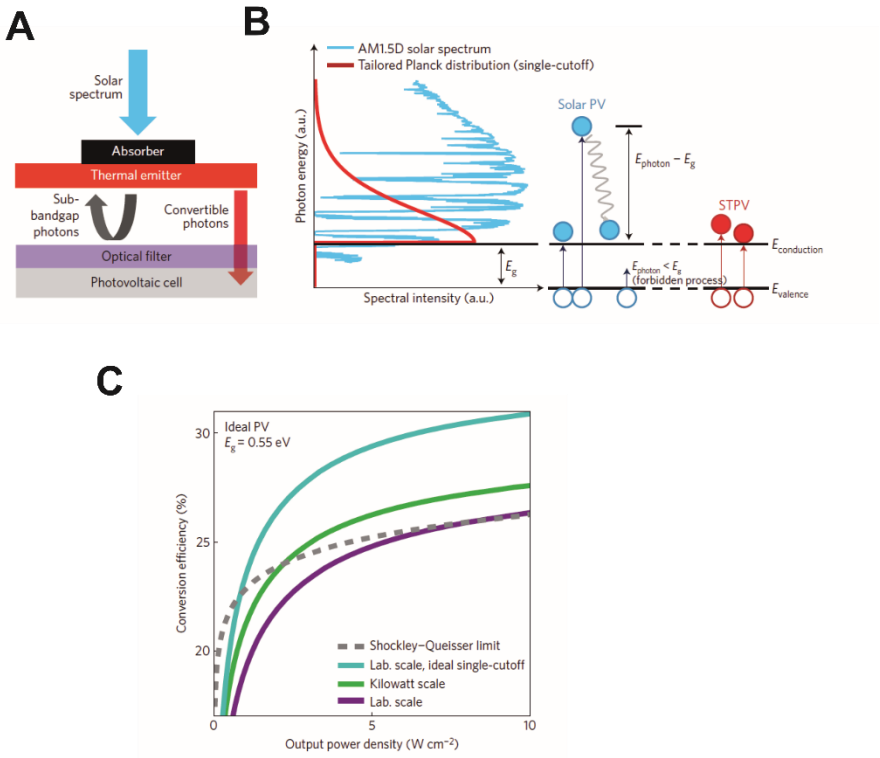

Figure 21

Comparison of solar thermophotovoltaic converting (STPV) and PV technologies and implications of surpassing the Shockley–Queisser limit. Reproduced from [123]. A: Schematic illustration of a solar thermophotovoltaic device. The incident concentrated light is thermalised at the absorber. Generated heat conducts to the thermal emitter surface depending on the temperature and spectral properties of the surface such that the engineered thermal emission is directed towards an optical filter. The filter is responsible of passing photons capable of exciting charge carriers in a single-junction PV cell and reflecting back to the emitter those photons that are not capable of doing so. B: Energy transformation mechanisms in the cell comparing illumination by engineered thermal radiation (STPV) with direct solar (PV). The schematic illustration on the right depicts electrons (full circles) being excited by incident photonic radiation from the level of the valence to the level of the conduction band of the semiconductor diode (solar-cells present diode-like behaviour, as it will be discussed further in this PhD thesis); the intensity of the photon reaching the cell is displayed as a function of the photon energy on the left. In the solar PV process, high-energy electrons generate heat within the junction of the cell as they decay down to the conduction band line, where, as the name implies, they can be extracted and conducted. The STPV process generates an equivalent number of free electrons but they are localised at the energy level of the conduction band, significantly diminishing heat generation at the interface of the solar

cell. C: Predicted performances of the three-component spectral converter demonstrated in [123] when paired with a PV (E_g = 0.55 eV) that functions in the radiative limit. The performance is displayed as a function of scale (4 cm^2) and at a kilowatt scale of 400 cm^2. As a reference, the Shockley–Queisser limit (dashed) shows the performance of the same ideal PV under AM 1.5 solar illumination. Additionally, the laboratory-scale device with an ideal single-cut-off emitter is displayed, and used to calculate the theoretical limits in **Panel A**.

1.3.3 Natural photosynthesis as a blueprint for biophotovoltaic and solar-to-fuel devices

Photosynthesis provides a blueprint for the design of the complete artificial leaf that would on one side conduct an oxidative chemistry of water splitting reaction and on the opposite side use the water-derived electrons and protons to conduct the reductive chemistry of molecular hydrogen or carbon-based solar fuel formation (see **Figure 22**).

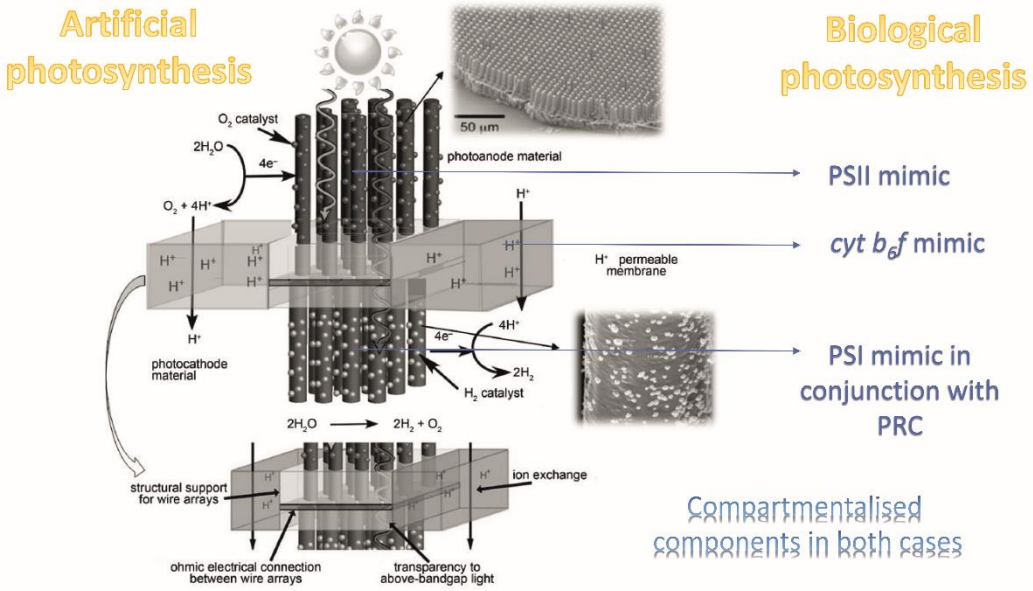

Figure 22

The concept of artificial photosynthesis. Natural photosynthesis shows that the major photosynthetic reactions must be compartmentalised, as displayed in the artificial setup shown in the left panel. Moreover, a proton permeable membrane must imitate the function of cyt *b*$_6$*f* such that the protons generated by water splitting can be transported properly to the other side of the leaf, where in nature PSI employs the reducing equivalents for NADPH generation. In

the artificial setup, these reducing equivalents should be employed ideally for proton or CO_2 reduction (not show). The artificial setup panel is reproduced from [126].

The primary reactions of photosynthesis do not use one single photosystem, and do not use one light absorber that is required to absorb light in the near-ultraviolet region to obtain sufficient energy from each incident photon to perform the chemical bond-making and bond-breaking that is needed to generate an energy-dense fuel. In natural oxygenic photosynthesis, PSII and PSI complexes are arranged in series, so that two red photons can generate a voltage equivalent to that produced by absorption of a single, ultraviolet photon which contains higher energy. Nonetheless, photosynthesis is not optimised in other aspects of its natural design for the purposes of solar energy conversion. For instance, Chl*a* and Chl*b* absorb at 670 nm, and thus, they compete for photons. Optimally, one material should absorb the more energised photons, leaving the less energised photons for the other material to drive electron flow efficiently [127].

Moreover, for production of solar fuels, the first law of thermodynamics imposes a compulsory constraint. In essence, the voltages provided by the two photosystems must combine in order to produce the voltage necessary to produce fuel, including the thermodynamically required voltage as well as any kinetic over-potentials and resistance losses that will, inevitably, be present in an artificial system [127]. In a solar cell, an engineer may trade voltage for current with no losses on the overall system efficiency. For instance, a solar cell that provides 1 V of voltage and 10 mA of current produces the same power as a solar cell that provides 2 V of voltage and 5 mA of current. In contrast, for fuel production, particularly for water splitting under "standard conditions," providing 1.2 V produces no fuel, regardless of how much current is produced, while the production of 1.23 V or larger can yield a fully operational solar-driven water-splitting system having a rate of H_2 production that is stated by the current that flows through the system. Thence, a viable blueprint for an artificial photosynthetic system involves two complementary, current-matching and voltage-adding photosystems, in combination with two different catalysts: one to oxidise water, and the other to reduce either protons into molecular hydrogen or reduce CO_2 to simple carbon-based solar fuels [127].

Another advantageous design principle implemented by biological photosynthesis is to separate the sites of oxidation and reduction reactions. As mentioned in the previous chapters, the OEC of PSII generates all O_2 in the atmosphere and the photosynthetic water-splitting

reaction is ultimately responsible for all oxygenic life on Earth. Although the OEC is not stable, the operational Mn complex is never exposed to a reducing environment. In a similar fashion, many of the key reducing enzymes in a cell, such as FNR, hydrogenases and nitrogenases, are the source of photosynthetically formed biofuels and, ultimately generated fossil fuels. These enzymes are not stable in an oxidative environment. Hence, compartmentalisation of these catalysts serves to avoid the constraint involved with ensuring that the catalysts and photochemical modules are chemically stable under the same conditions, at the same time. This compartmentalisation also brings an advantage as it produces flexibility in the choice of materials as well as in the choice of designs to achieve a practicable, fully-operational artificial photosynthetic system. Furthermore, a catalyst-separated design also requires a technique to ensure robust separation of the products; otherwise the energy-dense fuels and O_2 will tend to inevitably recombine, decreasing the efficiency of the system. Likewise, the mixture of the products could potentially result in explosion, for instance, if stoichiometric mixtures of H_2 (g) and O_2 (g) were produced over active catalysts in one compartment. The membrane that separates the products must also be selectively permeable to ions, to maintain charge neutrality in the system. Water photo-oxidation results in liberation of protons, whereas the reduction of water and/or CO_2 requires consumption of protons. Therefore, protons and/or hydroxide ions must cross the membrane to sustain the optimal pH of the system for the oxidative and reductive chemistry occurring separately in each compartment, or a continuously increasing pH gradient will result in an eventual operational arrest, as argued by Lewis [127].

1.3.3.1 Structure and function of photosystem I and its application in biomimetic solar-to-fuel systems (based on Kargul et al. JPP (2012) 169: 1639 – 1653)

As above-mentioned, PSI operates with a quantum yield of almost unity, despite its intricate structural complexity, and to date no man-made device has reached this impressive efficiency. The characteristic light-harvesting and electron-transfer properties as well as robustness of natural PSI make this macromolecular complex suitable for hydrogen production in the solar-to-fuel biomimetic devices. As PSI forms an exceptionally long-lived charge separated state of $P700^+ F_B^-$ (65 ms) and its distal F_B characterized by an exceptionally low redox potential (E_m of −0.58 eV), it provides a sufficient driving force to reduce protons to H_2 at neutral pH [66]. For these reasons, there is significant interest in utilising robust, ultrastable PSI for generation of solar fuels [66]. A considerable variety of biomimetic hydrogen

producing PSI-based nanodevices and/or reconstitution *in vitro* assays have been explored to date in which PSI was used in conjunction with metal calalysts (Pt, cobaloxime) and hydrogenase (H_2ase) catalytic modules, (see **Figure 23**). However, none has been turned into a scalable, viable device. Due to the technological limitations that this endeavour has posed, despite extensive efforts, operators have opted to employ the system for photoelectrical conversion, which holds a great promise and practicality by demonstration of solid-state nanodevices with gradually improved power conversion efficiencies.

Recently, Cliffel, Jennings and colleagues have reported a semi-solid-state solar nanodevice where electro-polymerisation of polyaniline (PAni) in the presence of solubilised PSI on a TiO_2 produces the photoactive biohybrid substrate [128]. The device is characterised by a photoactive composite layer for efficient charge separation and charge transfer from the higher plant PSI protein to the semiconductor electrode [128]. Employing a relatively facile and cost-effective preparative methodology, the PSI complex has been successfully incorporated into a conductive PAni network to ensure fast electron transfer within the all-solid-state device. By means of electrochemical polymerisation, this organic, bio-derived active layer was grown directly off transparent TiO_2 electrodes. The performance of these solid-state solar cells greatly exceeds the current state-of-the-art in PSI-derived solid-state photovoltaics by nearly 250-fold in the photocurrent output, while also being cost-effective and more robust than the previously reported PSI devices [128]. This result goes well in agreement with our reviews [5,9,66], as a semi-solid-state or all-solid-state platform for directed, specific and nanoengineered electron transfer at the interfaces is the key for enhanced, efficient unidirectional electron transfer with ultimate power conversion efficiency amelioration.

In another study, Richter, Blom, Herrman and colleagues implemented cyanobacterial PSI in organic electronic devices based on indium tin-oxide and titanium suboxide which combined the ease of processing of these organic semiconductors with the photochemical activity of PSI [129]. Importantly, this device enabled the authors to characterise the biophysical properties of the PSI complex and to demonstrate the performance of PSI as the only photoactive component in this novel solid-state bio-organic solar cell [129]. Significantly, the authors proved that the biological component and organic semiconducting materials may be successfully integrated without compromising their original optoelectronic properties. Moreover, the study is a proof-of-concept of the importance to orient the photoelectroactive complex, such as PSI, for maximisation of the operational capacity. To this

end, functional solid-state devices for solar energy conversion were constructed wherein properly oriented PSI complex is exclusively responsible for the produced photocurrent [129]. The functional hybrid solid-state solar cell displayed a large open circuit voltage and a photocurrent action spectrum exhibiting the typical absorption features of the trimeric cyanobacterial PSI complex [129].

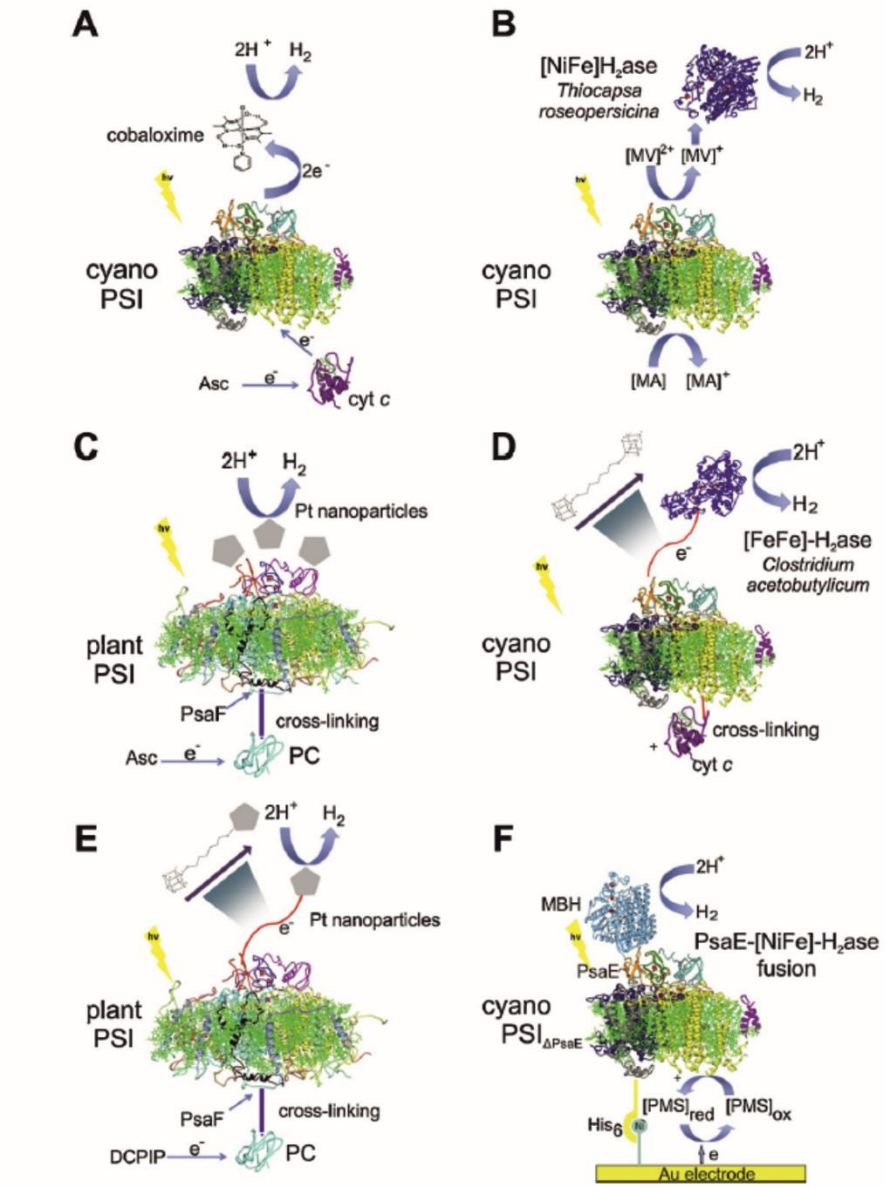

Figure 23

Biomimetic H_2-producing PSI nanodevices. Reproduced from [66]. A: Photocatalytic hydrogen production system from a PSI-cobaloxime hybrid complex. Two successive photo-generated electrons are necessary for the catalyst to produce one H_2 molecule. Electron donors depicted comprise Asc and cyt c_6 [130]. B: In-vitro hydrogen production system composed of

PSI, H_2ase, mercaptoacetic acid (MA) as electron donor and methyl viologen (MV) as electron acceptor [131]. C: H_2-evolution system consisting of platinised PSI with covalently linked plastocyanin (PC). The covalent linker is 1-ethyl-3-(3-dimethylaminopropyl) carbodiimide hydrochloride (blue stick). Ascorbate functions here as a sacrificial electron donor [132]. D: PSI-molecular wire-[FeFe]-H_2ase nanodevice. The wire indicated here is 1,6-hexanedithiol (red line). Cyt c_6 was cross-linked with a zero-length cross-linking agent to limit diffusion-based electron transfer to $P700^+$. The arrow indicates the directionality of electron transfer, including reduction of protons to H_2 by the hydrogenase (H_2ase) [133]. E: Bioconjugate consisting of PC cross-linked to PSI, 1,4-benzenedithiol as the molecular wire (red line) and a platinum nanoparticle catalyst, dichlorophenolindophenol (DCPIP) was employed as the sacrificial electron donor on this occasion [134]. F: Semi-solid state Au surface-immobilized PSI-[NiFe]-H_2ase photocathode. A reconstituted PsaF-His_6-tagged PSI-NiFe hydrogenase fusion complex was immobilised on a Ni-NTA functionalised electrode which provides electrons to reduce the oxidised form of phenylmethyl sulfonate (PMS) as the electron donor to $P700^+$ in PSI. The electrons are transferred from the F_B cluster at the PSI acceptor side to the distal iron–sulphur cluster of the [NiFe]-H_2ase and further to its active site, where protons are reduced to molecular hydrogen [135].

1.3.3.2 Oxygenic photosynthesis: translation to solar fuel technologies (based on Janna Olmos and Kargul, Act Soc Bot Pol (2014) 83(4):423 – 440)

As briefly overviewed, the overall solar-to-biomass efficiency of photosynthesis is extremely low, at an average of 0.2% [5]. The vast majority of incident solar radiation is lost in the form of transmission, reflection, scattering, and in higher plants, losses are due to the water column package effect (see **Figure 24**).

As above-mentioned, one of the characteristics of photosynthesis is the very high efficiency of the primary reactions. The main aim of artificial photosynthesis is to short-circuit natural photosynthetic reactions in order to harvest high energy photogenerated electrons so as to avoid major energy losses associated with complex biochemical processes of biomass generation (see **Figures 25-27**). In natural photosynthesis, the dark reactions consume most of the energy and result in the overall low solar-to-biomass efficiencies.

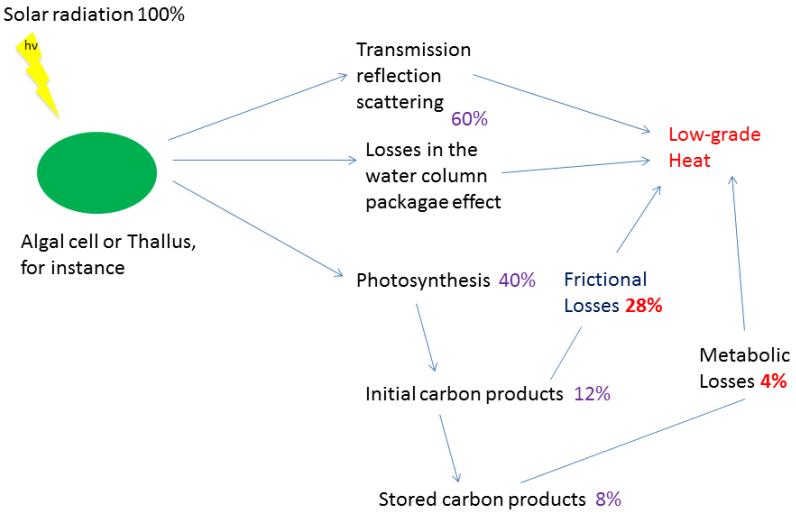

Figure 24

Energy losses and dissipation in natural photosynthesis. Reproduced from [5]. Much of the incident energy is lost as low-grade heat either directly or indirectly. Only a small amount of energy is stored as chemical free energy in new organic material, indicating that overall photosynthesis is a rather inefficient process.

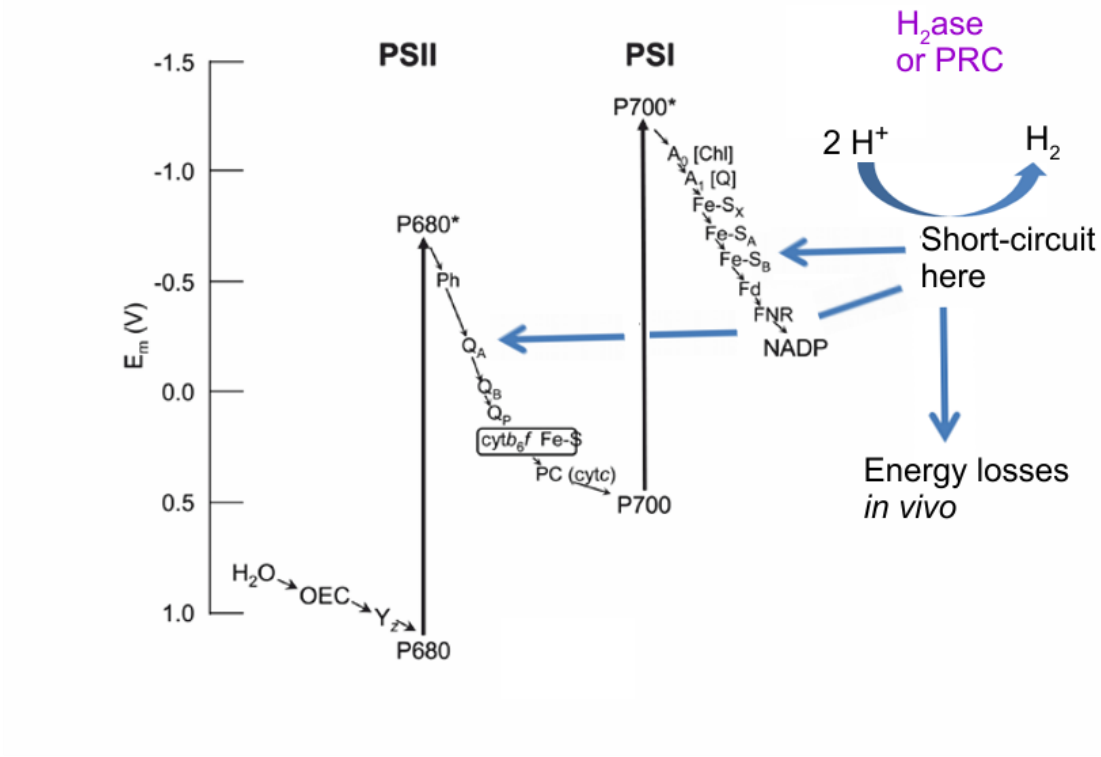

Figure 25

Short-circuiting the light reactions to maximise power conversion efficiency and minimise energy losses. Reproduced from [5]. The dark reactions of photosynthesis are energetically expensive, leading to losses of energy and hence significant reduction of overall solar-to-fuel/solar-to-biomass conversion efficiency. Short-circuiting of the primary photosynthetic events for proton reduction and photocatalysis may considerably enhance solar-to-fuel efficiency.

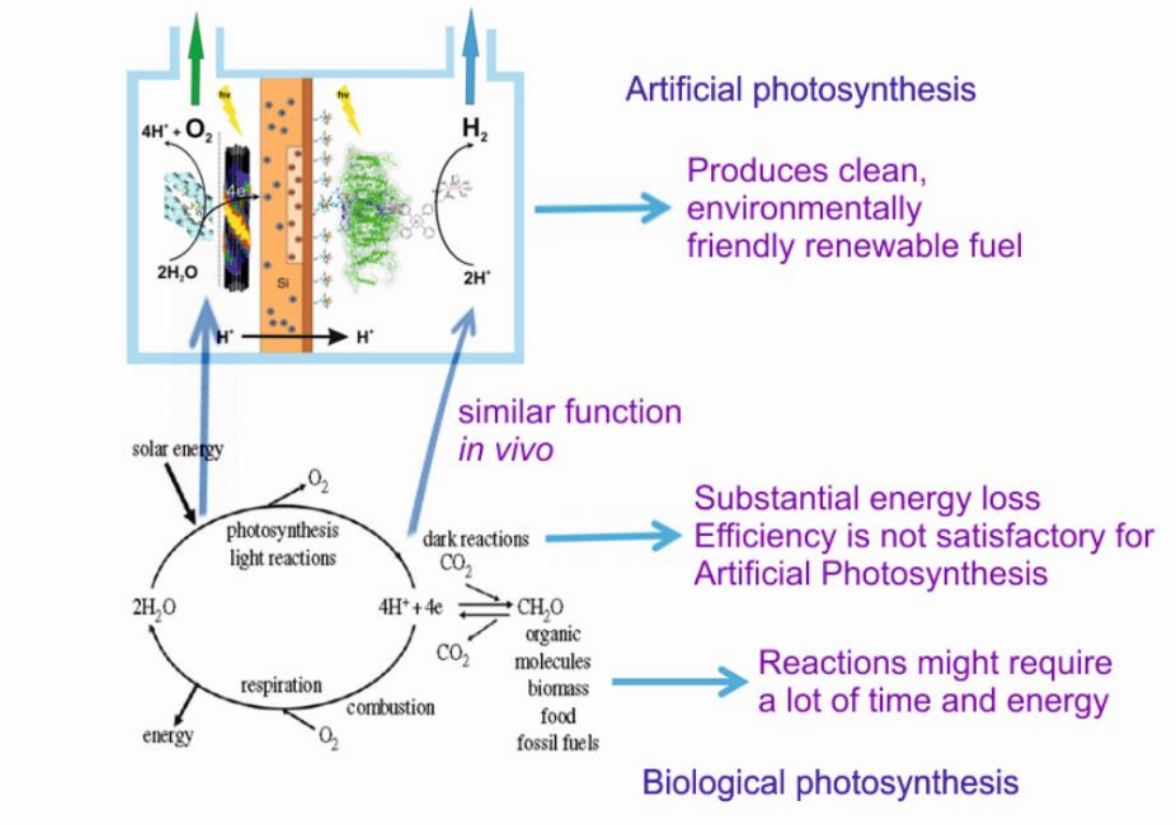

Figure 26

Artificial *versus* natural photosynthesis. Reproduced from [5]. A contrast between photosynthesis *in vivo* and artificial photosynthesis explains why it is more energetically viable to employ artificial photosynthesis for clean fuel production. Natural photosynthesis is extremely inefficient in terms of solar-to-biomass conversion. Artificial photosynthesis short-circuits the natural process by employing the most energetically efficient primary events of light capture, charge separation and charge transfer.

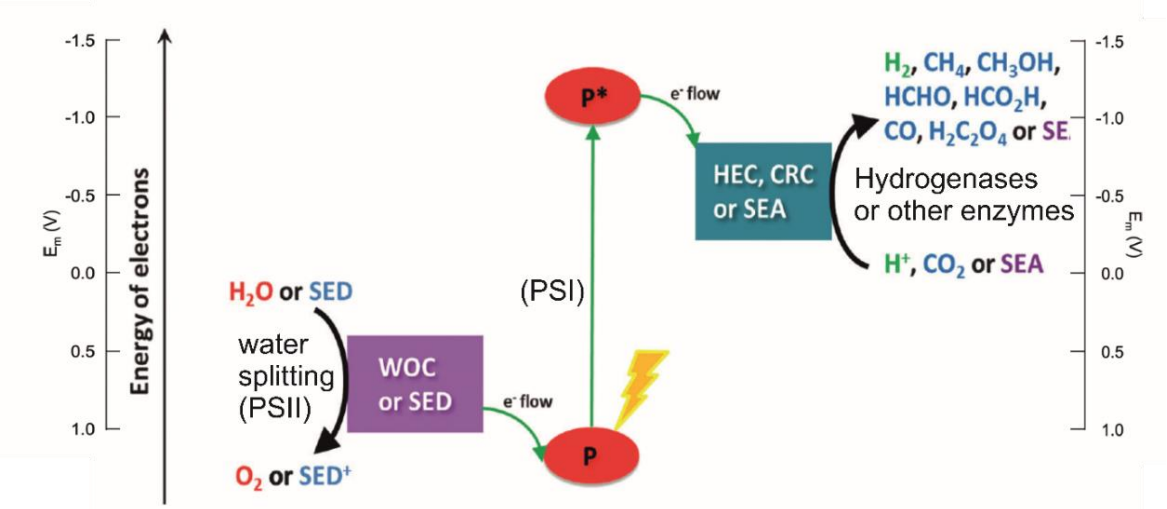

Figure 27

Reconstitution of the photosynthetic *Z*-scheme in biohybrid solar-to-high value product devices. Reproduced from [5]. Diagrammatic representation of artificial photosynthesis concept. Light converting modules (P), water oxidation catalyst (WOC), sacrificial electron donor (SED), hydrogen evolving catalyst (HEC), CO_2 reduction catalyst (CRC), sacrificial electron acceptor (SEA). E_m (V) are displayed on right and left with major tick marks inside indicating the respective energy levels for each reaction.

Recent advances have elucidated suitable semiconductor substrates for the construction of artificial leaves [5]. Hematite (α-Fe_2O_3) has recently become the material of choice for photoanodes due to the material's inherent characteristics, including low cost, lack of toxicity, corrosion resistance over a considerable pH range, peculiar robustness towards photocorrosion, a narrow bandgap (2.1 eV), and importantly, its photocatalytic activity in the visible part of the spectrum (approximately 40% solar light is absorbed by this *n*-type semiconductor) [5,136]. Hematite is considered by many essential and perhaps even critical for improvement of power conversion efficiency in an artificial leaf, therefore, its bulk and surface electronic properties have been investigated thoroughly for decades [5,136]. Lately, a novel photoanode heterostructure of *n*-type hematite and *p*-type NiO/α-$Ni(OH)_2$ has been reported by Bora and colleagues [137] which is considerably efficient in terms of solar energy conversion. The p-n-type water-splitting heterojunction assembly was engineered in order to lower a bias and to maximise current density output by overcoming the kinetic barrier of the water oxidation reaction. An impressive record current density of 16 mA cm^{-2} was recorded

for the full assembly [137]. Moreover, the system displayed charge-storing capacity along with electrochromic behaviour upon exposure to AM 1.5 light. This is normally not the case in the case of p-n-junction-like devices made by mere deposition of NiO on hematite by simple thermal annealing. Additionally, no such behaviour was observed for hematite alone. Therefore, this novel type of electrode offers a simple low-cost option for both water splitting and charge storage [137]. A similar approach features an electron/hole-doped film in the α-Fe_2O_3 photoanode upon electrochemical oxidation [138].

In contrast to this fully-synthetic water splitting photoanode, we have recently published the successful nanoengineering of nanocrystalline hematite/FTO with the robust red algal PSI-LHCI supercomplex, thus forming an alternative green biohybrid photoanode and the full dye-sensitised solar cell (DSSC) [139]. The synthetic and biological photoactive components were interfaced in order to construct a highly organised biophotoanode, which was further employed for assembly of the biohybrid DSSC using Pt counterelectrode for reduction of water-derived protons [139]. The XRD analyses and electron microscopy showed that red algal PSI-LHCI was immobilised as a structured multilayer over highly ordered nanocrystalline arrays of hematite. Compared to a related tandem system based on TiO_2/PSI-LHCI material, the α-Fe_2O_3/PSI-LHCI biophotoanode generated the largest open circuit photocurrent and incidentally operated at the highest power conversion efficiency due to a better electronic tuning between the conductive band of hematite and the PSI-LHCI layer [139]. The directed nanosctructuring of the PSI-LHCI multilayer in which subsequent layers of this complex were organised in the head-to-tail orientation was accomplished by surface charge manipulation at various pH, which enabled immobilisation of the PSI-LHCI supercomplex with its reducing side towards the hematite surface [139]. Significantly, upon illumination with visible light above 590 nm, the biohybrid PSI-LHCI-based DSSC was capable of sustained photoelectrochemical H_2 production at a very decent rate of 744 μmoles H_2 mg Chl^{-1} h^{-1}, representing one of the best performing biohybrid "green" solar-to-fuel nanodevices capable of sustained H_2 production under standard solar illumination [5,9,139].

1.3.3.3 A quest for the artificial leaf (based on Janna Olmos and Kargul, IJBCB (2015) 66: 37 – 44)

Natural photosystems and the associated light harvesting antenna are non-toxic. They possess versatile optical properties and are comprised of materials with low environmental impact and practically unlimited availability [9]. Particularly, PSI from extremophilic

microalgae has been successfully used for incorporation into solar-to-fuel nanodevices producing H_2 sustainably for over three months under intermittent illumination [139,140]. Contrasting with the traditional solar cell technologies, including organic and inorganic PV, photosystem-based solar cells have the unique characteristic to have been manufactured by solar power itself, being characteristically CO_2 neutral, biocompatible, and operational under very low light intensities and are designed to work in ultrathin films [9]. Technology based on such biosolar cells may very well end up in applications of small electronic devices (biophotosensors), low light intensity energy harvesting, do-it-yourself solar energy harvesting or large scale disposable printed solar cells for electric power and solar fuel generation (see **Figure 28**).

In contrast, the main remaining challenge in organic/inorganic PV technology is to reduce manufacturing costs and improve robustness of the PV systems without compromising the overall efficiency of the PV devices [9]. Furthermore, in thin-film PV the best performing devices are usually associated with the use of heavy metals for their construction and as such, their ultimate mass usage would result in a public health hazard. Nonetheless, there is currently intense research in the field of PV based on organic or inorganic semiconductors over the last decade and for some of these devices distinctly high efficiencies have been achieved (refer to [119] and references therein).

To date, four main categories of solution-processed solar cell technologies have exceeded 10% power conversion efficiency, which is the widely accepted threshold efficiency aimed for artificial photosynthetic devices [9,141]. These are: colloidal quantum-dots solar cells, organic PV, solution-processed bulk inorganic PV and DSSC cells [141]. Although many of the recently reported PV devices have reached impressive power conversion efficiencies of up to 46% (e.g. GaInP/GaAs//GaInAsP/GaInAs tetra-junction modules, [119]), the main challenges remain to lower their manufacturing cost, increase their stability and most of all, efficiently interface them with water splitting and hydrogen evolving/CO_2 reducing catalysts within the fully-functional solar-to-fuel device, i.e., a complete artificial leaf that uses water as the sole source of reducing equivalents, just like in natural photosynthesis [9].

Although the progress in the field of artificial photosynthesis has been momentous over the last decade, several major obstacles to commercialisation of this technology remain; chiefly redox compatibility of the working modules, low solar-to-fuel overall conversion efficiencies due to inefficient and improper nanostructuring and interfacing of the modules and most importantly, cost-effectiveness. The latter has imposed the major bottleneck;

scalability and realisation for widespread practical application as an alternative to fossil fuels [9]. Graetzel-type solar cells (DSSCs) seem to provide one of the best working solar-to-electric devices, operating at overall efficiencies above 10% and incorporating cheap, earth abundant materials as the photosensitisers, water splitting and proton reduction catalysts [9,141]. Recently, Graetzel and colleagues have reported a very efficient tandem solar cell composed of a solution-processed perovskite PV tandem module wired to a bifunctional NiFe catalyst that was capable of both reduction of protons to molecular hydrogen and water splitting in an alkaline electrolyte [9,142]. The study reported a record current density value of 10 mA cm^{-2}, equivalent to a solar-to-hydrogen efficiency of 12.3% [9,142]. Although the cell holds great promise, perovskite instability in aqueous environment compromised its robustness, rendering it unsuitable for long-term usage and hence scalability [9]. However, it is one of the best performing fully operational completely artificial photoelectrochemical devices reported to date that carries a great potential for further improvement [9].

A feat in the endeavour for a fully synthetic viable artificial leaf was the construction of the device capable of splitting water and generating molecular hydrogen under neutral pH, room temperature and standard illumination conditions (AM 1.5) [9,143]. The rather simple design of the device of Nocera and coworkers consisted of a triple junction, amorphous Si phosensitiser what was interfaced with self-renewing Co-oxo-borate as the catalyst responsible for water-splitting and the ternary alloy wafer of NiMoZn as the HEC, in either wireless or wired configuration [9,143]. Although the efficiencies of the device were only 2.5% and 4.7% for the wireless and wired assemblies, respectively, the use of earth-abundant cheap metal catalysts, particularly self-healing and self-assembling cobalt catalyst, their unsophisticated interfacing with a commercially available cheap Si PV module, and operation under ambient conditions carries tremendous potential for future macroscaling and commercialisation [9,143].

A major progress towards construction of the viable state-of-the-art artificial leaves was the employment of nanosctructured hollow nanospheres with optical range size and composed of a Pt-doped carbon nitride organic semiconductor exhibiting both PRC and WOC activities [9,144]. The nanospheres functioned as a scaffold for the co-catalyst. Additionally, they served as the artificial light-harvesting antennae. This novel, elegant and rather unsophisticated nanoscaffold assembly of controlled thickness was shown to operate at 7.5% solar-to-hydrogen quantum efficiency, placing it amongst one of the most efficient fully artificial leaves to date [9,144]. These hollow polymerised nanospheres with ideal thickness and

controlled surface functionalities provide a blueprint for future construction of different functionalities into complex nano- or macrostructures while, importantly, maintaining spatially separated compartments. This elegant, nature-inspired design follows essentially the blueprint provided by the thylakoid membrane, were both PSII (the natural WOC) and PSI (the natural PRC) complexes are spatially separated and ordered in tandem for highly efficient photoinduced energy/electron transfer within the structures of the photosynthetic reaction centres [5,9]. **Figure 28** emphasises the versatility of Nature's most proficient photoconverter and demonstrates how suitable this photoconverter is for incorporation into novel biophoelectric constructs.

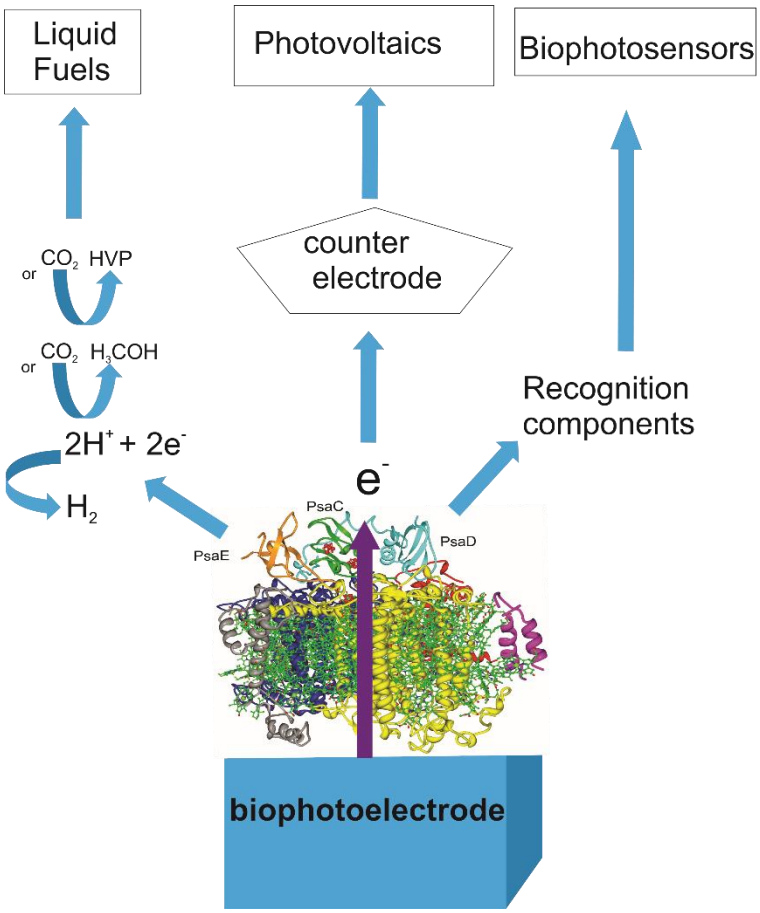

Figure 28

Applications of PSI-based biophotoelectrodes. Depending on the desired out-come, PSI immobilised on an electrode may be utilised to produce liquid fuels, for photovoltaic applications upon directed electron transfer or as part of a photo-recognition component for the construction of biophotosensors. The versatility of this complex allows for the following

applications: (i), its incorporation into semiconducting or conducting electrodes to produce photovoltaic devices capable of converting solar energy into photocurrent; (ii) its incorporation into nanoscale and mesoscale devices capable of harnessing sunlight and converting solar energy into storable renewable liquid or gas fuels; or (iii), its incorporation together with a field emission transistor (charge detector) to convert photons into electrons within biophotosensors, such as those used in the ultrasensitive imaging devices. Reproduced from [9].

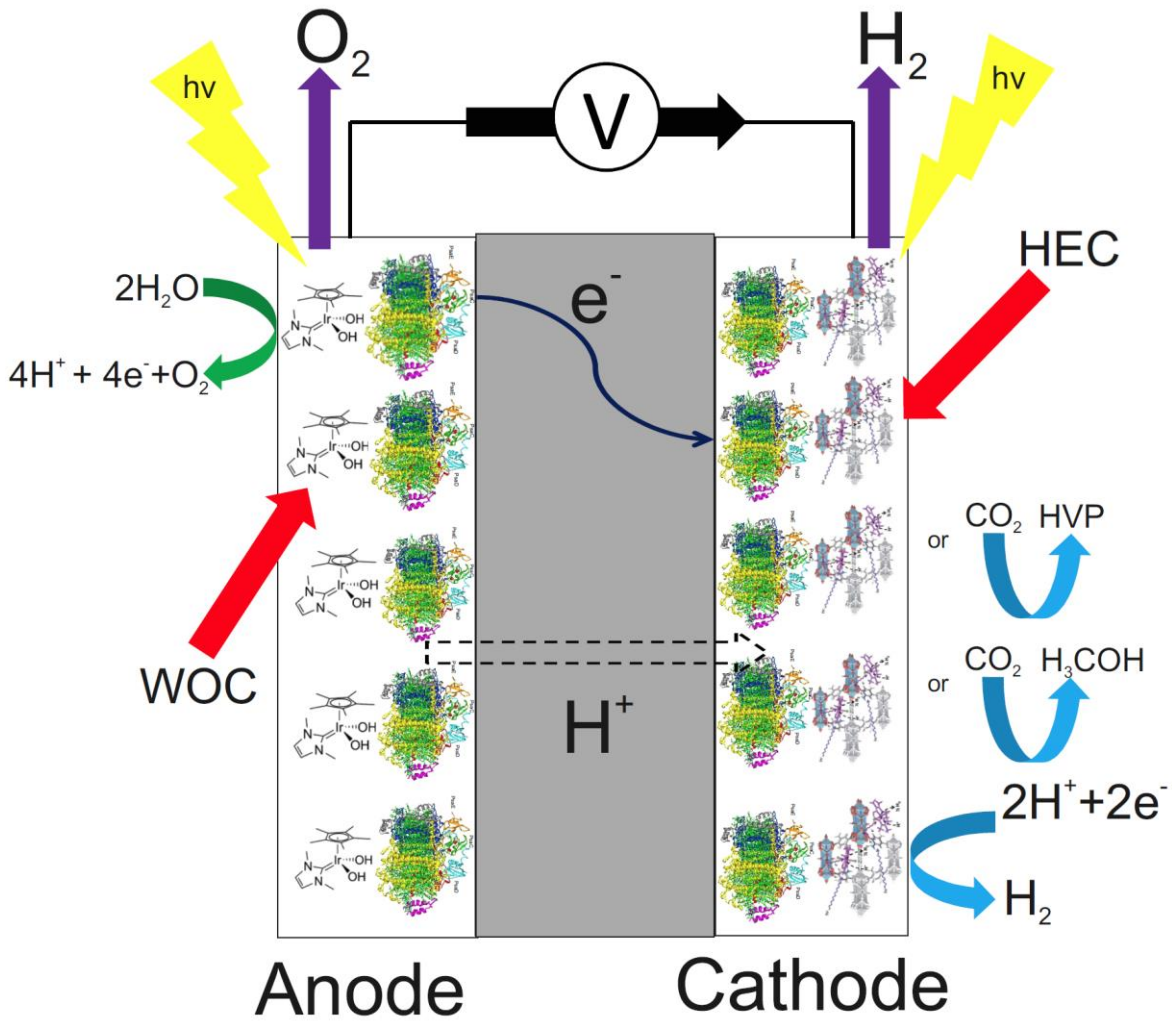

Figure 29

Biohybrid PSI-based artificial leaf. Diagrammatic representation of two artificial leaf configurations, whereby highly robust PSI linked to the iridium-based water oxidation catalyst (WOC) may be employed either as a photosensitiser of the semiconducting substrate or as a component of a biophotocathode linked to the hydrogen evolving catalyst (HEC), such as the cobaloxime derivative encapsulated within a photoactive metal–organic framework. The

versatile nature of PSI allows it to function in both configurations for production of anodic or cathodic photocurrents. Note, the artificial leaf is theoretical and only envisaged on the current available technologies where PSI applicability has been realised to the laboratory scale. Reproduced from [9].

Construction of the artificial leaf is a particularly attractive approach to tackle the energy gap problem that mankind faces in a couple of decades, when the global energy demand considerably exceeds the amount of energy produced globally from the waning fossil fuel reserves. **Figure 29** depicts a hypothetical yet ideal fully operational artificial leaf. It is still possible to build a highly efficient artificial system that is relatively facile to manufacture on a macroscale. Ideally, such a system should be engineered using robust self-renewing earth-abundant materials that can harvest a wide spectrum of solar light, whilst minimising spectral overlap on the anodic and cathodic segments of the leaf. Finally, the 'ideal' (**Figure 29**) artificial leaf should employ water as the sole source of electrons and protons for the reduction of CO_2 into high energy density liquid fuels. Obviously, this area of research requires an interdisciplinary approach to generate novel ideas that can be transcribed not only into fully operational prototypes but most importantly, viable and realisable scaled-up artificial leaves.

The field has been greatly advanced by revealing the molecular structures and mechanisms that permit the natural photosystems and their respective associated light harvesting complexes to operate with high internal quantum efficiencies. Important challenges remain in the field, like for instance, how to extend lifetimes of charge separation to minimise wasteful back reactions and competently manage proton coupled electron transfer during photo-catalysis. Optimisation of all these processes is of the utmost importance, as it is indispensable for the artificial leaf to outperform the overall natural photosynthetic process, a feat imperative for this system to become viable. Recent global initiatives are making tremendous progress to achieve this goal. Nonetheless, it is important to mention that a considerable amount of continuous investment is vital to ensure the steady progress in these endeavours.

Chapter 2 Aims and Goals

The main aim of this PhD study was to apply a highly robust PSI-LHCI complex from an extremophilic microalga *Cyanidioschyzon merolae* as the biological photochemically active module for nanoengineering of four types of biophotovoltaic devices with improved power conversion efficiencies compared to similar systems reported to date: (*1*), photo-driven *in vitro* hydrogen production system comprising PSI-LHCI complex, cyt c_{553}, and metallic or novel mononuclear proton reduction catalysts; (*2*), PSI-LHCI/cyt c_{553}/AgNWs bionanostructures with an improved light harvesting functionality; (*3*), all-solid-state PSI-LHCI/*p*-doped Si biophotoelectrodes, and (*4*), all-solid-state PSI-LHCI/cyt c_{553}/*p*-doped Si biophotoelectrodes.

For all the devices presented in this thesis, rational design and nanoengineering of the abovementioned PSI-LHCI nanoarchitectures and interfaces between the working modules were applied. The spectroscopic and *J-V* properties of the constructed PSI-LHCI-based bionanoarchitectures, as well as hydrogen production rates for type 1 devices was measured to evaluate the working hypothesis on the applicability of cyt c_{553} as the cofactor that promotes not only direct electron transfer in the all-solid-state PSI-based biophotovoltaic devices but also facilitates the specific orientation and formation of novel light harvesting properties of the PSI-LHCI complex upon its immobilisation on the metallic or semiconductor surfaces.

The specific goals of this PhD study were:

1. Examination of interaction of the PSI-LHCI complex with platinum or mononuclear nickel proton reduction catalysts for sustained photo-driven *in vitro* hydrogen production.
2. Investigation of the role of cyt c_{553} in promoting the highly ordered, oriented immobilisation of the PSI-LHCI assemblies with an improved light harvesting functionality within plasmon-emitting metallic nanostructures or *p*-doped Si semiconductor substrate.
3. Investigation of the role of cyt c_{553} in minimisation of surface charge recombination within the *p*-doped Si semiconductor substrate as the function of the distance and orientation of the redox active haem group with respect to the electrode surface.
4. Development of the all-solid-state mediatorless biophotovoltaic devices with highly ordered PSI-LHCI nanoarchitecture with an improved direct electron transfer through

the incorporation of cyt c_{553} as the conductive layer between the biophotoactive module of PSI-LHCI and the silicon semiconductor substrate.

Chapter 3 Materials and Methods

3.1 Materials

3.1.1 Strains

A) *Cyanidioschyzon merolae* strain NIES-1332 10D was obtained from the Microbial Culture Collection of the National Institute for Environmental Studies (Tsukuba, Japan)

B) *Thermosyneccocus elongatus* BP-1 strain NIES-2133 was obtained from Prof. Matthias Rögner and Dr. Marc Nowaczyk, University of Bochum, Germany

C) *Escherichia coli* DH5α (ThermoScientific®) strain was obtained from Prof. dr hab. Dariusz Bartosik, Department of Bacterial Genetics, Faculty of Biology, University of Warsaw

D) *Escherichia coli* BL21 (ThermoScientific®) strain was obtained from Prof. dr hab. Dariusz Bartosik, Department of Bacterial Genetics, Faculty of Biology, University of Warsaw

E) *Escherichia coli* MC1000 (ThermoScientific®) strain was obtained from Prof. dr hab. Dariusz Bartosik, Department of Bacterial Genetics, Faculty of Biology, University of Warsaw

F) *Escherichia coli* TOP10 (ThermoScientific®) strain was obtained from Prof. dr hab. Dariusz Bartosik, Department of Bacterial Genetics, Faculty of Biology, University of Warsaw

3.1.2 Growth media

A) *C. merolae* Allen 2 (A2) medium (M-Allen) [88]

Table 1

M-Allen (A2) medium composition

$(NH_4)_2SO_4$	19.8 mM
KH_2PO_4	4 mM
$MgSO_4 \cdot 7H_2O$	2 mM
$CaCl_2 \cdot 2H_2O$	1 mM
A2 trace element stock	0.2 mL
Distilled water	99.4 ml
pH 2.5*	

After adjustment to the final volume of 100 ml with distilled water, the medium was autoclaved, then 400 µl of filter-sterilised A2 Fe-stock solution was added.

*The pH was adjusted to 2.5 with 1M H_2SO_4.

Table 2

A2 trace elements stock solution

H_3BO_3	46 mM
$MnCl_2 \cdot 4H_2O$	9.1 mM
$ZnCl_2$	0.77 mM
$Na_2MoO_4 \cdot 2H_2O$	1.6 mM
$CoCl_2 \cdot 6H_2O$	0.2 mM
$CuCl_2 \cdot 2H_2O$	0.25 mM
Distilled water	100 ml

Table 3

A2 Fe stock solution

EDTA · 2Na	20.7 mM
$FeCl_3 \cdot 6H_2O$	14.8 mM
Distilled water	100 ml

After adjustment to the final volume of 100 ml, the solution was sterilised by passing through a Millipore filtering device (0.22 μm).

B) *T. elongatus* BG-11 medium [145]

Table 4

BG-11 medium composition

100 x BG-FPC (i)	10 ml
HEPES-NaOH, pH 8.2 (ii)	5 ml
1000 x ammonium ferric Citrate (iii)	1 ml or 2.3 mM ammonium ferric citrate
Na_2CO_3 (v)	1 ml
K_2HPO_4 (vi)	1 ml

After adjustment to 1000 ml with distilled water the medium was autoclaved.

Table 5

(Stock i) 100 x BG-FPC (Adjusted to 1000 ml with distilled H_2O)

$NaNO_3$	1.76 M
$MgSO_4$ x $7H_2O$	30 mM
$CaCl_2$ x $2H_2O$	25 mM
Citric acid	3 mM
Na_2EDTA, pH 8.0	0.3 mM
10% (v/v) microelements (iv)	100 ml

(Stock ii) 1 M HEPES-NaOH, pH 8.2. The stock solution was adjusted to 500 ml with distilled H_2O.

(Stock iii) Stock of ammonium ferric citrate (2.3 mM). The stock was adjusted to 100 ml with distilled H_2O.

Table 6

(Stock iv) Microelements stock solution (Adjusted to 1000 ml with distilled H_2O)

H_3BO_3	46 mM
$MnCl_2 \cdot 4H_2O$	9 mM
$ZnSO_4 \cdot 7H_2O$	0.77 mM
$Na_2MoO_4 \cdot 2H_2O$	1.6 mM
$CuSO_4 \cdot 5H_2O$	0.3 mM
$Co(NO_3)_2 \cdot 6H_2O$	0.17 mM

(Stock v) 189 mM Na_2CO_3. The stock solution was adjusted to 200 ml with distilled H_2O.

(Stock vi) 175 mM K_2HPO_4. The stock solution was adjusted to 200 ml with distilled H_2O.

C) *E. coli*: Standard LB-Miller medium (Lysogeny broth) [146]
Normally, 10 g tryptone was mixed with 5 g yeast extract and 10 g NaCl L^{-1}

3.1.3 Molecular biology materials

A) Primers: All primers have been synthesised by oligo.pl, at the Institute of Biochemistry and Biophysics, Polish Academy of Sciences, re-suspended in H_2O to a concentration of 100 μM, aliquoted and stored at -20º C as a stock solution. The sequences of primers used in this study are listed in **Table 7**.

Table 7

Forward and reverse primers for amplification of the *petJ* gene sequence

Primer name, length (bp) and amount produced (nmol)	**Primer sequence (5' to 3')**
petJ_C_f 33 bp 300 nmol	GCGCCCATGGAAAGCTTATTAACATTCATTTTG
petJ_C_r 0AA 33 bp 40 nmol	TTATGAGCTCCCCCAACCTTTTTTAGCTTGAGC
petJ_C_r 5AA 35 bp 40 nmol	TTATGAGCTCCCCCAACGGAAGTGGGCTCGAAACT
petJ_C_r 10AA 42 bp 40 nmol	TTATGAGCTCCGGGTCTGGCTCAGGTACTTGAAACAC TTA
petJ_C_r 12 AA 46 bp 40 nmol	TTATGAGCTCCCCCAACCTTTCGTCTGTTTAGCGGCTG CATTGGAA
petJ_C_r 19AA 50 bp 40 nmol	TTATGAGCTCCCCCAACCTTTTTTAGCTTGAGCGCGGA AGCCGCCGCTA

The forward (f) primer was employed equally for all PCR products. (r) reverse primer.

B) Polymerase Chain Reaction (PCR) mixture: DreamTaq™ Green PCR Master Mix (2x), which includes DreamTaq DNA Polymerase, 2x DreamTaq Green buffer, dNTPs, and 4 mM $MgCl_2$ (ThermoScientifc®)

C) Plasmids: pET28b-(+) was obtained from Invitrogen® (ThermoScientific®) and pBAD/HisA was obtained from Prof. dr hab. Dariusz Bartosik, Department of Bacterial Genetics, Faculty of Biology, University of Warsaw. The pEC86 vector was a kind gift from Prof. A. Szczepaniak, Wrocław University, Poland. Refer to **Chapter 7.2** for maps of all plasmids used and constructed in this study.

D) Restriction enzymes: All enzymes used for cloning were FastDigest—Thermo Scientific®. All enzymes were utilised with the 10x FastDigest universal buffer. Specific enzymes are listed in methods at each step when they were required. Refer to **Chapter 3.2.2.3** for detailed methods.

E) Ligase: *E. coli* DNA Ligase Invitrogen® (ThermoScientific®) was used for all DNA ligations. The buffer was 10X concentrated and was supplied with 188 mM Tris-HCl (pH 8.3), 906 mM KCl, 46 mM $MgCl_2$, 37.5 mM DTT, 1.5 mM λ-NAD and 100 mM

$(NH_4)_2SO_4$. The ligase was aliquoted and stored at -20º C. ATP was added freshly to the aliquot after thawing and gently mixed before use.

F) DNA extraction kits: GeneJET Plasmid isolation kits were used for plasmid isolation from ThermoScientific®. Miniprep Kits were applied for all plasmid purifications.

G) Gel extraction kits: GeneJET Gel extraction kits were employed for PCR isolation and purification of DNA from standard TAE agarose gels (ThermoScientific®)

3.1.4 Reagents

All standard reagents and essential laboratory consumables were purchased from Sigma-Aldrich®, POCH® (Poland), ROTH (Carl Roth®, Germany), Chempur® (Poland), or Witko® (Poland) and were used at 97-99.9% purity, unless stated otherwise.

3.1.5 Chromatography materials

A) DEAE TOYOPEARL 650 M resin (Sigma-Aldrich®)

B) DEAE TOYOPEARL 650 S resin (Sigma-Aldrich®)

C) Sephadex® G-25 Fine resin (GE Healthcare®, *via* Sigma-Aldrich®)

D) HisTrap™ Excel, 1 ml columns, (from GE Healthcare®, *via* Sigma-Aldrich®)

E) HisPur™ Ni-NTA Resin (ThermoScientific®) (20% slurry in EtOH)

F) Size exclusion (SEC-4000 column, Phenomenex®, Torrance, CA)

3.1.6 Standard buffers

3.1.6.1 DNA electrophoresis buffers

TAE (Tris-acetate EDTA) buffer for applied for DNA electrophoresis (40 mM Tris, 20 mM acetic acid, 1 mM EDTA, pH 8.0). Normally a 1.5% solution of agarose was employed, depending on the size of the DNA fragments and/or plasmids to be analysed.

3.1.6.2 Buffers for preparation of competent *E. coli* cells

A) TFB I (per 200 ml): [30 mM CH_3CO_2K, 100 mM RbCl, 10 mM $CaCl_2$, 50 mM $MnCl_2$ 15% glycerol (w/v)] was adjusted to pH 5.8 with (1.5 µM) acetic acid (CH_3COOH).

B) TFB II (per 100 ml): [10 mM MOPS, 75 mM $CaCl_2$, 10 mM RbCl, 15% glycerol (w/v)] was adjusted to pH 6.5 with (0.32 µM) sodium hydroxide (NaOH).

3.1.6.3 Chromatographic buffers

A) Standard Phosphate Buffer (10x SPB): 100 mM Na_2HPO_4, 18 mM KH_2PO_4, pH 7.5

B) *E. coli* resuspension buffer (carrier buffer) for Ni-NTA purification: 20 mM imidazole, 10 x SPB (as above), 25% glycerol (w/v) and 30 μM phenylmethylsulfonyl fluoride (PMSF) [or one tablet of Complete™ protease inhibitor cocktail (Roche®) and DNase I (5 mg) (Roche®)] per 50 ml of suspension, pH 7.5

C) Carrier Buffer for purifications (both FPLC and batch-type) was prepared as above but without protease inhibitor cocktail or DNase additives.

D) High Imidazole Buffer (elution buffer) for Ni-NTA purification composition:
FPLC: 500 mM imidazole, 10 x SPB, 25% glycerol (w/v), pH 7.5
Batch-type: 250 mM imidazole, 10 x SPB, 25% glycerol (w/v), pH 7.5

E) Resuspension Buffer for long term protein storage and manipulation (with glycerol removed as required): Standard Phosphate Buffer (10 x SPB) composed of 100 mM Na_2HPO_4, 18 mM KH_2PO_4, pH 7.5, 25% glycerol (w/v).

D) *C. merolae* thylakoid isolation buffer: 40 mM MES-KOH, pH 6.1, 10 mM $CaCl_2$, 5 mM $MgCl_2$, 25% (w/v) glycerol was supplemented with 1 tablet of Complete™ protease inhibitor cocktail (Roche®), DNase I (5 mg) (Roche®) per 50 ml of buffer suspension.

<u>*T. elongatus* thylakoid isolation buffers:</u>

A) 20 mM MES-KOH, pH 6.5, 10 mM $MgCl_2$ and 10 mM $CaCl_2$ supplemented with 1 tablet of Complete™ protease inhibitor cocktail (Roche®), DNase I (5 mg) (Roche®) and RNAse I (10 μl from stock) (Sigma-Aldrich®) per 50 ml of buffer.

B) As in A) with additional 0.5 M mannitol, pH 6.5

<u>*C. merolae* PSI and PSII purification buffers:</u>

I) *1st chromatographic step*

A) Carrier buffer: 40 mM MES-KOH, pH 6.1, 10 mM $CaCl_2$, 5 mM $MgCl_2$, 25% (w/v) glycerol, 0.03% n-dodecyl-β-D-maltoside (DDM)

B) Wash Buffer: 90 mM NaCl, 40 mM MES-KOH, pH 6.1, 10 mM $CaCl_2$, 5 mM $MgCl_2$, 25% (w/v) glycerol, 0.03% DDM

C) Elution Buffer: 250 mM NaCl, 40 mM MES-KOH, pH 6.1, 10 mM $CaCl_2$, 5 mM $MgCl_2$, 25% (w/v) glycerol, 0.03% DDM

II) *2nd chromatographic step*

A) Carrier buffer: 40 mM HEPES-KOH, pH 8.0, 3 mM $CaCl_2$, 25% glycerol (w/v), 0.03% DDM

B) Elution buffer: 250 mM NaCl, 40 mM HEPES-KOH, pH 8.0, 3 mM $CaCl_2$, 25% glycerol (w/v), 0.03% DDM

C) Low ionic strength buffer for sucrose gradient loading: 50 mM K_2HPO_4-KH_2PO_4, pH 8, (w/v) 0.03% DDM

D) Sucrose gradient buffer: 0.4 M sucrose, 0.45 M betaine, 5 mM Tris-HCl, pH 8, 0.05% (w/v) DDM

3.1.6.4 Sodium dodecyl sulphate-polyacrylamide gel electrophoresis buffers

Protocol and solutions were followed according to [147]. For preparation of the acrylamide-bisacrylamide AB-3 stock solution (49.5% T, 3% mixture), 48 g of acrylamide and 1.5 g of bisacrylamide were dissolved in 100 ml of water and filtered through a 0.22 µM pore-sized membrane. For the AB-6 stock solution (49.5% T, 6% mixture), 46.5 g of acrylamide and 3 g of bis-acrylamide were dissolved in 100 ml of water and filtered as above.

A) Gel buffer (3 X): 3 M Tris, 1 M HCl, 0.3% SDS, pH 8.45

B) Anode buffer (10 X): 1 M Tris, 0.225 M HCl, pH 8.9

C) Cathode buffer (10 X): 1 M Tris, 1 M Tricine, 1.0 % SDS, pH 8.25

D) Reducing sample buffer:
(5X): 0.225 M Tris-HCl, pH 6.7; 50% glycerol; 5% SDS; 0.05% bromophenol blue; 0.25 M 1,4-dithiothreitol (DTT)

E) Fixing solution: 50% methanol, 10% acetic acid, 100 mM ammonium acetate

F) Staining solution: 0.025% Coomassie brilliant-blue dye (R-250) (Carl Roth®), 10% acetic acid

G) De-staining solution: 10% acetic acid

H) Gel dry-out: standard gel drying system with 25% glycerol (Sigma-Aldirch®)

3.1.6.5 Western blotting and colourimetric reagents for protein detection and quantification

A) Polyvinylidene fluoride (PVDF) membranes were used for protein transfer (BioRad®)

B) Transfer buffer (for Western blotting, 25 mM Tris, 192 mM glycine)

C) TBST buffer: 20 mM Tris-HCl (pH 7.5), 150 mM NaCl, 0.05–0.1% Tween® 20 (Sigma-Aldrich®)

D) Blocking solution: 137 mM NaCl, 2.68 mM KCl, 1.47 mM KH_2PO_4, 8.1 mM Na_2HPO_4, 0.05%-0.1% Tween® (Sigma-Aldrich®) 2-5% powdered milk or 10% Bovine Serum Albumin (BSA) (Sigma-Aldrich®)

E) Ponceau S solution (SigmaAldrich®) was used for protein visualization

F) Bradford Reagent (SigmaAldrich®) was used for protein concentration determination via the Bradford colourimetric assay [148]

G) Bovine serum albumin (BSA) (SigmaAldrich®) was used as the protein standard.

3.1.7 Antibodies and immunodetection kits

A) ECL Western Blotting Substrate (Promega®): 250 ml Peroxide Solution and 250 ml Luminol Enhancer Solution

B) SuperSignal™ West Pico PLUS Chemiluminescent Substrate (ThermoScientific®)

C) HisProbe™-HRP conjugate (ThermoScientific®)

3.1.8 Plasmonic and electrode materials

A) Silver nanowires (AgNW) were synthesised in the laboratory of Prof. Sebastian Maćkowski (Nicolaus Copernicus University in Toruń, Poland) according to the procedure described in [149].

3.1.9 Proton Reducing Catalysts

A) DuBois-type proton reducing catalysts (PRCs) were synthesised in the laboratory of Prof. Joost Reek (University of Amsterdam, Amsterdam, Netherlands) according to the procedure described in [150].

B) Cobaloxime was purchased form Sigma-Aldrich®.

C) ~3.0 nm Pt nanospheres were obtained using a facile synthesis protocol described in **Chapter 3.2.8.1**.

3.1.10 Other materials

A) *p*-doped Si wafers were purchased and processed at the Department of Optoelectronics, Institute of Electronic Materials Technology (ITME, Warsaw, Poland).

B) 0.1 mm glass beads from ROTH (Carl Roth®, Germany)

C) Gold tablets, silver tablets and indium were purchased from Mennica Małopolska, Kraków, Poland.

3.2 Methods

3.2.1 Cell culturing and processing methods

3.2.1.1 *C. merolae* cell culturing

Liquid cultures of the *C. merolae* cells were grown in a temperature- and light-controlled growth chamber (Sanyo®, Japan) in standard 250-ml tissue flasks. Cells were grown in 50-75 ml of Allen 2 medium, pH 2.5 at 42º C under continuous white light illumination (90 µmoles photons m^{-2} s^{-1} (µE) for moderate light (ML) conditions) with continuous shaking at 115 rpm. Small scale cultures were grown to OD_{680} ~ 2.5 and then sub-cultured into 1 L interim cultures and finally grown as 5-10 L cultures in Allen 2 medium until the late log phase (until OD_{680} ~ 3.5) in the presence of 5% CO_2 administered at a constant flow rate of 30 L h^{-1} under continuous white light illumination of 150 µE. **Figure 30** displays a typical *C. merolae* growth curve for a 10 L culture under ML illumination conditions. **Figure 31** displays a representative RT absorption spectrum of an early log phase *C. merolae* cell suspension at the "day 0" timepoint of inoculation.

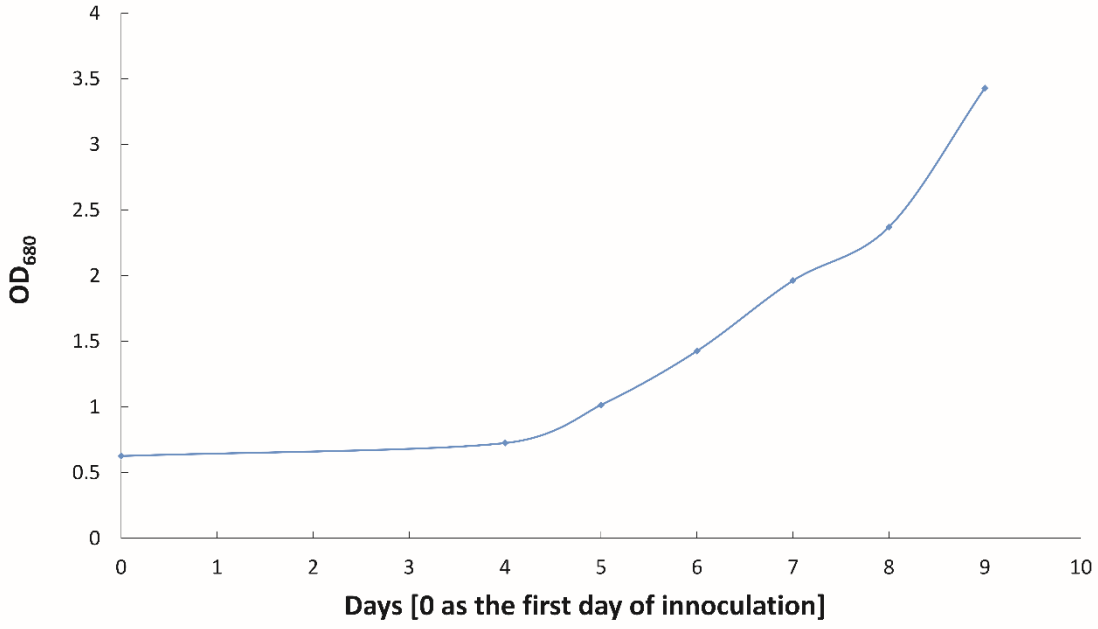

Figure 30

***C. merolae* growth curve for a 10 L culture under ML illumination.** Light intensity was increased from 90 µE to 150 µE for the last 2 days of growth to the late log phase. Absorbance of cell suspensions was measured at 680 nm daily to assess *C. merolae* liquid culture growth.

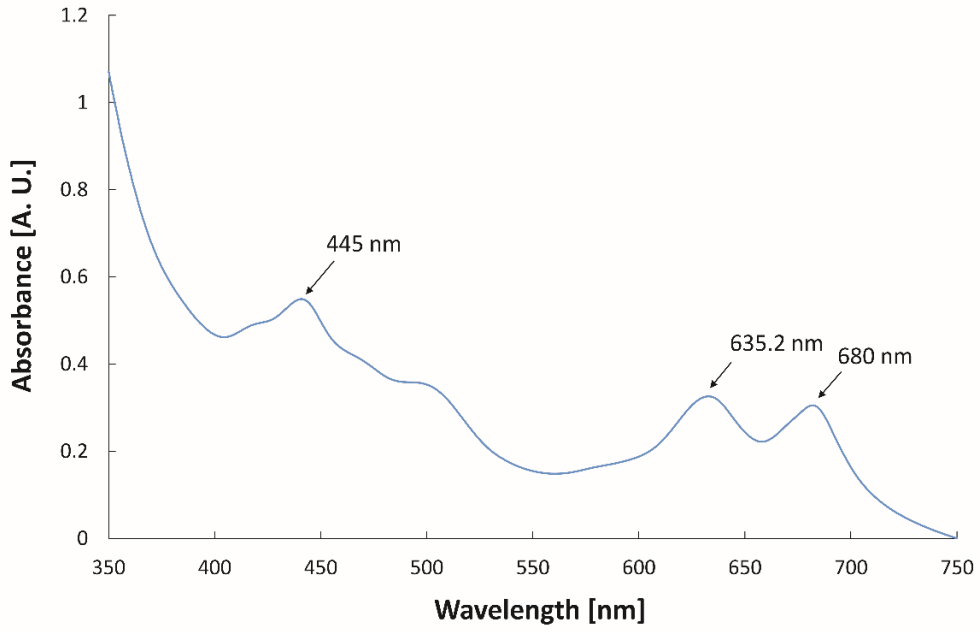

Figure 31

A representative RT absorption spectrum of an early log phase *C. merolae* cell suspension at "day 0" inoculation timepoint. Indicated are peaks corresponding to photosystems (445 nm and 680 nm) and phycobilisomes (635.2 nm). These peaks were indicative of the healthy cell growth.

3.2.1.2 *T. elongatus* cell culturing

The *T. elongatus* cells of were cultivated in BG-11 medium at 45º C, pH 8.0, with continuous white light of 90 µE with gentle bubbling with 5% CO_2 in air for 1-10 L cultures to aid the culture growth. Cultures were grown for approximately 7-13 days with continuous white light illumination of 90 µE to a maximum OD_{680} of 0.8-1.0 prior to thylakoid isolation.

3.2.1.3 *E. coli* cell culturing

The *Escherichia coli* liquid cultures were grown in a standard LB-Miller (Lysogeny broth, 10g L^{-1} NaCl, as specified above) medium at 37º C, with continuous vigorous agitation at 220 rpm. Cells were normally grown for 16 h unless a special overexpression system was employed (see below). Cells were also grown on 1.25 % agar plates with the standard LB-Miller medium. Antibiotic selection was used both for liquid and solid plate culturing using an appropriate concentration of the selection antibiotics. For double transformants, 30 µg ml^{-1} chloramphenicol and 100 µg ml^{-1} ampicillin were employed as the selection markers.

Specific culturing conditions were developed for the overexpression of cyt c_{553} variants for the double transformants. Overnight saturated cultures (16 h) were inoculated into a 1 L of LB-Miller liquid medium supplemented with antibiotics as specified above, and allowed to grow to an OD_{600} ~ 0.4. The cultures were then supplemented with 100 mg L^{-1} Fe_2SO_4 and 17 mg L^{-1} δ-aminolevulinic acid, and gene expression was induced with 0.2% arabinose for 20 hrs with a lowered rotation of 160 rpm at 37º C for Innova Incubators (New Brunswick™ Innova® 44/44R).

3.2.1.4 Preparation of *E. coli* competent cells

WT cells from the desired strain (TOP10 for cyt c_{553} overexpression) were inoculated to the desired volume from overnight saturated cultures. Cells were cultured (as specified above) until the OD_{600} ~ 0.4. Cells were then chilled on ice for 15 min. Cells were harvested at 3,000-5,000 x g for 5 min. Cells were re-suspended in 1/3 of the volume of the container (normally 16.7 ml for a 50 ml Falcon tube) in TFBI (as in **Chapter 3.1.6.2**) buffer and chilled on ice again for 15 min. Cells were harvested at 3,000 g for 5 min, then re-suspended in 1/30 of the volume of the container (normally 1.7 ml for a 50 ml Falcon tube) in TFBII (as in **Chapter 3.1.6.2**) buffer, re-chilled on ice for 15 min. and aliquoted to 200 µl and frozen immediately in liquid nitrogen and subsequently stored at -80º C.

3.2.1.5 *E. coli* transformation

All the competent cells were transformed using a heat shock method. Chiefly, 100 µl *E. coli* aliquots were used for transformation with recombinant plasmids and 200 µl *E. coli* aliquots were used for transformation with the ligation mixtures. Cell aliquots were thawed on ice. 10 ng of DNA was added (normally adjusted to a volume of 0.1 µL), and cells were kept on ice for further 10 min. Cells were heat-shocked in a heat block or hot water bath at 42º C for 90 s., then placed back on ice for precisely 2 min. One ml of LB-Miller medium was added and the cells were incubated at 37º C for 1 h with gentle shaking (~115 rpm), then pelleted at low speed (700-1,000 x g) and plated on the appropriate selective LB-agar plates. Plates were grown at 37º C for 16 hours after which the transformant colonies were selected and sub-cloned.

3.2.1.6 Cell harvesting and manipulation

For cell harvesting, cell cultures were centrifuged at 4,000 x g for 15 min. at 15º C and the cell pellets were transferred to ice in the cold room. The *C. merolae* cells were re-suspended in a prechilled buffer containing 40 mM MES-KOH, pH 6.1, 10 mM $CaCl_2$, 5 mM $MgCl_2$, 25% (w/v) glycerol supplemented with a Complete™ protease inhibitor cocktail tablet (Roche®), DNase I (5 mg) (Roche®) per 50 ml of buffer and kept in dim green light.

The *T. elongatus* cells were resuspended in 20 mM MES-KOH, pH 6.5, 10 mM $MgCl_2$ and 10 mM $CaCl_2$ supplemented with a Complete™ protease inhibitor cocktail tablet (Roche®), DNase I (5 mg) (Roche®) and RNAse I (10 µl from stock) (Sigma-Aldrich®) per 50 ml of buffer and kept in dim green light.

The *E. coli* cells were resuspended in a buffer containing 20 mM imidazole, 100 mM phosphate buffer (100 mM Na_2HPO_4, 18 mM KH_2PO_4, pH 7.5), 25% glycerol (w/v) and 30 µM phenylmethylsulfonyl fluoride (PMSF) (or one Complete™ protease inhibitor cocktail tablet (Roche®) and DNase I (5 mg, Roche®) per 50 ml of suspension, pH 7.5 and kept on ice at 4º C until further use or re-frozen in liquid nitrogen and stored at -80º C for the long term storage.

3.2.1.7 Cell disruption

All the cells used in this study were disrupted using a Bead Beater (Biospec®) system with 0.1 mm glass beads ROTH (Carl Roth®, Germany). After resuspension of the cell pellets in the specific buffers described for each cell material below, the cell suspensions were mixed with an equal volume of glass beads to the 80-90% of the bead beating chamber volume. Subsequently, the inner chamber was topped up with a mixture of ice and ice-cold water containing a pinch of NaCl, and the outer jacket was filled with ice. The specific protocols for cell rupture were applied for each cell material, as described in detail below.

For the *C. merolae* cell disruption, cells were resuspended in a buffer containing 40 mM MES-KOH, pH 6.1, 10 mM $CaCl_2$, 5 mM $MgCl_2$, 25% (w/v) glycerol, supplemented with a Complete™ protease inhibitor cocktail tablet (Roche®), DNase I (5 mg) (Roche®) per 50 ml of buffer. The cell suspensions were disrupted with equal intervals of a total of 13 cycles. Each cycle consisted of 10 seconds of beating followed by 4 minutes of rest. Ice levels were monitored closely, and were topped up as deemed necessary if the ice thawed.

For the *T. elongatus* cell rupture, the cells were resuspended in a buffer containing 20 mM MES-KOH, pH 6.5, 10 mM $MgCl_2$ and 10 mM $CaCl_2$ supplemented with a Complete™ protease inhibitor cocktail tablet (Roche®), DNase I (5 mg) (Roche®) and RNAse I (10 µl from stock) (Sigma-Aldrich®) per 50 ml of buffer. The cells were then disrupted by vigorous agitation with the beads at 10 sec. interim cycles with 4 min. of rest on ice, with a total of 17 cycles.

For *E. coli* cell disruption, cells were suspended in a buffer containing 20 mM imidazole, 100 mM phosphate buffer (100 mM Na_2HPO_4, 18 mM KH_2PO_4, pH 7.5), 25% glycerol (w/v) and 30 µM phenylmethylsulfonyl fluoride (PMSF) (or one tablet of Complete™ protease inhibitor cocktail (Roche®) and DNase I (5 mg, Roche®) per 50 mL of buffer. The cells were disrupted by vigorous agitation with the beads at 45 sec. interim cycles with 4 min. of rest on ice, with a total of 18 cycles. Prior to the *E. coli* cell lysate processing, the cell debris was removed by ultracentrifugation at 100,000 x g at 4º C for 45 min.

Cell lysates were briefly centrifuged at 1,000 x g to remove the unbroken cells, then filtered with the Whatmann paper to separate cell lysate from any residual cell debris or glass beads. All the photosynthetic samples were processed in dim green light at 15º C. The cell lysate obtained for each biological material was always filtered through 0.22 µM filtering devices and either processed immediately or frozen at -80º C for future use.

3.2.1.8 Thylakoid isolation from *C. merolae* cells

Thylakoids were pelleted by centrifugation at 100,000 x g for 30 min. at 4º C and washed once with *C. merolae* thylakoid isolation buffer. Final thylakoid pellets were resuspended in 40 mM MES-KOH, pH 6.1, 10 mM $CaCl_2$, 5 mM $MgCl_2$, 25% (w/v) glycerol, Chl*a* concentration was determined according to the Arnon method (see **Chapter 3.2.4.2**), and the membranes were snap-frozen in liquid N_2, and stored at -80º C for the long term storage or used immediately.

3.2.1.9 Thylakoid isolation from *T. elongatus* cells

Cyanobacterial cell homogenates were filtered as above with the same buffer (20 mM MES-KOH, pH 6.5, 10 mM $MgCl_2$ and 10 mM $CaCl_2$) supplemented with 0.5 M D-mannitol. The lysate was ultracentrifuged at 100,000 x g for 30 min. The pellet was then resuspended in the buffer as above but without D-mannitol. The same step was repeated two or three more times depending on the amount of phycobilisomes observed in the supernatant. The final

membrane suspension was resuspended in the buffer as above supplemented with 0.5 M D-mannitol, adjusted to a Chl*a* concentration of 3-5 mg ml^{-1} estimated by the Arnon method (see **Chapter 3.2.4.2**) and snap-frozen in liquid N_2 and stored at -80º C for long term storage or used immediately.

3.2.2 Molecular Biology methods

3.2.2.1 Primer design

All primers were designed employing Clone Manager™ software and later reverified with Sap Gene™ software. The *petJ* gene sequence encoding cyt c_{553} protein, was obtained from the *C. merolae* gene database (annotated CMV193C in the *C. merolae* gene database; http://merolae.biol.s.u-tokyo.jp/db/). The restriction sites of NcoI and SacI were added to the termini of the primer sequences to generate sticky ends upon digestion and facilitate cloning into the expression vectors. The full primer sequences are listed in **Table 7**.

3.2.2.2 Polymerase chain reaction protocols

Dream Taq™ Green PCR Master Mix (2x) was gently vortexed and centrifuged after thawing. Ideally, the preparation was aliquoted upon arrival and kept in aliquots to avoid freeze-thawing. A thin-walled PCR tube was placed on ice and the following components were added per 50 µl reaction (**Table 8**):

Table 8

Typical components of a PCR reaction mixture

Dream Taq ™ Green PCR Master Mix (2x)	25 µl
Forward primer	1µl (equivalent to 40 nmol)
Reverse primer	1µl (equivalent to 40 nmol)
Template DNA	10pg – 1µg (0.1 µl of *C. merolae* culture)
Nuclease-free H_2O	22.9 µl
Final volume	50 µl

The samples were gently vortexed and centrifuged quickly before placing in the thermocycler (Eppendorf® Mastercycler® ThermoScientifc®).

The following PCR protocol was performed:

Table 9

Typical PCR protocol for amplification of the *petJ* gene

Step	Temperature ºC	Time	Number of cycles
Initial denaturation	95	1-3 min.	1
Denaturation	95	30 s	25-40
Annealing	Tm-5 (68-72)	30 s	25-40
Extension	72	1 min./kb	25-40
Final extension	72	5-15 min.	1

3.2.2.3 DNA digestion methods

Standard DNA digestion reactions were performed by mixing the ingredients as in **Table 10** and incubating the reaction mixtures for 15 min. at 37º C to allow for the complete digestion.

Table 10

Composition of the plasmid and DNA fragment restriction digestion mixture

Component	Plasmid DNA	PCR DNA
Nuclease-free H_2O	15 µl	17 µl
10X FasDigest® Green Buffer	2 µl	2 µl
DNA	2 µl (up to 1µg)	10 µl (up to 5µg)
FastDigest® enzyme	1 µl	1 µl
Final volume	20 µl	30 µl

3.2.2.4 DNA agarose gel electrophoresis and DNA extraction from the agarose gels

Normally, 1.5% TAE gels were run at 100-150 V (depending on DNA fragment/plasmid size) until the bands were resolved properly. The DNA fragment extraction from the agarose gels was performed with the GeneJET™ Gel Extraction Kit (Fermentas, Thermo Scientific®) using the freshly prepared solutions, as specified in **Chapter 3.1.3.** Gel slices containing the DNA fragments were excised with a clean scalpel or razor blade minimising the gel volume. The slice was placed in a pre-weighed 1.5-ml Eppendorf tube to estimate its weight. UV light exposure, used for DNA visualisation, was minimised to avoid DNA damage. Binding buffer

was added in a 1:1 ratio to the gel slice (volume:weight), i.e., 100 µl of binding buffer for every 100 mg of agarose gel. The slice and the buffer were incubated at 50-60º C for 10 min. with gentle rotation until the agarose was completely dissolved. The solubilised gel solution was run through a GeneJET™ purification column (Fermentas, Thermo-Scientific®). The column was centrifuged for 1 min. at 13,000 x g using a benchtop microcentrifuge. The flow-through was discarded and the column was placed back in the same collection tube. 700 µl of wash buffer was added and the column was centrifuged for 1 min. The flow-through was discarded and the column placed back in the collection tube. The column was transferred to a new clean Eppendorf tube and 50 µl of elution buffer (or ultra-high-quality MilliQ H_2O) was added to the centre of the column membrane and the column was centrifuged for 1 min. to elute DNA. The DNA fragment was used immediately or aliquoted and stored at -20º C until further use.

3.2.2.5 Plasmid extraction from *E. coli* cells

E. coli strain DH5α was used for all the molecular biology manipulations unless stated otherwise. Normally, 1 mL of *E. coli* overnight saturated culture was used for plasmid extraction. All the subsequent purification steps were carried out at room temperature. All centrifugations were performed on a bench-top centrifuge at a maximum speed of 13,000 x g. All plasmid isolations were performed with the GeneJET™ Plasmid Miniprep Kit (Fermentas, Thermo Scientific®) as specified in **Chapter 3.1.3**, with freshly prepared solutions. Cells were pelleted and resuspended in 250 µl of Resuspension Buffer (Fermentas, Thermo Scientific®). The resuspension was vortexed vigorously to avoid any cell lumps. 250 µl of the Lysis Solution (Fermentas, Thermo Scientific®) was added and mixed thoroughly by inverting the tube 4-6 times until the solution became viscous and translucent. 350 µl of the neutralisation solution was added and mixed immediately and thoroughly by inverting the tube 4-6 times. The tube was centrifuged for 5 min. to pellet cell debris and chromosomal DNA. The supernatant was transferred to the supplied GeneJET™ spin column by decanting or pipetting, taking care not to transfer the white cellular debris precipitate. The column in the tube was centrifuged for 1 min. and the flow-through was discarded. The column was placed back in the same collection tube. 500 µl of the Wash Solution (Fermentas, Thermo Scientific®) was added (diluted with ethanol prior to first use as per manufacturer's instuctions) to the GeneJET™ spin column (Fermentas, Thermo Scientific®). The column was centrifuged for 30-60 s. and the flow-through discarded. The column was placed back in the same collection

tube. The procedure was repeated. The flow-through was discarded and the procedure repeated once more to remove any residual ethanol. The GeneJET™ spin column (Fermentas, Thermo Scientific®) was transferred into a fresh 1.5 ml microcentrifuge tube and 50 µl of the elution buffer (or ultra-high-quality Milli-Q H_2O) was added to the centre of GeneJET™ spin column (Fermentas, Thermo Scientific®) to elute the plasmid DNA. The column was incubated for 2 min. at room temperature and centrifuged for further 2 min. The purified plasmid DNA stored at -20º C.

3.2.2.6 Ligation protocols

Standard ligation mixtures were prepared as in **Table 11** below,

Table 11

Composition of the ligation mixture

Linear vector DNA (digested plasmid)	20-100 ng (normally 1.5 µl)
Insert DNA (PCR products)	5-6:1 molar ratio over vector (8.5 µl volume, concentration adjusted if deemed necessary)
10 x T4 DNA Ligase Buffer (Thermo Scientific®)	2 µl
T4 DNA ligase (Thermo Scientific®)	1 µl
Nuclease-free H_2O	7 µl (adjusted to reach a total volume of 20 µl)
Total volume	20 µl

Ligation mixtures were incubated in a water bath at 16º C or overnight at 4º C and were used for transformation the following day.

3.2.2.7 Selection of *E. coli* transformants

Single transformant colonies were selected on the selective media agar plates, the DNA was amplified with overnight *E. coli* cultures and the recombinant plasmids were purified and analysed by both restriction analysis and DNA sequencing.

3.2.2.8 Cloning of the *C. merolae petJ* gene

Genomic DNA from *C. merolae* was used as a template for polymerase chain reaction (PCR) to amplify the *petJ* gene (annotated CMV193C; http://merolae.biol.s.u-tokyo.ac.jp/db/). The original verified sequence of *petJ* was cloned into pET28b-(+) vector (Invitrogen®) together with 4 distinct sequences of AA linkers introduced by using different reverse primers (as depicted in **Table 7**) between the *petJ* sequence and the *C*-terminal His_6-tag encoded by the multiple-cloning site of the pET28b-(+) vector. The entire constructs were excised with NcoI and PstI restriction enzymes, and sub-cloned into a pBAD/HisA expression vector (Invitrogen®) using the same restriction enzymes and transformed into *E. coli* strain DH5α. The correct orientation and sequence of the petJ::pBAD/HisA constructs was confirmed by restriction analysis of recombinant plasmids and DNA sequencing. For all the maps of all the plasmids used and constructed in this study refer to **Chapter 7.2**.

3.2.3 Protein purification methods

3.2.3.1 Cytochrome c_{553} purification from the *E. coli* lysate

3.2.3.1.1 Batch purification on Ni-NTA agarose

Buffers were prepared in advance. The carrier buffer contained 20 mM imidazole, 10x SPB, 25% glycerol (w/v), pH 7.5. Wash buffers were prepared identically but the concentration of imidazole was increased as desired (normally up to a maximum of 60 mM). The elution buffer had the same composition but was supplemented with 250 mM imidazole. The pH of all the buffers was adjusted to 7.5. An appropriate amount of Ni-NTA resin was transferred to an Eppendorf tube. The tube was centrifuged for 2 min. at 700 × g and the supernatant was carefully removed and discarded. Two resin-bed volumes of the carrier buffer were added and mixed gently until the resin was fully suspended. The suspension was centrifuged for 2 min. at 700 × g and the buffer was carefully removed and discarded. The sample was prepared by mixing the cell lysate with an equal volume of the carrier buffer. The total volume was equal to at least two resin bed volumes. Thus prepared protein extract was added to the pre-equilibrated Ni-NTA resin as above and mixed on an end-over-end rotator for 30 min. either at room temperature or 4º C overnight, as required. The mixture was centrifuged for 2 min. at 700 x g. The resin was then washed with two bed volumes of the wash buffer, then centrifuged for 2 min. at 700 x g. The wash step was repeated and the supernatant monitored spectroscopically by measuring its absorbance at 280 nm until the

baseline stabilised. This step was repeated as many times as deemed necessary to remove excess of non-specifically bound proteins. Bound His_6-tagged proteins were eluted using 1:1 ratio of the resin-bed volume to the elution buffer. The agarose suspension was further centrifuged for 2 min. at 700 x g, and the supernatant carefully collected. This step was repeated twice, and each supernatant fraction was collected in separate tubes. Protein elution was normally monitored spectroscopically by measuring the absorbance of the fractions at 280 nm. The eluted protein fractions were analysed spectroscopically and by SDS-PAGE.

3.2.3.1.2 FPLC purification of the cytochrome c_{553} variants using immobilised metal affinity chromatography

After filtration, samples were applied on an FPLC preparative Ni^{2+}-nitrilo-triacetic acid (Ni-NTA) HisTrap™ FPLC/HPLC column (GE Healthcare®) at a flow rate of 0.5 ml min^{-1}. The non-specifically bound proteins were washed for 30 min. at a flow rate of 0.5 ml min^{-1} with 50 mM imidazole in 100 mM (10x) phosphate buffer (100 mM Na_2HPO_4, 18 mM KH_2PO_4, pH 7.5). The His_6-tagged cyt c_{553} fractions were eluted with a linear gradient of 50-420 mM imidazole in the same buffer. The column was further washed with 500 mM imidazole in 100 mM phosphate buffer (100 mM Na_2HPO_4, 18 mM KH_2PO_4, pH 7.5) for 30 min. Elution and the final washing steps were done at a flow rate of 0.5 ml min^{-1}. Elution of cyt c_{553} fractions was monitored simultaneously at 416 nm, 521 nm and 553 nm, corresponding to the absorption peaks of the reduced forms of cyt c_{553}. Cyt c_{553}-containing fractions were pooled and concentrated in the VIVASPIN-2 devices (3,000 MWCO, Sartorius-Intec®, Poland) and resuspended in 100 mM phosphate buffer (100 mM Na_2HPO_4, 18 mM KH_2PO_4, pH 7.5) supplemented with 25% glycerol (w/v).

3.2.3.2 Purification of the *T. elongatus* PSI trimer

Crude *T. elongatus* thylakoids were thawed for 3-4 hours on ice, or used directly after isolation. The Chl*a* concentration (a total of 66.3 mg Chl*a*) was adjusted to 1.61 mg ml^{-1} (1.8 mM) (Arnon method, see **Chapter 3.2.4.2**) before solubilisation with 0.5% (w/v, from a 10% stock solution) DDM (10 mM) at a detergent to Chl*a* molar ratio of ~5:1 in the presence of 1 tablet of Complete™ protease inhibitor cocktail (Roche®) for 20 min. at RT in the dark, with gentle rotation or stirring. The solubilised thylakoids were centrifuged at 104,200 x g for 45 min. at 4 ºC. The *T. elongatus* PSI trimers were purified from solubilised thylakoids by eluting from the DEAE TOYOPEARL 650M column with 0.09 M NaCl. Briefly, filtered supernatants

were applied onto a DEAE TOYOPEARL 650M column pre-equilibrated with 40 mM MES-KOH, pH 6.1, 10 mM $CaCl_2$, 5 mM $MgCl_2$, 25% (w/v) glycerol supplemented with 0.03% DDM. The loaded column was washed with 2 column volumes of 0.09 M NaCl, 40mM MES-KOH, pH 6.1, 3 mM $CaCl_2$, 25% (w/v) glycerol, 0.03% (w/v) DDM to elute the crude PSI trimers which were then processed as described below. All steps were performed at a flow rate of 5 ml min^{-1}, with the exception that the column equilibration was done at a flow rate of 7 ml min^{-1}. Eluted fractions were analysed spectroscopically, and the PSI-enriched fractions were pooled, then directly applied onto a 350-400 ml bed volume Spehadex G-25® (Sigma-Aldrich®) filtration column which had been previously equilibrated with the carrier buffer composed of 40 mM HEPES-NaOH, pH 8.0, 3 mM $CaCl_2$, 25% (w/v) glycerol, and 0.03% (w/v) DDM. The pooled fractions were applied and eluted continuously at 3-4 ml min^{-1}. Desalted PSI trimers were collected, concentrated with the 100-kDa MWCO filtering devices (Sartorius-Intec®, Poland). Following Chl*a* determination (Arnon method, see **Chapter 3.2.4.2**) the PSI samples were either used immediately for the next purification step or snap frozen in liquid nitrogen and stored at -80º C until further use. The crude, desalted PSI trimers were applied to a DEAE TOYOPEARL 650 S column that was pre-equilibrated with the carrier buffer (40 mM HEPES-NaOH, pH 8.0, 3 mM $CaCl_2$, 25% (w/v) glycerol, 0.03% (w/v) DDM). The bound PSI trimer complexes were extensively washed with the carrier buffer at 3 ml min^{-1} to remove the excess of phycobilisomes (PBS) and carotenoids, as verified by RT absorption spectroscopy. The PSI trimers were then eluted with a linear gradient of 0-0.5 M NaCl at 3 ml min^{-1}, with the trimers specifically and very strongly bound to the top of the column compared to PSI monomers which were bound less strongly, hence eluted in the early phase of the NaCl gradient. The eluted PSI trimers were then applied onto a desalting Sephadex G-25® (Sigma Aldrich®) column in the carrier buffer as above, collected, concentrated to 3-5 mg ml^{-1} Chl*a* (Arnon method, see **Chapter 3.2.4.2**) then snap-frozen in liquid nitrogen and stored at -80º C prior to use or used immediately for spectroscopic, 77K fluorescence, photochemical activity and SDS-PAGE analyses.

3.2.3.3 Purification of the *C. merolae* PSI-LHCI supercomplex

Thylakoids (1 mg ml^{-1} of Chl*a* (Arnon method, see **Chapter 3.2.4.2**)) were solubilized with 1% (w/v) DDM at 4º C with gentle yet continuous rotation for 40 min. in the dark. Solubilised membranes were centrifuged at 104,200 x g for 30 min. at 4º C to remove the insoluble fraction, then filtered and loaded at 5-7 ml min^{-1} onto a DEAE TOYOPEARL 650 M column (40 mL bed volume) pre-equilibrated with the equilibration buffer composed of 40 mM MES-KOH, pH 6.1, 10 mM $CaCl_2$, 5 mM $MgCl_2$, 25% (w/v) glycerol supplemented with 0.03% DDM. To elute the crude PSI-LHCI supercomplex sample, the column was washed with 2 bed volumes of the low-salt buffer comprising 0.09 M NaCl, 40 mM MES-KOH, pH 6.1, 3 mM $CaCl_2$, 25% (w/v) glycerol, 0.03% (w/v) DDM at 5-7 ml min^{-1}. All the subsequent steps were performed at a flow rate of 5-7 ml min^{-1}, with the column equilibration done at the maximal flow rate of 7 ml min^{-1} or slowly overnight. Eluted fractions were analysed spectroscopically to identify the PSI-enriched fractions. The PSI-enriched fractions were then pooled, and directly applied onto a 350-400 mL bed volume Spehadex G-25® (Sigma-Aldrich®) filtration column pre-equilibrated with the carrier buffer (40 mM HEPES-NaOH, pH 8.0, 3 mM $CaCl_2$, 25% (w/v) glycerol, 0.03% (w/v) DDM). The pooled crude PSI fractions were then eluted continuously at a 3-4 ml min^{-1} flow rate. The desalted crude PSI-LHCI sample was collected, concentrated with the 100-kDa MWCO filtering devices, and used either immediately for the next step of PSI purification or snap frozen in liquid nitrogen and stored at -80º C until further use. Crude desalted PSI-LHCI sample was applied onto a DEAE TOYOPEARL 650 S column (30 mL bed volume) and pure PSI-LHCI supercomplex fractions were eluted with a continuous 0-0.25 M NaCl gradient in the carrier buffer. The fractions were analysed by RT absorption spectroscopy to select the purest PSI-LHCI-containing fractions that were devoid of contaminating PBSs. For a representative spectrum of a PSI-LHCI fraction contaminated with PBSs, refer to **Suppl. Figure 1**. The pure PSI-LHCI fractions, obtained after the DEAE 650 S column, were pooled and subsequently concentrated to 1 mg ml^{-1} Chl*a* and further purified to remove any residual PBSs by the following two methods: (1) additional chromatography purification step performed on the desalting Superdex G-25® (Sigma Aldrich®) column in the carrier buffer (40 mM HEPES-NaOH, pH 8.0, 3 mM $CaCl_2$, 25% (w/v) glycerol, 0.03% (w/v) DDM) and (2) fractionation on a discontinuous sucrose gradient (0.4 M sucrose, 0.45 M betaine, 5 mM Tris-HCl, pH 8, 0.05% (w/v) DDM) prepared by a freeze-thaw method [151] (see below) and ultracentrifuged at 125,000 x g (SW Ti32 rotor,

Beckman-Coulter®, USA) for 20 hours at 4º C. Chl*a* concentration was determined using the Arnon method (see **Chapter 3.2.4.2**).

3.2.3.4 Discontinuous sucrose gradient fractionation

The discontinuous sucrose gradient preparation and fractionation was adapted from [151]. Briefly, a 0.4 M sucrose, 0.45 M betaine, 5 mM Tris-HCl, pH 8, 0.05% (w/v) DDM buffer was distributed on an equal weight basis into the polyallomer tubes (Beckman-Coulter®) up to 85% of their volume, covered with parafilm and frozen at -20º C or -80º C for at least 15 h prior to use. Tubes were thawed at 4º C vertically without any disturbance for approximately 5 h, and then the sample was applied. For the large-scale fractionation, a sucrose gradient was prepared in 35-ml polyallomer tubes and a maximum of 500 µg of Chl*a* was added per tube. Before application, the buffer of the PSI-containing sample was exchanged to a low ionic strength buffer composed of 50 mM K_2HPO_4-KH_2PO_4, pH 8.0, 0.03% (w/v) DDM, and the volume was adjusted so that 1-2 ml portions (corresponding to 350 µg Chl*a*) were very gently overlaid on top of the gradients, then centrifuged at 125,000 x g (SW Ti32 rotor, Beckman-Coulter®, USA) for 20 h at 4º C. The densest band(s) containing the pure PSI-LHCI supercomplex was/were concentrated and exchanged to the carrier buffer (40 mM HEPES-NaOH, pH 8.0, 3 mM $CaCl_2$, 25% (w/v) glycerol, 0.03% (w/v) DDM). Final Chl*a* concentration was determined using the Arnon method (see **Chapter 3.2.4.2**) and the sample was either snap frozen in liquid nitrogen and stored at -80º C, or used immediately for spectroscopic, 77K fluorescence, photochemical activity or SDS-PAGE analyses.

3.2.3.5 Size exclusion chromatography

Fractions containing the PSI-LHCI supercomplexes were further characterised by size exclusion chromatography (SEC), using a Biosep SEC-4000 column (Phenomenex®, Torrance, CA) equilibrated with a carrier buffer (20 mM MES-KOH, pH 6.5, 10 mM $MgCl_2$, 3 mM $CaCl_2$, 0.5 M mannitol, 0.05% DDM) at a flow rate of 2 ml min^{-1}.

3.2.4 Spectroscopic methods

3.2.4.1 RT absorption spectroscopy

For the *C. merolae* cells, thylakoids, and other photosynthetic material (5 µg of Chl*a* ml^{-1}), optical absorption spectra were recorded at room temperature in the range of 800-350 nm using a UV-1800 Shimadzu spectrophotometer with the TCC-100 temperature controlled cell holder using a quartz cuvette with an optical path length of 10 mm, a slit width of 0.1-0.5 nm and sampling intervals of 0.05-2.0 nm. Normally, a slit width of 0.1 nm and sampling intervals of 0.5 nm were employed.

3.2.4.2 Measurement of Chl*a* concentration

Chl*a* concentration was determined according to the Arnon method [152]. Briefly, 1-5 µL of photosynthetic material was diluted into 1 mL of freshly prepared 80% acetone. After vortexing for 2 min. and 13,000 x g centrifugation for 2 min., the absorption of Chl*a* was recorded at 663 nm, taking into account the dilution factor. An extinction coefficient of 86.3 μL^{-1} μg^{-1} cm^{-1} [152] was employed to calculate the Chl*a* concentration.

3.2.4.3 Redox difference absorption spectroscopy of cytochrome c_{553}

UV-VIS spectra [(5-20 µg ml^{-1} protein in 10 mM phosphate buffer (SPB x 1) or standard phosphate buffer (10 x SPB) (100 mM Na_2HPO_4, 18 mM KH_2PO_4, pH 7.5), as described in **Chapter 3.1.6.3**. Spectra were recorded in a Shimadzu UV 1800 spectrophotometer at RT. For redox difference spectroscopy, a few grains of sodium dithionite were added to fully reduce the cytochrome sample, and the corresponding spectrum was recorded. Subsequently, a grain of ferricyanide ($[Fe(CN)_6]^{3-}$, FeCN) was added to monitor oxidation of the cyt sample by measuring the absorption spectra, in which flattening of the 521 nm and 553 nm peaks was observed upon chemical oxidation of the sample. An equivalent amount of FeCN was added again, until the protein was fully oxidised. Excess FeCN had to be added to obtain the fully re-oxidised species. Re-reduction of the sample was initiated by titration with sodium dithionite, resulting in the reappearance of the 416 nm, 521 nm, and 553 nm peaks. The difference between absorption at 553 nm in the fully reduced and fully oxidised states of the cyt sample was used to calculate the exact concentration of redox active cyt c_{553} using a molar extinction coefficient of 24.1 mM^{-1} [153].

3.2.4.4 Fluorescence spectroscopy

Briefly, an LS 55 Fluorescence Spectrofluorometer (Perkin Elmer) with an adaptor for 77K measurements was used. For spectroscopic measurements, the PSI-LHCI samples were diluted to 3 μg ml^{-1} Chl in 40 mM HEPES-NaOH, pH 8.0, 3 mM $CaCl_2$, 25% (w/v) glycerol, 0.03% (w/v) DDM supplemented with 80% (w/v) glycerol, to a final concentration glycerol of 40% (w/v). The capillary tubes with the samples were frozen in liquid nitrogen and the fluorescence steady-state emission spectra were recorded in the range of 600-800 nm using an excitation wavelength of 435 nm for Chl*a* and in the range of 620-800 nm for an excitation wavelength of 600 nm for PBS emission. Action spectra were generated by exciting the samples at 400-700 nm and recording emission at 728 nm.

3.2.5 Fluorescence microscopy methods

3.2.5.1 Microscope slide preparation

The plasmonic nanohybrid samples were prepared on microscopic slides at RT as follows. For preparation of the reference sample, PSI-LHCI complexes (0.12 μg ml^{-1} Chl*a*) were enclosed within a polymer matrix of 0.05% aqueous polyvinyl alcohol (PVA) and spin-casted on a glass substrate. Such a low concentration of PVA allowed for the proper formation of a layer of PSI complexes. For preparation of the physisorbed sample (PSI-LHCI+AgNWs), functionalised silver nanowires (AgNWs) were first mixed with the buffer suspension of PSI-LHCI complexes (0.12 μg ml^{-1} Chl*a*) in 0.05% PVA and were then spin-coated on a glass substrate. For the generation of bioconjugated sample (PSI-LHCI@AgNWs), Ni-NTA-functionalised AgNWs were incubated for 60 min. with 90 μg ml^{-1} of cyt c_{553} resuspended in the standard PSI-LHCI carrier buffer (40 mM HEPES-KOH, pH 8.0, 3 mM $CaCl_2$, 25% glycerol (w/v), 0.03% DDM) (see **Chapter 3.1.6.3**). The bioconjugated AgNWs were centrifuged and rinsed 3 times in the same buffer to remove any unbound protein, then incubated with the PSI-LHCI complex (12 μg ml^{-1} Chl*a*) for 60 min. The sample was rinsed 3 times in the same buffer as above (40 mM MES-KOH, pH 8.0, 3 mM $CaCl_2$, 25% (w/v) glycerol, 0.03% DDM) to remove any unbound PSI, followed by resuspension in 0.05% PVA and spin-coating on a glass substrate.

3.2.5.2 Optical characterisation and fluorescence microscopy

Absorption and extinction spectra were measured using a Varian Cary 50 spectrophotometer. Emission spectra were collected with a Horiba Jobin Yvon Fluorolog 3 spectrofluorometer. The fluorescence intensity maps were measured using a Nikon Eclipse Ti-U body-based wide-field fluorescence microscope with the Nikon Plan Apo immersion oil objective lens (100x, NA of 1.4). This setup employs the Andor iXon3 Du-888 EMCCD camera as a detector, cooled to -75 ºC to minimize dark counts contribution in collected signals, together with a T650LPXR dichroic mirror (Chroma) as well as FELH0650 (Thorlabs) and FB670-10 (Thorlabs) optical filters. Fluorescence intensity maps measurements were conducted using two excitation wavelengths of 405 nm and 535 nm, provided by LED illuminators, both normalised to generate the 100 μW beam. Both LED illuminators were equipped with optical filters (FB405-10 and FEL0600, respectively; Thorlabs). In order to perform comparative analysis of results collected for both excitation wavelengths, for each area of the samples analysed a set of consecutive measurements was performed. Firstly, fluorescence intensity frames excited at 535 nm were taken followed by collection of the fluorescence signals from the same area of the sample, using excitation at 405 nm. Additionally, in the case of samples containing AgNWs, a picture of chosen sample area was taken in transmission mode to check correlation between the position of nanowires and spatial arrangement of emitting regions. Time-resolved fluorescence measurements were performed using a home-built confocal fluorescence microscope. The excitation laser of 485 nm in a pulsed mode with a repetition rate of 20 MHz and average power of 48 μW was used. Gaussian beam of the laser was achieved using a spatial filter with a 25 μm pinhole. The laser was focused on the sample using a microscope oil objective 60X, NA=1.49 (Nikon®). The sample was placed on a piezoelectric translation stage, which enabled a continuous movement with respect to the excitation laser beam. The emission was filtered by a long pass filter HQ655LP (Chroma®) and extracted with a bandpass filter HQ675/20 (Chroma®). The time-correlated single photon counting technique was used to measure dynamics of the fluorescence. The setup combines an SPC-150 module (Becker & Hickl) with fast avalanche photodiode (idQuantique id100-50) as a detector and gives the temporal resolution of 100 ps. (reproduced from Materials and Methods from [149]).

3.2.6 Photochemical activity measurements

Photochemical activity of the purified PSI-LHCI (5 µg Chl*a*) complex was measured by the O_2 consumption assay [154,155] using an oxygen Clark-type electrode (Hansatech®) (see **Figure 32**). Measurements were performed at 30º C in the reaction buffer (40 mM HEPES-NaOH, pH 8.0; 3 mM $CaCl_2$, 25% (w/v) glycerol, 0.03% DDM) in the presence of 0.1 mM methyl viologen (MV) and 0.1 mM dichlorophenolindophenol (DCPIP) as the exogenous electron acceptor and mediator, respectively. Samples (5 µg ml^{-1} Chl*a*) were incubated in the dark for 2 min. followed by the addition of 3 mM sodium ascorbate (NaAsc) as the sacrificial electron donor and illumination with a white light intensity of 5,000 µE, using a KL 2500 LCD white light source (Schott®, Germany). The sample was incubated with the three exogenous electron mediators as above and a background reaction (up to 15-20 µmoles O_2 mg^{-1} Chl h^{-1}) was observed in the dark, which was considered for all the final activity calculations. Following illumination of the sample a maximum oxygen consumption reaction proceeded until all the oxygen in the 1 ml reaction mixture was consumed. Each activity measurement was repeated at least three times. The same protocol was applied for all the PSI preparations from *C. merolae* and *T. elongatus*.

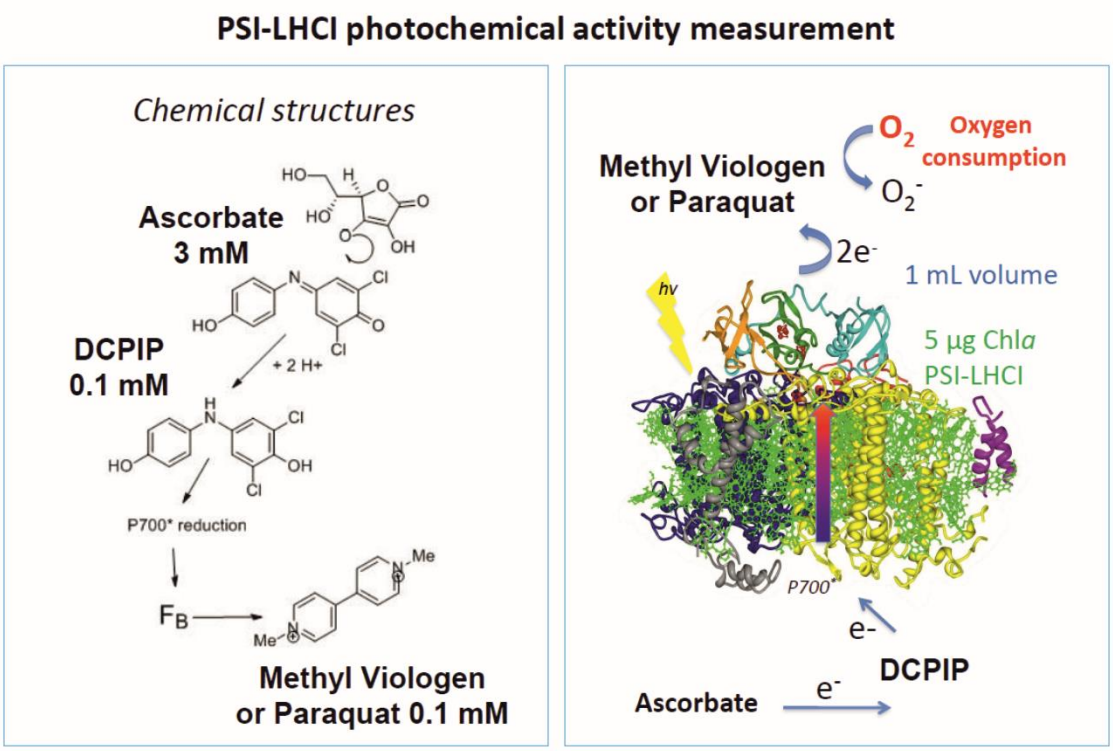

Figure 32

Schematic representation of the oxygen consumption assay for determination of the PSI-LHCI photochemical activity. Chemical structures of redox mediators with appropriate concentration or the amount of Chl*a* per 1 mL reaction mixture are displayed. The full electron transfer pathway is shown in the right panel.

3.2.7 Standard biochemical methods

3.2.7.1 Bradford colourimetric assay for protein quantification

The classic method from [148] was employed with an updated protocol and reagent composition. Briefly, a 3.1 ml assay mixture consisted of mixing 1 part of the protein sample with 30 parts of the Bradford Reagent (Sigma Aldrich®). The sample was either a blank, a protein standard, or an unknown sample. Blank samples consisted of a buffer with no protein. The protein standard consisted of a known concentration of protein, and the unknown sample was the solution to be measured for protein concentration. Bradford assay was performed at room temperature. Colour development began immediately. The absorbance at 595 nm was recorded and the protein concentration was determined by comparison to a standard curve freshly prepared each time. BSA was employed as a standard sample. Below is an example of a typical BSA standard table and curve (**Table 12** and **Figure 33**, respectively).

Table 12

Typical Bradford assay standard curve

Sample no.	Sample volume (ml)	[BSA] protein standard (mg/ml)	Bradford reagent (ml)
1	0.1	0	3
2	0.1	0.25	3
3	0.1	0.5	3
4	0.1	1.0	3
5	0.1	1.4	3
6	0.1	(unknown)	3

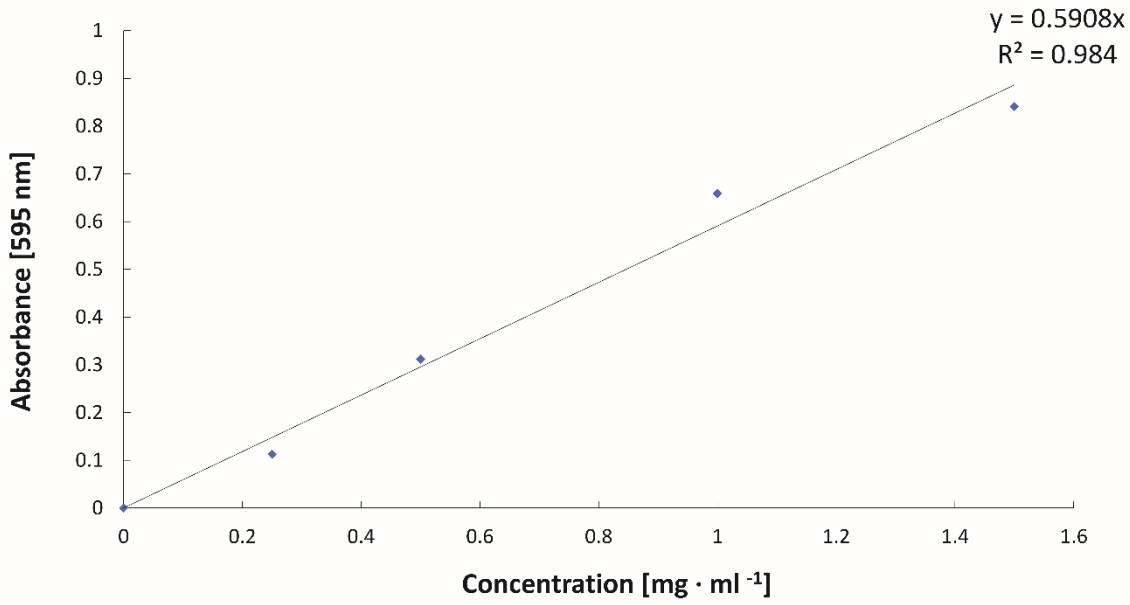

Figure 33

Typical BSA standard curve employed for determination of protein concentration. The maximum BSA standard concentration was 1.4 mg ml^{-1}.

3.2.7.2 Sodium dodecyl sulphate-polyacrylamide gel electrophoresis

The Tris-Tricine SDS-PAGE system was used according to [147]. Typically, 0.7 mm-thick gels were used with the BioRad Mini Protean II (BioRad®) system. Acrylamide solutions were prepared as stated in **Chapter 3.1.6.4**. All the electrode and gel buffers were prepared as described in **Tables 13** and **14**.

Table 13

Composition of SDS-PAGE running buffers and gel buffer

Concentration	Anode Buffer	Cathode Buffer	Gel buffer (3x)
Tris (M)	1.0	1.0	3.0
Tricine (M)	-	1.0	-
HCl (M)	0.225	-	1.0
SDS %	-	1.0	0.3
pH	8.9	~8.25	8.45

Table 14

SDS-PAGE gel composition depending on the desired polyacrylamide gel concentration

Ingredient amounts	4% casting gel	10% running gel	16% running gel	16% running gel/6 M urea
AB-3/AB-6 (ml)	1	6	10	10
Gel buffer (3X) (ml)	3	10	10	10
Glycerol (g)	-	3	3	-
Urea (g)	-	-	-	10.8
Water to final volume (ml)	12	30	30	30
APS (10%) (µl)	90	150	100	100
TEMED (µl)	9	15	10	10

6 M Urea was employed in all the gels used for separation of trans-membrane proteins. The freshly prepared ammonium persulfate (APS) solution and TEMED were added immediately before pouring the gels.

Protein samples were mixed 5:1 (v/v) with the appropriate amount of the 5x sample buffer composed of 0.225 M Tris-HCl, pH 6.7; 50% glycerol; 5% SDS; 0.05% bromophenol blue; and 0.25 M 1,4-dithiothreitol (DTT), as specified in **Chapter 3.1.6.4**. Normally, 0.2-3 µg of protein was loaded per lane for non-Chl*a* containing samples, whereas for Chl*a*-containing samples no more than 5 µg of Ch*a* was loaded per lane. Roughly 0.2–1 µg of protein for each protein band was sufficient for Coomassie staining or transfer onto PVDF membranes for the in-gel IMAC assay (see below). Accordingly, the desired protein concentration in the sample was estimated to be approximately 0.1 mg ml^{-1} for each protein band.

After mixing the protein sample and 5 x sample buffer on an equal amount or volume basis, soluble protein samples were incubated at 95º C for 8 min., with interim vortexing every 2 min., whereas membrane proteins (photosynthetic samples) were incubated in the same sample buffer in the dark for 45 min. at RT, with occasional vortexing every 10-15 min. The samples were then centrifuged at 13,000 x g using a benchtop microcentrifuge and the supernatant was loaded onto the SDS-PAGE gels. The supernatant was pippeted very carefully to avoid accidentally aspiring the pellet. A volume of 15-20 µl (3 µg protein or 5 µg of Chl*a*) was never exceeded to avoid cross-contamination between the wells. Normally, 3-5 µg of Chl*a* was sufficient for proper visualisation of all protein bands by Coommassie staining. The running conditions for SDS-PAGE are shown in **Table 15**.

Table 15

SDS-PAGE gel running conditions

	10% (0.7 mm)	**16% (0.7 mm)**	**16% (1-1.6 mm)**
Initial voltage	30 V	30 V	30 V
Next voltage step	190 V	200 V	90 V constant
Voltage at end of run	270 V	300 V	-
Time	1-2 h	2-3 h	5-6 h

The resolved SDS-PAGE gels were either incubated in a fixing solution composed of 50% methanol, 10% acetic acid, 100 mM ammonium acetate for 30 min., or washed with Milli-Q water prior to Western blotting (see below). Fixed gels were then stained overnight with 0.025% Coomassie Brilliant Blue (R-250) in 10% acetic acid. The gels were destained by washing several times with copious amounts of the destaining solution (10% acetic acid). Developed gels were transferred to water, photographed, and dried using a gel drying system (Sigma Aldrich®).

3.2.7.3 Western blotting

Immediately after electrophoresis, gels were equilibrated with Milli-Q water for 2 min., then with 1 x transfer buffer (25 mM Tris, 192 mM glycine, see **Chapter 3.1.6.5**) for 10–15 min. PVDF membranes were activated in 100% methanol (analytical or HPLC grade), then equilibrated in the 1 x transfer buffer for 5-10 min. The blot was placed towards the cathode and the gel towards the anode in the transfer sandwich, according the manufacturer's instructions (BioRad®). The transfer was performed at a constant current of 10 mA for 45 min.

using prechilled transfer buffer and an ice block. The protein bands were visualised by staining the blots with Ponceau S solution (Sigma Aldrich®) for 5 min., then washing away the excess stain with TBST buffer [20 mM Tris-HCl; pH 7.5, 150 mM NaCl, 0.05–0.1% Tween® 20 (Sigma-Aldrich®)].

3.2.7.4 Chemiluminescent His_6-tag detection using HisProbe-HRP conjugate

The blots were blocked overnight in the cold room with 10-20 ml of the Blocking Buffer (HisProbe™-HRP kit), 2-5% powdered milk or 10% BSA in TBST. The membrane was subsequently washed twice with 15 ml of TBST for 10 min. each. The blot was incubated with 10 ml of 1:5000 dilution of the HisProbe-HRP conjugate in TBST. The membrane was washed four times with 15 ml of TBST for 10 min. each, then incubated with 10 ml of SuperSignal® Working Solution for 5 min. Blots were normally exposed for 1-60 s. to obtain the best signal-to-noise ratio either with an X-ray film (Sigma-Aldrich®) or gel documentation system (ChemiDoc™ XRS + System, BioRad®).

3.2.8 *In vitro* hydrogen production methods

3.2.8.1 Platinum nanoparticles synthesis

The was protocol was adapted from [156]. An anaerobic Schlenk system was set up, cleaned thoroughly and dried with a heat gun. The Schlenk flask was dried and purged with nitrogen. 1 mL of 27.3 mM mercaptosuccinic acid (MSA) solution (3.56 mg MSA dissolved in 1 mL of MilliQ water) was added to 10 mL of 3.38 mM hexachloroplatinic acid solution. The contents were stirred vigorously for 1-3 min. at RT. The reducing solution was prepared by dissolving 67.6 mM sodium borohydride (12.78 mg in 5 mL MilliQ water), then added to the Schlenk flask dropwise. The reduction reaction proceeded for 20-30 min. at RT in the Schlenk in ambient light. The Pt nanoparticles were collected by centrifugation, washed several times with analytical methanol to remove excess MSA, borohydride and unreacted hexachloroplatinic acid. The Pt particles were dried in the air or in a gentle stream of N_2 gas overnight, and were used freshly for incubation with the PSI-LHCI complex.

3.2.8.2 Hybridisation of PSI-LHCI complex with proton reducing catalysts and platinum nanoparticles

Cobaloxime was prepared freshly as a 5 mM stock of $Co(dmgH)_2pyCl$ in dimethyl sulfoxide (DMSO). Other proton reducing catalysts (PRCs) were prepared as 5 mM stocks either in DMSO or acetonitrile depending on their solubility. The same was done for Pt nanospheres, although these had to be constantly shaken to avoid settling due to the element's high density. Dark-adapted 5 µM PSI-LHCI complex was incubated with 100-300 µM $Co(dmgH)_2pyCl$ or the DuBois-type Ni PRCs in a buffer containing 20 mM HEPES-KOH, 25% glycerol (w/v) pH 8.0, 3 mM $CaCl_2$, and 0.03% DDM. The PSI and $Co(dmgH)_2pyCl$/PRC mixture was tumbled at 20 rpm for 2 h at RT in the dark on a standard bench-top rotator/rocker (Fisher Scientific®). The PSI-LHCI/PRC hybrid samples were used immediately for the *in vitro* hydrogen production assay.

3.2.8.3 Determination of PSI-LHCI:proton reducing catalyst molar ratios by inductively coupled plasma mass spectrometry

All the samples were prepared in a final volume of 500 µl. For the H_2 production assay, 5 µM PSI-LHCI sample (equivalent to 380 µg Chl*a* per 500 µl of preparation) was hybridised with a freshly prepared 5 mM stock of a PRC at an appropriate molar ratio (see **Chapter 3.2.8.2**) in the carrier buffer (40 mM HEPES-NaOH, pH 8.0; 3 mM $CaCl_2$, 25% (w/v) glycerol, 0.03% DDM) for 2 h in the dark at RT with tumbling. To remove the unbound PRC, the sample was subjected to ultrafiltration by employing Amicon 100,000 MWCO filtration devices, then diluted (8x) with the carrier buffer twice to wash away any traces of the unbound PRC. The final 500 µl preparations were diluted to a 10-ml final volume in the carrier buffer. The pure carrier buffer and non-treated PSI-LHCI sample served as the blank references for determination of the molar ratios of the catalysts and PSI-LHCI by inductively coupled plasma mass spectrometry (ICP-MS) and inductively coupled plasma graphite furnace atomic absorbtion spectroscopy (ICP-FAAS). Both analyses were performed by Dr. Jakub Karasiński and Prof. Dr hab. Ewa Bulska, Expert Analytical Centre (Analityczne Centrum Eksperckie), Biological and Chemical Research Centre, University of Warsaw, Poland.

3.2.8.4 Gas chromatography system calibration and *in vitro* hydrogen production assay

The morning before the H_2 production assay, the Schlenk and gas chromatography (GC) systems were calibrated to ensure that there was no oxygen in the line and that the flow of hydrated N_2 was appropriate. The calibration of the GC system was performed by injection of a known volume of hydrogen gas, then integration of the resultant H_2 elution peak to determine the exact area-volume ratio. This calculation was used for the precise determination of the amounts of hydrogen detected. MES buffer (40 mM MES-KOH, pH 6.1, 10 mM $CaCl_2$, 5 mM $MgCl_2$) was purged with either nitrogen or argon gas for 2 h prior to the H_2 evolution experiment. Only after purging the MES buffer with an inert gas, DDM was added carefully to the same buffer to a final concentration of 0.03% (w/v), this was done by adding a specific amount of a concentrated stock to avoid frothing. The PSI-LHCI sample and the appropriate PRC compound were hybridised at an appropriate molar ratio (see **Chapter 3.2.8.2**), then used for H_2 production immediately, omitting the ultrafiltration step. The final reaction mixture had a final volume of 2 ml and consisted of 100 nM PSI-LHCI/PRC hybrid, 100 mM NaAsc and 15-20 µM cyt c_{553} (10AA linker variant; as determined by redox absorption spectroscopy). The reaction mixture was illuminated for 16 h at 8,130 µE m^{-2} s^{-1} (white light source, see below) and the total amount of hydrogen that accumulated in the headspace of the Schlenk system was measured by gas chromatography (GC, see below). Alternatively, the same procedure was performed in the sealed flasks if the Schlenk system was found to leak.

3.2.8.5 Gas chromatography analysis

The volume of the Schlenk system was 5 ml, and the headspace volume was approximately 1-2 ml. When using a 2 ml H_2 production reaction mixture, the headspace of the vessel was continuously pumped through the GC column with a 5 Å molecular sieve for gas separation (Compact GC, Interscience®) using 5 min. sampling intervals. A 500 W Hg-Xe lamp (Hamamatsu®, L8288) was used for the photocatalysis, using a water filter with a 30-cm path length to eliminate IR radiation. The amounts of hydrogen detected were determined specifically as per the calibration, as described above.

3.2.9 Preparation and *J-V* characterisation of cyt c_{553}/*p*-doped silicon, PSI-LHCI/*p*-doped silicon and PSI-LHCI/cyt c_{553}/*p*-doped silicon bioelectrodes

3.2.9.1 Chemical functionalisation of *p*-doped silicon substrate

Heavily *p*-doped Si wafers were obtained from the Department of Silicon Technology at the Institute of Electronic Materials Technology (ITME, Warsaw, Poland). Silicon wafers had a thickness of 500 ± 25 μm and a resistivity of 0.001-0.005 [Ω cm] equivalent to a boron doping density of 2.13 x 10^{19}-1.3 x 10^{20} cm^{-3}. Ni-NTA functionalisation of *p*-doped Si was performed according to the procedure of [157], as summarized in **Figure 34**. Briefly, a gas-phase aminosinilation was performed on the SiO_2 surface. Subsequently, 1,4-phenylene diisothiocyanate (DITC) was reacted with the amine for 2 hours at 40º C in ethanol. Si wafers were then rinsed thoroughly with water and ethanol and dried under a N_2 stream. N,N-bis(carboxymethyl)-L-lysine was reacted by immersion in an aqueous solution for 30 min. Samples were then rinsed thoroughly with water, then dried under a gentle N_2 stream. Ni^{2+} cations were chelated to the tricarboxylic acid functionality by immersion in a 1 mM aqueous $NiCl_2$ solution for 20 min. The functionalised Si wafers were used immediately for cyt c_{553} biofunctionalisation.

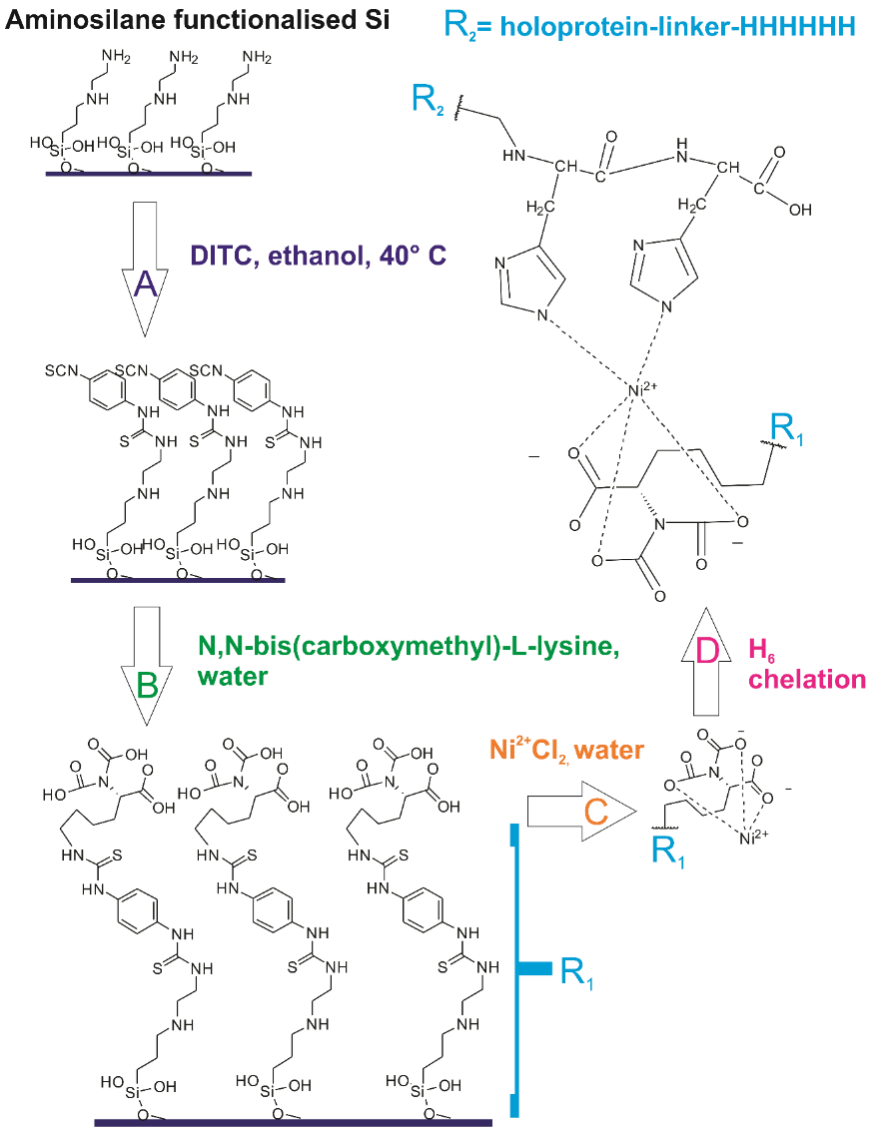

Figure 34

Workflow for the synthesis of nickel-nitrilo acetic acid self-assembled monolayer. Protocol was essentially reproduced from [157] using steps A-D. First, a gas-phase aminosinilation was performed on the SiO_2 surface. Subsequently, 1,4-phenylene diisothiocyanate (DITC) was reacted with the aminosilane functionalised Si for 2 hours at 40º C in ethanol (A). Wafers were then rinsed thoroughly with water and ethanol and dried under a N_2 stream. N,N-bis(carboxymethyl)-L-lysine was reacted by immersion in an aqueous solution for 30 min. (B). Samples were subsequently rinsed thoroughly with water and dried under a N_2 stream. Ni^{2+} was chelated to the tricarboxylic acid functionality by immersion in a 1 mM aqueous $NiCl_2$ solution for 20 min. (C). The functionalised Si wafers were employed immediately for cyt c_{553} biofunctionalisation (D).

3.2.9.2 Construction of cyt c_{553}/*p*-doped silicon devices

The *p*-doped Si wafers were pre-treated by submerging in the SWIPE® (Industrial Cosmetics Ltd.®) detergent for 24 hours. After removal of the detergent, the wafers were treated with hot, concentrated 96% sulphuric acid, and a solution of ammonia in hydrogen peroxide and water [H_2O:H_2O_2:NH_4OH/1:1:0.05, (v/v)], and finally in diluted hydrofluoric acid in water (HF:H_2O/1:10, (v/v)). Subsequently a 200 nm Ag layer was deposited through chemical evaporation on the back side of the wafers. The Rapid Thermal Processing method (RTP) was used to improve the formation of metal/semiconductor contacts. Subsequently, the wafers were treated with diluted hydrofluoric acid (as above) and then functionalised with Ni-NTA moiety, according to a protocol described in [157]. Briefly, *p*-doped Si wafers were placed in the vacuum using a vacuum-assisted spin coater (model: TSR 48/8 5Q85, Convac® (discontinued; property of the Deparment of Optoelectronics, ITME, Warsaw, Poland) then centrifuged at 150 rpm for 25 s. followed by centrifugation at 500 rpm for 60 s. as an extra step to remove any impurities from air that might be present on the surface of the silicon. After functionalisation, 500 µl of 125 µM cyt c_{553} variant solution was deposited using vacuum-assisted spin coating to ensure that only a thin layer of protein was homogeneously chelated to the Ni-NTA SAM. After application of the protein solution, the Si wafers were centrifuged as above. The biofuntionalised Si wafers were then dried with a gentle nitrogen stream and left in the nitrogen cabinet for 24 hours at RT for further drying. A transparent 5-nm layer of gold or Au/Cr was then deposited to ensure formation of the proper metal/cyt c_{553} electrical contact. Several contact points were made by chemical evaporation of Au by employing laser-cut masks, then the remaining surface was sealed with a transparent 50-nm layer of SiO_2. Four to six bioelectrodes were cut into rectangular shapes of the exact surface area of 3.24 cm^2. The *J-V* properties of the bioelectrodes were characterised in the dark by employing a home-made PV setup (Deaprtment of Optoelectronics, ITME, Warsaw, Poland), as described in detail in **Chapter 3.2.9.4.** At least 4 independent bioelectrodes were assessed per each cyt c_{553} variant using 3 independent *J-V* measurements. For electrochemical impedance spectroscopy experiments, an extra 50-nm layer of Au/Cr was chemically deposited on top of the bottom Ag contact to avoid any background electrochemical Ag oxidation.

3.2.9.3 Construction of PSI-LHCI/*p*-doped silicon and PSI-LHCI/cyt c_{553}/*p*-doped silicon devices

The *p*-doped Si wafers were prepared essentially as described in **Chapter 3.2.9.2**, with or without chemical modification, where appropriate. After biofunctionalisation with cyt c_{553} (see **Chapter 3.2.9.2**), the Si wafers were dried in a semi-anaerobic nitrogen box for 24 h. A 500 µl suspension of the *C. merolae* PSI-LHCI complex at 1 mg ml^{-1} Chl*a* was overlaid on the pretreated Si wafers and the protocol described in **Chapter 3.2.9.2** was followed for the vacuum-assisted spin coating of the protein sample, with the exception that instead of a 5-nm of Au layer, a 5-nm of Ag was employed.

3.2.9.4 *J-V* measurements, assessment of open circuit potential and photocurrent

All the *J-V* curves were acquired in a custom-made PV setup (Department of Optoelectronics, Intitute of Electronic Materials Technology, ITME, Warsaw, Poland). All the *J-V* data was acquired using a custom-made setup comprising a PC with an interface card (Texas Instruments®), an AGILENT 34401A digital multi-metre, the AGILENT 6634B system DC power supply and a home-made interface card (Department of Optoelectronics, ITME). Data was processed using ITME-customised LAB VIEW 8.6 software. Data was averaged using four independently prepared bioelectrodes using the selected area of 3.24 cm^2 which was employed as a standard area for all the electrodes constructed in this study. The entire protocol was repeated twice to ensure reproducibility of the *J-V* results. The *J-V* values were averaged for three independent bioelectrodes using the data from three most similar *J-V* curves from a total set of four measurements. All the J_0 values were calculated from **Eq. 8** below, and were also determined from the *J-V* curves presented on a semi-logarithmic scale, where the J_0 value corresponds to the *y*-intercept (see **Suppl. Figure 3**).

$$J = J_0^{(qV/enkT)-1}$$ [158] (**Eq. 8**)

where: *J*, the net current flowing through the diode; J_0, dark saturation current (diode leakage current in the dark); V, applied voltage across the terminals of the diode; q, absolute value of electron charge; n, ideality factor; k, Boltzmann's constant; T, absolute temperature (K).
Note: the above was done strictly for cyt c_{553} based devices only as this specialised set-up made the dark saturation current assessment facile.

All photoelectrochemical measurements (PSI-LHCI based devices) were performed with a CH Instruments CHI660a electrochemical workstation (CH instruments, Inc.®) The working electrode clip was attached to the Ag bottom contact layer, and the counter and reference electrodes were clipped on the top Ag layer contact as depicted in **Figures 95** and **99** of **Chapter 4.6**. The light source employed was an Industrial Solar Cell Testing Light Source (150/300W) (Solar Light®) and the intensity output was 100 mW cm^{-2} for all the photocurrent measurements, reassessed independently with a quantum metre (HD 2302.01) (DeltaOhm®) to a value of 2,200 µmoles photons m^{-2} s^{-1}. Samples were positioned in the same distance from the light source for all the measurements, with frequent verification of constant light intensity. Chronoamperometric data was collected with no bias between the reference and working electrodes for measurement of photo-driven open-circuit voltage changes or at -250 mV for the measurements of the cathodic photocurrents. Short circuit currents were measured when the voltage was 0 V.

The following equations were employed for determining fill factor (FF) and external quantum efficiency (η) of the PSI-LHCI-containing biophotoelectrodes:

$$FF = (V_{oc} - \ln(V_{oc} + 0.72))/V_{oc} + 1 \quad \textbf{(Eq. 9)}$$

$$\eta = (V_{oc} \cdot J_{sc} \cdot \mathrm{FF})/P_{in} \times 100\% \quad \textbf{(Eq. 10)}$$

where: P_{in}, power input was determined to be 0.324 W (with AM 1.5 irradiation) into an 18 x 18 mm^2 biophotoelectrode surface used throughout this study. Normalised V_{oc} was employed for all calculations and thermal equilibrium was assumed, with the ideality factor of 1 and the temperature 300 K.

3.2.9.5 Scanning electron microscopy imaging

All scanning electron microscopy (SEM) imaging was done using an SEM microscope (Phenom ProX, with EDS and a 15-kV acceleration voltage, PhenomWorld®). Briefly, four different regions of each cyt c_{553}/*p*-doped Si electrode were visualised using a magnification of 36,000 x and photographed accordingly after appropriate scanning and selection of the regions. Images were only processed to improve brightness/darkness contrast with CorelDraw X7.

Chapter 4 Results

Chapter 4.1

Purification and biochemical characterisation of photosystem I and its associated light harvesting antenna from *Cyanidioschyzon merolae*

4.1.1 Introduction

The photosynthetic machinery of a red thermoacidophilic microalga *Cyanidioschyzon merolae* has gained quite some interest over the last decade due to the unique evolutionary positioning of this species near the root of the red algal lineage that forms the basal group within eukaryotes, and diverged approximately 1.3 billion years ago within the most ancient algal order of *Cyanidiales* [159,160]. The photosynthetic machinery of this alga is considered an evolutionary intermediate between the apparatus of prokaryotic cyanobacteria and that of the eukaryotic phototrophs of the green lineage [66,99,161].

The red algal photosystem I with its associated light harvesting antenna (PSI-LHCI) supercomplex is evocative of the higher plant and green algal counterparts as it comprises the monomeric RC core complex composed of 13 subunits (PsaA-PsaF and PsaI-PsaO) [94,95] together with the crescent-like light harvesting antenna complex (LHCI) that binds asymmetrically to the RC on the PsaF/PsaJ side. The peripheral LHCI complex is composed of a variable number of Chl*a*-binding Lhcr subunits depending on the species, with a minimal number of 4 subunits [96–98]. Interestingly, this red algal PSI-LHCI supercomplex retains the cyanobacterial PsaM subunit and lacks the higher plant PsaH and PsaG subunits implied in docking of the mobile LHCII antenna and formation of the LHCI belt, respectively [66]. Moreover, the chimeric nature of the two core subunits, PsaF and PsaL, which accommodate both cyanobacterial and plant-like structural domains further supports the evolutionary intermediate character of the red algal photosynthetic machinery [66,99].

Recently, we have shown that PSI-LHCI from *C. merolae* is extremely robust due to its ability to (*i*) remodel its peripheral antenna complex to adjust the effective absorption cross-section as a molecular mechanism of adaptation to varying light intensities (similar to the green algae *Chlamydomonas reinhardtii*) [66,99] and (*ii*), accumulate a photoprotective carotenoid zeaxanthin in the LHCI antenna and possibly the PSI reaction centre [91]. Although

these findings go beyond the scope of this PhD thesis, an optimised purification methodology which yields a rather generous amount of the active, ultrastable, and robust PSI-LHCI supercomplex is described here, as it provided the biological photoactive material used for both molecular hydrogen production *in vitro* (see **Chapter 4.3**), and construction of PSI-LHCI-based nanodevices, including silver nanowire plasmonic bionanostructures (see **Chapter 4.4**) and biophotoelectrodes (see **Chapter 4.6)**. This chapter shows that not only is the optimised purification methodology reproducible, but it yields generous amounts of highly active and robust PSI-LHCI complex outside of its native photosynthetic membrane environment that can be utilised for the subsequent nanoengineering studies. Here, and in **Chapter 4.3**, it is shown that the purified PSI-LHCI complex from *C. merolae* retains up to 60-70% of its activity when treated with increased concentrations of organic solvents. This has facilitated the subsequent development of the functional assay for the *in vitro* H_2 production using this photoactive complex and organic proton reducing catalysts, as described in detail in **Chapter 4.3**.

4.1.2 Purification and biochemical characterisation of the *C. merolae* PSI-LHCI complex

In order to improve yield and purity of the PSI-LHCI supercomplex, a two-step anion chromatography purification protocol was developed in conjunction with a preparative size exclusion/desalting column followed by a final step of sucrose gradient fractionation to remove any residual phycobilisomes. During the anion exchange chromatography step, the PSI and PSII complexes were separated as described in detail in **Chapter 3.2.3.3**. **Figure 35** shows a representative chromatogram of the first step of anion-exchange chromatography (AEC) which was highly reproducible following the protocol optimisation.

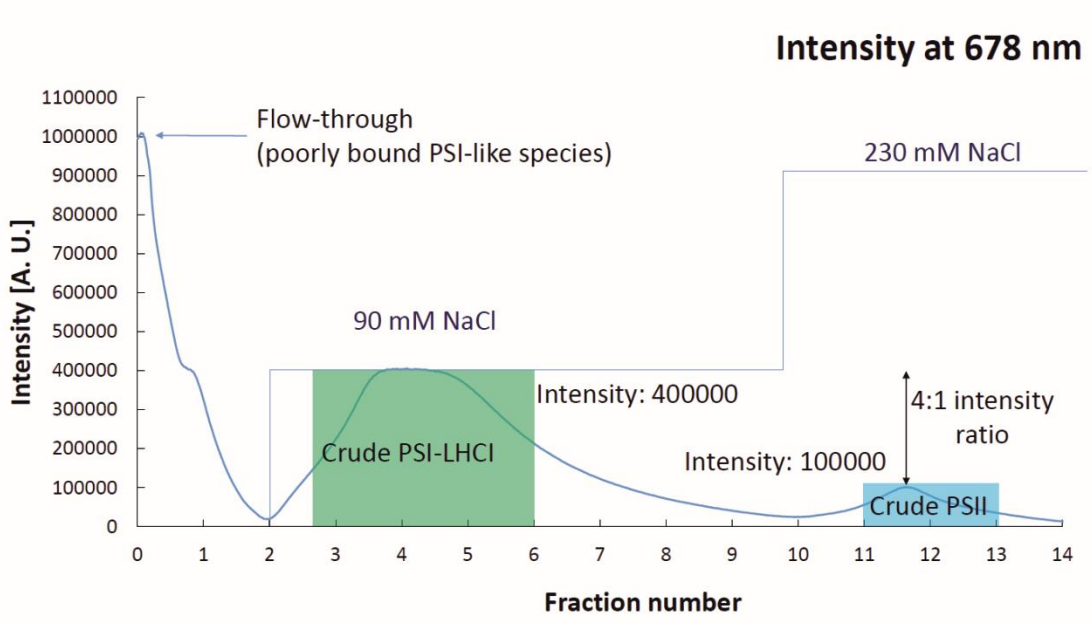

Figure 35

A representative anion-exchange chromatogram for purification of the crude *C. merolae* PSI-LHCI sample. Normally, 30-40 mg of Chl*a* from solubilised thylakoids were loaded onto the DEAE-M column. For all moderate light (ML, 90 µE) thylakoids, a 4:1 intensity ratio of PSI-LHCI to PSII was observed for at least three independent preparations. PSI-LHCI fractions collected for spectroscopic analysis, pooling and desalting are highlighted in green, and normally comprised fractions 3-6.

After elution from the DEAE-M column, fractions containing the pure PSI-LHCI complex (reproducibly fractions 3-6 in the chromatogram in **Figure 35**, highlighted in green, comprising a total volume of 20-21 ml), were characterised by RT absorption spectroscopy, then pooled and desalted by gel filtration chromatography to remove NaCl and any residual PBSs. The samples were desalted as described in detail in **Chapter 3.2.3.3.** After desalting, the PSI-LHCI sample was subjected to a second AEC step on a DEAE-S column, then was subjected to a second chromatographic step on a desalting column followed by concentration on filtering devices. In the last step, the PSI-LHCI supercomplex was purified to homogeneity by sucrose gradient fractionation.

Figure 36 displays a representative chromatogram of the PSI-LHCI complex purification using the second step of anion exchange chromatography (DEAE-S column). As shown in the figure, two PSI-LHCI subpools were identified (see retention times indicated above each peak). Monitoring of the two subpools by absorption spectroscopy revealed that

the first subpool (main peak in the centre of the chromatogram) contained a small amount of PBS and carotenoid contamination (see **Suppl. Figure 1**). The major PSI-LHCI subpool (which was highly devoid of PBS) was the most strongly bound one that eluted at 33.5 min. from the DEAE-S column. Interestingly, most of the pure PSI-LHCI complex eluted at the same retention time very reproducibly from preparation to preparation (33.5 min) but the other subpool, reproducibly eluted at ~ 44.5 min. as well, suggesting the presence of the damaged or possibly improperly formed complex in this particular subpool. As this subpool was not of interest, it was not investigated further.

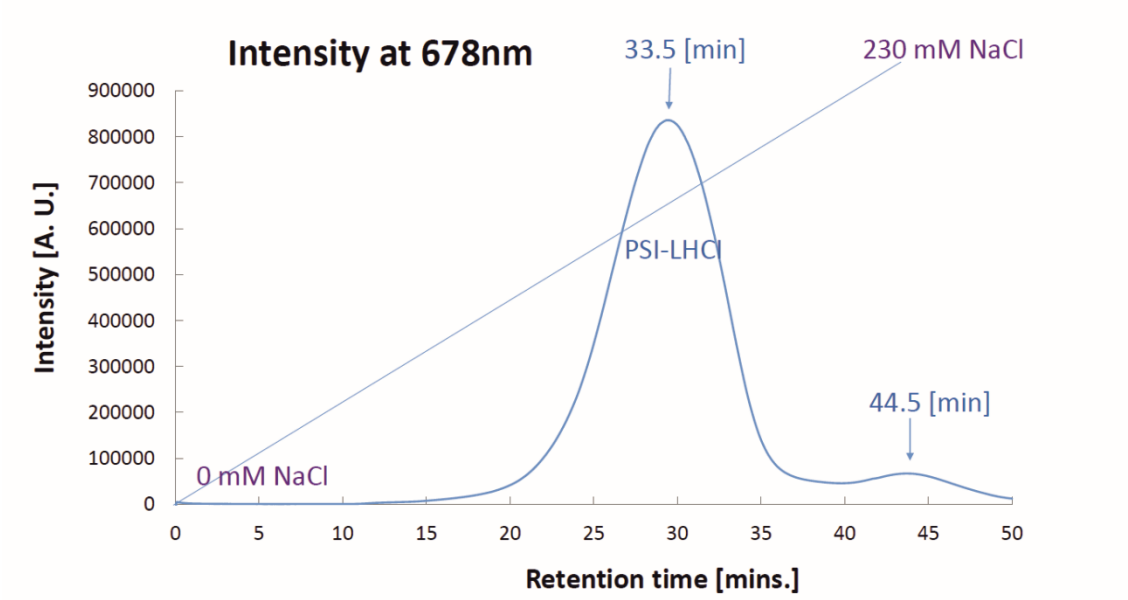

Figure 36

A representative anion-exchange chromatogram for the purification of the *C. merolae* PSI-LHCI complex. Representative chromatogram of the fractions eluted from an AEC DEAE-S column used as the 2nd chromatographic purification step with monitoring the peak intensity at 678 nm. The diagonal line represents the increase in concentration of NaCl as a function of retention time.

After elution from the second anion exchange column, the PSI-LHCI-enriched fractions were characterised spectroscopically (see **Figure 37)** to select the purest PSI-LHCI fractions that were devoid of PBSs and carotenoid contaminations. These fractions normally eluted at the centre of the chromatogram and corresponded to the fractions with retention time of 33.5 min. (see **Figure 36**), or fractions no. 90-96 (see **Figure 37**).

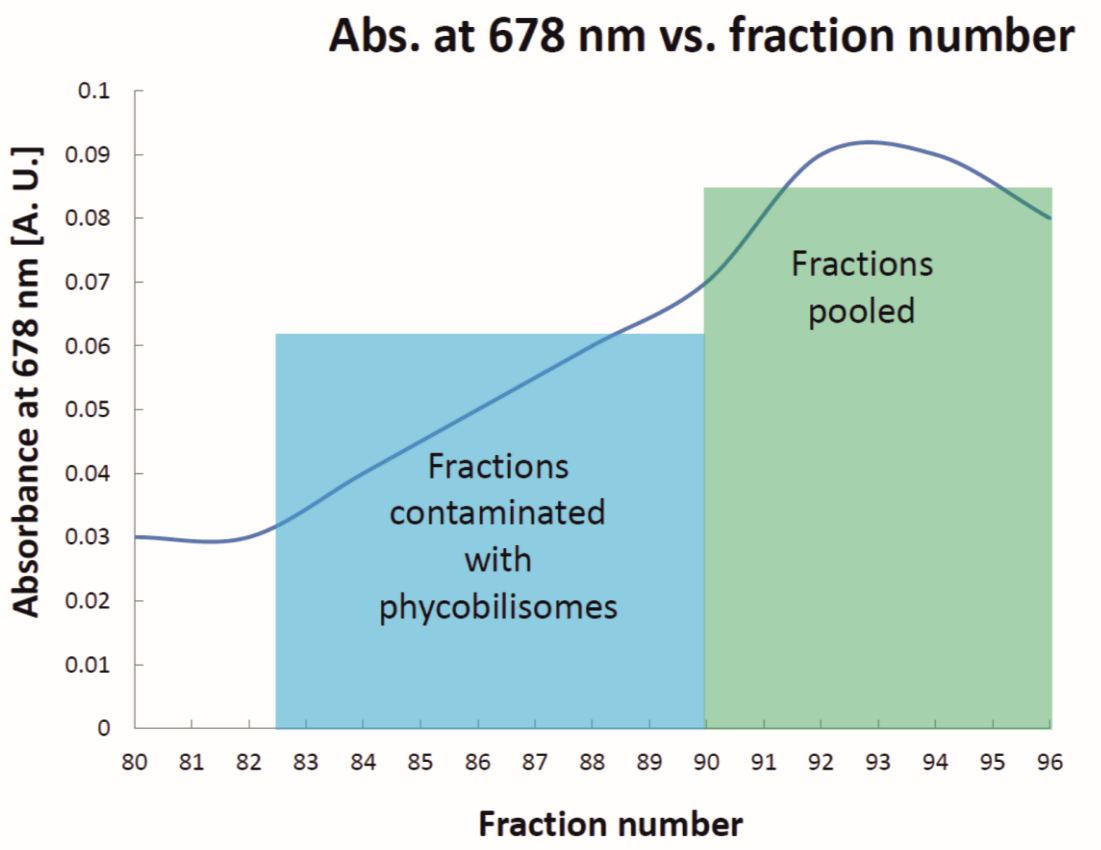

Figure 37

RT absorption of the *C. merolae* PSI-LHCI-containing fractions eluted from the DEAE-S AEC column. After elution, PSI-LHCI-enriched fractions were analysed spectroscopically for the presence of PBSs. Typically, only fractions no. 90-96 were selected for pooling and subsequent desalting, as they were devoid of PBSs.

Following the spectroscopic characterisation, the PSI-LHCI-enriched fractions devoid of PBSs were desalted, and further purified by sucrose density fractionation as described in detail in **Chapters 3.2.3.3** and **3.2.3.4**. **Figures 38** and **39** show representative sucrose gradient results, including fraction identification and the RT absorption spectra of fractions of interest, respectively.

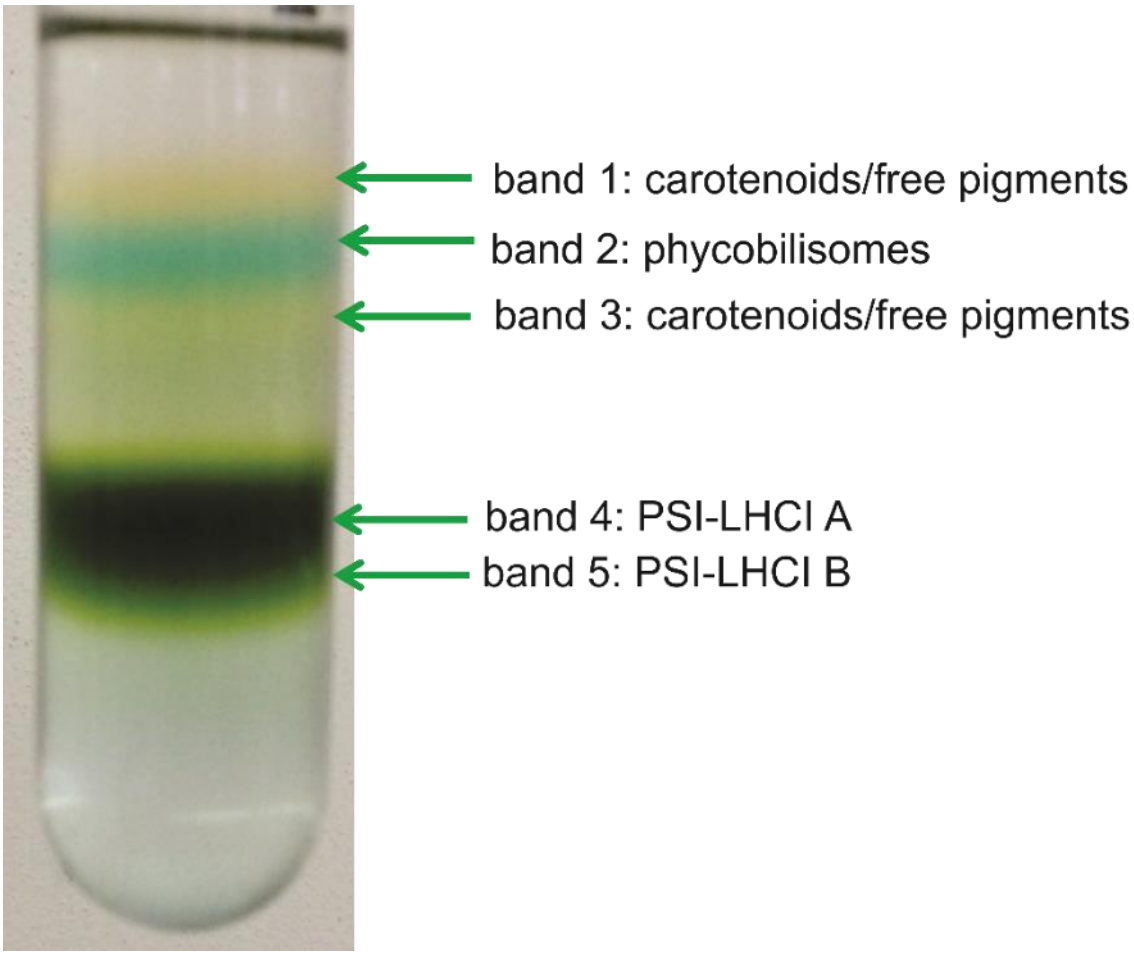

Figure 38

Discontinuous sucrose gradient fractionation of the *C. merolae* PSI-LHCI-enriched sample obtained by a two-step anion exchange chromatography-desalting approach. The fractions were collected following 20-h ultracentrifugation at 125,000 x g at 4ºC.

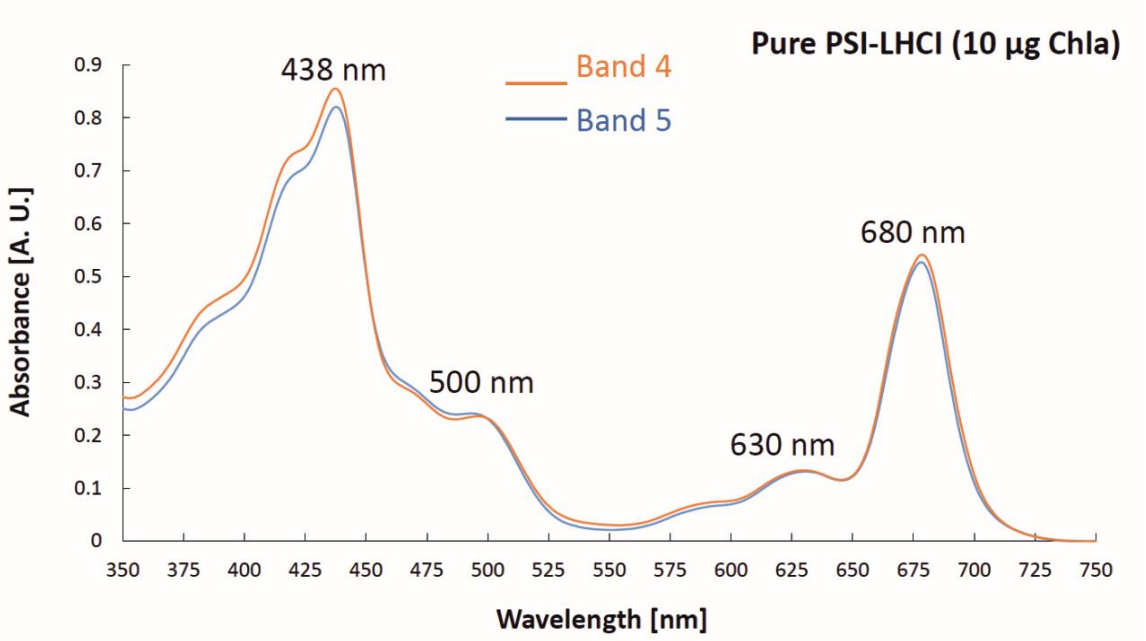

Figure 39

Representative RT absorption spectra of bands 4 and 5 obtained through sucrose gradient fractionation (See Figure 38). For clarity, RT absorption spectra of bands 1-3 are not shown, as these correspond to free carotenoids and contaminating PBSs (See **Figure 38**).

As bands 4 and 5 were found to be spectroscopically identical, they were pooled and used together for all the further studies. The purity of these pooled bands was further confirmed by RT absorption, 77K fluorescence, RT fluorescence and SDS-PAGE analyses, as shown in **Figures 40**, **41** and **42**.

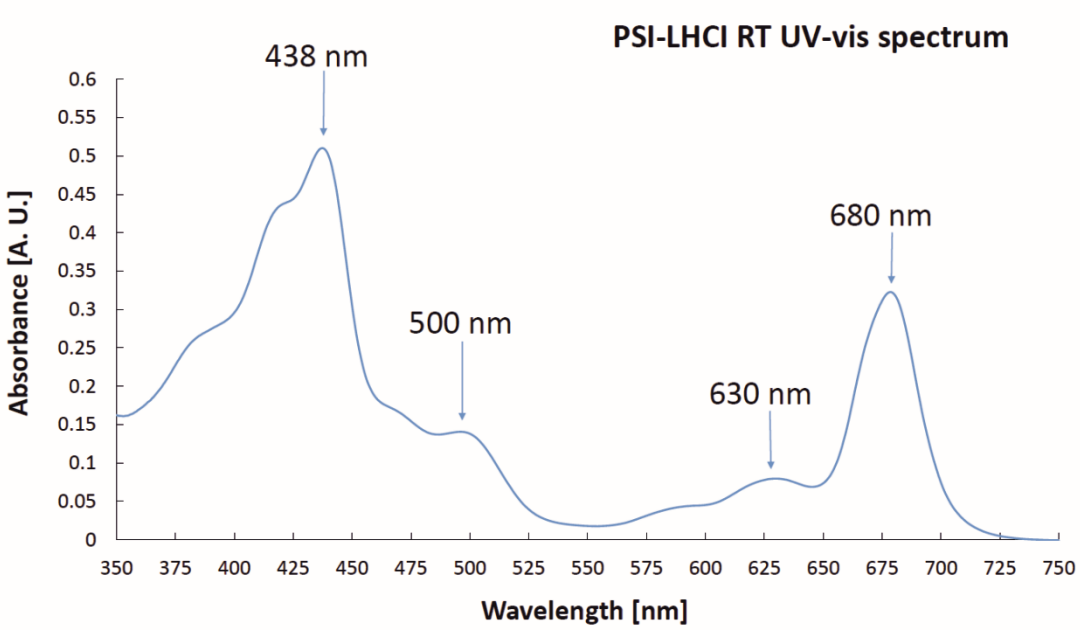

Figure 40

A representative RT absorption spectrum of the pure *C. merolae* PSI-LHCI supercomplex following sucrose gradient fractionation. Note the distinctive peaks at 438 nm and 680 nm corresponding to Chl*a* bound to PSI.

Prior to sucrose gradient fractionation, PSI-LHCI-enriched samples typically displayed a 77K emission spectrum with a major peak at 724 nm and a small peak at 675 nm when Chl*a* was excited at 440 nm, as shown in **Figure 41**, **Panel A**. As can be clearly seen, allophycocyanin, phycocyanin and Chl*a* peaks are well separated, indicating the lack of excitonic coupling between PSI-LHCI and PBSs, in contrast to Busch *et al*. [97], who suggested the existence of a PSI-LHCI subpool in which some functional coupling between PBSs and *C. merolae* PSI-LHCI complex may occur.

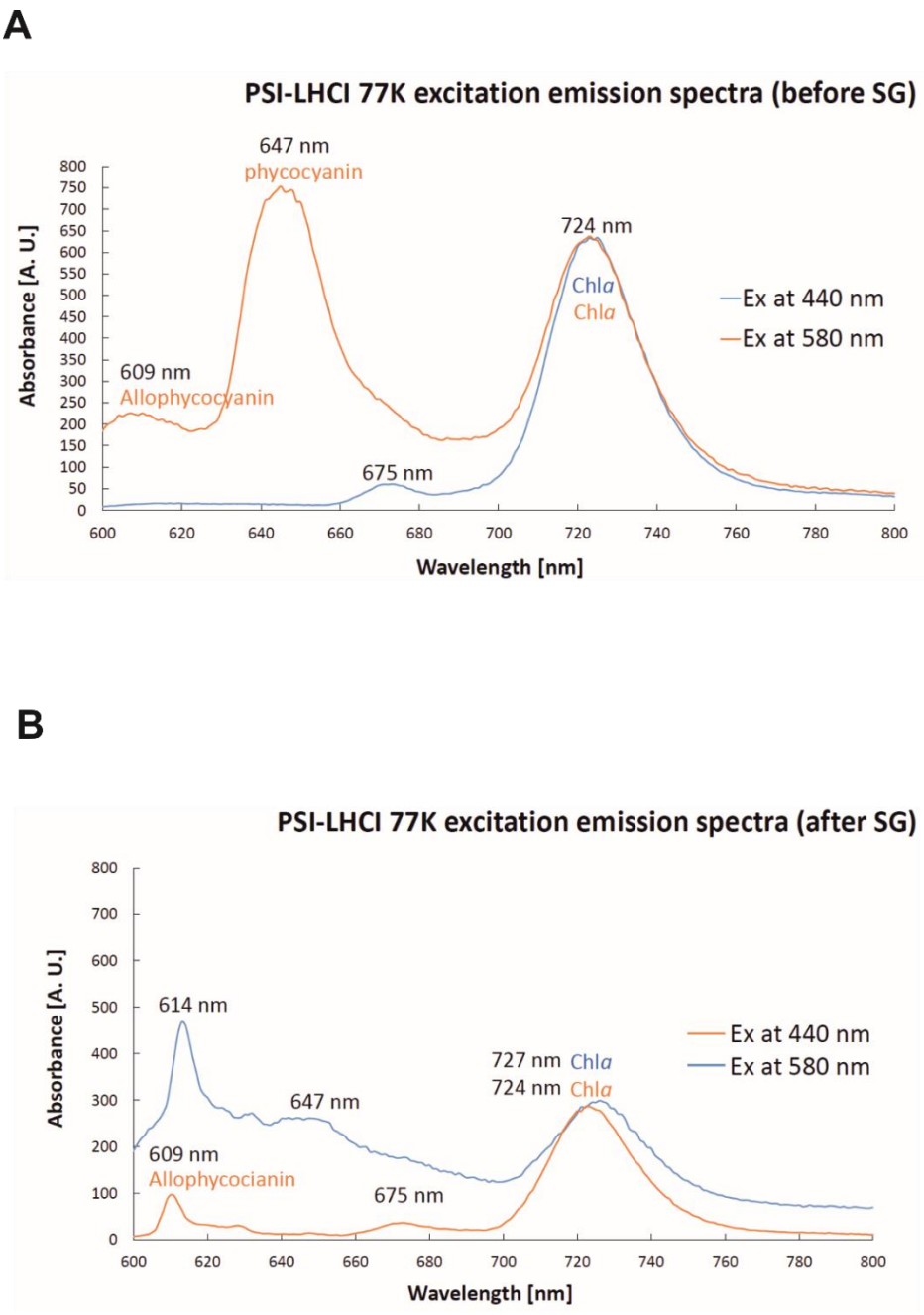

Figure 41

Representative 77K excitation spectra of the *C. merolae* PSI-LHCI complex before and after sucrose gradient fractionation. Panel A: steady-state 77K PSI-LHCI emission spectra before sucrose gradient fractionation. Panel B: steady-state 77K PSI-LHCI emission spectra after sucrose gradient fractionation. Chl*a* was excited at 440 nm, whereas PBSs were excited at 580 nm. Emission spectra were recorded from 600 nm to 800 nm. In some cases, a small amount of allophycocyanin remained bound to PSI-LHCI, as evidenced in **Panel B**. Note that Chl*a* is not excitonically coupled to phycocyanin and allophycocyanin, as shown here by the two well separated peaks. SG, sucrose gradients.

Although sucrose gradient fractionation allowed for the depletion of the majority of PBSs, a small amount of phycocyanin and allophycocyanin was still detectable in the pure PSI-LHCI sample, as evidenced by the 77K emission spectra of PBS in the sucrose gradient fractionated PSI-LHCI sample (see **Figure 41, Panel B)** and RT fluorescnece emission maxima observed for the same sample at approximately 630 nm (see **Figure 42, Panels C and D**).

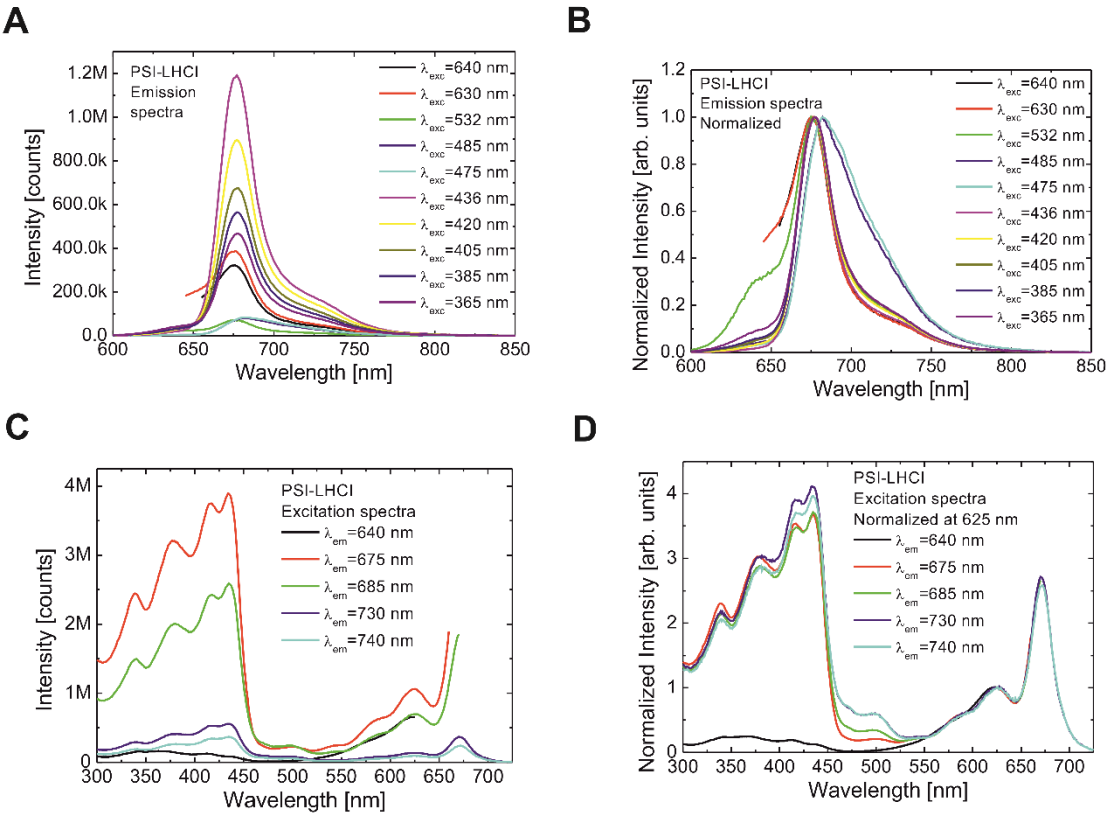

Figure 42

Representative RT excitation and emission fluorescence spectra of the pure *C. merolae* PSI-LHCI sample devoid of PBSs following sucrose gradient fractionation. A: PSI-LHCI emission spectra at different excitation wavelengths. B: PSI-LHCI emission spectra at the same wavelengths (normalised). C: PSI-LHCI excitation spectra recorded at different emission wavelengths. D: PSI-LHCI excitation spectra (normalised at 625 nm). Samples were excited at 300-750 nm range.

To verify further the purity of the final PSI-LHCI sample, the complex was analysed by size-exclusion chromatography (SEC). **Figure 43** shows a representative SEC chromatogram of the pure PSI-LHCI supercomplex following sucrose gradient fractionation, in which a single peak of PSI-LHCI complex can be observed, with no other contaminating proteins. Moreover, no signs of complex degradation are observed, further confirming biochemical integrity of the purified *C. merolae* PSI-LHCI complex.

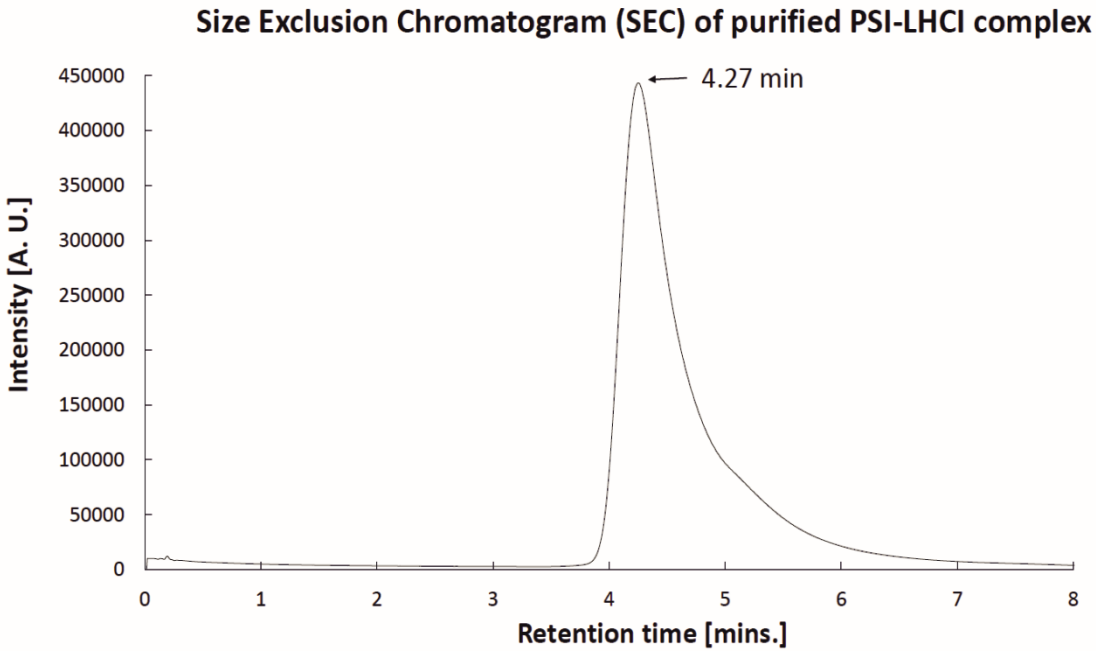

Figure 43

A representative SEC chromatogram of ultrapure *C. merolae* PSI-LHCI sample. The sample was eluted at a flow rate of 2 ml min^{-1}.

Figure 44 shows the representative SDS-PAGE protein profiles of the crude (before sucrose gradient fractionation) and pure (after sucrose gradient fractionation) PSI-LHCI supercomplex samples, confirming the presence of all the major PSI protein subunits. The PBSs were clearly visible in the crude PSI-LHCI sample in contrast to pure counterpart, where their presence was negligible following an additional purification step by sucrose gradient fractionation.

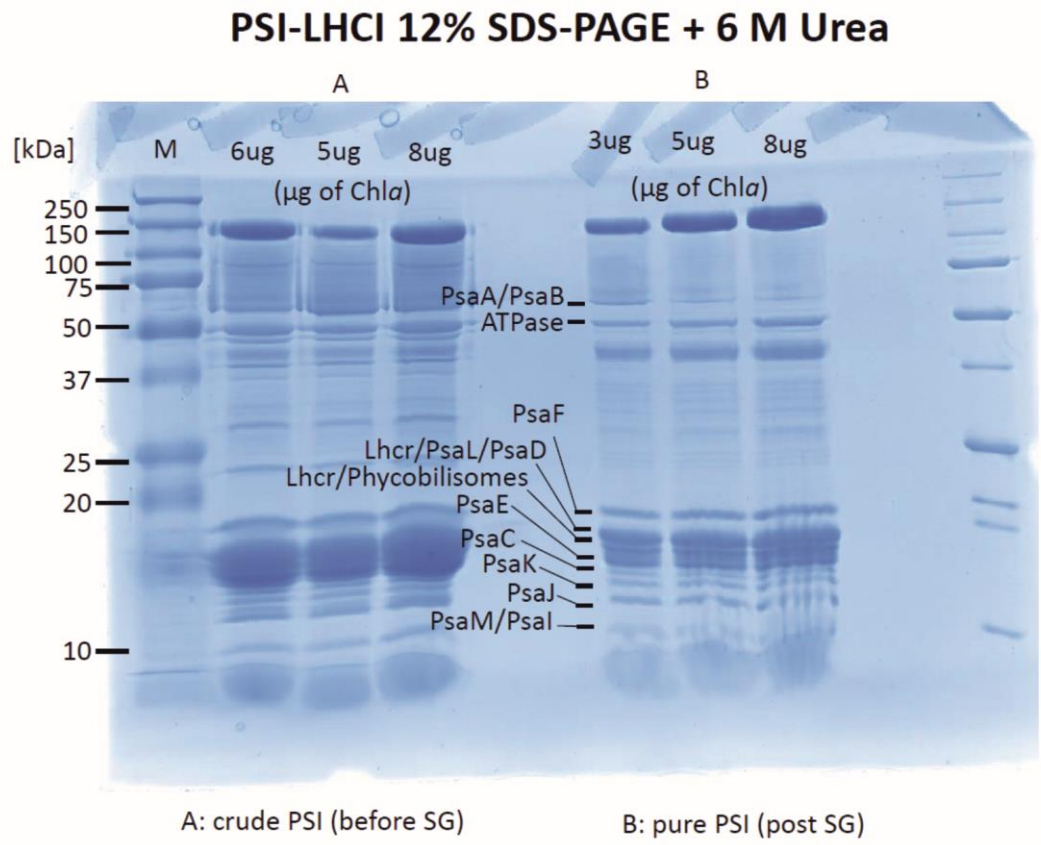

Figure 44

A representative SDS-PAGE gel of the *C. merolae* PSI-LHCI samples before (crude PSI) and after (pure PSI) sucrose gradient fractionation. A 12% Tris-Tricine gel with 6 M urea was used to obtain protein profiles of the PSI-LHCI complex, as described in detail in **Chapter 3.2.7.2**. SG, sucrose gradients. Protein size markers in kDa are indicated on the left.

The photochemical activity of the purified PSI-LHCI sample was routinely assessed by an oxygen consumption assay (see **Chapter 3.2.6**). The PSI-LHCI samples purified in this study displayed very similar activities, ranging from 800 to 1,200 µmoles O_2 mg^{-1} Chl*a* hr^{-1}. To test the robustness of the purified PSI-LHCI complex, the sample was subjected to a treatment with an organic solvent dioxane at the varying concentration. **Figure 45** shows that the PSI-LHCI complex retains up to 60% of its photochemical activity after treatment with 10% dioxane, often used for preparation of solar cells [139], indicating a relative robustness of this complex, even in the presence of significant amount of this organic solvent.

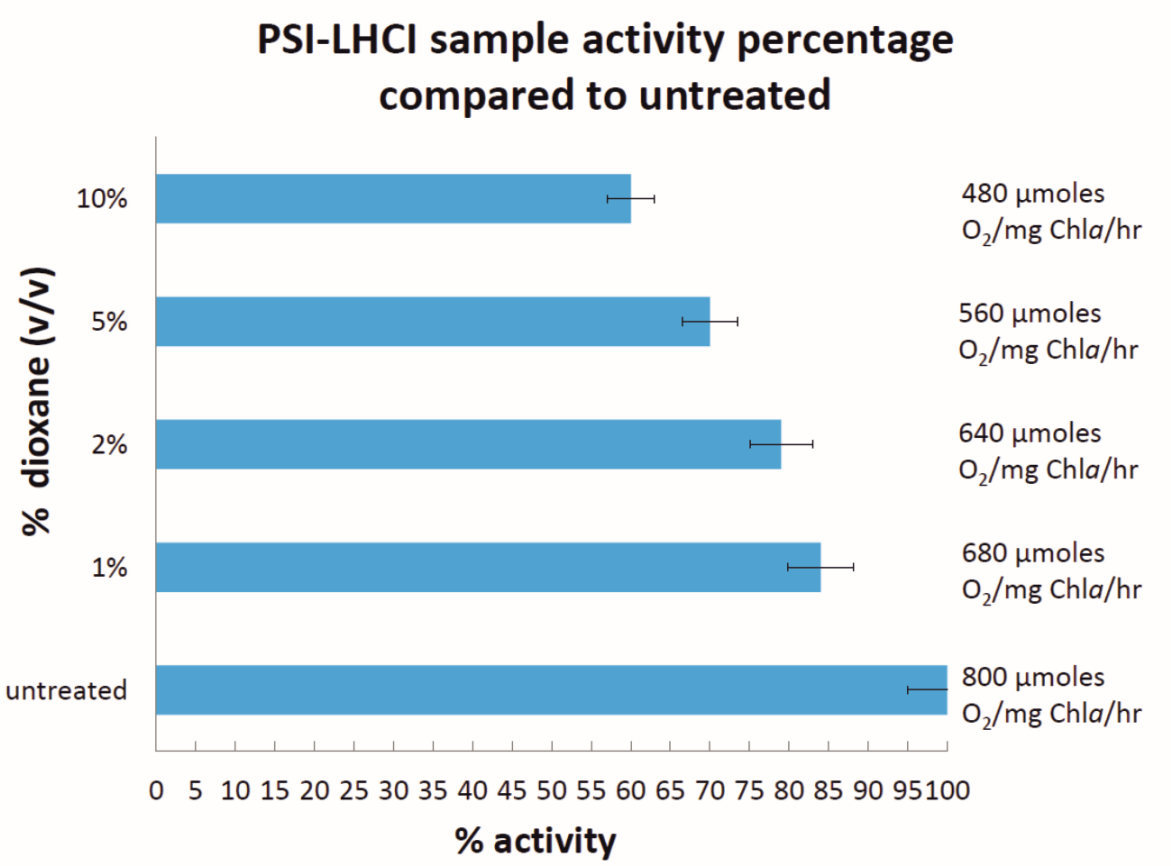

Figure 45

Photochemical activity of the *C. merolae* PSI-LHCI complex in the presence of the increasing concentration of dioxane. The PSI-LHCI complex retains 60% of its activity in the presence of 10% (v/v) dioxane.

4.1.3 Concluding remarks

An improved and optimised procedure for purification of homogeneous, highly active PSI-LHCI supercomplex from *C. merolae* was developed in this study. The PSI-LHCI complex was purified to homogeneity from cells grown at moderate light of 90 µE as specified in detail in **Chapter 3.2.1.1**. The purification methodology differed from the one described by Hippler and colleagues [97], in that the PSI and PSII complexes were separated first through a two-step AEC protocol followed by sucrose gradient fractionation rather than starting from sucrose gradient fractionation followed by an AEC step as reported in [97]. The main advantage of the approach described in this Chapter is that the PSI-LHCI complex can be purified in large quantities to homogeneity, whilst still retaining its full photochemical activity. The amount of purified PSI-LHCI complex ranged from 3 mg to 11 mg Chl*a* of the pure PSI-LHCI complex

per 30-40 mg Chl*a* of thylakoids, corresponding to the overall yield of 10-27.5%, which was sufficient to conduct a large scale *in vitro* hydrogen production assays, prepare the plasmonic bionanoconstructs of this complex on silver nanowires, and perform the construction of the biosolar cells described in the subsequent chapters. The latter, as will be mentioned further on, demanded a considerable amount of the supercomplex, particularly for optimisation experiements. The optimised protocol presented here can be reproducibly used for rapid purification of highly active and robust PSI-LHCI complex that provides the suitable photoactive biological material for construction of biophotoelectrodes, solar-to-fuel nanodevices and nanoconstructs.

In contrast to the findings of [97], PSI-LHCI complex purified from the *C. merolae* cells grown at 90 µE was found to be excitonically de-coupled from residual PBSs identified in the final sample. As seen in **Figure 41**, the maxima corresponding to allophycocyanin, phycocyanin and Chl*a* are well separated, suggesting excitonic decoupling between them. In contrast, Hippler and colleagues [97] observed some excitonic coupling between allophycocyanin, phycocyanin and a subpool PSI-LHCI purified from the low light (LL)-grown cells of *C. merolae*. At the LL intensity, excitonic coupling between PBSs and PSI-LHCI is believed to be advantageous to increase the light harvesting capability of the PSI-LHCI complex. Nevertheless, such a putative PBS-PSI-LHCI complex is very labile and more stringent purification protocols were shown to disrupt PBS association with PSI [91]. Another explanation as to why Hippler and colleagues [97] observed some association of PBSs with their purified PSI-LHCI complex could be due to the fact that that they employed a salt of the lower ionic strength for the elution of their complex by AEC ($MgSO_4$), compared to NaCl which was employed as the eluting agent in the present study. Moreover, the small 77K PBS emission peaks presented by Hippler and colleagues [97] in the same study in the PSI-LHCI fractions are well separated from the PSI-LHCI emission peak, indicating that the PBSs observed by these authors are not excitonically coupled with the PSI-LHCI supercomplex.

Chapter 4.2

Heterologous expression, purification and biochemical characterisation of cytochrome c_{553} from *Cyanidioschyzon merolae*

4.2.1 Introduction

Cytochromes *c* (cyt *c*) play a central role in the biological electron transport systems and they have been a popular subject for study in main areas of protein chemistry and redox reactions for more than thirty years [162]. Our current knowledge of cyt *c* proteins has advanced enormously through the contributions of disciplines as different as, structural biology, physical chemistry, microbial physiology and a plethora of magnetic and optical spectroscopic techniques [162].

A family of cyt *c* proteins comprise cationic haemoproteins composed of 94-114 amino acid (AA) residues depending on the species [163]. They are the most studied proteins, very likely due to their exceptional thermodynamic stability. Their characteristic red colour, due to the presence of the redox active haem group, makes protein purification easier when the cyt protein is in a sufficiently reduced state [162]. Cytochromes *c* can bind one or several *c*-type haems through two thioether bonds involving the sulphydryl groups of two Cys residues. The X-ray structure of mitochondrial cyt *c* has been solved in the late 1960s to up to 4.0 Å resolution, followed by several other X-ray structures from various sources which were solved to 1.5–2.8 Å resolution in the late 1960s and up to the early and late 1980s [164–167]. The small size, considerable solubility, exceptionally high helical content, and the presence of the haem cofactor have allowed mitochondrial, bacterial and algal cyt *c* proteins to be studied through a plethora of spectroscopic and other biophysical techniques [102,162,168,169].

The structure of cyt c_6 from the red alga *Porphyra yeoenzis* has been determined at 1.57 Å resolution [102]. The overall structure of cyt c_6 follows the topology of Class I *c*-type cytochromes in which the haem prosthetic group covalently binds to Cys14 and Cys17 within a CXXCH-consensus/recognition motif, and the iron has an octahedral coordination with His18 and Met58 as the axial ligands [102]. The redox potential of the *Porphyra yeoenzis* cyt c_6 was determined via potentiometric redox titration to be +210 ± 10 mV [102]. A close homologue of cyanobacterial cyt c_6, cyt c_{553} present in an extremophilic red microalga *C.*

merolae, is a mono-haem protein that is encoded by a single, intronless *petJ* gene present in the chloroplast genome of this alga [87].

For the cyanobacterial cyt c_6 counterpart, the polypeptide chain consists of four α-helices (I-IV), connected by loops [170]. The long N-terminal helix I (Ala3-His18) has a distinctive kink at Cys14. The two Cys residues forming the covalent bonds to the haem group and the fifth iron-containing ligand, His18, are also present in this helix. As in other cyt c_6 molecules, the three successive amino acids Ala19-Gly-Gly21 form a 3_{10}-helix followed by an Ω-loop composed of a AA sequence Asn22–Lys32 [170]. This Ω-loop separates helix I from the short helix II (Ala33–Tyr39). Residues Gly46–Ser49 and Leu40–Tyr43 form type VIII-β and type IV-turns, respectively [171].

In the structure of *P. yezoensis* cyt c_6, four α-helices, Asp2-Asn13 (I), Lys33-Ala38 (II), Ile44-Asn53 (III) and Asp67-Lys83 (IV), are observed as fundamental elements of the secondary structure, with the arrangement of helices I and IV crossing at an angle of 90º C [102]. Helices II and III in this protein, are shorter than helices I and IV, and reside on different sides relative to the haem plane, whereas those of the mitochondrial counterparts are located on the side of the Met ligand [102]. In addition to these α-helices, the region Ala15-His18, which is involved in the covalent bonding of the haem prosthetic group in the red algal cyt c_6, forms a normal α-helix (I') rather than the 3_{10}-helix observed in the corresponding region of the cyanobacterial homologue [104,170].

As described in **Chapter 1.2.5**, cyt c_6/c_{553} proteins function as the mobile electron carriers, present on the lumen of thylakoids, and they shuttle electrons between cyt b_6f complex and the photo-oxidised P700 reaction centre of the PSI complex. These proteins are the functional counterparts of plastocyanin, a small copper protein, in the lumen of chloroplasts from higher plants and green algae.

In this study, the genes encoding five different variants of the *C. merolae* cyt c_{553} were cloned, co-transformed with a specific haem-maturation cassette and overexpressed in *E. coli*. The corresponding fully functional protein products were purified to homogeneity and thoroughly characterised biochemically and spectroscopically. The cyt c_{553} variants differed in lengths and structures of AA linkers engineered at the *C*-terminus of cyt c_{553}, between the holoprotein and a His_6-tag. All the variants were then applied as the electroactive modules of the biophotoelectrodes in order to investigate electron transfer kinetics at the interface between the electrode surface and the photoelectroactive modules within the all-solid-state silicon-based biohybrid electrodes. The overall aim of this analysis was to select the ideal cyt c_{553}

variant that would promote the most efficient direct electron transfer from the Si substrate to the photo-oxidised P700 RC within the complete biophotoelectrode, containing PSI-LHCI as the photoactive module (see **Chapter 4.6**).

In *E. coli*, haem maturation enzymes are encoded by the *ccm*ABCDEFGH gene cluster, found in the *aeg*-46.5 operon [172], and the mature enzymes are located in the periplasm and/or cytoplasmic sub-membrane region. The expression of the *aeg*-46.5 operon was found to be consistent with this localisation, as all bacterial cyt *c* proteins are either periplasmic or are present on the periplasmic side of the cell membrane [173]. The pEC86 vector is constitutively expressed in *E. coli*. This means that the genes encoding the haem maturation enzymes do not require the specific induction of expression [173]. **Table 16** displays *ccm* genes and Ccm *E. coli* gene products, respectively.

Table 16

***ccm* genes and Ccm *E. coli* gene products**

Gene*	***E. coli* gene product (no. of resides)**
ccmA/yejW	CcmA (205)
ccmB/yejV	CcmB (219)
ccmC/yejTU	CcmC (245)
ccmD/yoiM	CcmD (69)
ccmE/yejS	CcmE (159)
ccmF/yejR	CcmF (647)
ccmG/yejQ	CcmG (185)
ccmH/yejP	CcmH (350)

***** The initial designation of the *E. coli* ORFs submitted to the GenBank database by Richterich et al. (accession number U00008) is given on the right hand side of the left panel (reproduced from [172]).

4.2.2 Cloning of the *C. merolae petJ* gene and its variants

The *petJ* gene in the chloroplast genome of *C. merolae* encodes cyt c_{553}, being the structural and functional counterpart of the cyanobacterial cyt c_6 [87]. As throughly overviewed in **Chapter 1.2.5**, maturation of thylakoid lumen proteins proceeds post-translationally through an intermediate precursor. Interestingly and in constrast to cyt c_{553}, a close relative, the green algal cyt c_6 from *C. reinhardtii*, is in fact synthesised outside the chloroplast as a larger molecular weight precursor and is subsequently processed to its mature size during protein translocation to the lumenal space [110–112,174]. This may be due to the fact that *petJ* is encoded in the nuclear genome in *C. reinhardtii* whereas in *C. merolae petJ* is encoded in the chloroplast genome [87]. The maturation of pre-apo-cyt c_6 to its mature form involves several

post-translational steps, including translocation of the precursor across the chloroplast envelope and thylakoid membranes, processing of the pre-sequence, and covalent ligation of haem to the apoprotein [110–112,174]. The same process occurs in cyanobacterial cytochrome c_6, where import to the thylakoid lumen is mediated by TOC and TIC proteins, as described in **Chapter 1.2.5**. In *C. merolae*, transcription and translation occurs in the chloroplast, as cyt c_{553} is encoded by the chloroplast genome, and, as the *petJ* gene is intronless, protein processing and assembly is believed to occur much more efficiently and quickly [110,111]. This could explain to some extent why the photosynthetic apparatus of *C. merolae* is so robust and able to cope so quickly with severe fluctuations in the immediate environment for extreme conditions of pH, light intensity and temperature as discussed in more detail in **Chapter 1.2.5**.

The *C. merolae* cyt c_{553} AA sequence of 104 AA includes a 20-AA signalling peptide at the N-terminus, which is subsequently post-translationally excised [175,176], most likely after the cyt c_{553} precursor's translocation into the thylakoid lumen [111,176]. The pre-pro-protein has an observable size of 11.33 kDa, whereas the mature form of this protein is 9 kDa in size. **Figure 46** shows the full DNA sequence of the intronless *C. merolae petJ* gene [87] as well as the AA sequence of the gene product, including the signalling peptide in the cyt c_{553} pre-pro-protein.

The aim of the present study, was to introduce four different peptides between the *C. merolae* cyt c_{553} holoprotein and its genetically engineered *C*-terminal His_6-tag in order to investigate electron transfer properties between the haem group and the electrode surface within all-the-solid state biolelectrodes following immobilisation of this protein *via* its His_6-tag on the Ni-NTA-functionalised semiconductor substrate of *p*-doped Si.

The AA sequence and physicochemical properties of each linker peptide are summarised in **Table 17. Figure 47** shows the corresponding 3D structures of all the cyt c_{553} variants genetically engineered in this study. The 0AA variant comprises the cyt c_{553} holoprotein genetically engineered with a His_6-tag at its *C*-terminus. The 5AA peptide linker is composed mainly of small, polar amino acids allowing for limited structural flexibility particularly at the more charged *C*-terminal end of the sequence. The 10AA linker comprises mainly polar Gly/Ser repeats and a charged Glu residue allowing for a higher degree of structural flexibility of the immobilised cyt c_{553} variant compared to 5AA variant. The 12AA linker corresponds to the original linker peptide encoded within the multiple cloning site of the expression vector between the cyt c_{553} holoprotein sequence and a *C*-terminal His_6-tag. It comprises polar Gly/Ser residues, non-polar Val/Ala/Leu residues, and negatively charged

Asp/Glu residues. Finally, the 19AA variant was designed to introduce a semi-helical peptide linker to the immobilised cyt c_{553} holoprotein. For this variant the Phi/Psi angles of each AA residue were determined to be equal to -62/-41, which corresponds to the average values found experimentally for α-helixes which are non-geometrically ideal [177].

A

petJ nucleotide sequence:

atgaaaagcttattaacattcattttgaccacaatttttgtattcaacaagtatgggccgcagatttagcacatg
gtgaacaaatttttttcggctaattgtgcagcatgtcatgccggtggcaacaatgtgatcatgccagaaaaaac
attgaagttagatgctttagaagccaatcaaatgaatagtgtagaagcaattagcactcaagttcgtaacgga
aaaaatgctatgccatcatttagtcgtttaactgacagtgatattgaagacgtagcgaattacgtacttgctcaa
gctaaaaaaggttgg

B

petJ peptide sequence:

MKSLLTFILT TIFCIQQVWA ADLAHGEQIF SANCAACHAG
GNNVIMPEKT LKLDALEANQ MNSVEAISTQ VRNGKNAMPS
FSRLTDSDIE DVANYVLAQA KKGW

Figure 46

***petJ* nucleotide sequence and cyt c_{553} primary structure.** A: *petJ* nucleotide sequence. B: cyt c_{553} pre-pro-protein AA sequence, with the N-terminal signalling peptide highlighted in red.

Table 17

Physicochemical properties of cytochrome c_{553} variants

Name of variant/ linker type	AA sequence	Linker length (AA no.)	Molecular weight (Da)	Theoretical pI
0 AA	cyt c_{553}-H_6	0	0	N/A
5 AA	cyt c_{553}-**GSGLE**-H_6	5	461.4	4.00
10 AA	cyt c_{553}-**GSGSGSGSLE**-H_6	10	836.8	4.00
12 AA	cyt c_{553}-**GSSVDKLAAALE**-H_6	12	1160.2	4.37
19 AA	cyt c_{553}-**AEAAAKEAAAKEAAAKALE**-H_6	19	1814.0	4.95

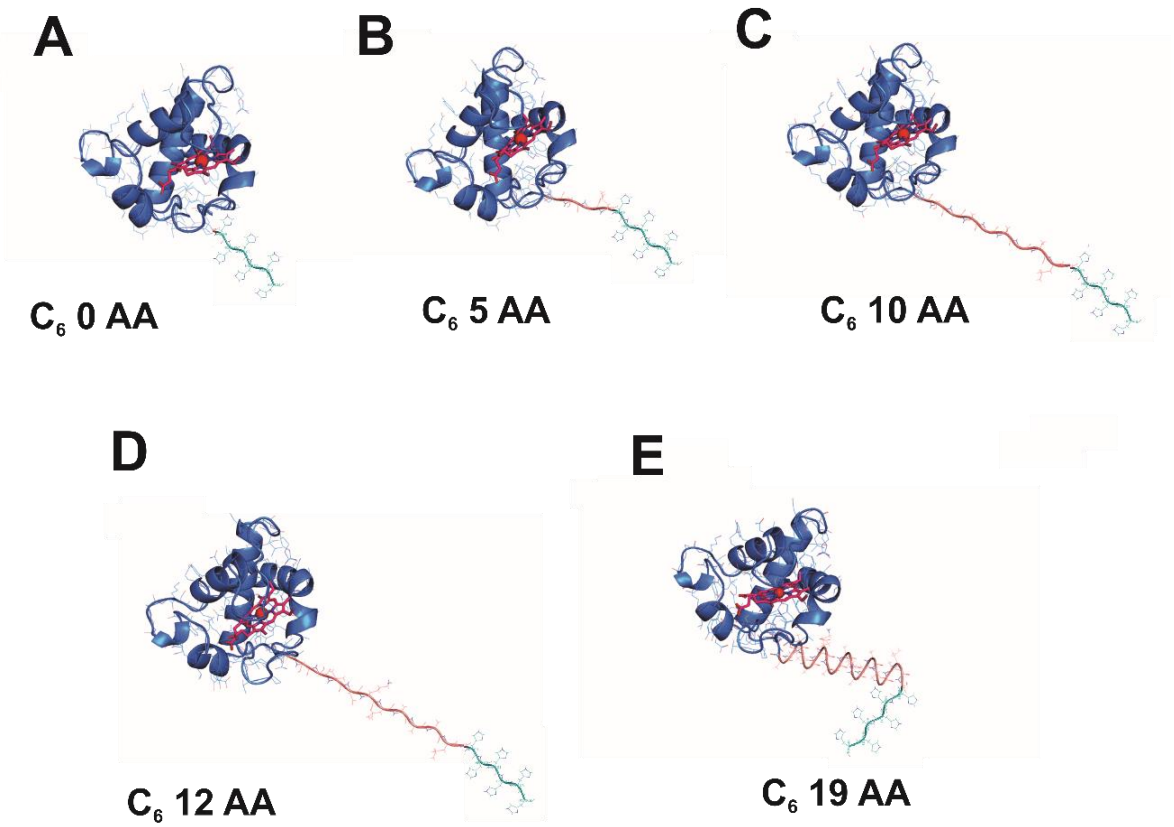

Figure 47

Modelling of 3D stuctures of His$_6$-tagged cyt c_{553} variants with the linker peptides. A: 0AA, B: 5AA, C: 10AA, D: 12AA, E: 19AA (note that all the cyt c_{553} holoprotein sequences are identical). Modelling of AA linkers into the crystal structure of cyt c_6 from *Synechococcus* sp. PCC 7002. The cyt c_6 structure (PDB code: 4EIC) [171] is the highest resolution type I c-type cytochrome (cyt c_{553} from *C. merolae* is a type I *c*-type cytochrome) crystal structure

available to date and was used to model in five distinct AA linkers used in this study. The haem group of cyt c_6 with its central Fe atom is displayed in red.

For genetic engineering of all the cyt c_{553} variants used in this study, a cloning strategy was designed, whereby five different constructs containing the *petJ* sequences were cloned into the pET28b-(+) vector, and subsequently subcloned (including the *C*-terminal His_6-tag encoded within the pET28b-(+) vector multiple cloning site (MCS) sequence) into the pBAD/HisA expression vector. As the pBAD/HisA vector only encodes for a His_6-tag at the N-terminus of the MCS, this subcloning step was essential due to the cleavage of the N-teminal His-tag upon N-terminal proteolytic processing of the cyt c_{553} precursor during its translocation to the periplasm of *E. coli*, where the haem synthesis and its insertion into the mature cyt c_{553} protein also occur. **Figure 48** summarises the cloning strategy.

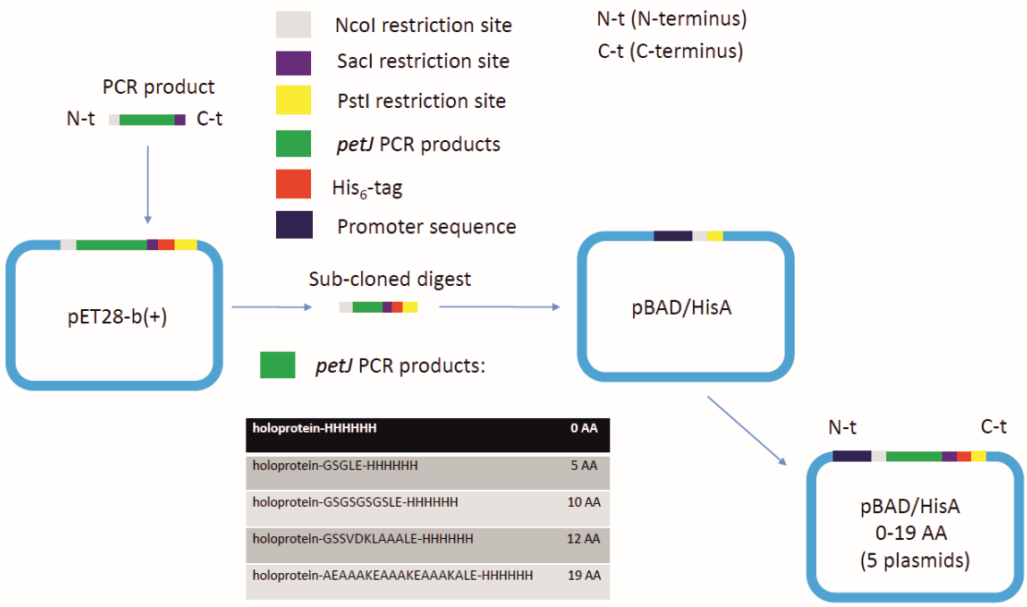

Figure 48

***C. merolae petJ* gene cloning strategy.** Briefly, the *petJ* PCR products were engineered so that an NcoI and SacI restriction sites would be present at the *N*- and *C*-terminus of the sequence, respectively. Thus modified PCR products were subsequently cloned into the pET28b-(+) vector, subsequently, they were excised with NcoI and PstI to contain the full *petJ* sequence with the C-terminal His_6-tag, and finally subcloned into the pBAD/HisA expression vector. Using this strategy, five distinct recombinant plasmids were cloned, including pBAD/HisA-0AA, pBAD/HisA-5AA, pBAD/HisA-10AA, pBAD/HisA-12AA and pBAD/HisA-19AA containing no (0AA) or 4 different peptide linkers between the cyt c_{553}

holoprotein and its *C*-terminal His_6-tag. Refer to **Chapter 7.2** for the maps of all plasmids used in this study.

Figure 49 shows the gel analysis of the five different PCR products produced in this study. For cyt variants 0 and 5, some non-specific products were apparent; however, the main PCR product was ~ 300 bp in size, as expected for the *petJ* gene. Following ligation of the PCR products with the pET28b-(+) vector, five *petJ*-pET28 recombinant vectors were produced (see **Figure 48**). **Figure 50** shows the restriction analysis results, demonstrating the appropriate size of the *petJ* insert (300 bp) and linearised vector (5,600 bp). The correct sequence of all the recombinant vectors was additionally directly verified by DNA sequencing. The NcoI- and PstI-digested inserts were ligated with the pBAD/HisA vector which had been previously linearised with the same restriction enzymes. Restriction analysis of all the recombinant vectors (see **Figure 51**) confirmed the correct insert and vector size and insert orientation. Furthermore, all the finally cloned *petJ* sequences containing the distinct peptide and His_6-tag sequences were directly verified by DNA sequencing.

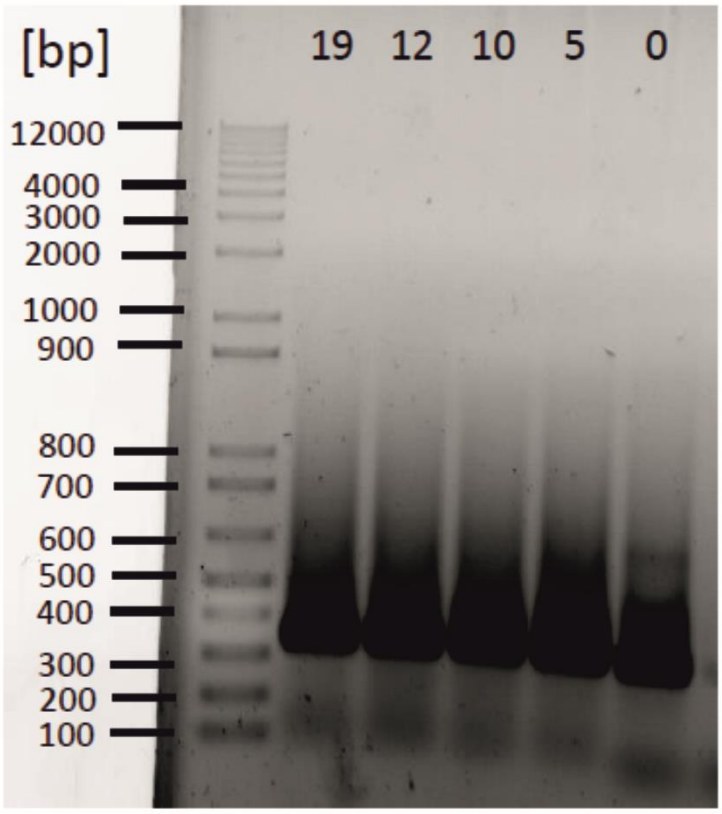

Figure 49

Gel analysis of the PCR products obtained for five different variants of cyt c_{553}. As expected, the PCR *petJ* products for the longer AA linker variants (19AA, 12AA and 10AA) are larger due to the longer peptide sequences present. The PCR reaction for the 5 and 0AA was not completely specific, yet most the product was the *petJ* gene with appropriate sequences as expected. The name of each cyt c_{553} variant is presented above each lane and it is simplified by the number of AA in the peptide sequence. From left to right: 19; 19AA, 12; 12AA, 10; 10AA, 5; 5AA, 0; 0AA.

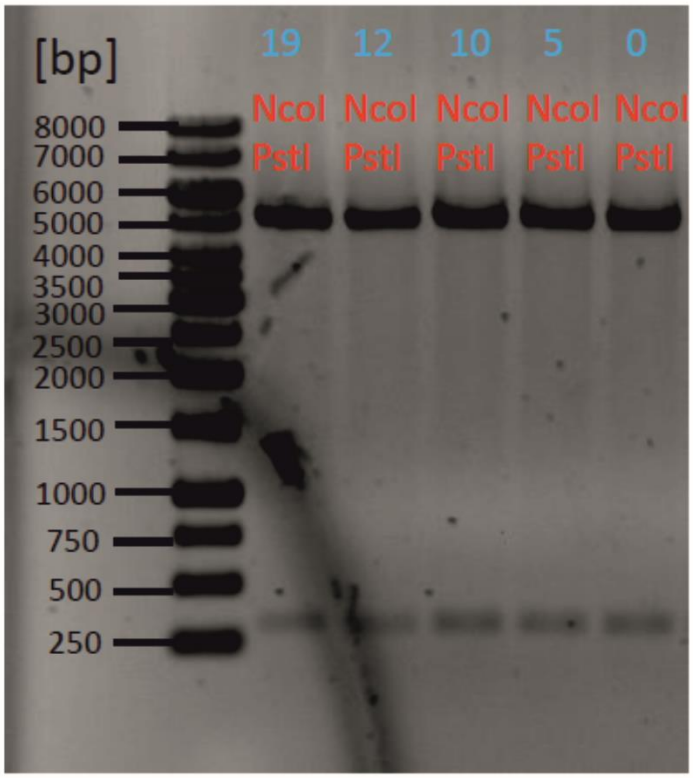

Figure 50

Restriction analysis of the recombinant *petJ*-pET28b-(+) vectors. As expected, the size of the digested *petJ* fragments was approximately 300 bp, and that of the linearised vector approximately 5,600 bp. The name of the restriction enzymes is displayed in red. The name of each cyt c_{553} variant is presented above each lane in blue and it is simplified by the number of AA in the peptide sequence. From left to right: 19; 19AA, 12; 12AA, 10; 10AA, 5; 5AA, 0; 0AA.

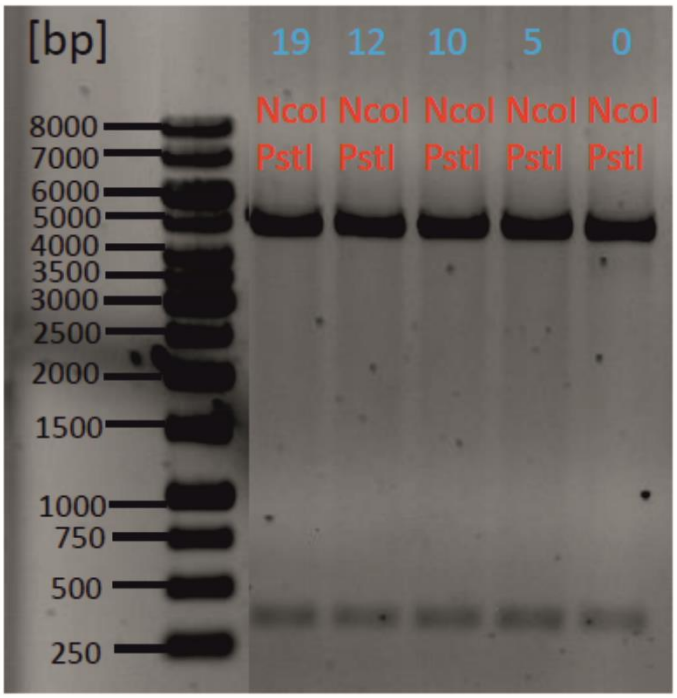

Figure 51

Restriction analysis of the final recombinant *petJ*-pBAD/HisA vectors. As expected, the size of the digested *petJ* fragments was approximately 300 bp, and that of the linearised vector approximately 4,300 bp, which is more than 1,000 bp smaller than the size of pET28b-(+). The name of the restriction enzymes is displayed in red. The name of each cyt c_{553} variant is presented in blue above each lane and it is simplified by the number of AA in the peptide sequence. From left to right: 19; 19AA, 12; 12AA, 10; 10AA, 5; 5AA, 0; 0AA.

4.2.3 Heterologous expression of the *petJ* gene variants in *E. coli*

In order to express His_6-tagged cyt c_{553} holoprotein and its peptide linker variants, each recombinant *petJ*-pBAD/HisA (0-19 AA) expression vector was co-transformed into *E. coli* together with the pEC86 vector encoding for the ccm haem maturation cassette [172]. This cassette includes the ORF (yejWVUTSRQP) genes encoding CcmABCDEFGH haem synthesis and processing enzymes as shown in **Table 16** of **Chapter 4.2.2.1**. Co-transformants with pBAD/HisA 0AA, pBAD-HisA 5AA, pBAD-HisA 10AA, pBAD-HisA 12AA and pBAD-HisA 19AA and pEC86 vectors were produced in two *E. coli* strains, MC1000 and TOP10, and the overall expression yield of cyt c_{553} holoproteins was assessed by redox difference spectroscopy after induction of the *petJ* gene expression for three controlled time intervals (2 h, 4 h and 20 h). Two expression systems, pET28b-(+) and pBAD/HisA (both double transformed with pEC86), were compared for the yield of expressed cyt c_{553} holoprotein variants, under the identical expression conditions (see **Chapter 3.2.1.3**). Of the two expression vectors used, the pBAD/HisA system proved to be useful for further expression studies of cyt c_{553}, as the pET28b-(+) overexpression system yielded the inclusion bodies under the experimental conditions used, resulting in no or extremely low amount of cyt c_{553} holoprotein produced in the soluble fraction of the *E. coli* cell lysate, below the spectroscopic detection level (data not shown).

Two strains of *E. coli*, TOP10 and MC1000, were used for optimisation of cyt c_{553} holoprotein synthesis. To this end, the appropriate double transformants were obtained, as described above. The first double transformant obtained from the recombinant plasmid pBAD/HisA 10AA and pEC86 vector, was employed for the initial optimisation studies, as shown in **Figure 52**. Overall, the double transformant of the MC1000 expression strain produced lower yield of the 10AA cyt c_{553} variant protein (5.3 mg redox active cyt c_{553} L^{-1}) compared to the expression level of this protein in the double transformants of the TOP10 strain (18.93 mg redox active cyt c_{553} L^{-1}). Therefore, the TOP10 strain was used for all the further cyt c_{553} expression studies.

The overall yields of all the cyt c_{553} variants produced in the double transformants under optimised expression conditions varied between 12.5 mg L^{-1} and 24.78 mg L^{-1}, and are summarised in **Table 18**.

Table 18

Yield of redox active cyt c_{553} variants depending on *E. coli* expression strain (after optimised expression conditions, as specified in Chapter 3.2.1.3).

His-tagged cyt c_{553} variant double transformant	Yield of redox active cyt c_{553} variants depending on expression strain employed (TOP10 yield/MC 1000 yield)
pBAD/HisA 0AA/pEC86	18.82 mg L^{-1}/4.1 mg L^{-1}
pBAD/HisA 5AA/pEC86	24.78 mg L^{-1}/6.8 mg L^{-1}
pBAD/HisA 10AA/pEC86	18.93 mg L^{-1}/5.3 mg L^{-1}
pBAD/HisA 12AA/pEC86	12.50 mg L^{-1}/5.0 mg L^{-1}
pBAD/HisA 19AA/pEC86	15.96 mg L^{-1}/2.0 mg L^{-1}

The amount of cyt c_{553} was determined by redox difference spectroscopy using ΔAbs (red_{553nm}-ox_{553nm}) and extinction coefficient 24.1 mM^{-1}, as described in **Chapter 3.2.4.3**. The yield is calculated in mg of redox active cyt c_{553} protein purified from 1 L of *E. coli* culture.

It is important to mention that at the time that pilot expression experiments were being performed, the cell disruption protocol was still being optimised. The fully optimised protocol was employed for the data presented in **Table 18** using the bead beating technique (see **Chapter 3.2.1.7**). For the data presented in Figures **52-55**, sonication was employed, as this was the most accessible method for cell disruption at the time the experiments were performed.

Initially, the batch method with Ni-NTA resin was used for the optimisation of cyt c_{553} 10AA variant purification. Following optimisation of haem maturation time period (see **Figure 52**) by monitoring cyt c_{553} reduced spectra on an equal volume basis, in which the increase of absorbance for the distinctive α (553nm), β (521 nm) and γ (416 nm) peaks of redox active reduced cyt c_{553} was observed, the expression studies recombinant cells were allowed to grow for 20 hours directly after the expression induction.

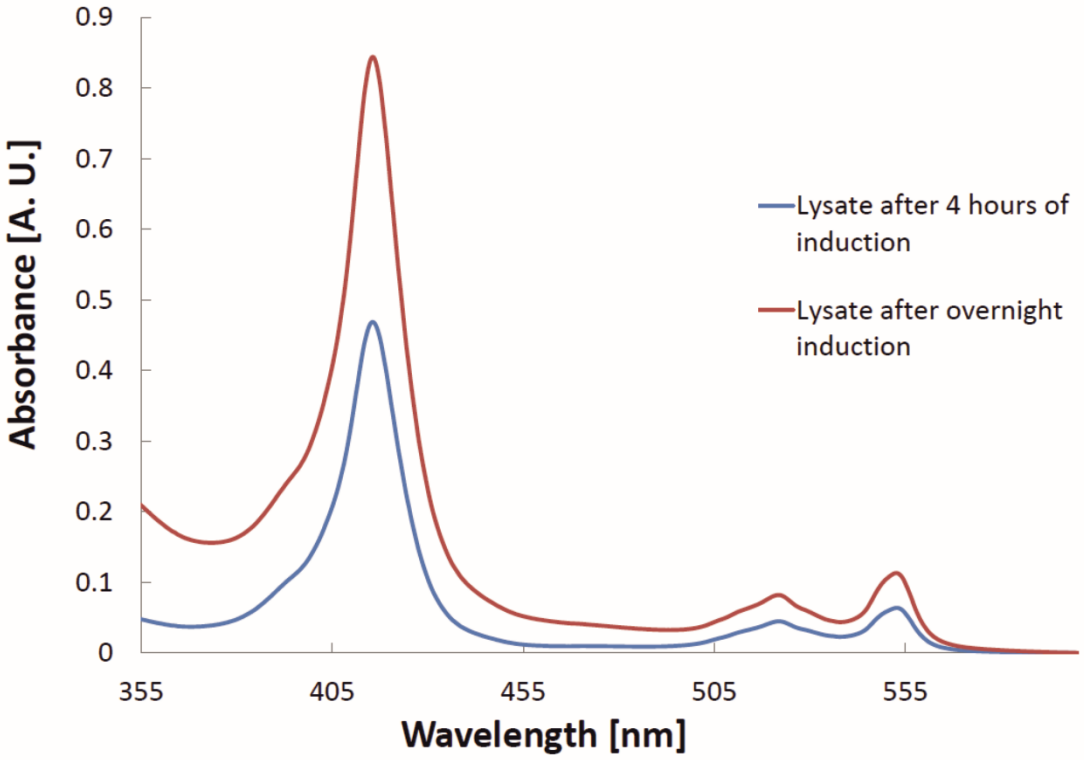

Figure 52

Optimisation of cyt c_{553} holoprotein synthesis in the *E. coli* TOP10 expression strain. The data shows the expression levels of *petJ* gene product (10AA variant) in pBAD/HisA 10AA/pEC86 double transformants of the TOP10 *E. coli* strain. A total yield of 1.8 mg L^{-1} of redox active cyt c_{553} was obtained after 4 h expression induction, compared to the maximum yield of 18.93 mg L^{-1} after 20 h induction (displayed as overnight induction in the figure). For spectral analysis 100 µL of the total cell lysate was diluted to a 1000 µL final volume with standard phosphate buffer as specified in **Chapter 3.2.4.3**.

The optimisation of the batch purification method began by investigating the optimal imidazole concentration necessary for maximal elution whilst minimising elution of non-specifically bound proteins. Application of 30 mM–60 mM imidazole in the wash buffer resulted in some minimal release of cyt c_{553} from the Ni-NTA matrix, with the elution of the main pool of this protein at a 250 mM imidazole concentration. As can be observed from **Figures 53**, **54**, and **55**, the cyt c_{553} elution was quite non-specific and on many occasions a considerable amount of cyt remained bound to the Ni-NTA resin. Moreover, **Panel B** of **Figure 55** shows that the SDS-PAGE elution profile at 250 mM imidazole clearly

demonstrates non-homogeneity of the eluted cyt sample, rendering this method suboptimal for further purification studies of cyt c_{553} variants.

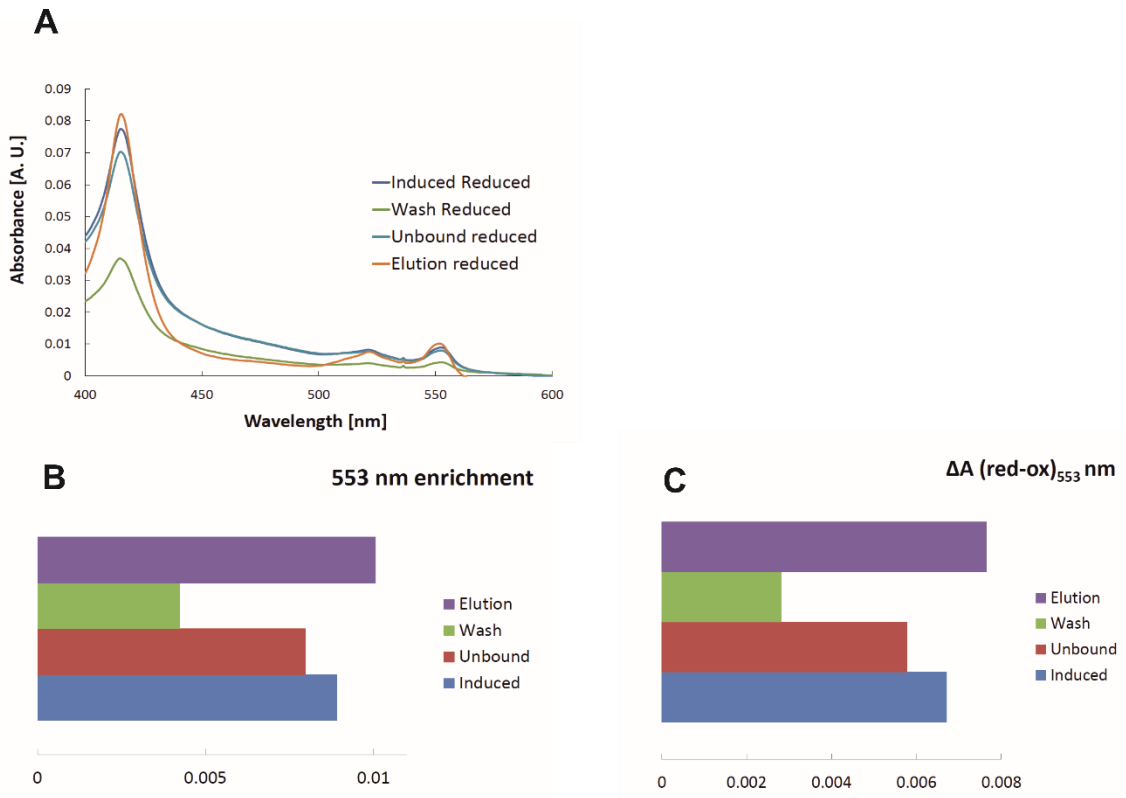

Figure 53

Yield optimisation for cyt c_{553} batch purification with Ni-NTA in the *E. coli* Top10 expression strain. A: Enrichment of cyt c_{553} (10AA variant) elution fraction monitored by reduced absorption spectroscopy on an equal total protein basis (570 µg protein, as determined by the Bradford colourimetric assay). B: 553 nm absorbance enrichment calculated from A. C: Overall enrichment of reduced-oxidised (redox difference) change in absorbance at 553 nm, demonstrating that all fractions are active in electron transfer. Induced: total cell lysate including overexpressed cyt c_{553}; Unbound: non-binding proteins; Wash: cyt c_{553} elution at low (60 mM) imidazole concentration; Elution: cyt c_{553} elution at high (250 mM) imidazole concentration.

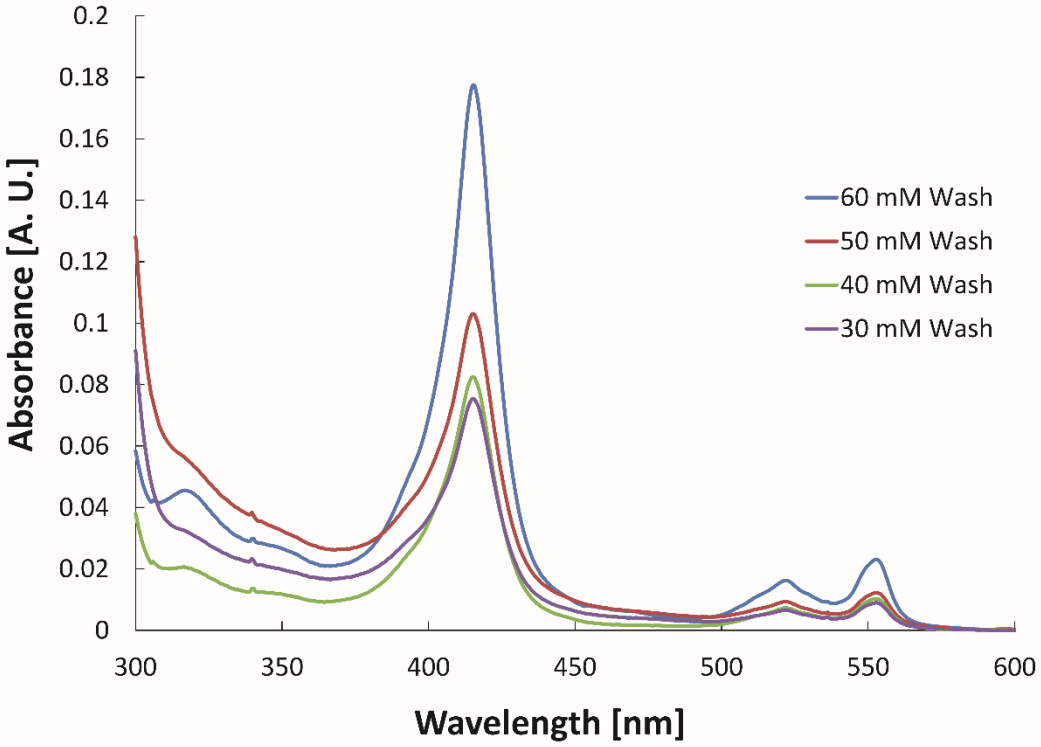

Figure 54

Spectroscopic assessment of the batch purification of His_6-tagged cyt c_{553} on an equal volume basis. Note the increased absorbance at 553 nm of the wash fractions with an increasing concentration of imidazole, corresponding to the increasing amounts of the His_6-tagged reduced form of cyt c_{553} (10AA variant) in the respective wash fractions. With the batch method, cyt c_{553} normally eluted completely at 250 mM imidazole.

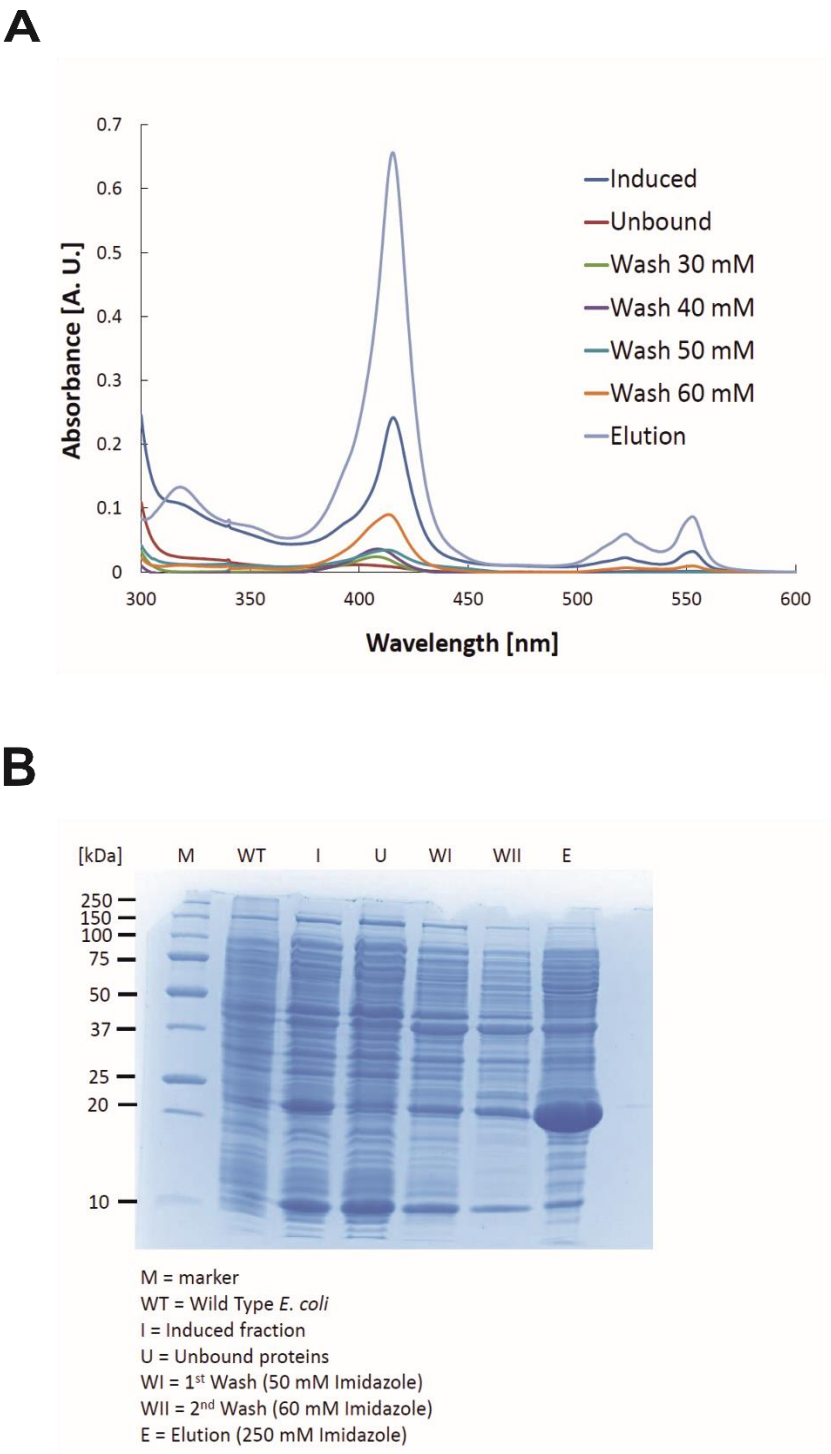

Figure 55

Spectroscopic assessment of the batch purification of His$_6$-tagged cyt *c*$_{553}$ on an equal protein basis. A: redox difference absorption spectra of the fractions on an equal protein basis (350 µg, as determined by the Bradford colourimetric assay). B: SDS-PAGE protein profile of the fractions obtained by the batch purification method. From left to right: M, protein size marker; WT, total *E. coli* protein extract from a wild type TOP10 culture; I, induced total cell

lysate including overexpressed cyt c_{553} (10AA variant); Unbound: non-binding proteins; WI, 1st wash (50 mM imidazole); WII, 2nd wash (60 mM imidazole); E, elution (250 mM imidazole). The 20-kDa band observed in fraction E most likely corresponds to improperly denatured cyt c_{553}.

Due to the lack of homogeneity of the cyt c_{553} samples obtained by batch purification method (see **Figure 55, Panel B**), an alternative approach was used by employing the FPLC purification of cyt c_{553} (initially 10AA variant) using commercially available Ni-NTA His-TRAP columns (see **Chapter 3.2.3.1.1**). **Figure 56** shows the representative chromatograms obtained by loading 20 mg of redox active cell lysate containing the 10AA cyt variant (determined by redox difference absorption spectroscopy) onto the His-TRAP® column. Two well separated pools of the 10AA variant of cyt c_{553} were obtained which corresponded to the reduced and oxidised form of this protein. The reduced pool was 3-fold more abundant than the oxidised one, as shown in **Figure 56**.

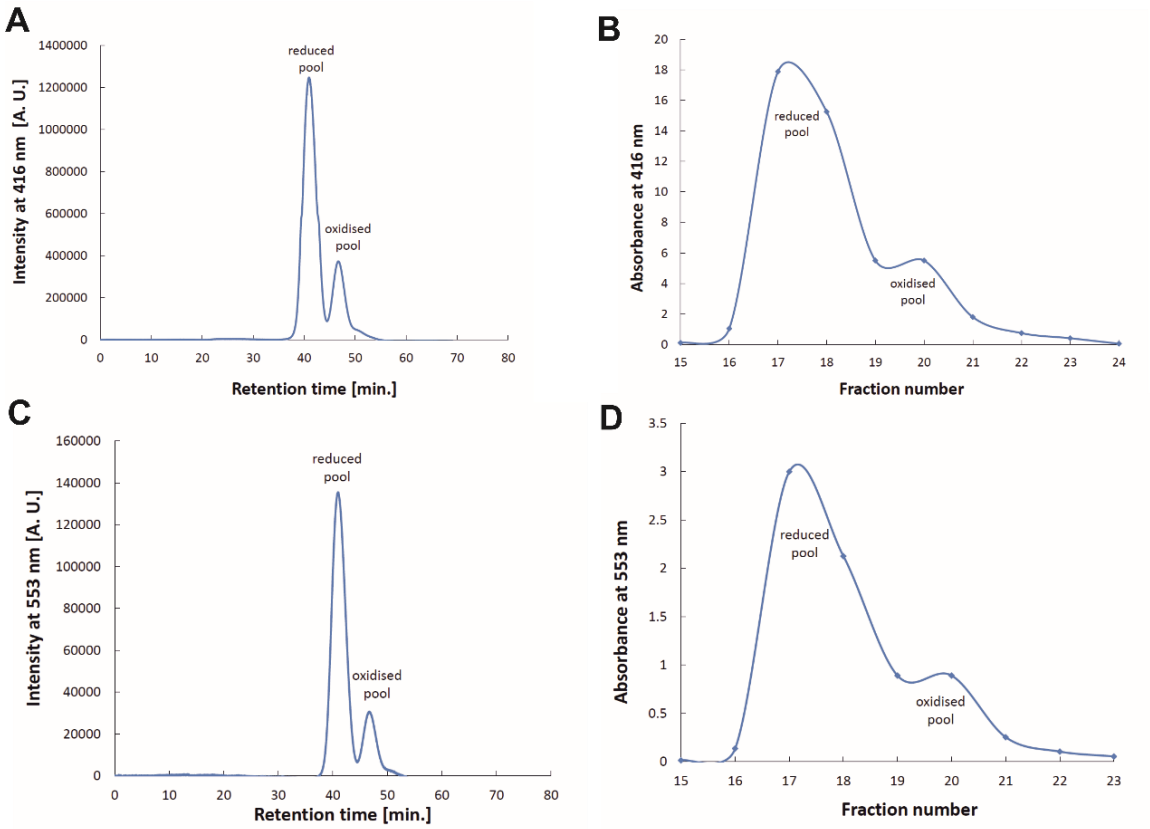

Figure 56

Representative elution chromatograms for FPLC-IMAC purification of cyt c_{553}. 20 mg of redox active *E. coli* lysate containing 10 AA cyt variant (as determined by redox difference absorption spectroscopy) was loaded onto the His-Trap Ni-NTA column. A: Absorption at 416 nm *vs* retention time. B: Absorption at 416 nm *vs.* fraction number. C: Absorption at 553 nm *vs.* retention time. D: Absorption at 553 nm *vs.* fraction number. Absorbance values on Panels B and D correspond to neat absorbance.

4.2.4 Biochemical and spectroscopic characterisation of cytochrome c_{553} variants

Once the protocol for FPLC cyt c_{553} purification was optimised, a large effort was put to maximise protein yield without compromising homogeneity. It was shown that upon loading of 30 mg of redox active lysate onto the 1 ml His-TRAP columns, chromatograms displayed three main peaks, corresponding to different pools of cyt c_{553}. At first it was believed that these pools corresponded to different isoforms of the protein, but later it was shown that they reflected different oxidations states of the protein, with the first pool always being the most reduced and the most impure, compared to the second and third pool which were more homogenous. Pool 3 corresponded to the oxidised cyt c_{553}, and was always bound to the His-TRAP column with greatest specificity and strength. **Panel A** of **Figure 57** shows a typical chromatogram of an FPLC purification of cyt c_{553} (10AA variant) using 30 mg of redox active lysate bound to the His-TRAP® column as the starting material.

To verify the presence of the His_6-tag at the *C*-terminus of the cyt c_{553} holoprotein, SDS-PAGE replica gels were analysed in parallel by Coomassie (R-250) staining and IMAC detection of the His_6-tag by the HisProbe-HRP detection. **Panel B** of **Figure 58** shows an SDS-PAGE protein profile of the eluted fractions (A) together with the parallel HisProbe detection (B) of the corresponding His_6-tagged cyt c_{553} bands in elution Pools 1 and 2.

Following optimisation of the cyt c_{553} overexpression, purification and spectroscopic characterisation with the 10AA linker variant, the same optimised protocol was performed for all the other variants of cyt c_{553}. **Figure 59** shows the respective SDS-PAGE profiles of the five preparations of cyt c_{553} variants, including the profiles of two 10AA linker variant preparations where 20 and 30 mg of redox active lysate was processed, as evidenced for preparations displaying two and three pools, respectively. As mentioned previously, these pools were found to be biochemically identical, yet differing in the oxidation state of the purified cyt c_{553}. This was an interesting observation, as this difference in oxidation state for the distinct pools was strictly reproducible.

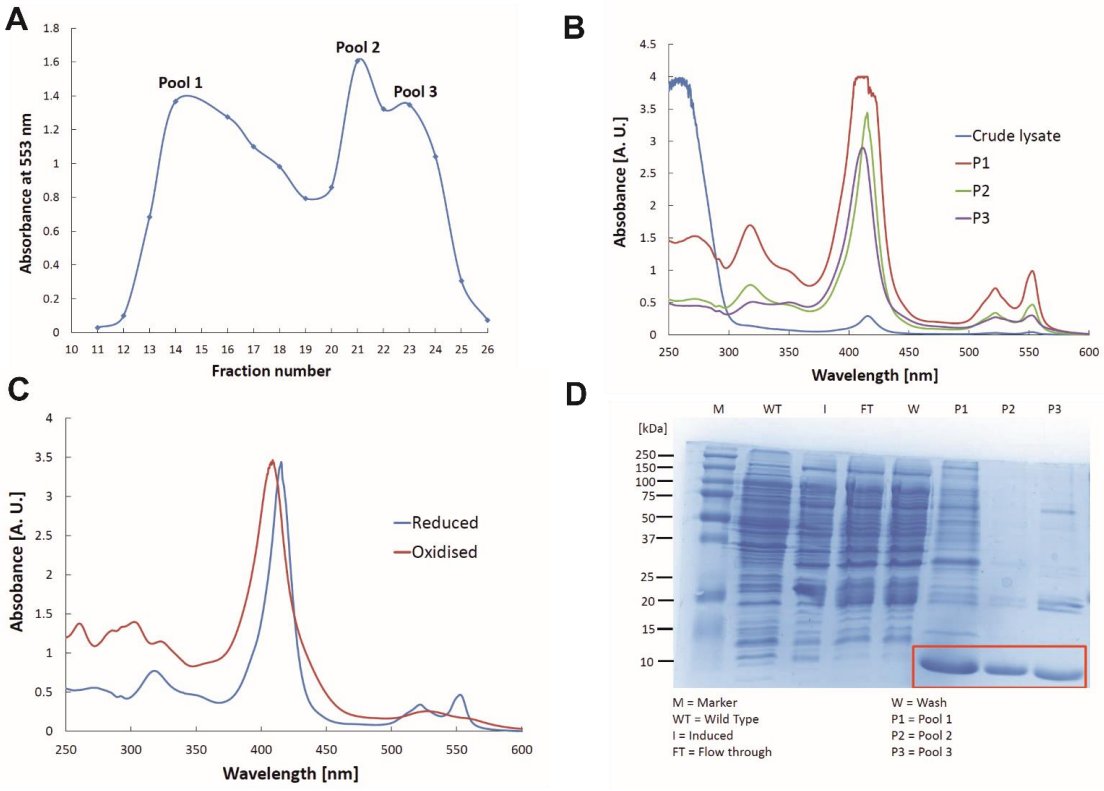

Figure 57

Biochemical and spectroscopic characterisation or FPLC-IMAC purified cyt c_{553} samples. Data are presented for samples purified from 30 mg of redox active *E. coli* lysate containing the 10AA variant, as determined by redox difference absorption spectroscopy. A: A_{553} *vs* fraction number. B: 553 nm enrichment on 300 µg of protein as determined by the Bradford colourimetric method. C: Redox difference spectra of Pool 2, the most homogeneous from this preparation as evidenced in Panel D. D: SDS-PAGE protein profiles of various fractions obtained during FPLC purification of His_6-tagged cyt c_{553}. 16% SDS-PAGE gels were loaded with 15 µL of each fraction per lane (equal volume basis) to assess enrichment of each fraction with cyt c_{553}. The bands corresponding to cyt c_{553} are boxed. M, protein size marker; WT, total *E. coli* protein extract from a wild type TOP10 culture; I, induced total cell lysate including overexpressed cyt c_{553} (10AA variant); FT, flow-through; W, wash (50 mM imidazole); E, elution (175-250 mM imidazole). Note that Pool 2 corresponds to the most homogeneous cyt c_{553} pool isolated.

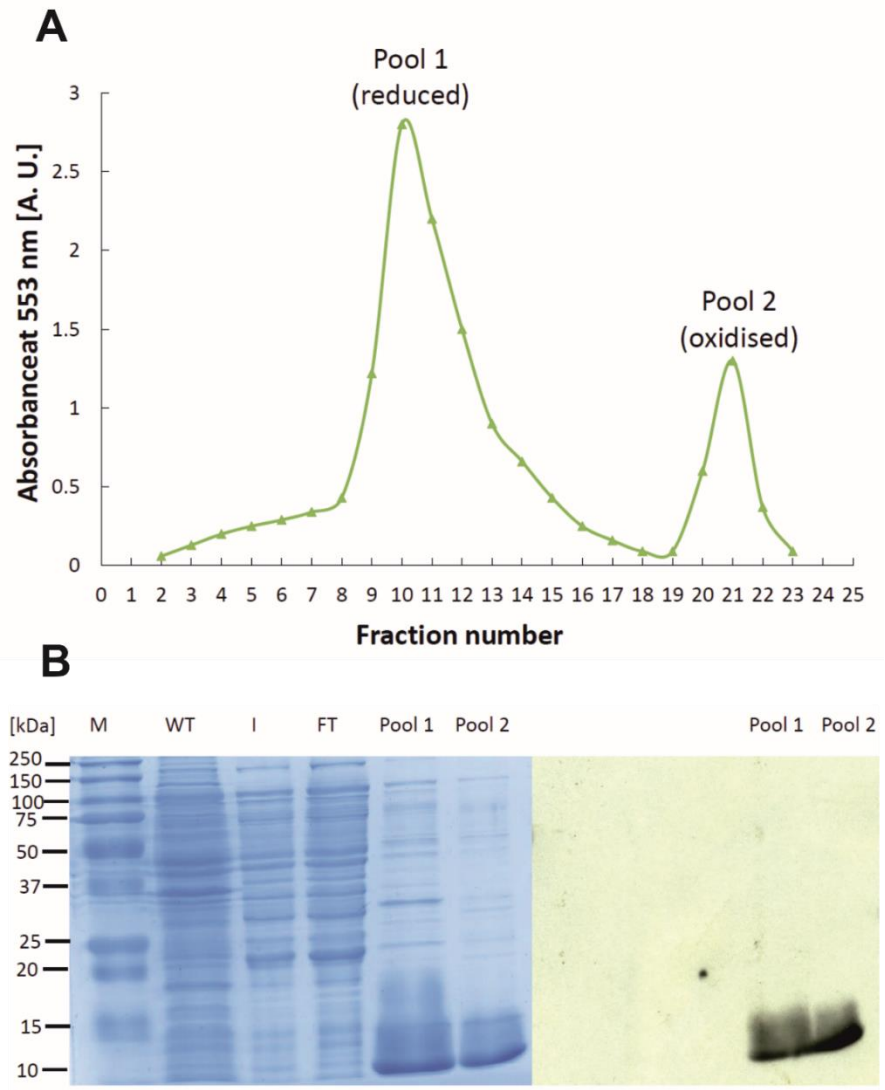

Figure 58

FPLC purification of His$_6$-tagged cyt c_{553}. Data is presented for samples (10AA variant) purified on His-TRAP Ni-NTA columns from 20 mg of redox active *E. coli* lysate (as determined by redox difference absorption spectroscopy). A: Representative IMAC chromatogram showing absorption of each fraction at 553 nm *vs.* fraction number. B: SDS-PAGE protein profiles of each fraction. M, protein size marker; WT, total *E. coli* protein extract from a wild type TOP10 culture; I, induced total cell lysate including overexpressed cyt c_{553} (10AA variant); FT, flow-through; E, elution (175-250 mM imidazole). Note that Pool 2 corresponds to the most homogeneous elution fractions. Bottom-right: HisProbe-HRP detection of the His$_6$-tagged purified cyt c_{553} fractions. Note that only bands belonging to eluted cyt c_{553} display a chemiluminescent signal, confirming the presence of the His$_6$-tag cyt c_{553} in Pools 1 and 2.

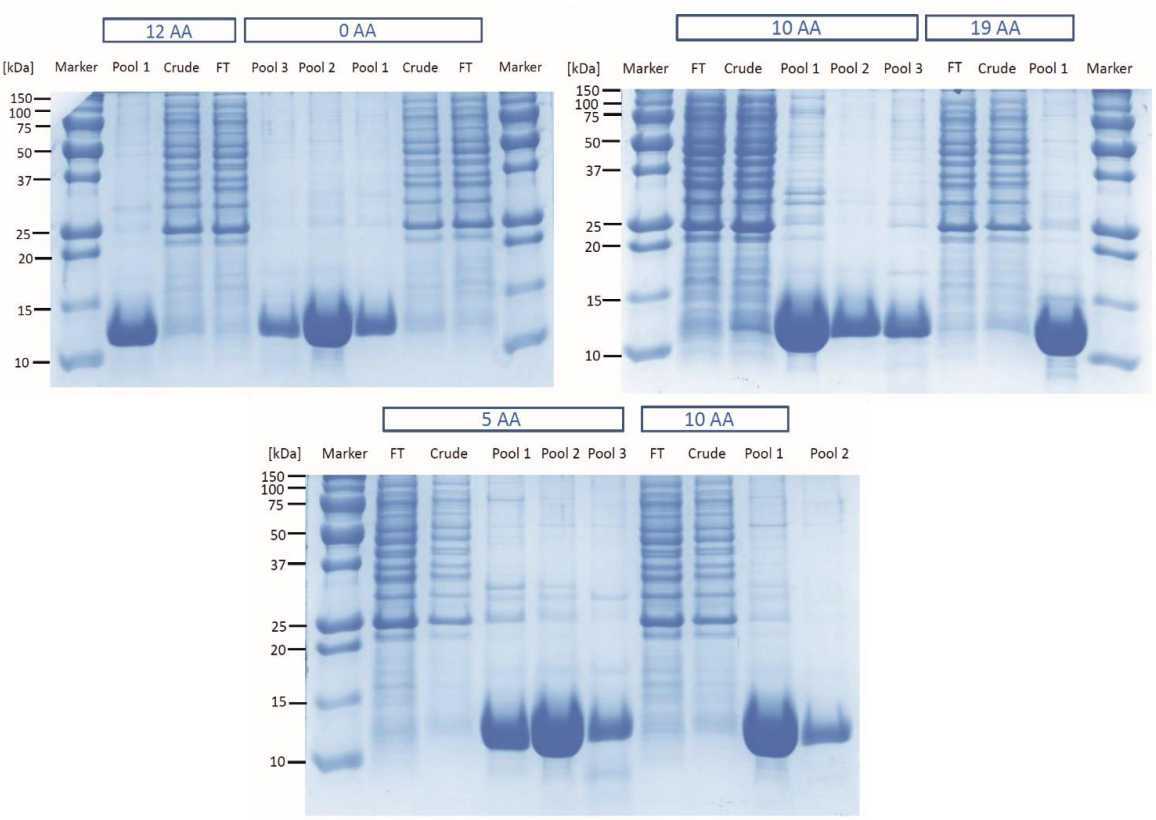

Figure 59

SDS-PAGE protein profiles of the purified variants of cyt *c*$_{553}$. The name of the variant and the AA sequence of the linker peptide is presented on top of each profile preparation. For the 10AA cyt *c*$_{553}$ variant, two preparations were purified, one employing 20 mg of redox active lysate and the other one employing 30 mg of the redox active lysate. As can be distinguished, the preparation where 20 mg of redox active lysate was employed contained 2 pools, in contrast to the one where 30 mg of redox active lysate was employed, where 3 pools can be distinguished. All the lanes were run on an equal volume basis. M, protein size marker; Crude, unbound lysate; FT, flow-through; Pool 1 and 2, pools corresponding to each purification where 20 mg of redox active lysate was employed as displayed in the previous chromatograms (see **Figures 57** and **58**), Pools 1-3, pools corresponding to each purification where 30 mg of redox active lysate was employed as displayed in the previous chromatograms (see **Figure 57**).

Figure 60 displays the protein profiles for all the cyt c_{553} variants used in this study (**Panel A**), confirming not only the purity of the samples obtained through the optimised IMAC approach but also their full redox activity, as shown by redox diffrerence spectroscopy (**Panels B** and **C**).

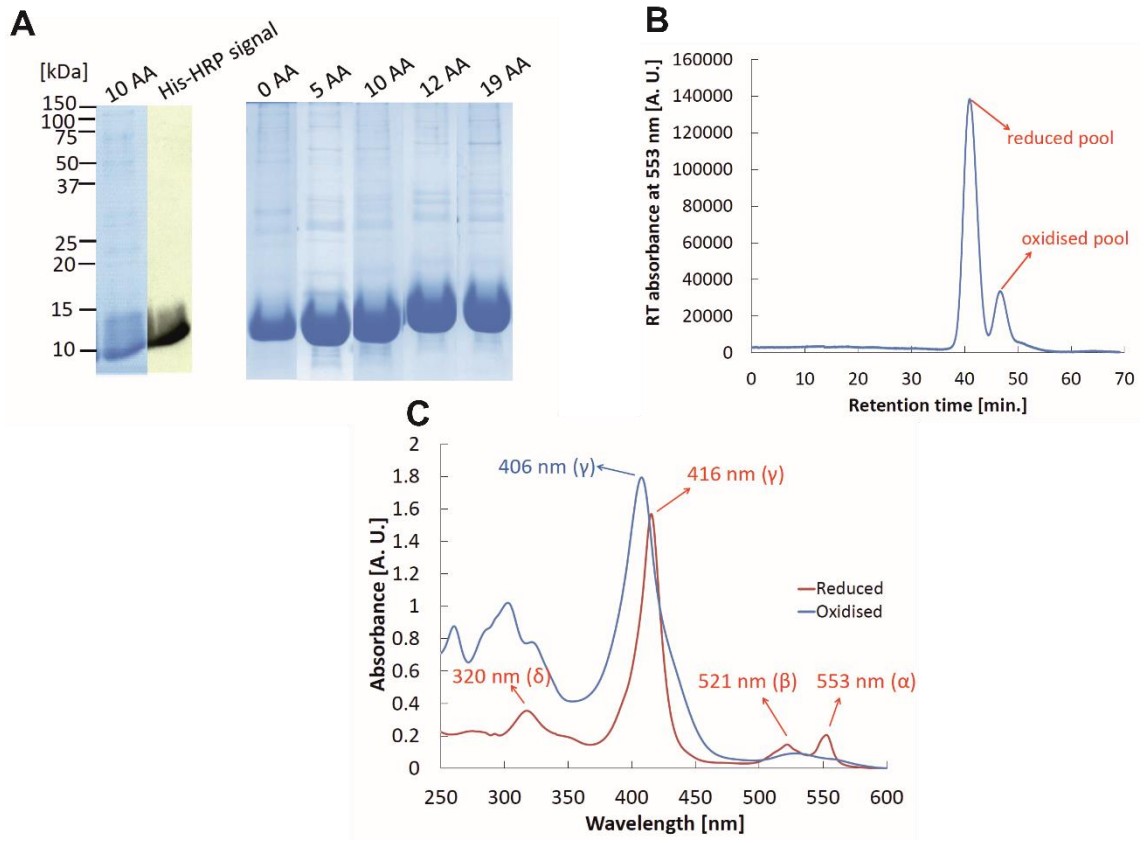

Figure 60

Optimised purification, spectroscopic and biochemical characterisation of cyt c_{553} variants. A: SDS-PAGE protein profiles of the five cyt c_{553} variants synthesised in *E. coli* (30 µg of redox active cyt c_{553} per lane as determined by redox difference spectroscopy and the Bradford colourimetric assay) in conjunction with a representative HisProbe detection of His_6-tagged protein products (10AA cyt c_{553} variant). B: A representative FPLC chromatogram of cyt c_{553} (10AA variant) purified from *E. coli* via IMAC technology when 20 mg of redox active lysate was loaded into the His-TRAP column. C: A representative redox difference absorption spectrum of cyt c_{553} variant (10AA) showing reduced and oxidised species. Spectra from all other variants were identical (see **Suppl. Figure 2**).

4.2.5 Concluding remarks

A robust, reproducible and scalable *C. merolae* cyt c_{553} overexpression procedure was developed, which yielded over 12.5-25 mg of redox active protein per litre of *E. coli* culture (depending on the variant of cyt c_{553}). The overexpression system described here reports the highest yield of redox active *c*-type cytochrome compared to other cyt *c* expression studies reported to date [153,170,178–181]. The system involves a tightly controlled expression system based on the pBAD/HisA vector, combined with a constitutively expressed cyt *c*-type maturation cassette in the *E. coli* strain TOP10. Although the genes encoding five distinct variants of cyt c_{553} exhibited different expression levels, they were all well above 10 mg of redox active protein per litre of the recombinant *E. coli* culture. Optimisation of conditions such as selection of the most appropriate *E. coli* host strain, choice of the inducible expression system in conjunction with constitutively expressed haem maturation enzymatic system, and cell disruption technique all assisted dramatically with the enhancement of the overall yield of redox active cyt c_{553} holoprotein.

All the five cyt c_{553} variants isolated in this study proved to be fully active in electron transfer, as evidenced by redox difference absorption spectroscopy and redox responsiveness of cyt c_{553} functionalised nanodevices upon external illumination as discussed in **Chapter 4.5** and shown in **Suppl. Figure 4**. Moreover, the overexpression and purification system optimised in this PhD study is reproducible in yielding redox active lysate and purified protein to almost homogeneity in all the cases, as evidenced by **Figures 59** and **60**.

Chapter 4.3

In vitro hydrogen production using *C. merolae* PSI-LHCI complex and cytochrome c_{553}

4.3.1 Introduction

4.3.1.1 Hydrogen and Nature inspired proton-reducing catalysts

Hydrogen gas combustion produces only water as a side product. The reaction is characterised by an extremely low enthalpy of combustion, at -286 kJ/mol. As a result, 572 kJ of energy is released, which is thermodynamically quite impressive. These, along with many other desirable properties of molecular hydrogen, make this compound "the holy grail" of sustainable energy. To this end, hydrogen gas as a secondary energy carrier which can be stored, transported and used in manifold applications is actively investigated [182]. As displayed in **Figure 61**, molecular hydrogen (hydrogen gas, 100% H_2) displays the largest volumetric energy density value (280 kWh/m^3), compared to other forms of hydrogen fuel, making it the most desired form of hydrogen fuel for energy storage.

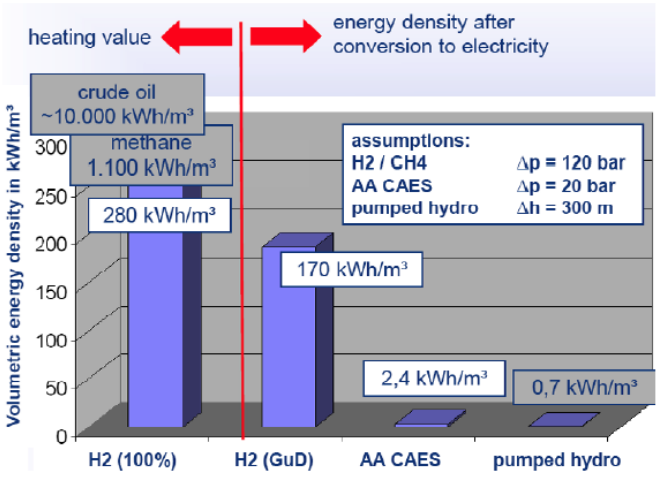

Figure 61

Energy densities for different hydrogen based energy storage systems. Figure reproduced from [182]. Note the large discrepancy between pumped hydrogen (far right) and H_2 (100%) on (far left). H_2 (100%); Pure hydrogen gas, H_2 (GuD); liquified hydrogen, AA CAES; Advanced Adiabatic Compressed Air Energy Storage Hydrogen, pumped hydro; pumped hydrogen gas produced by hydroelectricity.

As PSI forms an exceptionally long-lived charge-separated state $P700^+ F_B^-$ (~60 ms) and is characterised by an exceptionally low redox potential associated with the distal F_B cluster (E_m of -0.58 eV), it provides a sufficient driving force to reduce protons to H_2 at neutral pH. For these reasons, there is significant interest in utilising the highly stable forms PSI for generation of solar fuels, such as molecular hydrogen. As described in Chapter **1.3.3.1**, a number of *in vitro* and solid-state H_2 production approaches with the successful incorporation of PSI have yielded very promising results, reporting up to 3,000 µmol H_2 mg Chl^{-1} h^{-1} [66,135] (see **Figure 23**).

To date, only higher plant and cyanobacterial PSI have been used for H_2 production using *in vitro* reconstitution and solid-state systems [66]. As highlighted in Chapter **4.1**, *C. merolae* PSI-LHCI supercomplex displays exceptional long-term stability and robustness, also at high light intensities of up to 20,000 µmoles photons m^{-2} s^{-1} ([91,139] **Chapter 4.1**), making it the candidate par excellence for *in vitro* hydrogen generation, when hybridised with the specific proton reducing catalysts (PRCs).

It is undisputed that platinum (Pt) is the metal catalyst of choice when it comes to proton reduction, as it displays very high activity and stability at very low overpotential [183]. In contrast to iridium, there should be sufficient Pt for Terawatt (TW) scaled up hydrogen production as enough turnonvers occur with considerably low Pt loadings [184]. Nonetheless, scarcity and high cost of this metal impose obvious limitations for its large-scale industrial employment, and thence, avoiding a dependence on this noble metal is by all possible means desirable. Many efforts have been made in the development of highly active, robust proton-reduction catalysts based on earth-abundant materials during the last decade [185]. Various metal phosphides (e.g. CoP, FeP and MoP) and NiMo perform well under basic conditions, and they have shown to be very active PRCs at low pH values [183]. Over the last decade, the gap between these earth-abundant catalysts and Pt has been considerably diminished, but improvements are still essential. Nanostructuring of the catalysts aides with the activity improvement, but at the cost of corrosion. Improvement of PRCs robustness, either by material choice or specific supramolecular organisation by light harvesting/stabilising modules is therefore greatly desired.

Nature provides us with PRC counterparts which work rather efficiently. Excellent catalysts are found in the form of hydrogenase (H_2ase) enzymes that reduce protons at near-zero overpotential [183]. Unfortunately, most [FeFe]-H_2ases (the most active class of this enzyme) are known for their severe aerobic instability, limiting their practical use in solar-to-

fuel devices [183]. This fact has inspired the development of molecular mimics of these enzymes in the form of stable, efficient, inexpensive alternatives [183]. Several transition metal complexes, mostly based on Co, Ni and Fe, have been synthesised and evaluated with the ultimate purpose of improving catalyst performance and understanding the mechanistic milieu of proton reduction [186]. Many [FeFe]-H_2ase mimics have been synthesised and investigated as PRCs [187]. The latest generation of these catalysts have displayed very high activities and stabilities in water at low pH, although the low overpotential of the natural system is difficult to parallel [188]. Modifications of the outer coordination sphere of these natural mimics might result in the enhancement of catalytic performance due to a similar phenomenon observed in the stimulation of the [FeFe] active site of H_2ase by neighbouring amino acid residues [183]. **Figure 62** displays the structural similarity between the active site of [FeFe]-H_2ase and the [FeFe] centre of an efficient, state-of-the-art [FeFe] PRC.

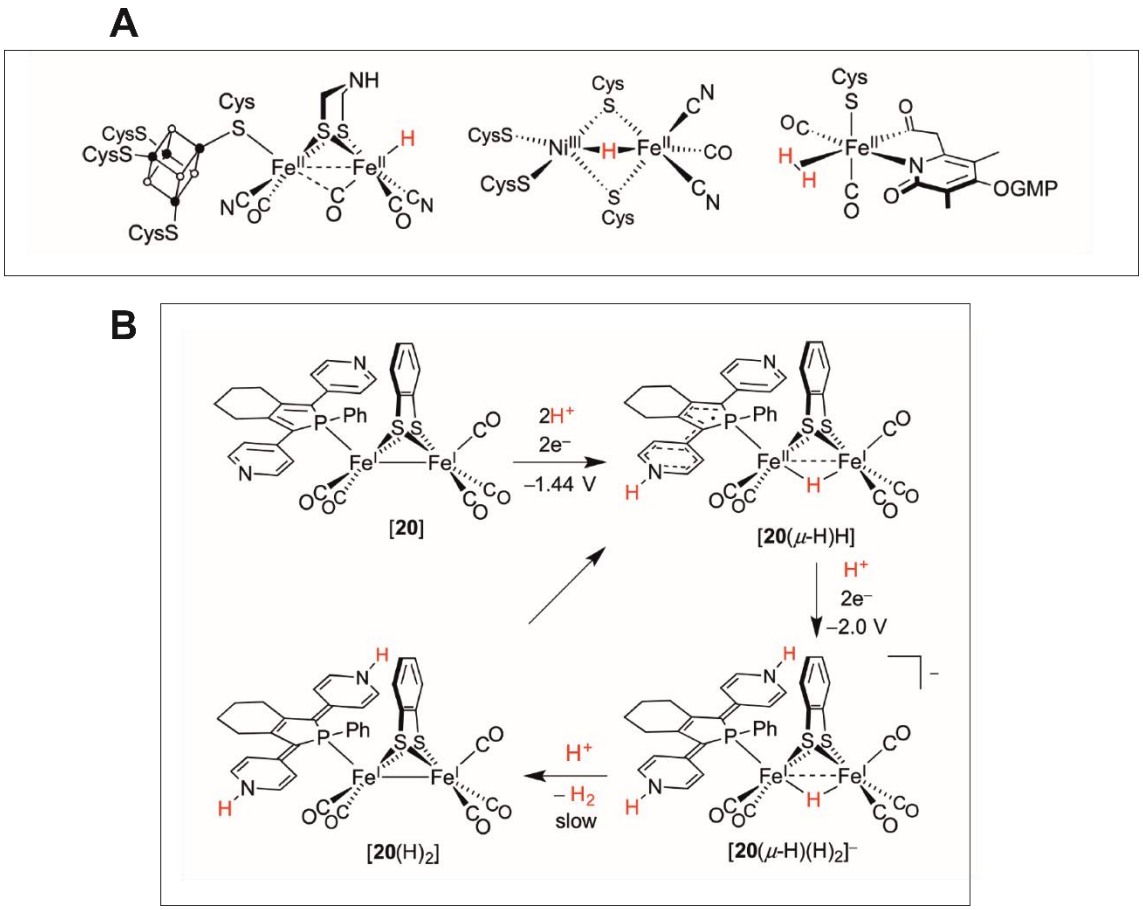

Figure 62

Structural similarity between the active site of [FeFe]-H_2ase and the [FeFe] catalytic centre of PRC #20. A: Schematic representations of the active sites in [FeFe]-H_2ase (left), [NiFe]-H_2ase (centre) and [Fe]-H_2ase (right). The presence of H^- and H_2 ligands in [FeFe]-

H_2ase and [Fe]-H_2ase, respectively, has yet to be confirmed. B: Hydrogen-evolution reaction (HER) catalytic cycle proposed for compound #20 from [188]. Figures reproduced from [187].

One of the best PRCs known to date is the DuBois-type Ni(II) complexes with amine-based containing diphosphine ligands. Some of these catalysts have demonstrated to reduce protons at rates greater than 100,000 s^{-1} in organic solvents, although at an overpotential of ~ 0.6 V [150]. A rather simple adjustment of the coordination sphere around the Ni(II) by introduction of amino ligands in the side chains of the suspended amine ligand ameliorates reversible H_2 addition/release [189]. This results in catalytic rates for proton reduction in acidic water of greater than 300 s^{-1} at near-zero overpotential demonstrating the influence of the outer coordination sphere on the catalytic centre and ultimately its influence in the catalysis reaction rates and stability of these catalysts [183].

A great number of approaches have been pursued to anchor molecular catalysts on surfaces employed in the assembly of device structures. Other strategies employ noncovalent adsorption techniques, such as supramolecular binding motifs, π-π interactions, and hydrophobic interactions [183]. Moreover, metal-ligand interactions are an alternative significant approach to bind catalysts on metal oxide surfaces (for instance, with phosphate binding, carboxylate, hydroxyamate or siloxane) [190]. In most of the examples reported thus far, the application of electrodes with molecular catalysts results in a rapid drop (normally within one hour) of the catalytic activity due to either cleavage or deactivation of the catalyst [183]. Clearly, more efforts are required to upsurge the robustness of such systems [183].

To date, several PRCs, capable of reducing protons *in vitro* under simulated solar light, have shown a lot of promise [191]. However, many of these catalysts are unable to reduce hydrogen at times due to poor electron transfer because of catalyst aggregation, charge recombination between the catalyst and the substrate, or instability of the catalyst after the first cycle of the proton reduction reaction [191].

4.3.1.2 PSI-based systems for hydrogen production

There is a precedent in the literature for the employment of Pt and earth-abundant Co and Ni-based catalysts in conjunction with PSI for photogenerated hydrogen production. Platinization of PSI has been achieved by two different methods to date. Iwuchukwu and colleagues [140] have achieved platinization of PSI *via* a photo-precipitation of hexachloroplatinic acid $[PtCl_6]^{2-}$ onto cyanobacterial (*Synechocystis PCC* 6803 and *T.*

elongatus) PSI monomers, while Utschig and colleagues [192] have achieved platinization of *Synechococcus leopoliensis* and *Synechococcus lividus* PSI monomers *via* electrostatic association of ~ 3.0-nm Pt nanospheres. The former methodology yielded a maximal hydrogen production rate of 5.5 μmol H_2 mg Chl^{-1} h^{-1} while the latter yielded a maximal hydrogen production rate of 244 μmol H_2 mg Chl^{-1} h^{-1}. These studies demonstrate that highly efficient photoproduction of H_2 can be obtained for a self-assembled, noncovalent complex between PSI and Pt nanoparticles [140,192]. As abovementioned, due to cost and scarcity Pt is not suitable for potential large-scale industrialisation of H_2 generation process and hence, hybridisation of PSI has been investigated with the molecular catalysts based on earth-abundant elements, such as Co and Ni.

Utschig and colleagues [130] have reported an alternative strategy for H_2 production that involves the adsorption of a Co-based catalyst onto the PSI complex, in the vicinity of F_B cluster [130]. One of the benefits of this particular design is that both the redox potential and chemical structure for the specific covalent binding of the catalyst can be tuned through known chemical modifications, and this might enable future modular creation of multiple hybrid systems with different functions [130]. Cobaloxime, a well-known proton reduction electrocatalyst, was chosen for this purpose. Cobaloximes are pseudomacrocyclic bis(dimethylglyoxamato)cobalt complexes that were originally developed as vitamin B_{12} mimics and found to catalyse electrochemical proton reduction [193,194]. Unlike hydrogenase mimicking catalysts, cobaloximes in general are oxygen tolerant, readily synthesised, and the H_2 production catalysis proceeds at a low overpotential ([130] and references therein). Cobaloximised-PSI hybrids resulted in a record hydrogen production at a rate of 120 μmol H_2 mg Chl^{-1} h^{-1}, half of that reported for the platinized counterpart [130]. These results are comparable to those presented in this Chapter for the *C. merolae* cobaloximised PSI-LHCI supercomplex, as shown in the subsequent sections.

Utschig and colleagues extended their work by performing a non-covalent hybridisation of mononuclear DuBois-type Ni catalyst $[Ni(P_2^{Ph}N_2^{Ph})_2](BF_4)^2]$ to the acceptor side of *Synechococcus leopoliensis* and *Synechococcus lividus* PSI monomers [195]. The methodology was very similar to that reported previously for cobaloxime [130], although the record hydrogen production rate was much lower, close to 30 μmol H_2 mg Chl^{-1} h^{-1}. It is important to mention that the attempts to hybridise either cobaloxime or DuBois-type Ni catalysts have only been performed to date on cyanobacterial PSI, which as mentioned in

Chapter 1.2.3, is trimeric and lacks the LHCI complex characteristic of the eukaryotic PSI complex.

This Chapter describes development of an *in vitro* system for the biohybrid H_2 photoproduction using the eukaryotic, extremophilic red algal PSI-LHCI supercomplex conjugated with Pt nanospheres, cobaloxime or a small library of DuBois-type Ni molecular catalysts. It has been recently shown that the *C. merolae* PSI-LHCI supercomplex operates under a wide range of pH conditions [91] which would normally impair PRCs, such as very basic or very acidic conditions as these conditions would render the catalysts prone to degradation and most likely unwanted chemical rearrangements [150,183,191]. Moreover, the preliminary data presented in this chapter indicates that *C. merolae* PSI-LHCI complex may play a critical role in stabilising the selected PRCs under intense and prolonged illumination, which, as aforesaid, is highly desirable for continued, robust and scalable molecular hydrogen production.

Importantly, it is shown in this Chapter that cyt c_{553} is essential to promote PSI-based *in vitro* H_2 production, as in the absence of cyt c_{553} no hydrogen evolution was detected. The data presented here is a testament to the fact that employing nature's most perfect photoconverter in conjunction with man-made PRCs and the photoconverter's native electron donor lays the foundation to developing a cheap and potentially scalable technology for production of molecular hydrogen.

4.3.2 Optimization of PSI-LHCI:mononuclear nickel catalyst, PSI-LHCI:cobaloxime and PSI-LHCI:platinum hybrid formation

Several novel Dubois-type mononuclear Ni catalysts were employed for this study and their chemical structures are presented in **Figure 63**. These catalysts were synthesized *via* advanced organic synthesis methods in the laboratory of Prof. Joost Reek (University of Amsterdam). The PRCs were adsorbed on the *C. merolae* PSI-LHCI supercomplex, following the procedure described for cobaloxime and cyanobacterial PSI [130], as described in detail in **Chapter 3.2.8.**

To determine optimal molar ratios of PRC/PSI-LHCI for the highest rates of H_2 production, various amounts of the constituents were incubated together and tumbled in the dark to allow for physisorption of PRCs on the acceptor side of *C. merolae* PSI-LHCI supercomplex. After removal of the unbound catalyst, the PSI-LHCI/PRC hybrid was analysed for the amount of the catalyst adsorbed on PSI-LHCI complexes by inductively

coupled plasma-graphite furnace atomic absorption spectrosocopy (ICP-GFAAS) in the Expert Analytical Centre, Biological and Chemical Research Centre, University of Warsaw, Poland. The results of this analysis are presented in **Table 19**.

Compound 1: MW = 1428.37 g · mol^{-1}

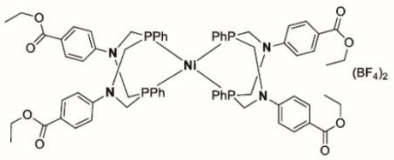

Compound 2: MW = 1456.85 g · mol^{-1}

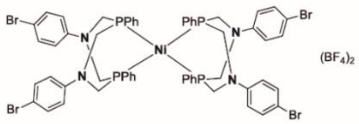

Compound 3: MW = 1141.27 g · mol^{-1}

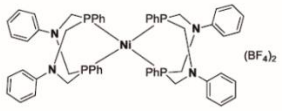

Compound 4: MW = 1139.93 g · mol^{-1}

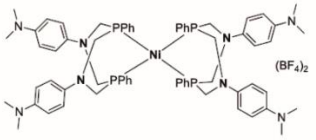

Cobaloxime: MW = 403.71 g · mol^{-1}

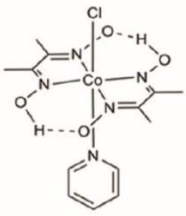

Figure 63

Chemical structures of proton-reducing mononuclear nickel catalysts and cobaloxime employed in this study. Please refer to name coding for all the data presented in this Chapter. M_{wt} (MW) (g·mol^{-1}) is displayed above each compound structure.

Table 19 shows that the molar ratios of PSI-LHCI supercomplex to DuBois-type Ni catalysts (compounds 1-4, see **Figure 63**), cobaloxime and Pt were directly proportional to the initial molar ratios of the hybrid constituents, but on several occasions, a saturation point was reached. This was the case particularly for compounds #2, #3, cobaloxime and interestingly for Pt as well. Cobaloxime presented a rather interesting precipitate in the bottom of the Eppendorf when the 1:60 molar ratio was employed for the preparation for the PSI hybrid complexes, whereas such a precipitate was not observed when a 1:40 molar ratio was employed. A similar phenomenon was observed for compound #2, also at the higher catalyst loading (1:50 and 1:60 molar ratios, respectively). Interestingly, these were the only two hybrid complexes (compound #2:PSI-LHCI and cobaloxime:PSI-LHCI) that yielded hydrogen production under the conditions used in this investigation. It is believed that in order to get a successful delivery of electrons to the metal active site, the catalyst should be present in the vicinity of the F_B cluster of PSI. As the *C. merolae* PSI-LHCI complex is considerably larger compared to cyanobacterial PSI monomer, which lacks the peripheral antenna complex, it is unsurprising that this complex requires a much higher catalyst loading than that reported for the cyanobacterial counterpart hybrid complexes [130,195] in order to ensure the presence of at least one catalyst in the vicinity of the F_B cluster.

As observed in **Figures 64** and **65**, the activity of PSI-LHCI and its UV-VIS RT absorbance spectra are barely affected by the hybridisation of this complex with the DuBois-type Ni catalysts or cobaloxime. Moreover, the hybrid complexes retain in average 60% of the photochemical activity upon hybridisation with the PRCs. **Figures 66-70** summarise the optimisation of the binding of the Dubois-type mononuclear Ni catalysts and cobaloxime to the *C. merolae* PSI-LHCI complex, presenting the final molar ratios of the catalyst and PSI-LHCI complex obtained in this study. **Figure 71** displays the molar ratios obtained for the Pt/PSI-LHCI hybrid complexes containing ~3.0 nm Pt nanopspheres(s) (assumed nanostructure and diameter). The nanospheres are believed to have a diameter of ~3.0 nm as the protocol from [156] was reproduced *sensu stricte* (see Chapter **3.2.8.1)**. **Figure 71** shows that even at high molar ratios of Pt and PSI-LHCI used for hybridisation, only one Pt nanosphere adsorbs onto one PSI-LHCI complex, similar to the results obtained by Utschig and colleagues [192].

Table 19

ICP determination of PRC:PSI-LHCI molar ratios in the PSI hybrid complexes

Compound number	PSI-LHCI:PRC initial molar ratio used for hybridisation	Final PRC:PSI-LHCI molar ratio[1]
1	1:2	subs
1	1:4	subs
1	1:6	subs
1	1:20	1-2
1	1:40	6
1	1:50	7
1	1:60	8-9
2	1:2	subs
2	1:4	subs
2	1:6	subs
2	1:20	1
2	1:40	3
2	1:50	3-4*
2	1:60	2-3*
3	1:2	subs
3	1:4	1
3	1:6	subs
3	1:20	2-3
3	1:40	10-11
3	1:50	16-17
3	1:60	18-19
4	1:2	subs
4	1:4	1-2
4	1:6	2-3
4	1:20	14-16
Cobaloxime	1:2	subs
Cobaloxime	1:4	subs
Cobaloxime	1:20	3-4
Cobaloxime	1:40	7-8
Cobaloxime	1:60	In solution saturation reached*
Pt	1:4	subs
Pt	1:8	subs
Pt	1:20	~1
Pt	1:40	~1

Compound numbers 1-4 correspond to Ni-based molecular catalysts as presented in **Figure 63**.

[1]as determined by elemental analysis by ICP-GFAAS analysis.

*as observed by formation of precipitate most likely due to in solution saturation of the catalyst.

Subs, sub-stochiometric.

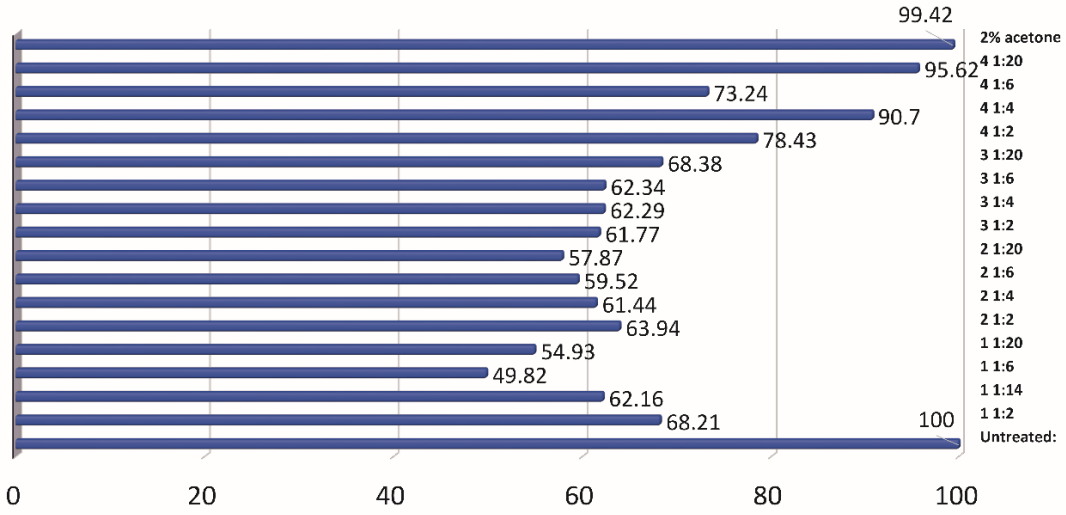

Figure 64

Mononuclear DuBois-type Ni PRC/PSI-LHCI hybrid complex activity. The photochemical activity of the PSI hybrid complexes is expressed as the percent of the control corresponding to the untreated *C. merolae* PSI-LHCI sample. The PSI-LHCI hybrid complexes retain over 60% of the activity, confirming the robustness of the supercomplex, and showing almost 100% activity in the presence of 2% acetone in the incubation buffer. The numbers to the right correspond to the compound number (as in **Figure 63**) and molar ratio employed (see **Table 19**). Acetone was employed for solubilisation of all the DuBois-type mononuclear Ni catalysts used in this study. A final PSI-LHCI hybrid suspension contained 2% acetone (v/v), and was compared to the control PSI-LHCI sample in the buffer containing the equivalent amount of acetone (top right, 2% acetone).

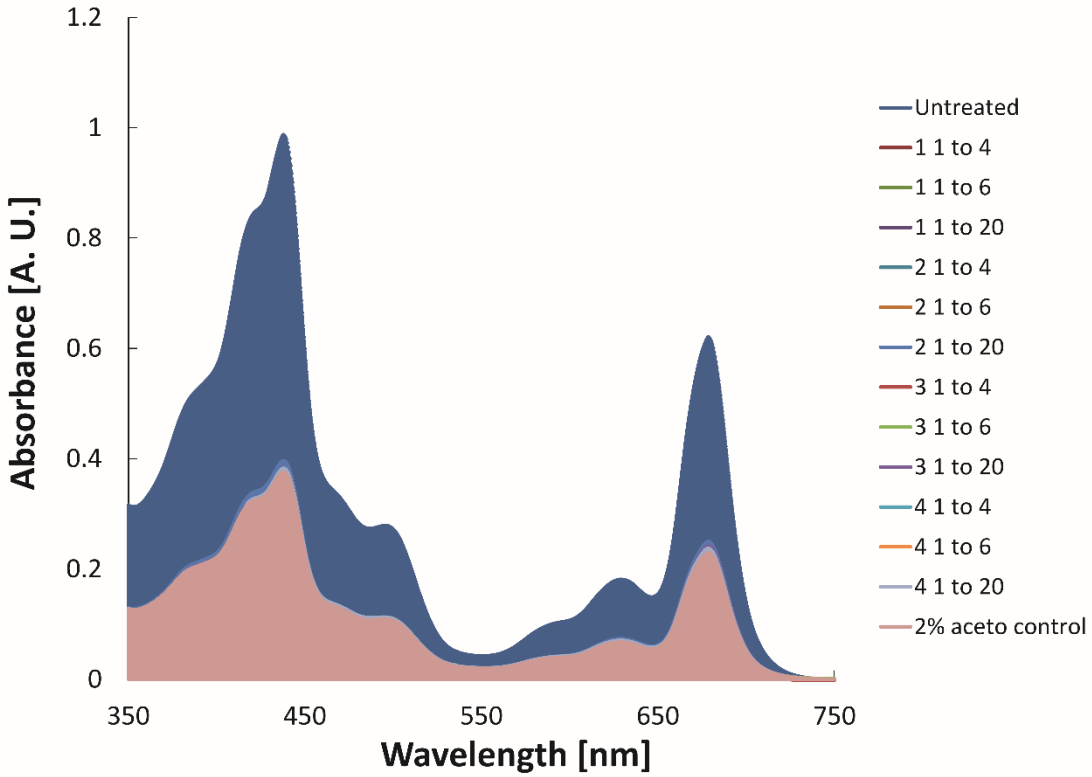

Figure 65

RT absorption spectra of hybridised PRC/PSI-LHCI samples. The untreated sample was measured at twice the concentration of Chl*a* to get a higher definition of the peaks, but all the other samples were found to be spectroscopically identical. Displayed on the right is the number of the compound (see **Figure 63**) followed by the PRC/PSI-LHCI molar ratio (see **Table 19**).

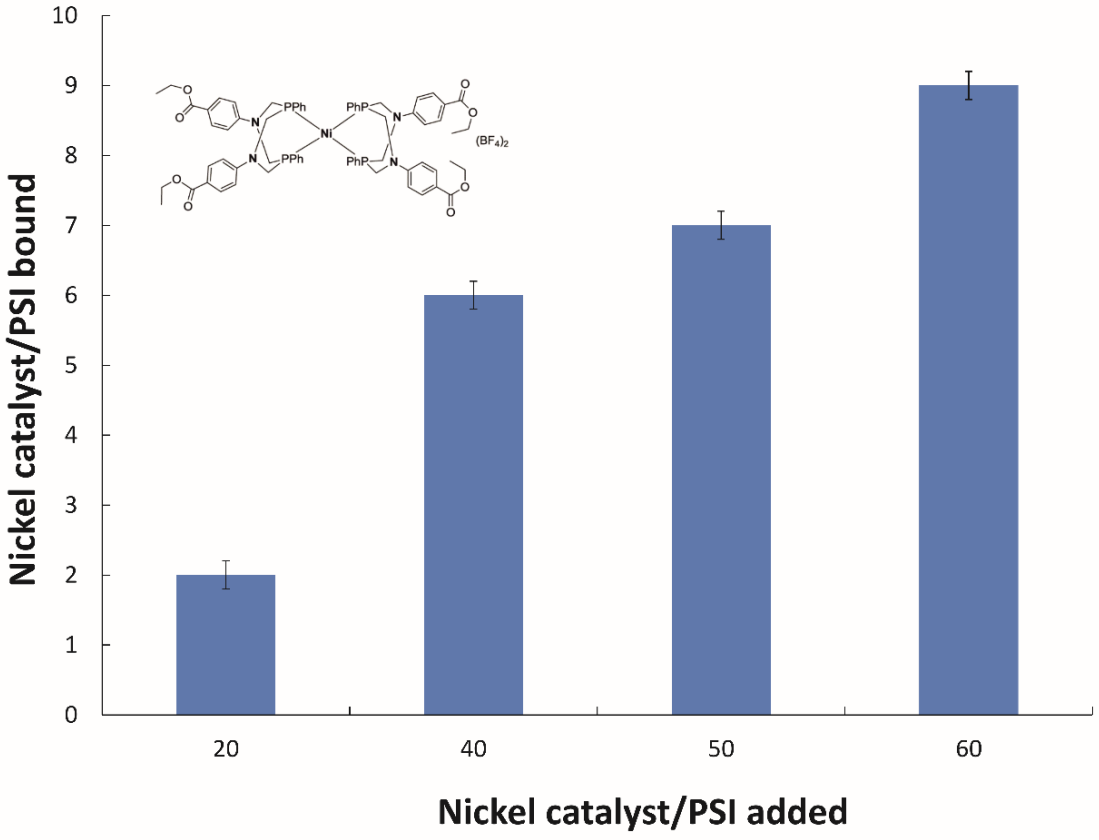

Figure 66

PRC catalyst #1 loading onto *C. merolae* PSI-LHCI. PRC:PSI-LHCI molar ratios were determined by ICP elemental analysis. This is a diagrammatic representation of the results shown in **Table 19**. The number of moles and the chemical structure of the catalyst are shown.

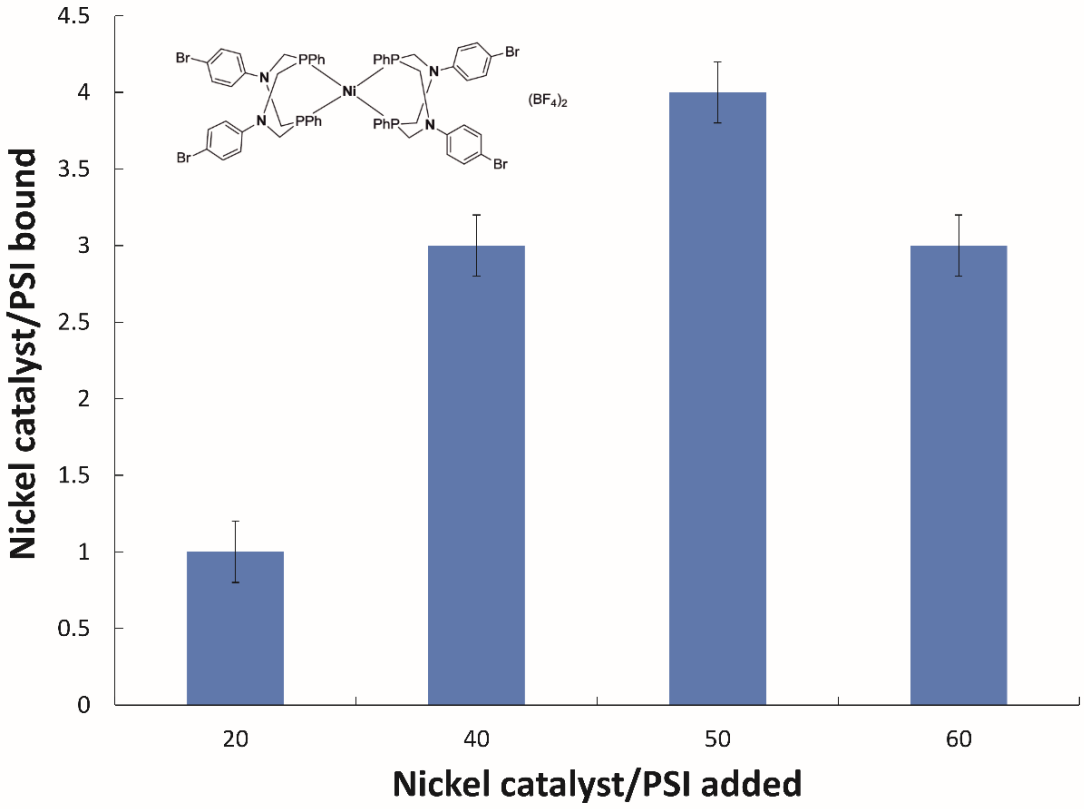

Figure 67

PRC catalyst #2 loading onto *C. merolae* PSI-LHCI. PRC:PSI-LHCI molar ratios were determined by ICP elemental analysis. This is a diagrammatic representation of the results shown in **Table 19**. The number of moles and the chemical structure of the catalyst are shown.

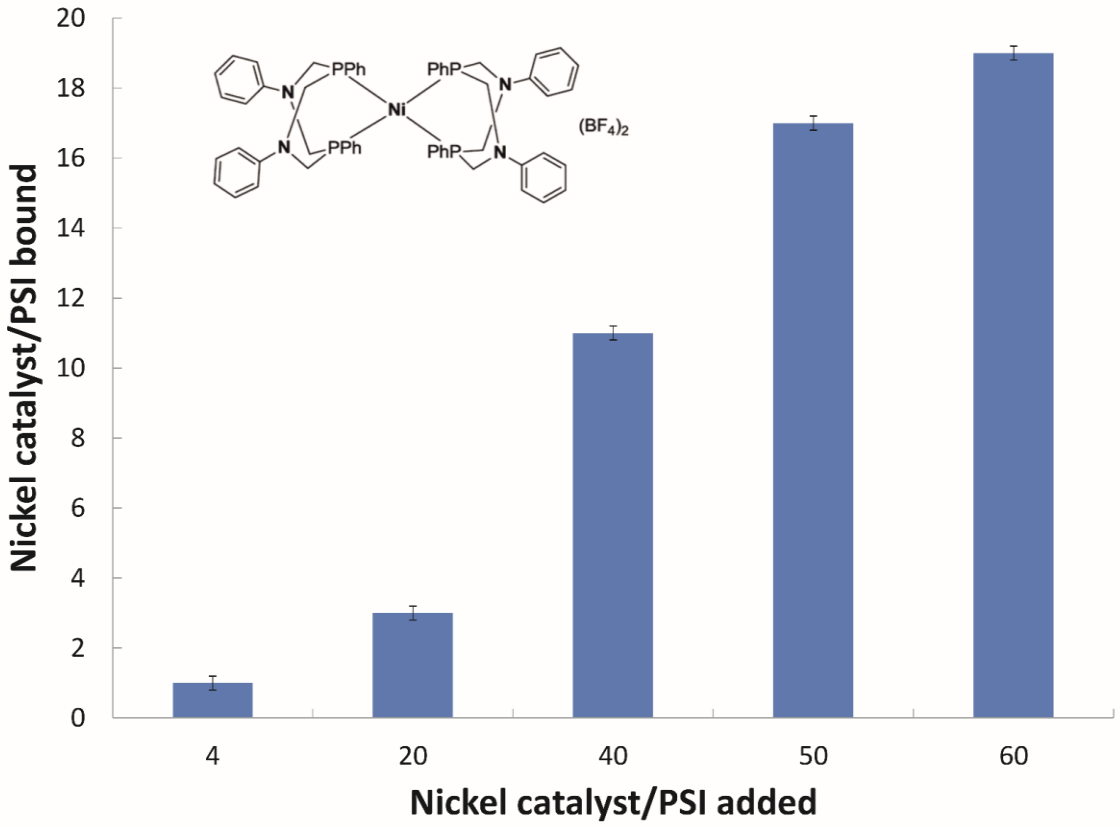

Figure 68

PRC catalyst #3 loading onto *C. merolae* PSI-LHCI. PRC:PSI-LHCI molar ratios were determined by ICP elemental analysis. This is a diagrammatic representation of the results shown in **Table 19**. The number of moles and the chemical structure of the catalyst are shown.

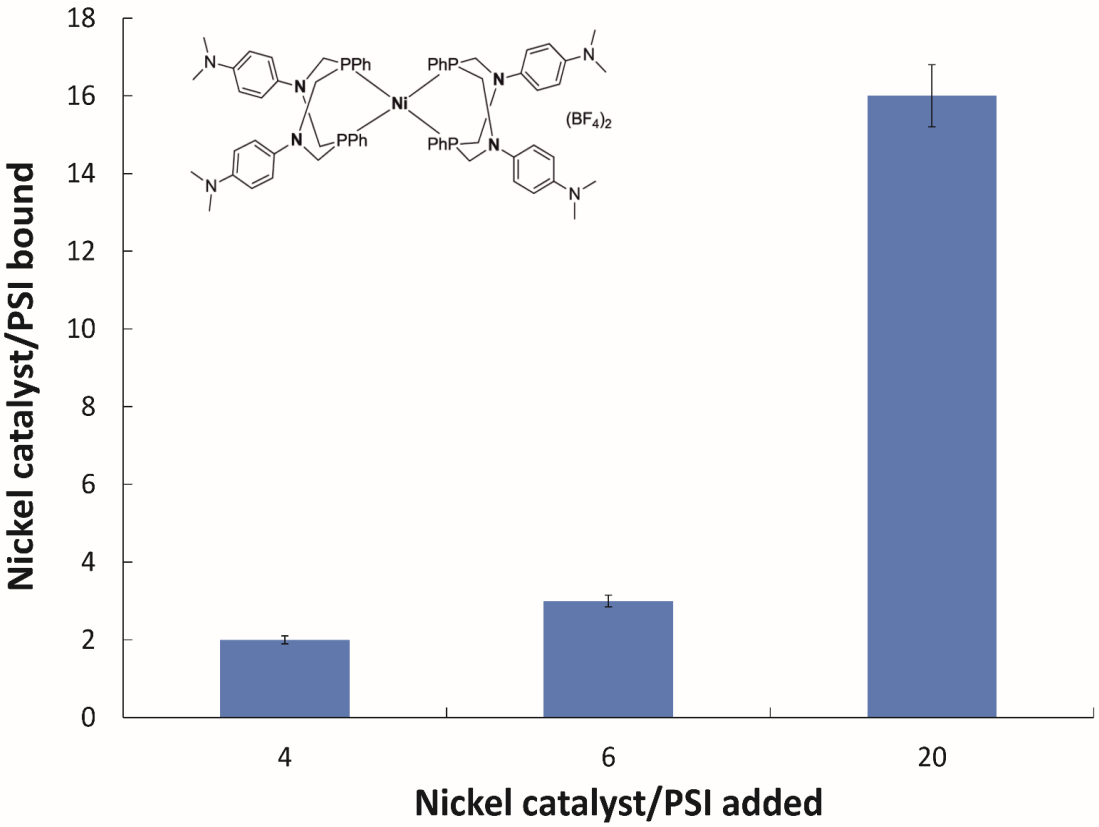

Figure 69

PRC catalyst #4 loading onto *C. merolae* PSI-LHCI. PRC:PSI-LHCI molar ratios were determined by ICP elemental analysis. This is a diagrammatic representation of the results shown in **Table 19**. The number of moles and the chemical structure of the catalyst are shown.

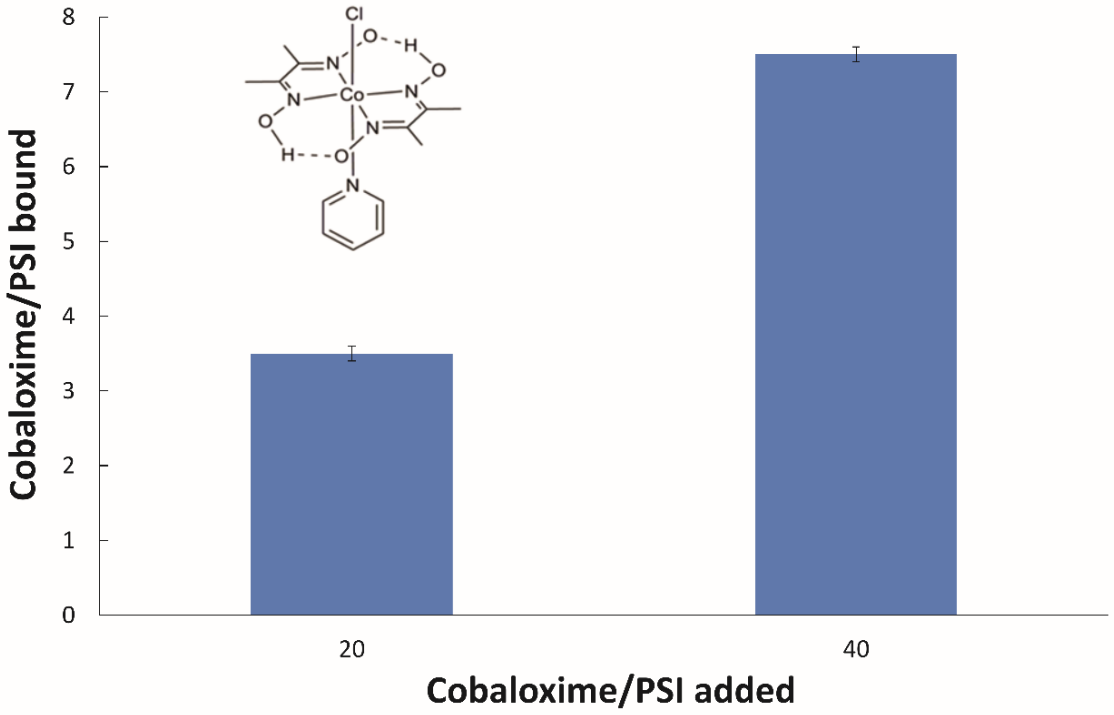

Figure 70

Cobaloxime loading onto *C. merolae* PSI-LHCI. PRC:PSI-LHCI molar ratios were determined by ICP elemental analysis. This is a diagrammatic representation of the results shown in **Table 19**. The number of moles and the chemical structure of cobaloxime are shown.

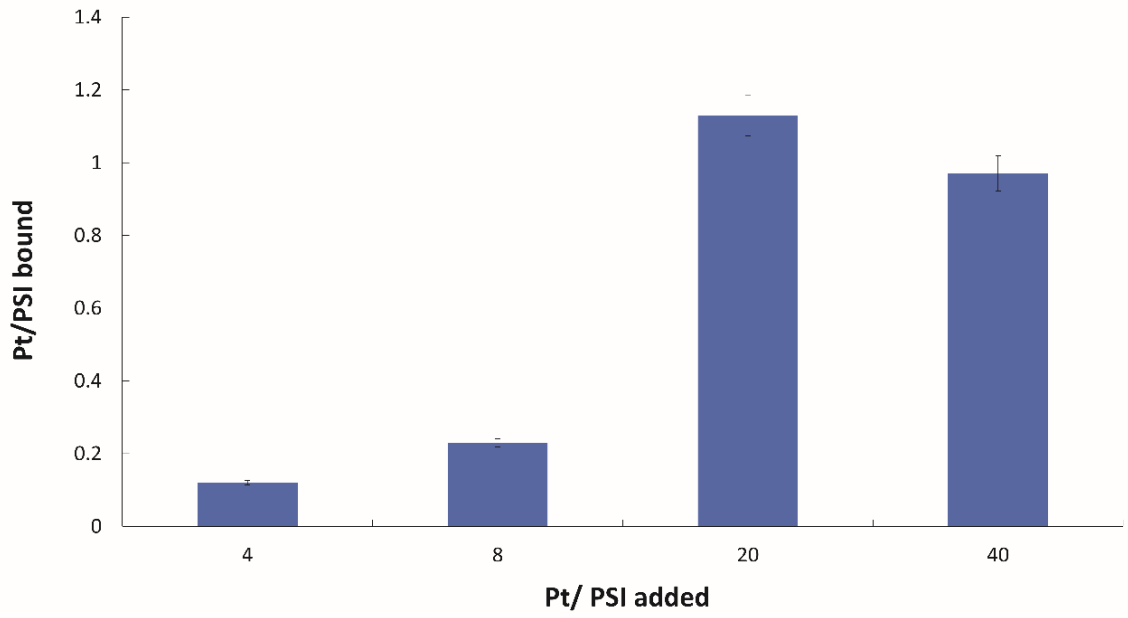

Figure 71

Platinum nanoparticle loading onto *C. merolae* PSI-LHCI. The ICP analysis determined approximately 1.0 ± 0.2 Pt nanoparticles per PSI-LHCI complex, even at molar excess of Pt used for hybridisation. The nanosphere is assumed to have an approximate diameter of ~3.0 nm as the protocol from [156] was reproduced. The number of moles is shown as per the previous figures. This is a diagrammatic representation of the results shown in **Table 19**.

4.3.3 Investigation of *in vitro* hydrogen production using PRC/PSI-LHCI hybrid complexes and cytochrome c_{553}

Following optimisation of the binding of the DuBois-type Ni catalysts, cobaloxime or Pt to PSI-LHCI complex, the photo-driven hydrogen production was investigated for the selected PRC/PSI-LHCI hybrid complexes obtained in this study. Typically, H_2 production reconstitution assays were composed of 60-100 nM given PSI-LHCI hybrid complex, 100 mM sodium ascorbate and 15-20 μM cyt c_{553} (10AA variant, see **Figure 72**). All the reaction mixtures were illuminated with a white light intensity of 8,130 μE m^{-2} s^{-1}. The catalysis was performed in an air-tight cell which was directly coupled to a gas chromatography (GC) system to determine *in situ* H_2 production.

As shown in **Table 20**, of all the PRCs tested only compound #2 and cobaloxime yielded measurable amounts of molecular hydrogen upon continuous illumination for up to 16 h. Interestingly, both the mononuclear Ni catalyst and cobaloxime were used at the same molar ratios for preparation of the PSI-LHCI hybrids. **Figures 73** and **74** display the total hydrogen yield obtained with these two types of PRC/PSI-LHCI hybrid complexes after 16 h continuous illumination with white light of 8,130 μE m^{-2} s^{-1}. They were determined as 100 μmoles and 140 μmoles of H_2 evolved over 16 h using 100 nM PSI-LHCI/cobaloxime and 100 nM PSI-LHCI/compound #2 PRC hybrid systems, respectively. The total TON values were 500,000 mol H_2 (mol PSI)$^{-1}$ and 700,000 mol H_2 (mol PSI)$^{-1}$, for the PSI-LHCI/cobaloxime and PSI-LHCI/compound #2 Ni PRC hybrid systems, respectively. The TOF values were 521 mol H_2 (mol PSI)$^{-1}$ min^{-1} and 729 mol H_2 (mol PSI)$^{-1}$ min^{-1} for the PSI-LHCI/cobaloxime and PSI-LHCI/compound #2 Ni PRC hybrid systems, respectively.

Importantly, the hydrogen production was absolutely dependent on the presence of cyt c_{553} in the reaction mixture (**Figure 75**), in agreement with the previous studies [130,140,192,195]. **Figure 75** shows that in the absence of cyt c_{553} no photo-induced H_2 production was detected with the PSI-LHCI/PRC hybrid system, employing the same conditions as those for **Figures 73** and **74**.

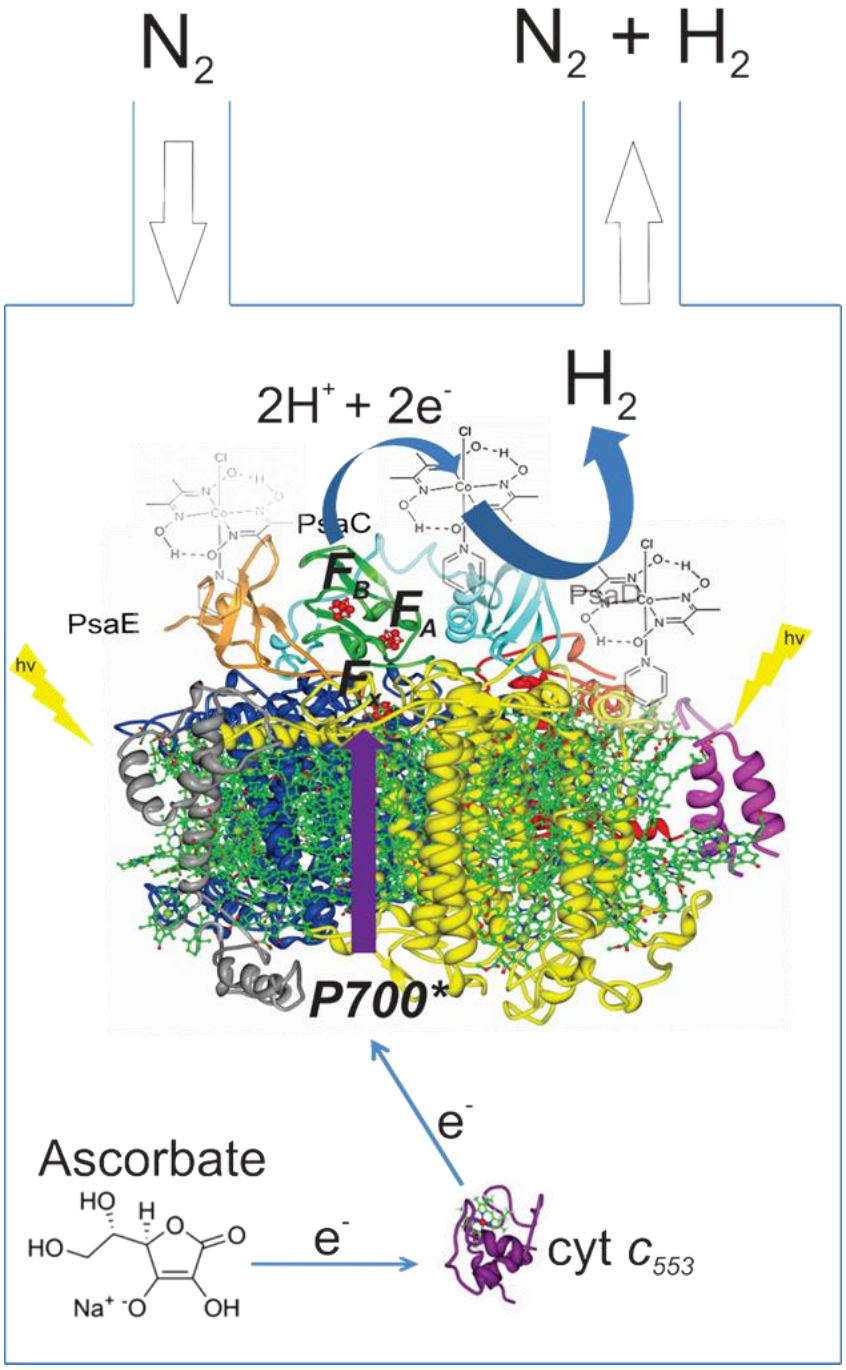

Figure 72

Diagrammatic representation of a typical *in vitro* hydrogen production assay using PSI-LHCI complex. The crystal structure of a *T. elongatus* PSI monomer is shown instead of PSI-LHCI from *C. merolae*, as no structure for the latter is currently available. As an example of a PRC, cobaloxime is shown in close proximity to the PsaE, PsaC and PsaD subunits, as it is believed to be in sufficient proximity of the F_B cluster to allow for an efficient turnover of proton reduction. In all the H_2 production assays of this study, the 10AA cyt c_{553} variant was used (see **Chapter 4.2**). Note, the components are not to scale.

Table 20

Photo-driven hydrogen production by PRC/PSI-LHCI hybrid complexes

Compound number	PSI-LHCI:PRC[1]	Hydrogen produced in the *in-vitro* reaction mixture[2]
1	1:20	TBD
1	1:40	-
1	1:50	TBD
1	1:60	TBD
2	1:20	TBD
2	1:40	+*
2	1:50	TBD
2	1:60	TBD
3	1:4	TBD
3	1:20	TBD
3	1:40	-
3	1:50	-
3	1:60	-
4	1:4	TBD
4	1:6	TBD
4	1:20	-
cobaloxime	1:20	TBD
cobaloxime	1:40	+
Pt	1:20	TBD

* data for a single assay due to the lack of readily available PRC.
TBD, to be determined, as the PRC was not available at the time of the experiments or the system presented technical limitations, as was the case for Pt.
[1]Molar ratios used for preparation of the PRC/PSI-LHCI hybrid complexes.
[2]The reaction mixture comprised 100 mM NaAsc, 15-20 μM cyt c_{553} and 60-100 nM PRC/PSI-LHCI hybrid, and was illuminated continuously for 16 h with white light of 8,130 μE m^{-2} s^{-1}.

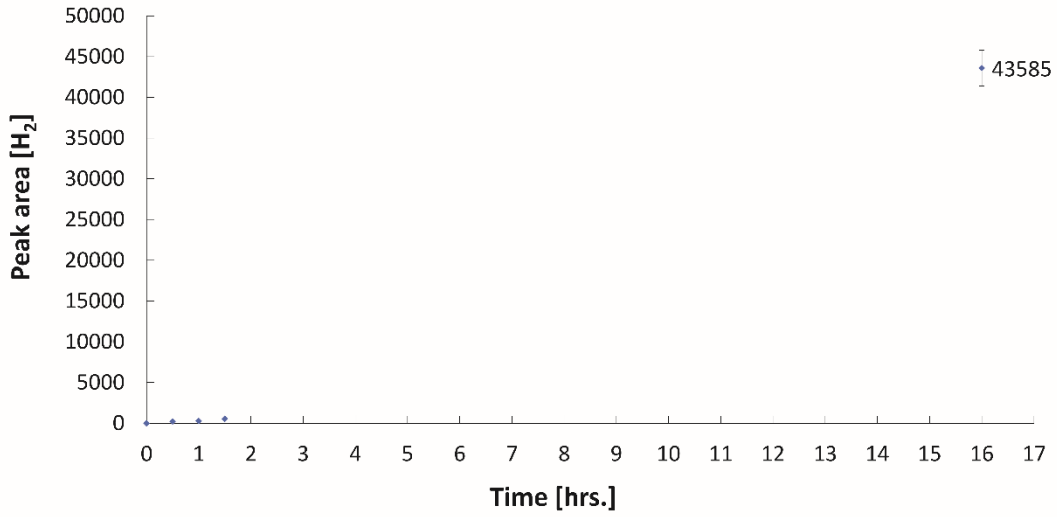

Figure 73

Hydrogen production with the PSI-LHCI/cobaloxime hybrid complex. The hybrid constituents were mixed at a 1:40 molar ratio for precipitation of cobaloxime onto PSI-LHCI (equivalent to 3-4 cobaloxime molecules per PSI-LHCI supercomplex). The reaction mixture contained 100 nM PSI-LHCI/PRC hybrid and 15-20 µM cyt c_{553}, added freshly before illumination. The TOF was 521 mol H_2 (mol PSI)$^{-1}$ min^{-1} during continuous illumination at 8,130 µE m^{-2} s^{-1} for 16 h. The peak area (*y*-axis) was determined by integrating the hydrogen peaks generated in the GC system; before each round of experiments the GC system was calibrated with a given volume (measured analytically) of hydrogen gas as a control. This calibration was repeated three times before the experiment to ensure reproducibility of the generated peak area and precision of measurements. Refer to **Chapters 3.2.8.4** and **3.2.8.5** for details.

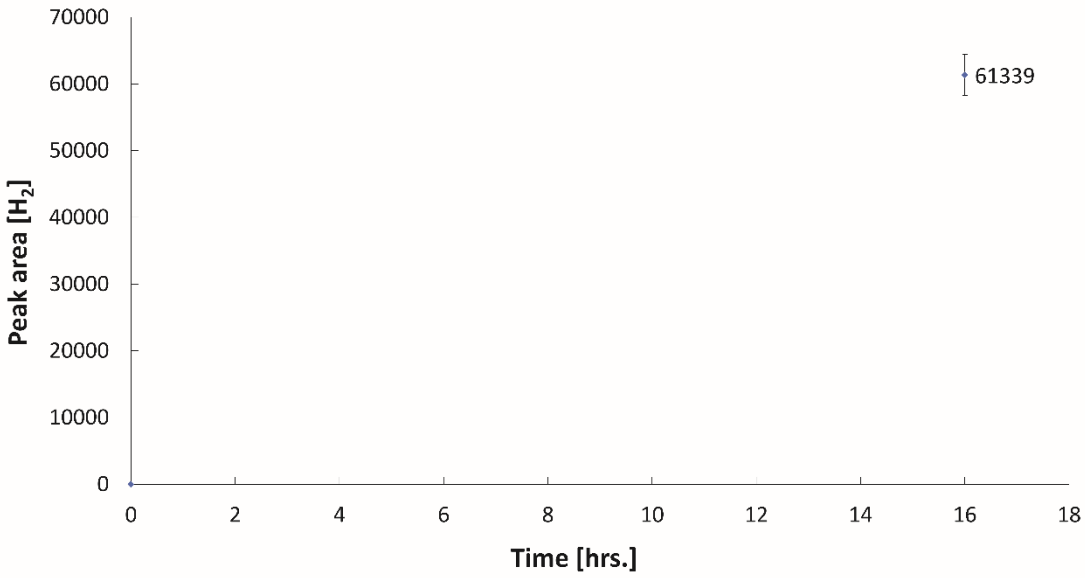

Figure 74

Hydrogen production with the PSI-LHCI/compound #2 hybrid complex. The hybrid constituents were mixed at a 1:40 molar ratio for precipitation of the PRC onto PSI-LHCI (equivalent to 3 PRC molecules per PSI-LHCI supercomplex). The reaction mixture contained 100 nM PSI-LHCI/PRC hybrid and 15-20 μM cyt c_{553}, added freshly before illumination. The TOF was 729 mol H_2 (mol PSI)$^{-1}$ min^{-1} during continuous illumination at 8,130 μE m^{-2} s^{-1}. The peak area (*y*-axis) was determined by integrating the hydrogen peaks generated in the GC system; before each round of experiments the GC system was calibrated with a given volume (measured analytically) of hydrogen gas as a control. This calibration was repeated three times before the experiment to ensure reproducibility of the generated peak area and precision of measurements. Refer to **Chapters 3.2.8.4** and **3.2.8.5** for details.

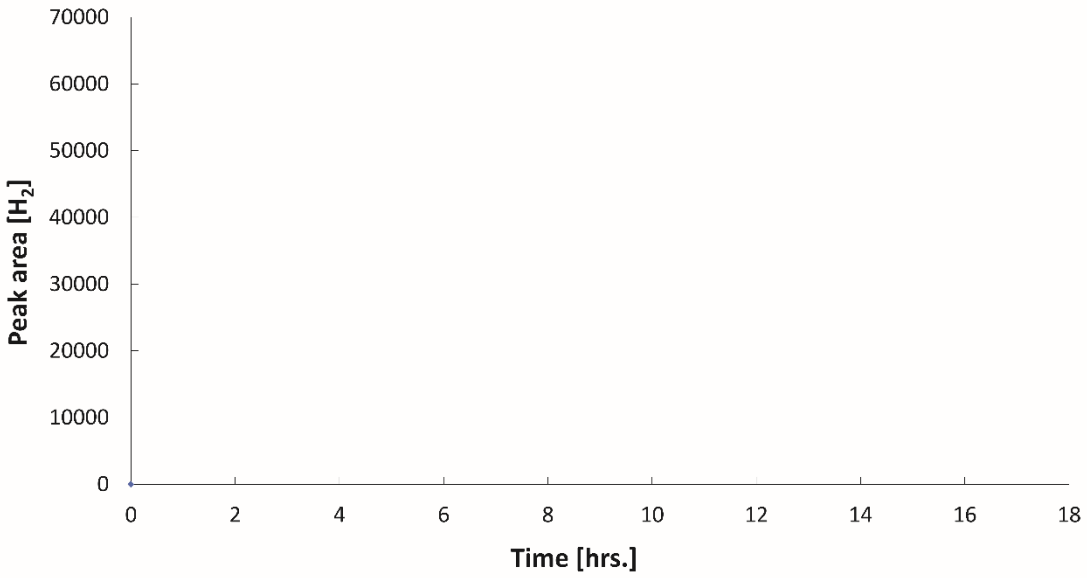

Figure 75

Lack of hydrogen production in the absence of cyt c_{553}. The hybrid constituents were mixed at a 1:40 molar ratio for precipitation of the PRC onto PSI-LHCI (equivalent to 3-4 PRC molecules per PSI-LHCI supercomplex, both for compound #2 or cobaloxime). The reaction mixture did not contain any cyt c_{553}. No photo-driven H_2 production was detected after 16 h of continuous illumination of the PSI-LHCI/PRC hybrid, following identical conditions as in **Figures 73** and **74**. The peak area (*y*-axis) was determined by integrating the hydrogen peaks generated in the GC system; before each round of experiments the GC system was calibrated with a given volume (measured analytically) of hydrogen gas as a control. This calibration was repeated three times before the experiment to ensure reproducibility of the generated peak area and precision of measurements. Refer to **Chapters 3.2.8.4** and **3.2.8.5** for details. The GC system was so sensitive that it can be assured that no hydrogen was detected.

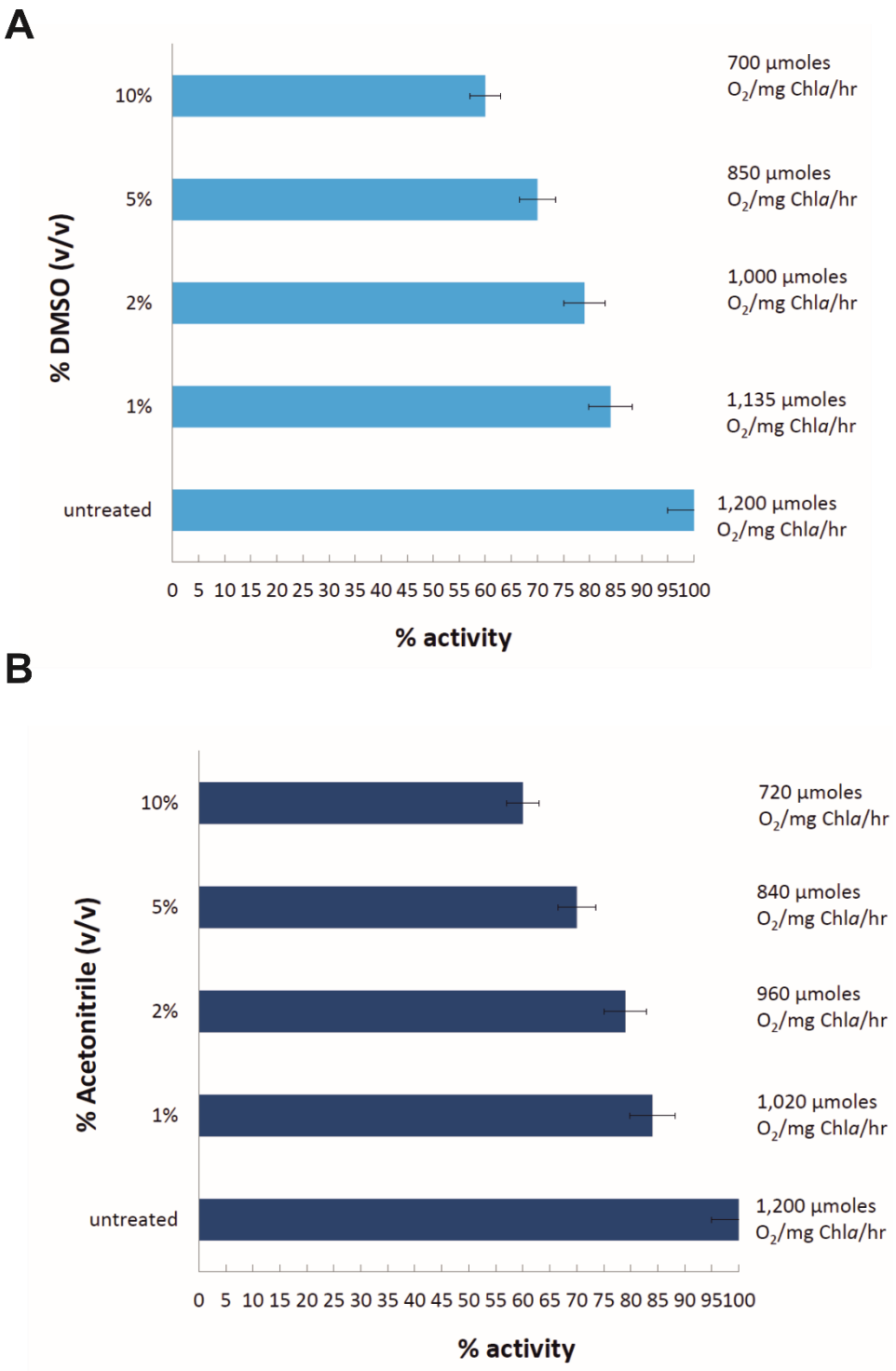

Figure 76

Photochemical activity of the *C. merolae* PSI-LHCI complex in the presence of the increasing concentration of acetonitrile and DMSO. The PSI-LHCI complex retains ~60% of its activity in the presence of 10% (v/v) organic solvents used for solubilisation of PRCs, similar to the activity measured in the presence of 10% dioxane (**Figure 45,** Chapter **4.1**) [139].

4.3.4 Concluding remarks: Hydrogen as a potential fuel of the future. Challenges for implementation of a hydrogen-based economy.

Although the results presented in this chapter are to some extent preliminary due to limited availability of some of the most promising PRCs, they present a potential 'green' alternative to produce molecular hydrogen as the solar fuel, using the simple biological components: photoactive robust PSI-LHCI complex and its natural electron donor, cyt c_{553}. In fact, the *C. merolae* PSI-LHCI complex is ideal for these purposes, as it can operate in extreme conditions and still retain nearly 100% of its photochemical activity [91], even in the presence of up to 10% organic solvents needed for dissolving the organic PRCs, such as dioxane [139] (**Figure 45**, **Chapter 4.1**), dimethyl sulfoxide (DMSO) (this study, **Panel A** of **Figure 76**) and acetonitrile (this study, **Panel B** of **Figure 76**). The ongoing work focuses on further optimisation of hydrogen production in this biohybrid system, including fine tuning of the catalyst loading, illumination intensity, and the pH of the reaction mixture. Nevertheless, this study provided a rigorous analysis of both the catalyst loading and amount of cyt c_{553} required for the sustained photo-driven H_2 production. Importantly, it demonstrated that a sufficient amount of cyt c_{553} is critical (**Figure 75**) for the proton reduction cycle to occur efficiently and continuously under prolonged, intense illumination. No hydrogen gas was produced in the absence of cyt $c_{553,}$ indicating that this electroactive protein is essential for biomediated electron transfer between the sacrificial electron donor (ascorbate), and the photooxidised P700 reaction centre of the PSI-LHCI/PRC hybrid complex (**Figure 75**).

To date, hydrogen can be produced as a solar fuel by photochemical water splitting through different strictly inorganic realisable approaches, such as homogeneous solutions and a variety of photoelectrochemical cells (PECs) and dye-sensitised photoelectrochemical cells (DSPEC) [113]. More pertinently, PSI-based hydrogen production has been attempted numerously in the past [66]. The H_2 production rates (TOF values) obtained in the present study were 3-fold and 16.6-fold higher than those published for cyanobacterial PSI/PRC hybrid systems employing cobaloxime [130] and a similar Ni mononuclear PRC [196], respectively. As mentioned previously in this thesis (**Chapter 1.3.3.1**) [66]), one of the limitations of employing in solution systems is "loss of electron transfer efficiency" due to electron diffusion in solution. Despite this inherent in-solution limitation, PSI-LHCI from *C. merolae* displays unprecedented robustness as it operates in such high light illumination intensity, specifically that of 8,130 $\mu E\ m^{-2}\ s^{-1}$, which is most likely the main reason for significantly higher TOF for H_2 production obtained in this study. This has not been reported

to date for its cyanobacterial counterpart (either monomeric or trimeric forms of PSI) and seems to be an inherent robustness of PSI-LHCI from this extremophilic red microalga [91].

As mentioned in **Chapter 1.3.3.1** and [66], the ideal hydrogen producing configuration should employ a semi-solid state or ideally and all-solid-state system. As shown in **Chapter 4.6**, all-solid-state configurations which incorporate PSI-LHCI are highly desired so as to maximise electron transfer competence to P700 and enhance the overall solar-to-hydrogen efficiency, resulting in ameliorated hydrogen yields. Heberle and colleagues reported a spectacular configuration, whereby they demonstrated that immobilising a PSI-[NiFe]-H_2ase (oxygen tolerant) on a gold electrode resulted in the impressive hydrogen production rate of 3,000 μmoles H_2 mg^{-1} Chl*a* hr^{-1} [135]. The work was revolutionary at the time, as it featured one of the first attempts to minimise the distance between the P700 reaction centre of PSI and the electrode surface, by employing IMAC technology (His_6-tagged PSI was chelated to a Ni-NTA functionalised gold electrode). Although the configuration was semi-solid-state (PMS was employed to relay electrons between gold and P700, as an artificial electron donating module to P700), it demonstrated rather elegantly that the key to enhancement of electron transfer competence lies in minimising the distance between the modules and matching redox potentials of the modules such the electron transfer chain/cascade is thermodynamically favourable [5,9,66,135]. Whether an oxygen tolerant H_2ase or a synthetic PRC is employed in conjunction with PSI or PSI-LHCI for hydrogen production, the key to enhancing hydrogen production rates and ultimately hydrogen production yield lies in minimising electron transfer diffusion by employing all-solid-state set-ups over in-solution-based systems together with more robust photocatalytical biohybrid systems [5,9,66]. As a matter of fact, the work from Heberle and co-workers [135] still holds the record for hydrogen production rate for a semi-solid-state PSI-H_2ase assembly to date [9,66,135].

The aforementioned efforts are still the object of intensive research; unfortunately, none has yet reached a technological development enabling market entry. The main bottlenecks encompass poor choice of redox compatible constituents, improper nanoarchitecture and instability and/or availability of the modules/materials [5,9,66] along with cost-effectiveness at the GW/TW scale [196]. Moreover, although attempts of PSI-based hydrogen production systems have been successful (this work, [130,135,140,192,195], scalability seems to be the culprit of severe technical limitations. Therefore, none of these attempts have been able to compete with current PEC, DSPEC and PV-electrolyser system technologies which have a much greater potential for scalability [113].

Currently, PEC cells cannot compete with PV-electrolyser systems [113]. Although PEC technology is still at its infancy, a life-cycle net energy assessment of a large-scale PEC hydrogen production facility has been attempted recently [197]. The data obtained give an approximate estimation of the dimension of the H_2 production effort. To make a 1 GW annual average plant, that means, 610 metric tons of H_2 per day, corresponding to the amount needed to power 0.62% of all the present light duty US vehicles and assuming a 10% solar-to-hydrogen efficiency, a PEC solar collection area of 41.1 km^2 would be needed (180 km^2 of gross facility land area) [197]. Scalability is also an issue, evidently. Different routes to obtain hydrogen by means of electricity production by PV cells have been followed by water electrolysis [113]. This technology is considered mature because both PV panels and water electrolysers have been commercially available for quite some time. Unfortunately, it is by no means cost effective. It has been shown that the electricity consumption accounts for more than 80% of the final hydrogen production price [198]. Hence, the initial investment costs for the electrolysis systems are less appropriate, as compared, for instance, to fuel cell systems. With an electricity price of 2.4 € kW h^{-1} (which is very close to the current electricity price in western Europe as of 2016 (slightly higher this year)), the production cost has been estimated to be 2.6 € kg^{-1} H_2, to be compared with the cost of hydrogen produced by steam reforming of methane, which is approximately 1 € kg^{-1} H_2 [198]. Recently, technological advances to reduce energy consumption of hydrogen production have been freshly overviewed [199].

Industrialising such a technology could potentially solve the following issues: (i) system engineering, (ii) materials and fabrication procedures and (iii) safety and environmental issues [200]. The number of power-to-gas plants that produce hydrogen from fluctuating renewable power sources is increasing, either using it for electricity generation or injecting it into the gas distribution system [201]. Most of them, however, have been in operation for a short time, unfortunately, so that long term experience is still lacking.

Even though PV-electrolyser systems are the most mature technology for H_2 production to date, research on PEC cells must be pursued, because it may very well have lower environmental impact and, in the long run, might be the most cost-effective solution [113]. If we leave aside the problem of hydrogen production, there are several other scientific and technological hurdles on the pathway to a hydrogen-based economy [113]. Perhaps the most challenging issue is, hydrogen storage for mobile applications [113]. Compared to hydrocarbons, hydrogen gas has good energy density by weight (33.3 kWh kg^{-1} *vs.* 13.9 kWh kg^{-1} for natural gas), but poor energy density by volume. To increase its volumetric energy

density, hydrogen may be liquefied (2.4 kWh L^{-1} at -253º C vs. 5.8 kWh L^{-1} of liquefied natural gas) but unfortunately, 30-40% of the energy content of the hydrogen is required for its liquefaction (See **Figure 61**). Moreover, insulation for liquid hydrogen tanks is usually expensive and problematic [113]. The preferred solution in most hydrogen cell prototype cars is hydrogen compression. Even at 700 atm, hydrogen has a 4.6 times lower energy content per volume than gasoline, which means that the hydrogen tank must be much larger. Moreover, compressed hydrogen tanks have to be cylindrical to ensure integrity under high pressure. Furthermore, this proves to be problematic as integration in a road vehicle remains a technical challenge. As shown in **Figure 61** and as discussed at the beginning of this Chapter, pure hydrogen gas (100% H_2) has the largest volumetric energy density value (280 kWh m^{-3}), compared to other forms of hydrogen fuel, making it the most desired form of hydrogen fuel for energy storage.

An alternative to address the storage issue is the employment of porous organic materials or by using metals or alloys that absorb hydrogen to form hydrides [202]. To be efficient, the absorption, desorption processes must be reversible, complete and fast—a challenging combination of demanding requirements. Moreover, hydrogen distribution, either in a centralised fashion (production in big plants and storage in relatively few locations) or in a decentralised fashion (production on site by distributed electricity) presents challenges [113].

An alternative route for fuel production involves the combination of CO_2 with hydrogen obtained through electrolysis from wind and solar energy to produce synthesis gas (syngas, a mixture of H_2 and CO). Syngas can then be converted into various types of synthetic fuels, such as methane, methanol, and dimethyl ether. Diesel and synthetic petrol may also be produced from syngas Fischer–Tropsch process (F-T) [113].

Solid proton conducting electrolysis cells (SPCECs) and solid oxide electrolysis cells (SOECs) may electrolyse not only H_2O, but also a mixture of H_2O and CO_2 to produce syngas [113]. Thence, by co-electrolysis of H_2O and reduction of CO_2, it is possible, in principle, to produce synthetic fuels from renewable energy, a rather viable approach that would avoid major modifications of existing infrastructure in the transport sector [113] (**Figure 77**).

In conclusion, with our current electricity prices, high-temperature electrolysis cannot compete with hydrogen production by steam reforming of natural gas. Nonetheless, FT-diesel can be produced by co-electrolysis of CO_2 and H_2O at a price that although higher than that of hydrogen produced by H_2O electrolysis is comparable with that of diesel obtained from fossil fuels, 1.1–1.2 € L^{-1} [113,198]. **Figure 77** displays a scheme of a solar-powered co-electrolysis

of H_2O and CO_2 yielding syngas that can be used to produce diesel fuel by the Fischer–Tropsch (F-T) synthetic process.

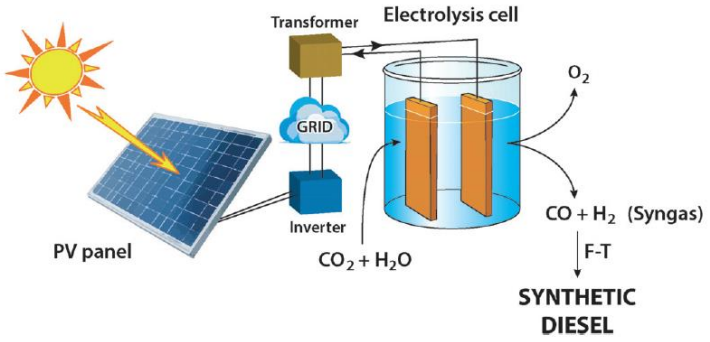

Figure 77

Scheme of solar-powered co-electrolysis of H_2O and CO_2 reduction, yielding syngas that can be used to produce diesel fuel by the Fischer–Tropsch synthesis. Reproduced from [113].

Chapter 4.4

Cytochrome c_{553} as a facilitator of plasmonic interactions between PSI-LHCI complex and silver nanowires

4.4.1 Introduction

Due to the unprecedented quantum yield of PSI-LHCI supercomplex (in terms of formation of the primary radical pair) and its extensive absorption cross-section, incorporation of this complex into state-of-the-art plasmon-generating nanostructures is highly desired for generation of novel biosolar cells and biophotosensors of improved efficiencies compared to existing non-plasmonic biophotovoltaic devices. In the case of biomimetic systems employing natural photosynthetic units, excellent progress has been made on improving their inherent optical and photochemical properties by nanoengineering of electromagnetic interactions between these natural light harvesting complexes and plasmon-emitting metallic nanoarchitectures [203–207].

For metallic nanoparticles with sizes in the range of the wavelength of incoming photons, localised plasmon resonance events occur, and these events can be used for modifying the optical properties of photoactive molecules located in their neighbouring vicinity. In particular, the efficiency of both absorption and emission may be influenced by plasmonic interactions [208,209], as well as intra-molecular energy transfer [210]. The nature of these rather fascinating and peculiar interactions between the plasmonic nanostructures and the photosynthetic modules depend strongly on their distance, and particularly, and as shown in this thesis, their geometry and order with respect to one another [209,211–215]. It has also been shown that in the case of complex multipigment-containing systems, such as natural photosynthetic complexes, plasmon excitations in metallic nanoparticles can activate emission of otherwise non-emitting Chl molecules [204]. This opens up a unique possibility to utilise metallic nanostructures as highly advanced nanotools for tailoring the function of naturally evolved photosynthetic complexes, especially in the context of construction of solar-to-fuel, solar cell and biosensor devices of improved efficiencies.

This chapter describes development of a novel approach for the controlled assembly of the *C. merolae* PSI-LHCI complex on silver nanowires (AgNWs) that yields the considerable improvement of the absorption cross-section of this light harvesting macromolecular complex. By orienting the PSI-LHCI complex *via* its native electron donor, the His_6-tagged cyt c_{553} protein on Ni-NTA functionalised AgNWs, an improved absorption

of this complex was achieved within the spectral range that is normally not absorbed by this photosystem. Moreover, no fluorescence quenching was observed for such novel nanoarrangements, which is normally not the case for this type of plasmonic-complex fluorophore nanoconstructs. Comprehensive spectroscopic studies, including fluorescence imaging, show clearly the scale of the absorption improvement, including the precise quantitification of fluorescence enhancement in such novel biohybrid plasmonic nanoarchitectures. In addition, time-resolved fluorescence measurements reveal almost complete homogeneity of the nanostructure fabricated using the cyt c_{553}-mediated bioconjugation, in contrast to the randomly oriented PSI-LHCI sample.

4.4.2 Photosynthesis and plasmonics

The intricate and inevitable ability of photosystems to absorb light and transfer energised electrons within their reaction centres have powered the research to employ natural photosynthetic light-harvesting modules in the vicinity of plasmonic nanostructures in order to investigate the effects of plasmonic energy transfer on the photo-physical properties of such nanobiohybrid structures. Recently, it has been demonstrated that the light-harvesting efficiency of Chls can be drastically enhanced by tuning the plasmon frequency of the constituent silver nanostructure (in this case silver island films) to coincide with the maximal photon flux of sunlight [216]. These findings demonstrate that the Chls interacting with plasmons can be even better light harvesting molecules around the red/infrared region than Chls that are unassisted by plasmons. The study serves as another example of how solar energy can be utilised more efficiently when a man-made nanomaterial system interacts plasmonically with a natural material system to improve functionality of the latter [216].

As seen in **Panel B** of **Figure 78**, the Time Correlated Single Photon Counting (TCSPC) decay curve demonstrates that the most efficient system investigated in the aforementioned study is that of a silver film interacting with a mixture of Chl*a*, as evidenced by the t_d/t_c ratio. In simple terms, Chl*a* molecules are assisted by plasmons resulting in energy transfer efficiency enhancement, as surface plasmons travel much faster in this particular system. These results are well in agreement with the results presented in this chapter, and particularly, they underline the importance of plasmonic interactions between Chl*a* fluorophores and metallic nanostructuctures to fine tune the optical properties of the light-harvesting pigments.

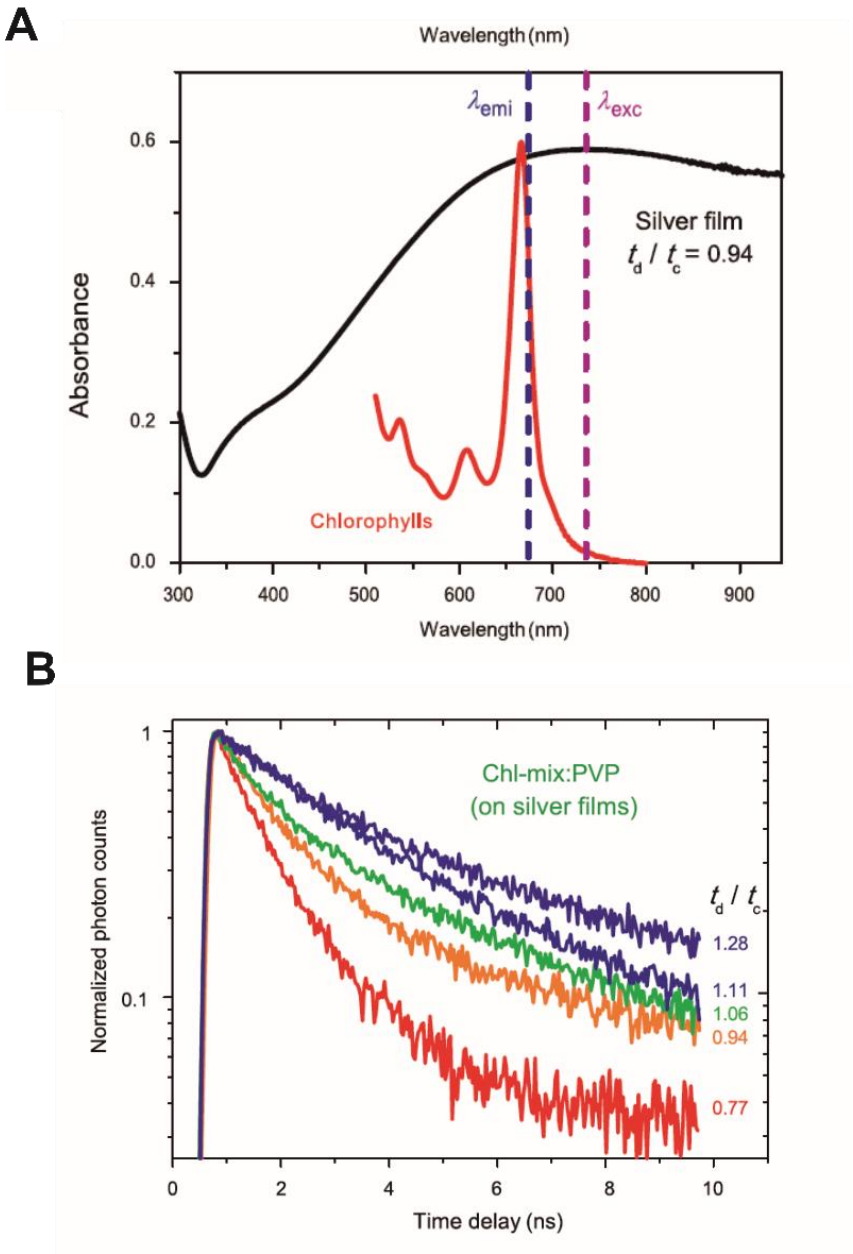

Figure 78

Absorption and time resolved fluorescence decay measurements of Chl/PVP films on silver. Reproduced from [216]. A: Dashed lines indicate a picosecond pulse laser excitation wavelength of 735 nm and Chl*a* emission wavelength of 675 nm. B: Normalised fluorescence decay curves of the Chl/PVP films on silver films with t_d/t_c = 0.77, 0.94, 1.11, and 1.28, respectively. The decay rate Γ reaches the maximum when λ_{SP} of silver film is around λ_{emi} = 675 nm (t_d/t_c = 0.77).

4.4.3 Plasmonic nanostructures

Although AgNW are an excellent example of plasmonic nanostructures, other nanostructures exist and have been widely employed for construction of plasmonic nanoarchitectures, including Ag spheres and Ag cubes [206].

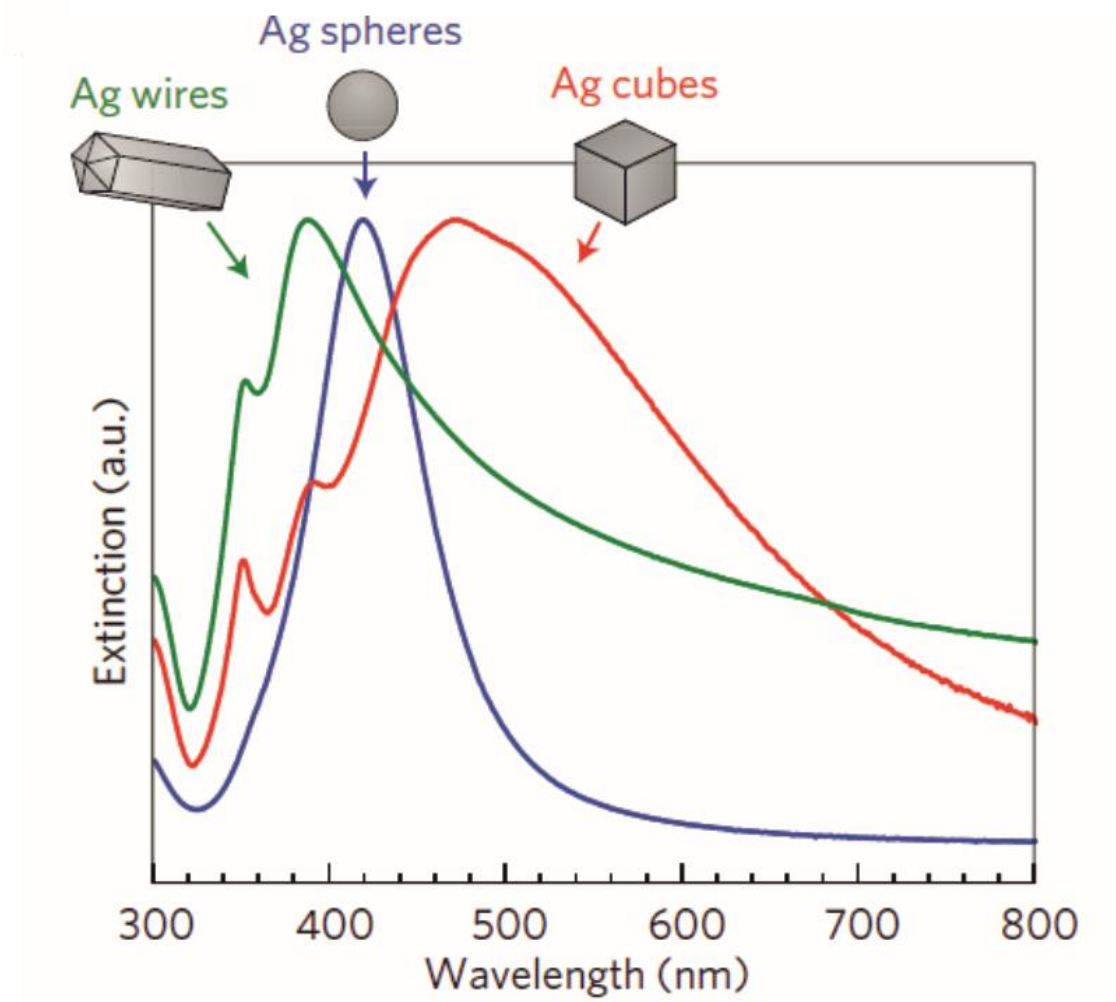

Figure 79

Normalised extinction spectra for Ag wire, cube and sphere nanoparticles. Reproduced from [206]. These particular nanowire-shaped particles are 90 ±12 nm diameter and >30 aspect ratio, cubic particles are 79 ± 12 nm edge length and spherical particles are 38 ±12 nm diameter.

Gold, silver and copper nanostructures exhibit resonant behaviour when interacting with photons in the UV and VIS spectral ranges [206]. Because a large fraction of the abundant solar flux consists of UV–VIS photons, these particular noble metals are of particular interest. The resonant wavelength and surface plasmon resonance (SPR) intensity depend not only on

the nature of the metal, but also on the size and shape of metallic nanostructures. By purposely manipulating the composition, shape and size of plasmonic nanoparticles, it is possible to design nanostructures that interact with the entire solar spectrum and beyond [206].

4.4.4 Generation of surface plasmons

Surface plasmons may be generated on any noble metal surface. One could think of surface plasmons as packets of energy travelling on the surface of a metallic surface, or metallic nanoparticle. These plasmons represent a collection of delocalised electrons travelling on top of the metal surface. As one electron pushes the neighbouring electron out of place, they travel together until they reach the end of the structure. The total excitation, including both the charge motion and associated electromagnetic field, is called either a surface plasmon polariton at a planar interface, or a localised surface plasmon for the closed surface of a small specifically shaped particle [217,218]. This could explain, incidentally, why excited silver AgNWs are brighter at the tips compared to the rest of the structure. Photons concentrate at the tips due to the nanoarchitecture of the wire and result in much stronger emission at the tips of the wires.

4.4.5 Improving functionality of photosystem I and its associated light harvesting antenna from *Cyanidioschyzon merolae* by the orientation-dependent plasmonic interactions with silver nanowires (based on *Szalkowski, Janna Olmos et al., Plasmon-induced absorption of blind chlorophylls in photosynthetic proteins assembled on silver nanowires,* under review)

Three different experimental configurations were generated in this study, including (i) PSI-LHCI supercomplex spin-casted on a glass substrate; (ii) PSI-LHCI supercomplex deposited onto Ni-NTA functionalsed AgNWs and (iii) PSI-LHCI supercomplex deposited onto cyt c_{553} bioconjugated Ni-NTA functionalsed AgNWs (**Figure 80, Panel B**). In brief, we wanted to investigate whether organised dispersion or organised recovering of PSI-LHCI around AgNWs would be beneficial for enhancement of emission particularly at a wavelength where PSI-LHCI absorbs poorly. Moreover, knowing that cyt c_{553}-P700 interaction is transient but very specific, we could qualitatively determine whether this interaction is strong enough so as to result in an organised nanoarchitecture of PSI-LHCI complexes recovering the cyt c_{553} bioconjugated Ni-NTA functionalised AgNWs. It is now well established that efficient electron transfer from cytochrome *c* to eukaryotic PSI depends on the PsaF subunit of eukaryotic PSI [219]. Although the cyt c_{553}-PsaF interactions are purely electrostatic, $P700^+$

is reduced with first-order kinetics and has a half-time of 3μs in the case of *Chlamydomonas reinhardtii* [219], a green algae which is a close relative of *C. merolae*, leading us to believe that the interaction might be intensified when the reaction centre is opened [149]. This was in fact the case, as presented in this chapter and could explain why the interaction was so stable, particularly upon illumination [149]. In order to assess whether energy transfer (in the form of surface plasmons on this occasion) was significant from the AgNWs to PSI-LHCI, we probed the entire three experimental configurations (see above, (i), (ii), and (iii), respectively) at two wavelengths; one wavelength was selected where PSI-LHCI absorbs strongly, and the other wavelength was selected where PSI-LHCI absorbs poorly yet the AgNWs have considerable absorption at this wavelength (**Figure 80, Panel A**). The two wavelengths were 405 nm and 535 nm, respectively (**Figure 80, Panel A**). If we detect strong emission at the latter wavelength, then we could conclude of course that energy transfer is enhanced and in fact most of the emission of the entire bioconjugated system comes from a spectral region where PSI-LHCI absorbs poorly (or more specifically this particular pool of Chls absorbs poorly), rendering the PSI-LHCI-AgNW hybrid suitable for enhanced emission and an excellent nanoconstruct for expanding the cross-section of the natural PSI photoconverter substantially.

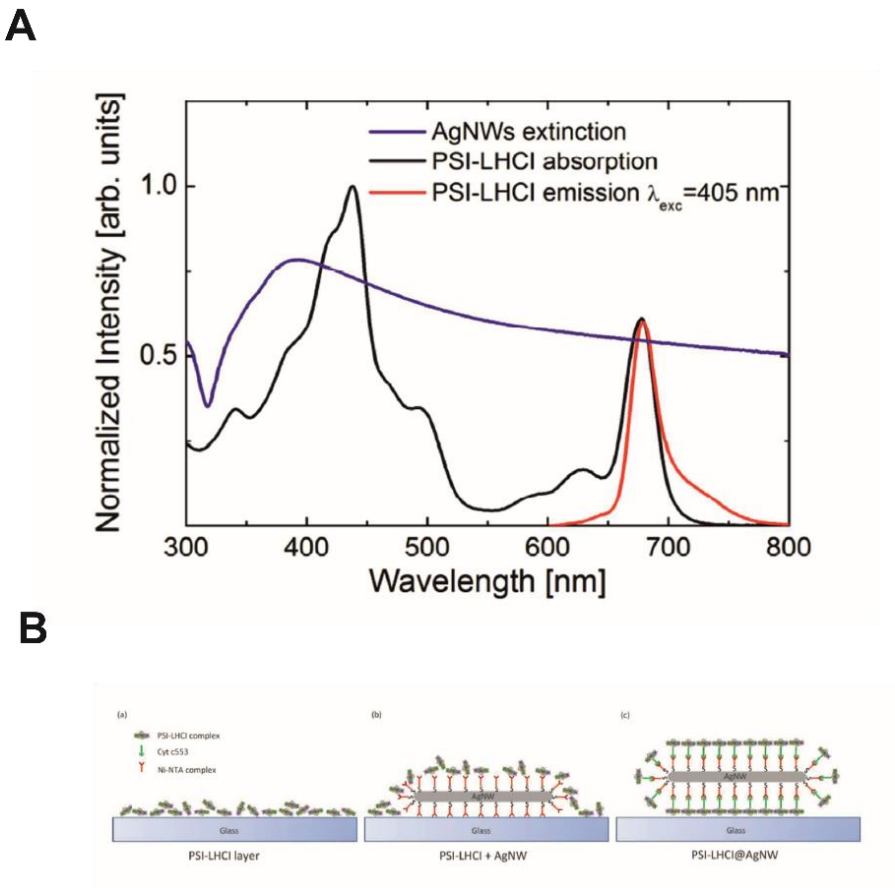

Figure 80

Absorption spectra of an aqueous suspension of AgNWs (blue) and buffer suspension of the PSI-LHCI complex (black) and architecture of investigated samples. A: The emission spectrum of PSI-LHCI suspension upon excitation at 405 nm is displayed in red. B: Architecture of investigated samples: (a) PSI-LHCI layer spin-casted on a glass substrate, (b) a layer of PSI-LHCI complexes deposited randomly onto the Ni-NTA functionalized AgNWs, and (c) PSI-LHCI complexes bioconjugated with the Ni-NTA functionalized AgNWs *via* a His_6-tagged cyt c_{553}. Note, that the diagrammatic representations are not to scale.

An illustrative example of a result for the PSI-LHCI-cyt c_{553}-AgNW experimental set-up is a nanoconstruct that was excited at 405 nm. Along the 5 µm nanowire, the surface plasmon polaritons could be observed along the wire and at the tips localised surface plasmons can be observed, as visualised by fluorescence of AgNW (see **Figures 81** and **82**). For optimisation of signal-to-noise ratio, various incubation time periods were investigated for conjugation of cyt c_{553}-functionalised AgNWs with the PSI-LHCI complex. **Figure 82** displays the distribution of fluorescence intensity along the bioconjugated AgNWs, measured

after excitation at 405 nm. After a 60 min. incubation period the highest value of fluorescence occurrences was observed upon excitation at 405 nm, with more than 600 counts detected (see **Panel C** of **Figure 82**). Therefore, this incubation time period was employed for all the subsequent analyses. The conclusions of this step of the investigation are summarised by **Figure 83**. As may be observed, emission at 535 nm was significantly higher for the nanoconstruct which incorporates cyt c_{553} compared to the nanoconstruct which lacks this plasmonic facilitator, indicating without any doubts that cyt c_{553} interaction is (i) sufficiently strong such as to place PSI-LHCI (specifically P700, as it is in close proximity to the PsaF subunit and the PsaF subunit interacts strongly with cyt c_{553} as aforementioned) in close proximity to the nanowire (according to our calculations the distance is approximately 7 nm, [149]) and (ii) the absorbtion cross-section of PSI-LHCI is undoubtedly and significantly expanded as the emission comes from a wavelength in which absorption is virtually blind for this photoconverter (**Figure 80, Panel A**).

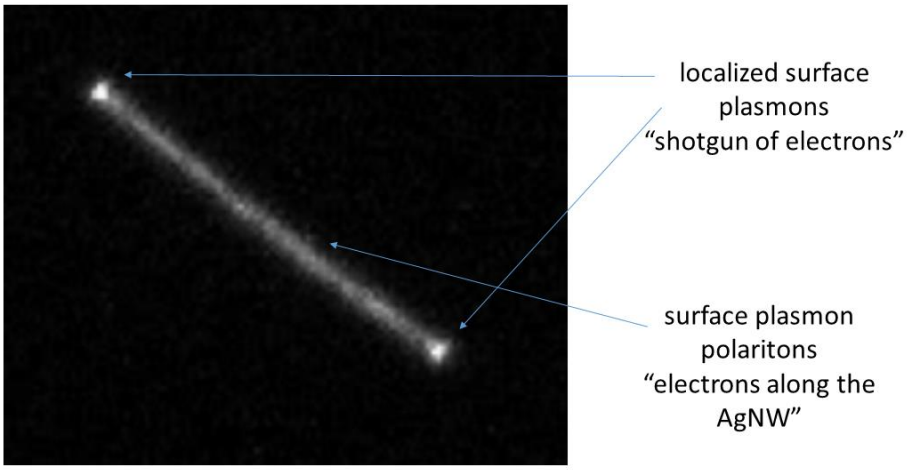

Figure 81

A representative micrograph of Ni-NTA-functionalised AgNW bioconjugated with *C. merolae* cyt c_{553} and PSI-LHCI complex following excitation at 405 nm. The distinctive qualitative shape and emission profile of all AgNW was similar, albeit with different AgNW length (this is normal, as it is very difficult to control homogeneously the length of the wires due to the nature of this metal which is quite brittle at this thickness). The distinctive shape and emission profile of all fluorescent AgNWs attests to the robustness and reproducibility of surface plasmon generation of noble metallic nanostructures, particularly silver nanostructures.

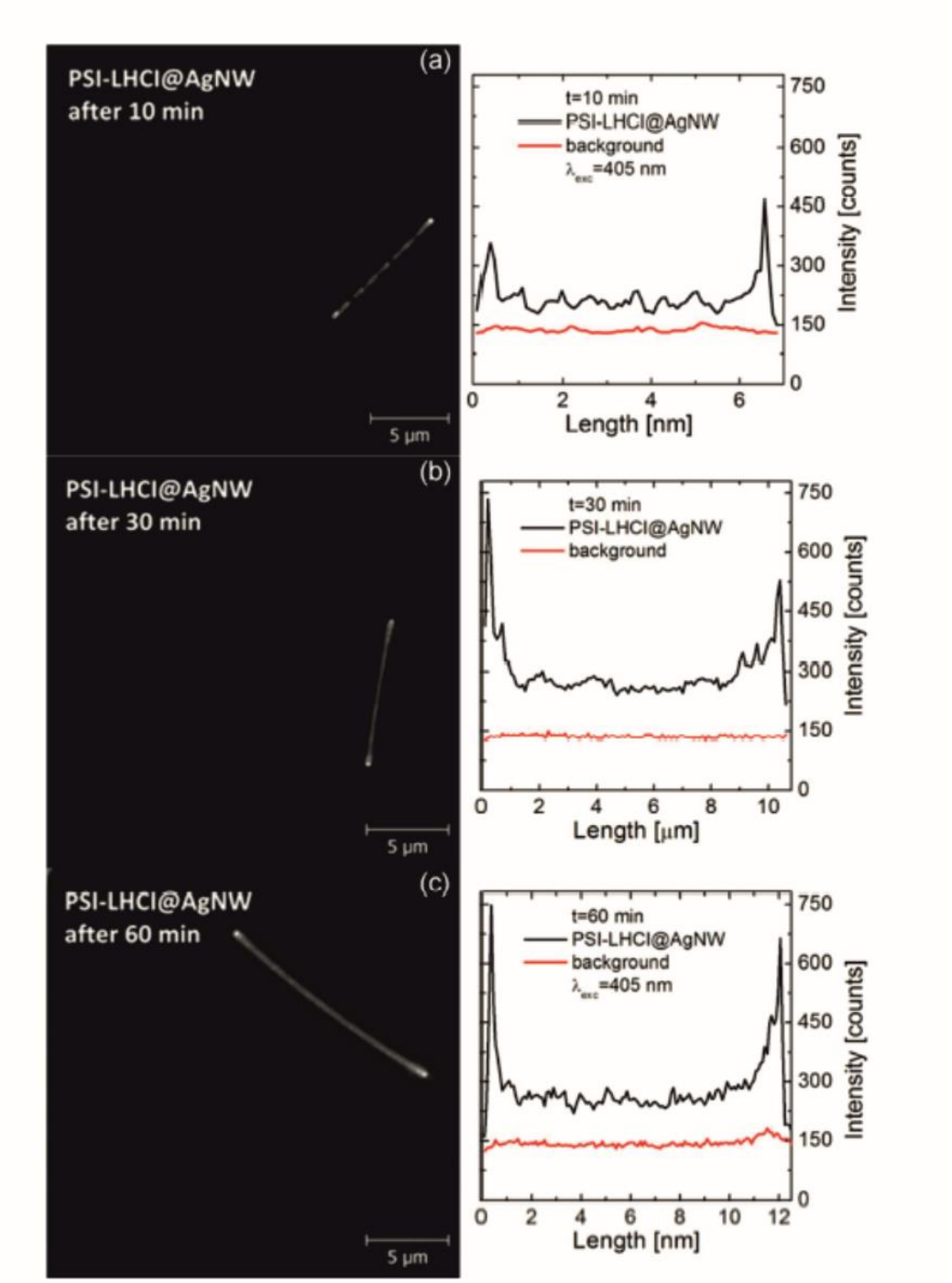

Figure 82

Fluorescence intensity maps the PSI-LHCI complexes conjugated with AgNWs *via* cyt c_{553} measured for 405 nm excitation over (a) 10 min. (b) 30 min. and (c) 60 min. incubation periods. Corresponding fluorescence intensity cross-sections are shown on the right.

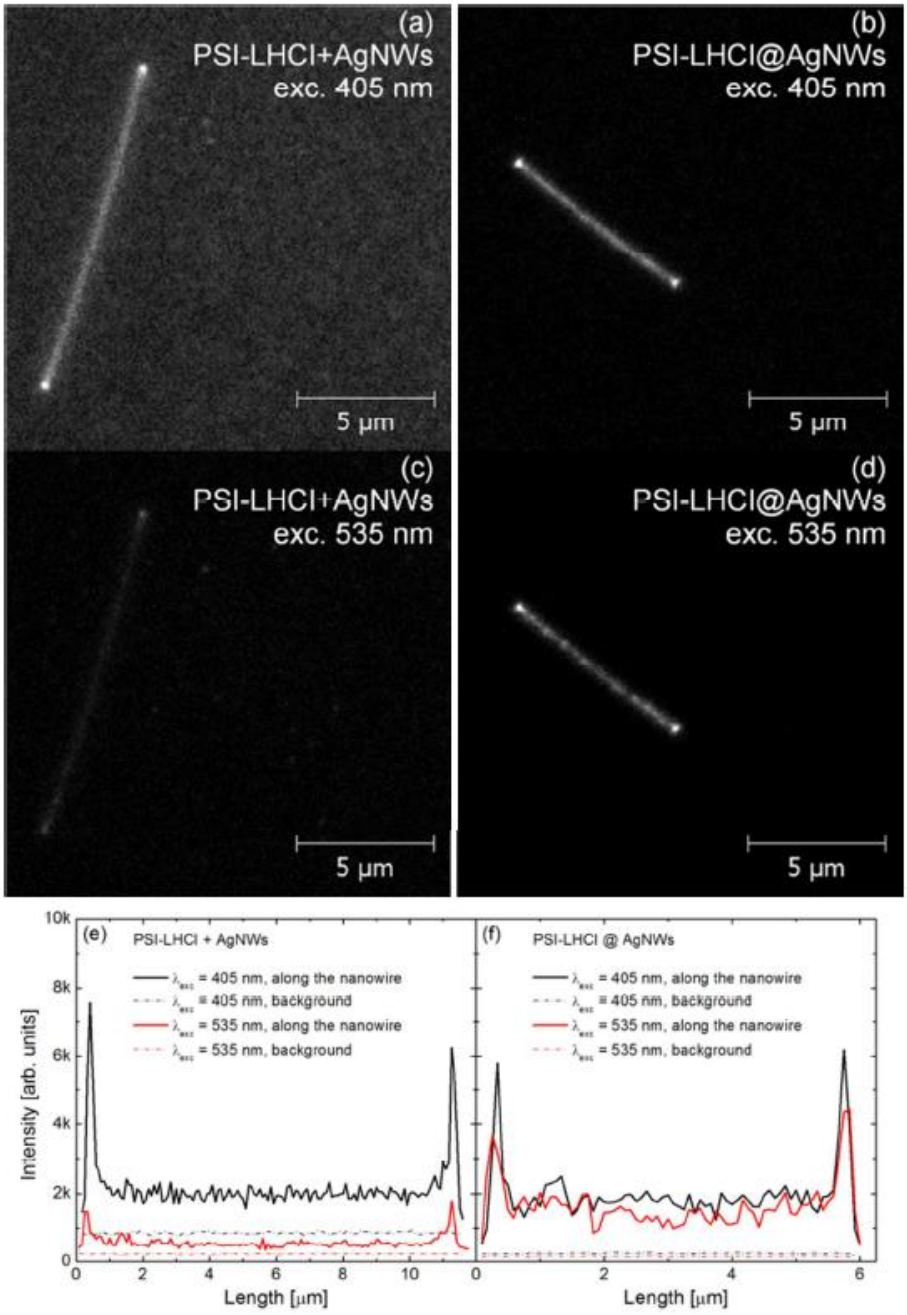

Figure 83

Fluorescence imaging obtained for PSI-LHCI+AgNWs (left column, a and c) and PSILHCI@AgNWs (right column, b and d). The images were obtained for the same nanowire in each structure for the excitation wavelength of 405 nm (a and b, respectively), and 535 nm (c and d, respectively). The cross sections along the nanowires are displayed in (e) and (f) for PSI-LHCI+AgNWs and PSI-LHCI@AgNWs, with black and red lines corresponding to excitation at 405 nm and 535 nm, respectively.

In order to investigate further the nature of this rather peculiar cyt c_{553}-PSI-LHCI interaction, the emission of the nanoconstructs was collected always at the tips and along the nanowires. The set of data, presented in **Figure 84, Panel A,** as a set of histograms, was obtained and processed. Two selected wavelengths, namely that of 405 nm and 535 nm, respectively, were selected for the reasons stipulated above. **Table 21** summarises the results of the histograms obtained by indicating the relative intensity of emission at these wavelengths. As can be distinguished from this table, the highest emission at 535 nm is achieved for the spatially well-organised nanoconstruct, when cyt c_{553} is present and had been previously chelated to the Ni-NTA AgNWs *via* its His_6-tag. Therefore, the lowest $<I_{em}405>/<I_{em}535>$ ratio was observed for the body and the tips of the bioconjugated AgNWs with the highest degree of organised nanoarchitecture of PSI-LHCI with respect to the plasmonic structures (PSI-LHCI/cyt c_{553}/AgNW). **Panel A** of **Figure 84** confirms this phenomenon and shows that the intensity at 535 nm is similar to that of 405 nm in the case of the organised PSI-LHCI/cyt c_{553}/AgNWs nanoarchitecture, as can be seen in sub-panel (f) and in agreement with **Table 21.**

Table 21

Average values of emission intensity of PSI-LHCI on glass, PSI-LHCI + AgNWs and PSI-LHCI@AgNWs nanoconstructs upon excitation at 405 nm and 535 nm

	PSI-LHCI on glass	**PSI-LHCI + AgNWs**		**PSI-LHCI@AgNWs**	
		along the AgNWs	at the ends of AgNWs	along the AgNWs	at the ends of AgNWs
$\mathbf{<I_{em}^{405}>}$	446.0	1755.0 (3.9)	5538.0 (12.4)	1605.0 (3.6)	5756.0 (12.9)
$\mathbf{<I_{em}^{535}>}$	70.0	340.0 (4.9)	1104.0 (15.8)	866.0 (12.4)	3305.0 (47.2)
$\mathbf{<I_{em}^{405}>/<I_{em}^{535}>}$	**6.4**	**5.2**	**5.0**	**1.9**	**1.7**

The respective enhancement factors, calculated with the assumption that PSI-LHCI forms a monolayer on glass, are given in parenthesis. The bottom row contains calculated ratios of the average emission intensity measured for 405 nm and 535 nm.

To finalise the study, we investigated the decay curves of the three experimental configurations by highly advanced ultra-sensitive TCSPC. Generally, measurements of fluorescence intensity are insufficient so as to determine alone the complex nature of the observed phenomena. Time-resolved fluorescence decay measurements can shine light onto

the excited state dynamics but also into special arrangements of the proteins relative to the AgNW structure [149]. Therefore, we examined the kinetic components of the PSI-LHCI fluorescence decay upon 485 nm excitation of the three different experimental configurations.

Panel B of **Figure 84** displays the representative normalised fluorescence decay curves (dots) as well as bi-exponential fits (lines). Fluorescence intensity decay of the PSI-LHCI layer on glass (green) exhibits bi-exponential behaviour, with the fast and slow components (0.35 ns and 4.1 ns). Interaction of PSI-LHCI with plasmonic excitations in AgNWs qualitatively changes the kinetics of fluorescence. In the case of the physisorbed sample (PSI-LHCI+AgNW) (purple fit), where no control over the distance between the AgNW and the supercomplex is present, we would expect either fluorescence quenching for the complexes that are in the proximity of the AgNWs, as well as substantially weaker interaction for the complexes that are more distal. This inhomogeneity results in: (i), considerable shortening of the fluorescence decay; and (ii), the presence of substantial contribution of fluorescence quenching (particularly by disorganised neighbouring complexes in an non-homogenous proximity) marked by a long decay constant. In stark contrast, the highly organised nanostructure (PSI-LHCI@AgNW) (grey fit) seems to exhibit the fast component of the fluorescence decay, with the slow component significantly weakened. Nonetheless, this fast decay component features no measurable reduction over the kinetics obtained for PSI-LHCI on glass [149]. These observations suggest that (i), for the highly organised nanoarchitecture the fluorescence enhancement can be mainly attributed to the increase of absorption cross-section of PSI-LHCI and (ii), most of the PSI-LHCI complexes attached to AgNWs in a spatially controlled fashion *via* cyt c_{553} interact in a similar way with plasmonic excitations. These observations leads us to believe that Chls present in the periphery of the LHCI antenna, might be interacting with each other from PSI-LHCI to PSI-LHCI. Particularly, this could be the case for specialised Chl pairs, quite possibly red Chl pairs indetified in the LHCI antenna, as stipulated in the latest crystal structure of the eukaryotic super complex (603a-609a red Chl pairs) [3] (See **Chapter 1.2.3**). Moreover, this could also explain why no fluorescence quenching is observed in this particular configuration; red Chls might function as “energy tuners” impeding quenching and maximizing energy transfer.

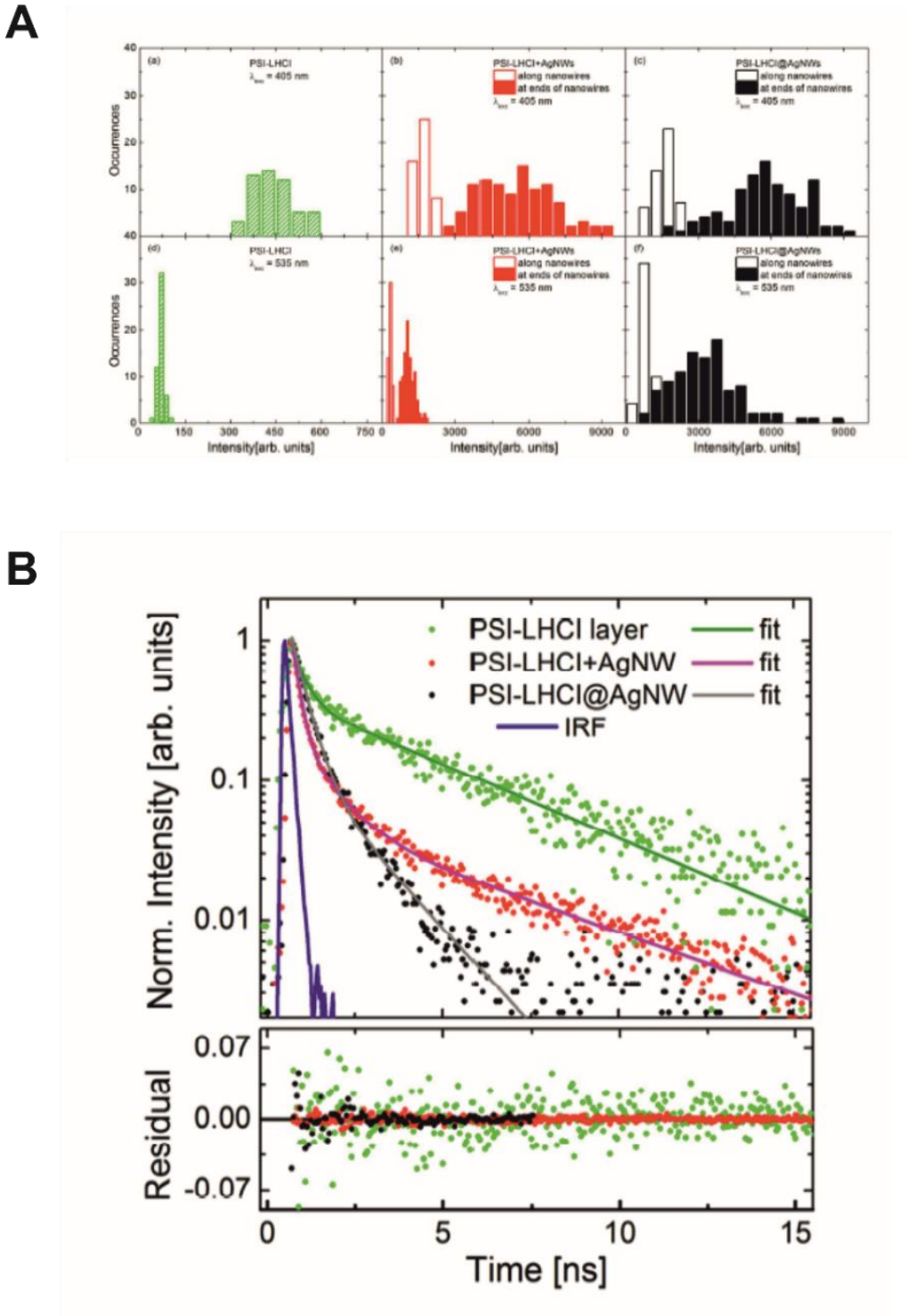

Figure 84

Histograms of fluorescent intensity and TCSPC decay curves for all the investigated experimental configurations of bioconjugated AgNWs. A: (a) Histograms of fluorescence intensity for the PSI-LHCI layer on glass, (b) PSI-LHCI + AgNWs, and (c) PSI-LHCI@AgNWs structures following excitation at 405 nm. Analogous results measured for excitation at 535 nm are shown in panels (d)-(f). Intensities along the nanowires and at their

ends are shown in empty and filled bars, respectively. B: Fluorescence decay curves measured with the excitation at 485 nm for PSI-LHCI layer on glass (green), PSI-LHCI physisorbed on AgNWs (red), and PSI-LHCI bioconjugated with AgNWs (black) together with fitted decay curves and residual plots. IRF, Internal Reflective Factor.

Figure 85 shows the level of occurrences *vs*. the ratio of fluorescence intensity at 405 nm compared to fluorescence at 535 nm. As observed in **Panel A** of **Figure 80**, PSI-LHCI absorbs very poorly at 535 nm. **Figure 85** abridges succinctly the results, as it shows that the ratio of I_{405}/I_{535} is significantly lower (by more than a factor of 2.0) when the nanoconstruct employs cyt c_{553} as a plasmonic cofactor between the Ni-NTA functionalised AgNW and the PSI-LHCI complex. This means that the emission at 535 nm is indisputably much higher, which means that the absorption cross-section of PSI-LHCI in this rather organised nanoarchitecture is significantly enlarged. Moreover, as the complex is normally non-absorbing at this spectral region, it strongly suggests that a non-absorbing pool of Chls is activated in this macromolecular organisation. As stipulated above, this could also explain why energy transfer from 603a-609a red Chl pairs to other adjacent pairs of neighbouring PSI-LHCI complexes could occur. Although this is hypothetical and requires direct verification, it could in principle explain emission at this normally non-absorbing wavelength (see above).

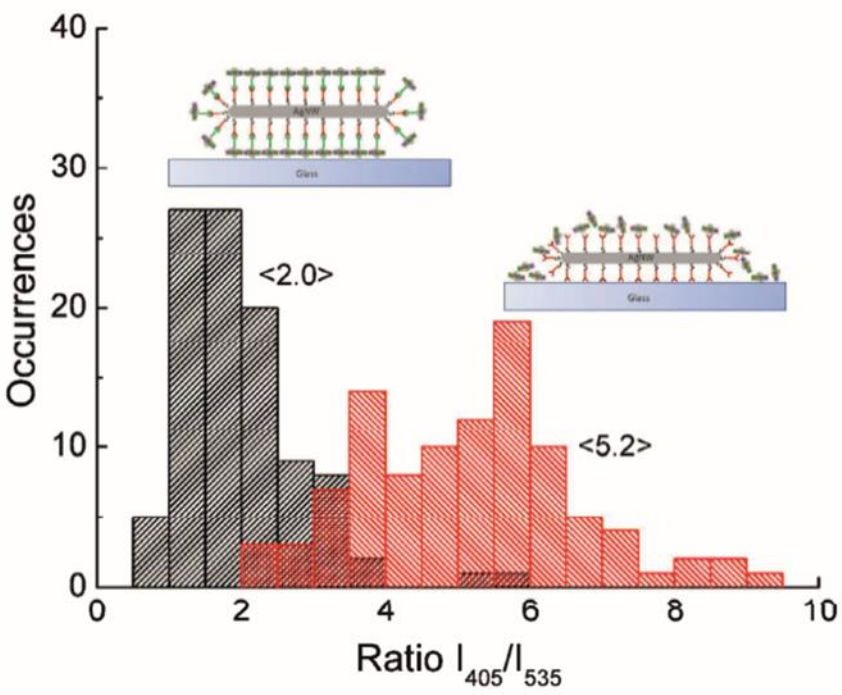

Figure 85

Novel highly organised plasmonic nanoarchitecture is generated by site specific conjugation of PSI-LHCI with silver nanowires *via* cyt c_{553}. The values in brackets correspond to the calculated ratios of the average emission intensity measured at 405 nm and 535 nm. The light harvesting properties of PSI-LHCI are improved by plasmonic interactions, whereby absorption at 535 nm of otherwise non-absorbing pigments is significantly enhanced only when a uniform orientation of this light harvesting/charge separating complex is maintained by the specific interaction with cyt c_{553}.

4.4.6 Concluding remarks

This chapter describes the construction of the novel biohybrid system through the controlled assembly of eukaryotic PSI-LHCI complex on plasmonically active AgNWs through application of the His_6-tagged cyt c_{553} monolayer formed as the bio-interface between both modules. In this configuration, cyt c_{553} may be considered as a "plasmonic facilitator" or "plasmonic cofactor." By comparing fluorescence intensities measured for PSI-LHCI complex randomly oriented on AgNWs and the results obtained for the organised PSI-LHCI-cyt c_{553} bioconjugate with AgNWs it was concluded that the specific binding of photosynthetic complexes with defined uniform orientation yields selective excitation of a pool of Chl molecules that are otherwise non-absorbing. This discovery shows for the first time, that

plasmonic excitations in metallic nanostructures can not only be used to enhance native absorption of photosynthetic pigments, but also – by utilising cyt c_{553} as the conjugation cofactor – to activate the specific Chl pools which are otherwise effectively non-absorbing in PSI-LHCI. As absorption of PSI alone is relatively low, this approach lends itself as an innovative approach to outperform the reported-to-date biohybrid devices with respect to solar energy conversion.

By specific conjugation of photosynthetic complexes on plasmonically active metallic nanoparticles we have shown that the control of distance and orientation of PSI-LHCI complexes with respect to the AgNWs allows for selective and concerted excitation of Chl fluorophore subpopulations yielding the innovative fluorescence properties of this complex. Tuning of energetic properties of these subpopulations, possibly of a subpool of red Chls, results in an increased light harvesting functionality of the PSI-LHCI supercomplex. This means that it is possible to extend the active absorption spectral range by engineering plasmonic interactions within highly ordered and oriented light harvesting/electroactive geometries. Interactions within such plasmonic/light harvesting nanostructures may thus be considered, in this context, as a powerful tool for "improving nature," particularly with the ultimate purpose of constructing efficient solar-to-fuel nanodevices, biosolar cells, (bio)medical devices and biosensors that would absorb a specific wavelength or at a wavelength range. Significantly, the native electron donor of PSI-LHCI, cyt c_{553}, specifically from the same organism, was employed in this work for the first time as the bioconjugating electroactive protein that allowed for a uniform orientation of the PSI-LHCI complex with the P700 specilized Chl*a* pair oriented towards the plasmonic nanostructure. In this way, oriented nanoarchitecture of PSI-LHCI complexes enhances the specific plasmonic interactions that ultimately improved functionality of PSI-LHCI itself, providing a proof-of-concept that increasing light absorption efficiency of this complex is feasible in an artificial leaf by application of plasmonic nanostructures.

Chapter 4.5

Application of cytochrome c_{553} in the *p*-doped silicon biophotoelectrode for the improved direct electron transfer

4.5.1 Introduction

The main limitation of the present-day biomimetic approaches for generation of electricity and solar fuels in a viable manner is their low solar-to-hydrogen quantum efficiency (well below 1%) [129,139,220–225]. The low efficiency of the biohybrid PSI-based solar cells is mainly due to the recombination of photo-excited electron-hole pairs that takes place at the interfaces of the electrode modules, rather than being limited by the PSI itself. The main reasons for such low output are losses due to diffusion-based electron transfer in such devices and wasteful reactions of charge recombination/short circuiting of electron transfer in the working modules and at their interfaces. Therefore, it is important to develop rational approaches to overcome the latter limitations. This Chapter describes one of such approaches, namely biopassivation of the *p*-doped Si substrate with the electroactive cyt c_{553} protein.

There is a precedent in the literature showing that different lengths and 3D structures of AA linkers that connect the electroactive proteins, such as ferredoxin, with photoactive components such as PSI result in varied electron transfer rates [226]. It has been shown that engineering different AA linkers of varying lengths within ferredoxin, a native electron acceptor of PSI, and linking this protein in the vicinity of the PsaC subunit on the acceptor side of PSI results in enhanced electron transfer rates in the linker-dependent manner [226]. Using a similar rationale, in this PhD project a working hypothesis was put forward to test whether the AA linker peptides that were engineered between the cyt c_{553} holoprotein and its *C*-terminal His_6-tag (see **Chapter 4.2**) can enhance electron transfer rates between the haem group of cyt c_{553} and $P700^+$ reaction centre within the all-solid-state state biophotovoltaic devices. The rationale behind this hypothesis was that depending on the length and even structure of the peptide linkers a varying degree of movement of immobilised cyt c_{553} may influence the kinetics of electron transfer between the semiconductor substrate and the photoelectroactive modules of the biophotoelectrode.

Si photovoltaics is the most mature solar-to-electric technology to date, and it carries great potential for generation of cheap renewable energy from sunlight. With over 80% of the current solar energy market and a growth rate exceeding 40% p.a., Si solar cells have the potential to make a substantial contribution towards meeting the globally increasing energy demand [113,118,227]. The global share of Si-based technologies in photovoltaics has increased from about 80% in 2009 to more than 90% in 2014 [113]. There is no risk of Si shortage in any foreseeable future as it is the second most abundant and evenly distributed element in the earth's crust [113]. Incorporation of Si-based photoelectrodes that are sensitised with natural light harvesting proteins, such as PSI, into the solar-to-fuel devices is a particularly novel and attractive concept, as such a biosolar technology employs the cost-effective and robust semiconducting material that absorbs the visible part of the electromagnetic spectrum together with the highly efficient natural light-harvesting/charge separating protein complex that operates with the internal quantum yield close to unity (see **Chapters 1.2.3** and **1.3**).

Generation of highly efficient biohybrid solar cells requires cost-effective techniques and methodologies for producing semiconductor/dielectric surfaces with very low inherent charge recombination. To this end, various surface passivation approaches have been developed based on chemical modification of the semiconductor surface and electric field effects [228–230]. Recently, a new generation of chemically passivated Si solar cells with an efficiency of 22.1% has been reported by Savin *et al*. [231]. In the study, the authors employed atomic layer deposition of Al_2O_3 on the surface of the nanostructured Si in order to significantly decrease surface charge recombination by extending minority carrier lifetimes to the millisecond timescale range due to significantly reduced Auger recombination [231].

Si-solar cells hold great promise, as they have the highest reported solar-to-electric efficiencies to date. The second highest most efficient solar cell reported to date is a black Si solar cell with a solar-to-electric efficiency of 27.6 ± 1.2% [119,232]. The authors used a similar approach to that of Savin *et al*. [231] but incidentally managed to improve the efficiency by increasing the thickness of the rear passivating layer, employing the same approach that we use in the present chapter with a biological passivating layer, namely cyt c_{553}. The key to recombination minimisation at the semiconductor surface and hence, maximisation of the power conversion efficiency lies in the optimisation of the interfaces between biological, organic and inorganic modules of the semiconductor electrode [227,231,232]. This chapter describes a novel strategy to tackle this grand challenge by

developing the biophotoelectrodes based on *p*-doped Si substrate that has been biopassivated with *C. merolae* cyt c_{553} in a haem-Si orientation and distance-dependent manner.

4.5.2 Selection of *p*-doped silicon as the electrode material

In the past, metal electrodes have commonly been used in PSI-based photobioelectrodes [128,222,233–237]. However, application of semiconducting electrode materials allowed for a significant enhancement of photocurrent and photovoltage outputs [128,129,139,221]. The *p*-doped Si was chosen as the electrode material in this study as it has been previously shown to serve as an excellent substrate for cyt c_{553} [238], as the mid-point potential of this haem-containing protein (+210 ± 10 mV) is very close to the estimated Fermi level of the conduction band of *p*-doped Si (0.5 V *vs*. SHE) with this level of doping, as shown in **Figure 86** and **Suppl. Figure 4**. Furthermore, *p*-doped Si was found to be an excellent platform for electron donation to the photo-oxidised P700 reaction centre of PSI (see **Chapter 4.6**) [222,234] due to well matched valence and conduction bands for Si (0.5 V and -0.6 V *vs.* SHE, respectively), the P700 primary electron donor and F_B iron-sulphur cluster (terminal electron acceptor) of PSI (0.43 V and -0.58 V vs. NHE, respectively) [234].

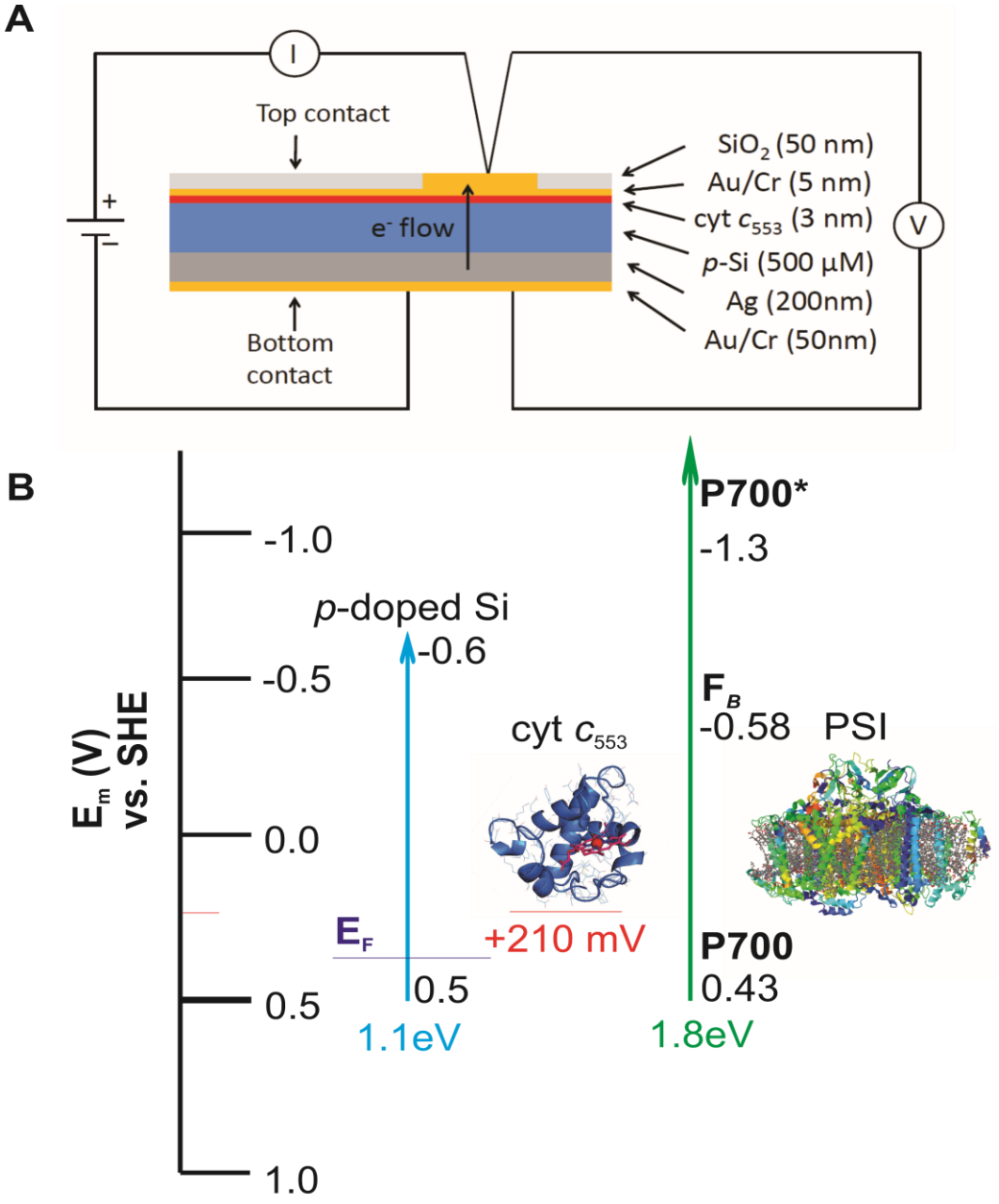

Figure 86

Diagrammatic representation of the second (II) generation cyt *c*$_{553}$/*p*-doped Si device organisation and the corresponding energy band diagram. A: A diagram displaying the cyt *c*$_{553}$/*p*-doped Si device (second (II) generation device). The thickness of the layers was estimated with sputtering detection. The circuit displays schematically how the devices were characterised, strictly in the dark for the assessment of their inherent recombination parameter (J_0). B: The energy band diagram displays valence band (0.5 V *vs.* SHE) and conduction band (-0.6 V *vs.* SHE) of *p*-doped Si and the midpoint potential of cyt *c*$_{553}$ along the estimated Fermi level for this level of B-doped Si. The proximity of the estimated Fermi level of Si with this level of boron *p*-doping is shown (in purple) with respect to the redox midpoint potential of

cyt c_{553}, emphasising their redox compatibility. This implies that injection of electrons from the valence band of photoactivated *p*-doped Si to the haem group may proceed efficiently. On the right handside the P700 primary electron donor and F_B iron-sulphur cluster (terminal electron acceptor) of PSI (0.43 V and -0.58 V *vs*. NHE, respectively) are displayed so as to emphasise the energetic compatibility of valence and conduction bands of the modules.

4.5.3 Construction of first (I) and second (II) generation biophotoelectrodes

Five distinct biophotoelectrodes have been constructed by immobilisation of the experimentally designed and purified His_6-tagged cyt c_{553} variants (see **Chapter 4.2**) on *p*-doped Si substrate that had been previously functionalised with a Ni-NTA self-assembled monolayer (SAM). Diagrammatic representation of the constructs is shown in **Figures 87** and **88**. For the construction of the cyt c_{553}/Si biophotoelectrodes an estimated 3-nm monolayer of each cyt c_{553} variant was immobilised on a heavily *p*-doped Si wafer using a His_6-tag as a molecular anchor. We introduced the Ag and Au/Cr recovering (200 nm and 50 nm, respectively) contacts for generation of a closed circuit, as schematically shown in **Figures 87** and **88**.

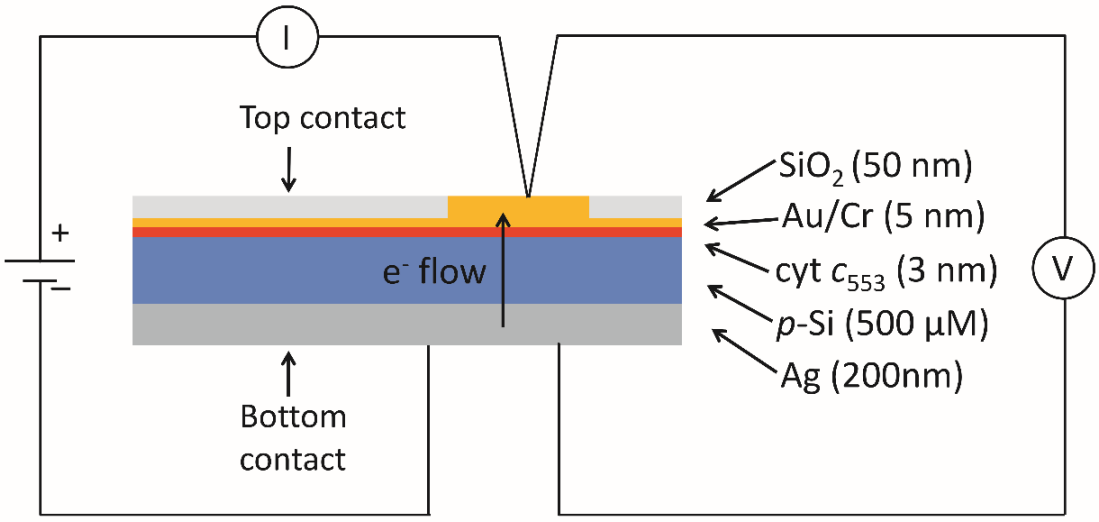

Figure 87

First (I) generation of all-solid-state cyt *c*$_{553}$/*p*-doped Si nanodevice. The thickness of the layers was estimated using an atomic force detector built into the specialised sputtering device. All the devices were constructed at ITME (Department of Optoelectronics, Institute of Electronic Materials Technology, Warsaw, Poland). Refer to **Figure 94** of **Chapter 4.6** for a flow-chart describing construction of the nanodevices.

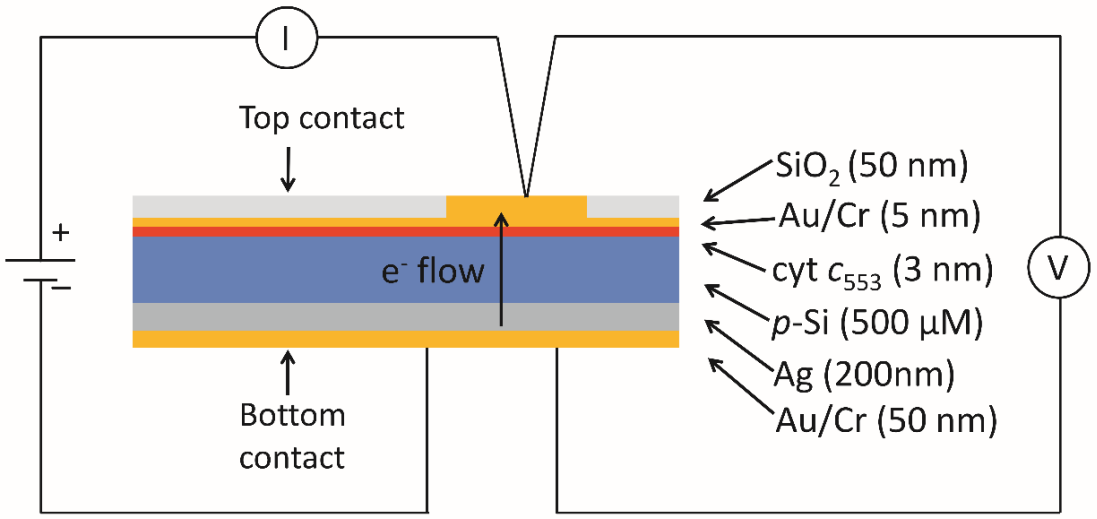

Figure 88

Second (II) generation of all-solid-state cyt c_{553}/*p*-doped Si nanodevice. The thickness of the layers was estimated using an atomic force detector built into the specialised sputtering device. All the devices were constructed at ITME (Department of Optoelectronics, Institute of Electronic Materials Technology, Warsaw, Poland). An additional layer of 50 nm Au/Cr alloy was added to the bottom of the layer to avoid any oxidation of Ag contact upon submersion of the device into a photo-electrochemical cell with a Ag/AgCl counter electrode. Moreover, it was found that this recovering prolongued and imrpoved the quality fo the bottom Ag layer. Refer to **Figure 94** of **Chapter 4.6** for a flow-chart describing the construction of the nanodevices.

4.5.4 Biopassivation of *p*-doped silicon substrate with cytochrome c_{553} (based on *Janna Olmos et al., Biopassivation of p-doped silicon with cytochrome c_{553} leads to minimisation of charge recombination and leakage current at the semiconductor surface,* under review)

The main objective of this study was to optimise the direct electron transfer between the *p*-doped Si semiconductor electrode and cyt c_{553} by manipulating both the distance and orientation of the redox active haem group with respect to the electrode surface. As a first step to understand the kinetics of electron transfer of the cyt c_{553} variants chelated to the Ni-NTA SAM-functionalised *p*-doped Si surface, bioinformatics simulations of the Gibbs free energy using the PyRosetta® software were performed to obtain an insight into the thermodynamic properties of the distinct variants of cyt c_{553} upon their immobilisation on the electrode surface. Firstly, a Monte Carlo minimisation approach was applied to calculate the acceptance rate for each cyt c_{553} variant, corresponding to the ratio of a number of energetically permissive moves to a number of rejected moves. The acceptance rate was used in this context as a measure of the thermodynamic freedom of motion of each cyt variant upon its attachment to the Si surface *via* a His_6-tag. It is worth noting that the acceptance rate largely depends on the degree of flexibility of the different AA side-chains present within the linker peptides. A Monte Carlo object was used to calculate the probability of free motion of the cyt c_{553} variants. These are commonly defined by the Metropolis criterion [239]. **Figure 89** shows that the highest acceptance rate (0.6851 ± 0.04) was calculated for the shortest (5AA) cyt variant, whereas the lowest acceptance rate value (0.3868 ± 0.02) was attributed to the cyt variant containing a structured semi α-helix (19AA) linker peptide.

Subsequently, the 2D Gibbs free energy maps for each cyt c_{553} linker peptide variant were calculated related to the absolute distance of the haem group of cyt (central Fe atom) and the relative planar angle between the haem and flat electrode surface. **Panel A** of **Figure 90** shows that the presence of the longer peptide linkers within the cyt c_{553} structure evokes a significantly larger number of thermodynamically favourable conformations of the anchored cyt *c* (in terms of probability of energetically favourable alignment of the haem group to the electrode surface) after a given move, and consequently, a lower acceptance rate (see **Figure 89**), according to the Monte Carlo criteria. On the other hand, a short linker is more likely to adopt a thermodynamically unfavourable conformation, since very few combinations of dihedral angles are possible within the whole linker length and hence a lower probability of proximal alignment of the haem group to the Si surface. For the 0AA variant, two distinct

populations of thermodynamically favourable conformations were identified, as shown in **Figure 89**.

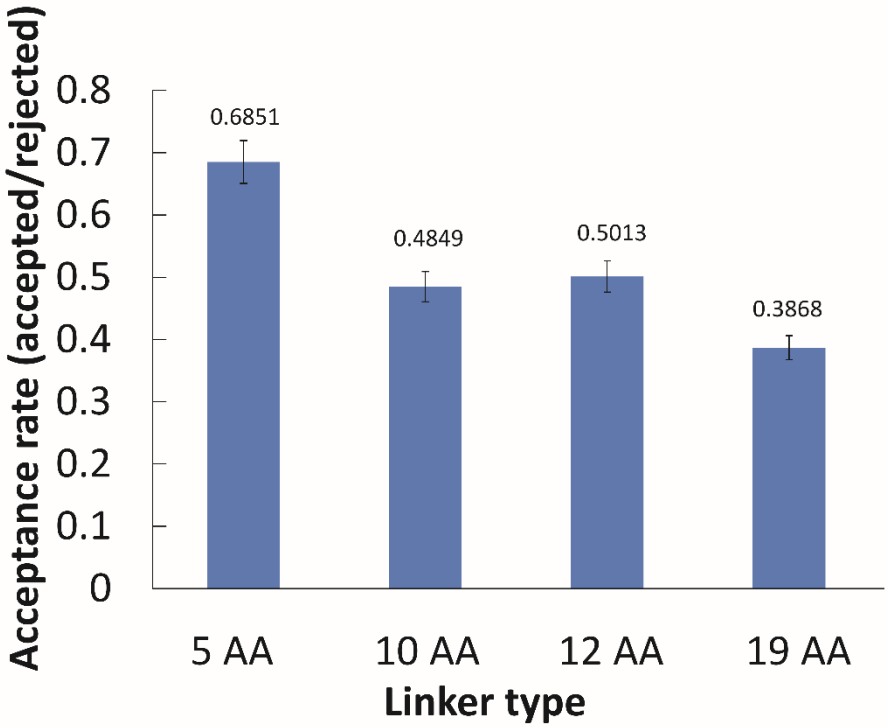

Figure 89

Acceptance rates of different cyt c_{553} variants after Monte Carlo simulation. The acceptance rate is calculated as the ratio of the number of energetically permissive moves to the number of rejected moves (using standard Metropolis criterion) [239], after applying random modifications of geometrical conformation to each cyt c_{553}, each having a different version of AA linker. The acceptance rate was not calculated for the 0AA linker variant as there is no AA linker peptide between the two *ab initio* points of this simulation; namely the *C*-terminus of the holoprotein sequence and the first histidine residue of the His_6-tag. Values for acceptance rates are displayed above the error bars of each different variant.

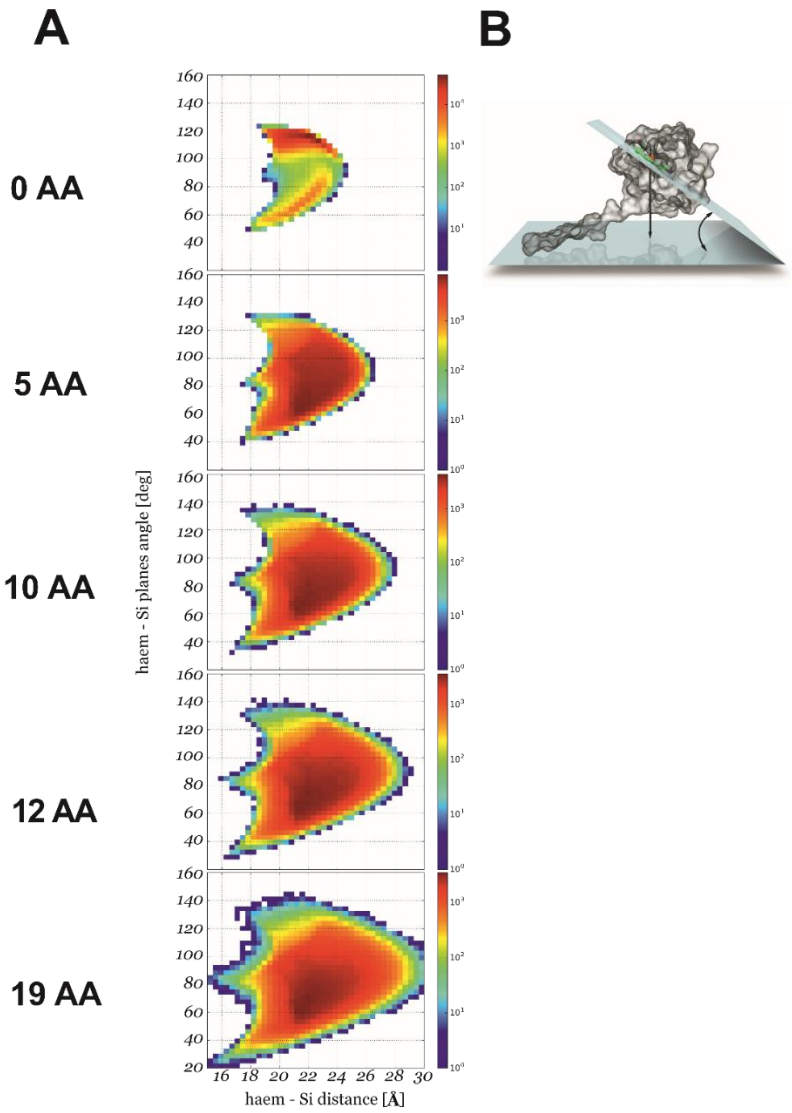

Figure 90

2D conformational flexibility maps for different cyt *c*$_{553}$ variants. A: The maps show relative probability of conformations for a given orientation of haem plane described by its distance to the Si plane and the angle between the two planes: X and Y axis, respectively (see **Panel B** for the definition). The probability in logarithmic scale is directly proportional to the Gibbs free energy of a given state. Note the significant difference between the 0AA and 19AA linker variants. B: Definition of internal coordinate system used to describe haem-Si mutual orientation. Haem is displayed in green with Fe central atom (red ball). Two coordinates were used: the dihedral angle between the plane of the haem group and Si plane as well as the distance between the two planes. Figure reproduced from *Janna Olmos et al.*, under review [227].

To evaluate semiconductor surface coverage with different cyt c_{553} variants scanning electron microscopy (SEM) was performed for visualisation of the bioelectrode surface (see **Figure 91**). **Panel A** shows a control which is a pristine surface of the *p*-doped Si covered by Au. **Panels B-F** show homogenously deposited cytochromes. In the case of 19AA linker we obtained less dense coverage of the semiconductor area which could be attributed to a larger and more rigid structure of the peptide linker, resulting in more steric hindrance upon spin-coating. Overall, in all cases immobilisation of this redox active protein was successful and SEM images confirmed that chosen deposition technique (i.e. vacuum spin-coating) is appropriate for this all-solid-state device construction.

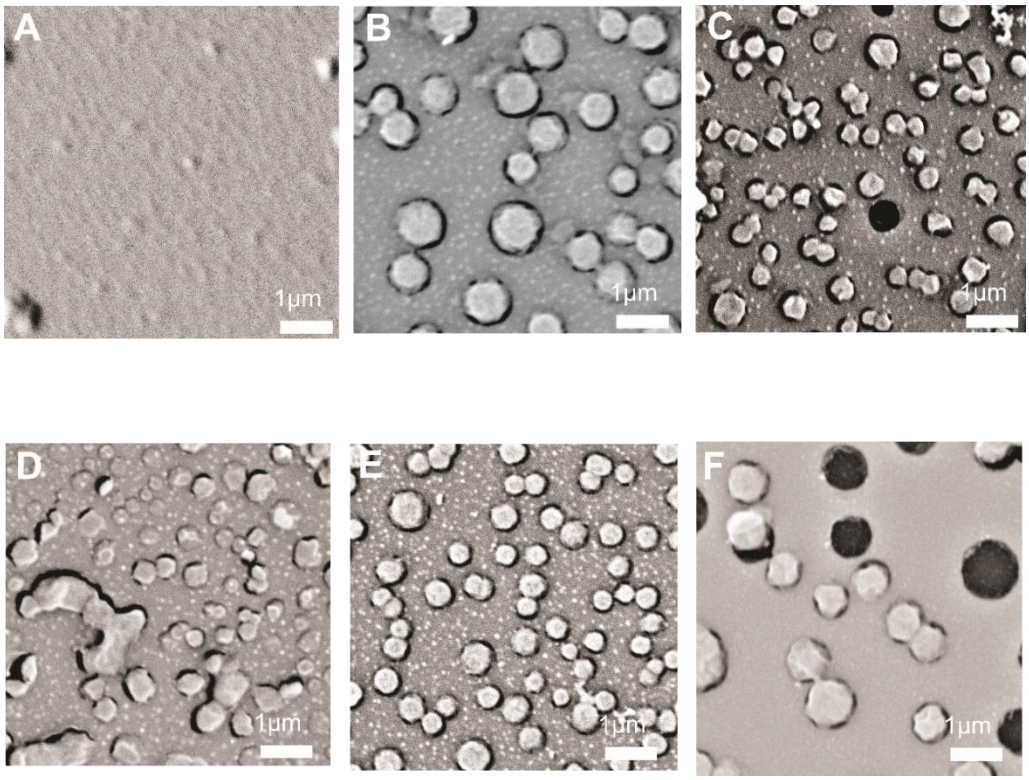

Figure 91

Scanning electron micrographs of the surface of cyt c_{553}/*p*-doped Si bioelectrodes. The five bioelectrodes constructed in this study display the homogenous cyt c_{553} protein distribution on the Si/Au electrode surface. The nanostructure of the biofunctionalised Si electrodes is notably different compared to the Si control (with Ni-NTA SAM) which contains no cyt (shown in A). B: 0AA, C: 5AA, D: 10AA, E: 12AA, F: 19AA. Three different regions of each biodevice were investigated and all presented almost identical appearance. Micrographs were obtained using 36,000 magnification. Scale bar, 1 µm.

4.5.5 Assessment of *J-V* properties of the all-solid state cyt c_{553}/*p*-doped silicon devices

To evaluate the Si surface charge properties of the constructed cyt c_{553}/*p*-doped Si devices dark saturation currents were measured. The dark saturation current value, also known as the recombination parameter (J_0) [158] (**Eq. 8**) is used to quantify the level of surface charge recombination of a semiconductor. It can be referred to as the "background recombination" parameter, i.e., the higher the J_0 value, the more recombination events exist. As clearly displayed in **Table 22**, dark saturation current values obtained for all the cyt c_{553}/*p*-doped Si devices were inversely proportional to the length of the AA linker sequence present in the cyt c_{553} variant, with the lowest J_0 recorded for the 19AA cyt c_{553} variant Si bioelectrode.

The data presented in **Table 22** goes well in agreement with that presented in **Figures 92** and **93**, where the *J-V* and solid-state voltammograms display the highest dark currents for the 5AA linker variant and the lowest for the 19AA linker variant. In agreement with the thermodynamic calculations, two classes of 0AA variant biolelectrodes were identified which displayed either very low or very high J_0 values.

Table 22

Characterisation of dark saturation currents in the all-solid-state cyt c_{553} variant/*p*-doped Si bioelectrodes

Biodiode type	J_0 (mA/cm^2)
Control (with SAM)*	1.2 x 10^{-1}
0 AA[a]	4.5 x 10^{-2}
0 AA[b]	2.8 x 10^{-3}
5 AA	6.9 x 10^{-2}
10 AA	2.3 x 10^{-2}
12 AA	3.5 x 10^{-2}
19 AA	7.5 x 10^{-3}

J_0, dark saturation current (inherent recombination parameter) of each solid-state device. The J_0 values were obtained from **Eq. 8** (assuming that at 300K, kT/q = 25.8 mV)
*For a scheme depicting SAM synthesis refer to **Figure 34**
[a]value obtained for two 0AA linker variant electrodes which displayed similar *J-V* curves (see **Figure 92**)
[b] value obtained for two 0AA linker variant electrodes which displayed similar *J-V* curves (see **Figure 92**)

$J = J_0^{(qV/enkT)\ -1}$ [158] **(Eq. 8)**

All the J_0 values were calculated from **Eq. 8** above, and were also determined from the *J-V* curves presented on a semi-logarithmic scale, where the J_0 value corresponds to the *y*-intercept (see **Suppl. Figure 3**).

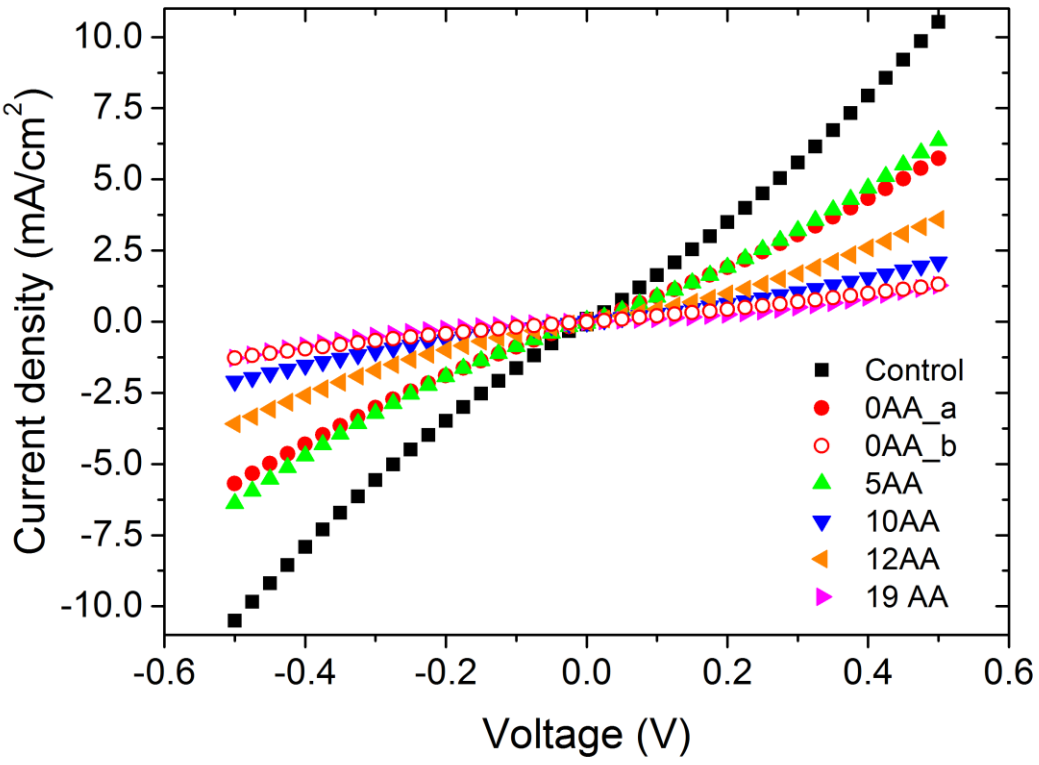

Figure 92

***J-V* characteristisation of cyt c_{553}/*p*-doped Si bioelectrodes.** The five bioelectrodes constructed in this study display the biodiode characteristics, albeit at different kinetic rates of e^- transfer. Short, rigid AA linkers allow for a higher degree of recombination (measured by J_0 parameter) compared to longer, more flexible linkers. The data indicates that the 5 AA-linker-cyt c_{553} variant potentially allows for the highest degree of recombination within the bioelectrode, which agrees with the 2D maps displayed in **Figure 90**. The degree and probability of alignment of the haem group to the *p*-doped Si surface translates to its degree of charge recombination; short rigid AA linker peptides have a much higher degree of recombination compared to longer, more flexible peptides which allow more efficient electron transfer as they permit more favourable haem alignment to the Si surface. The 0AA linker variant presents anomalous behaviour displaying either very low or very high J_0 values. We attribute this behaviour due to the extreme restriction of movement of this variant linker peptide, which contains no linker peptide between the *C*-terminus of the protein and the first Histidine residue of the His_6-tag, rendering the haem group ether completely perpendicular or completely parallel to the Si plane. The control is the Si functionalised with Ni-NTA SAM (see **Figure 34**).

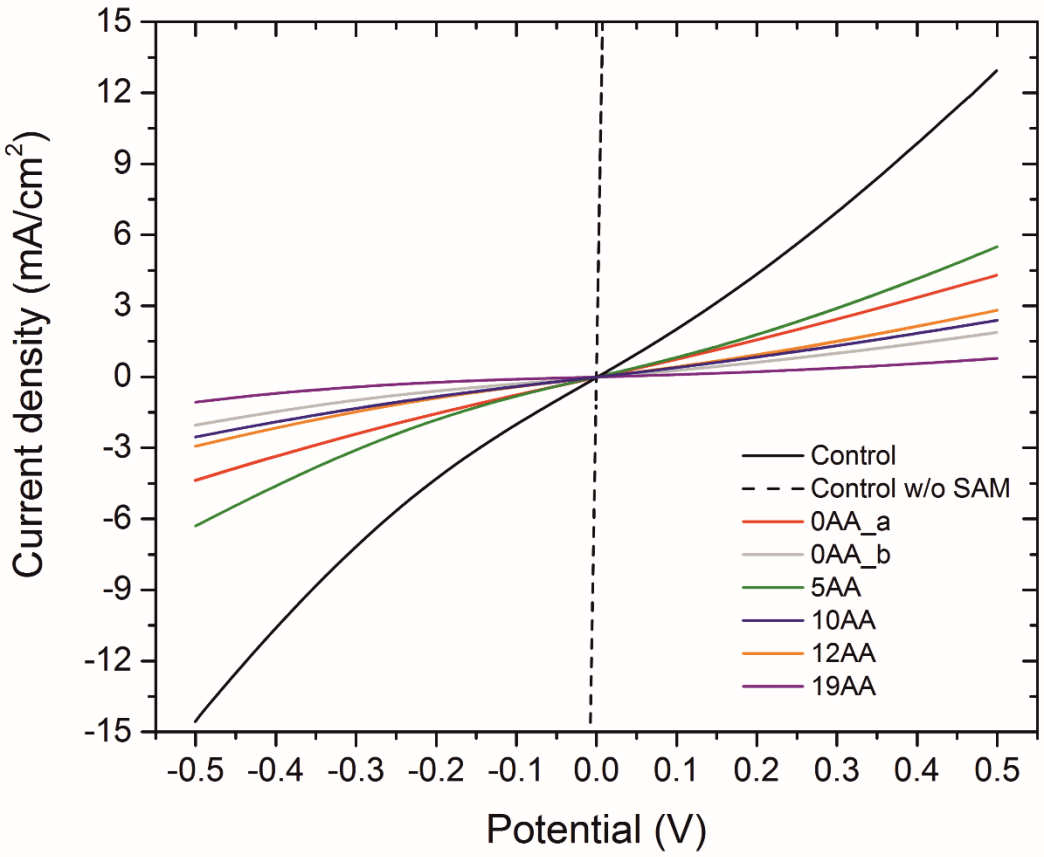

Figure 93

Linear sweep voltammograms of the all-solid-state cyt *c*$_{553}$/*p*-doped Si bioelectrodes. The CVs were obtained in a specialised two electrode measuring setup at a scan rate of 10 mV/s. The potential was cycled from -500 mV to 500 mV. Note that the Ni-NTA SAM contributes to the redox activity of the solid-state construct, as shown above. The absolute value of the current (mA) is inversely proportional to the length of the linker peptide, having the highest current for 5AA and the lowest for 19AA. Note that the anomalous behaviour for the 0AA linker is also observed here, as seen in **Figure 92** and **Table 22**.

4.5.6 Concluding remarks

In this study, five novel cyt c_{553}/*p*-doped Si bioelectrodes were engineered which differed in the length and structure of the peptide linkers inserted between the *C*-terminal His_6-tag and the cyt c_{553} holoprotein (see **Chapter 4.2** and **Table 17**). First, the His_6-tagged variants of cyt were immoblised on Si surface through a Ni-NTA-containing SAM, as shown diagrammatically in **Figure 34**, and their *J-V* properties were characterised in order to select the best cyt c_{553} variant for optimal direct electron transfer (DET) within all-solid-state PSI-based Si biophotoelectrodes (described below in **Chapter 4.6**).

The data presented here show that introduction of longer peptide linkers to the structure of redox active cyt c_{553} leads to a much more significant degree of passivation in the Si surface of the biodiode, as evidenced by the significant minimisation of dark saturation current (J_0) (**Figures 92** and **93**). Furthermore, dark currents were measured in the range of 1.0-6.25 mA cm^{-2} attesting to the advantage of employing all-solid-state devices over constructs that rely on mediated electron transfer [227]. These observations are discussed in **Chapter 4.6**, in the context of a rational design of optimal DET within the full biophotoelectrode, comprising the Si substrate, cyt c_{553} conductive module and light-harvesting/charge separating module of PSI.

Immobilisation of His_6-tagged cyt c_{553} variants at the all-solid-state Ni-NTA functionalised *p*-doped Si interface resulted in a considerable reduction of surface charge recombination [227]. Moreover, it was shown that different lengths and shapes of linkers between the His_6-tag and the *C*-terminus resulted in different degrees of passivation (minimisation of recombination), showing clearly that there is a correlation between haem alignment geometry and passivation at the all-solid-state interface [227]. This phenomenon could be explained by the geometrical restrictions imposed to the movement of the haem group with relative proximity to the Si substrate/surface. Longer, more flexible linkers could allow closer proximity of the haem group to the Si surface, thus interacting better with the surface by allowing a more favourable geometrical alignment of the haem group with respect to the Si surface. In contrast, shorter more restricted linkers have much more geometrical restrictions imposed on the haem group, and therefore interact less favourably with the Si surface. This is the reason why parallel Si-haem alignment is more favourable for electron transfer and thus minimisation of recombination at the Si surface. This could also explain why longer linkers have significantly much lower dark saturation current by nearly three orders of magnitude compared to shorter linkers and Si-SAM control (see **Figures 92**, **93** and **Table 22**).

The Gibbs free energy calculations and mapping of energetically favourable conformations of cyt c_{553} variants upon their anchoring to the Si surface (see **Figures 89** and **90**) demonstrated that the variants display different degrees of flexibility and alignment with respect to the Si surface in this novel all-solid-state setup. Therefore, by introducing the specific linker peptides (12AA-19AA) within the cyt c_{553} structure we were able to manipulate the alignment of the haem group respective to the semiconductor surface, which was confirmed by the *J-V* characterisation of the cyt c_{553}/*p*-doped Si devices (see **Figs 92**, **93** and **Table 22**). This molecular approach has allowed for the developing of an alternative, cheap and facile route for significant reduction of the inherent minority charge recombination of the *p*-doped Si semiconductor substrate while producing solid-state biodevice currents in the mA cm^{-2} range. Importantly, this study demonstrated that one of the linker variants, the 19AA linker variant is a good candidate as the conductive biopassivating module of the full all-solid-state PSI-based biophotovoltaic device, as investigated in the subsequent **Chapter 4.6**.

Chapter 4.6

Towards construction of efficient PSI-LHCI/silicon biophotoelectrodes

4.6.1 Introduction

Leading renewable energy production data show a substantial growth of solar electricity technologies and indicate that crystalline silicon PV primes the initial wave of renewable energy disposition on the TW scale around the globe [113]. Presently, renewable energy encompasses only 9% of the entire global supply of commercially traded primary energy (see **Figure 18**). This is an insufficiently small share in the global energy supply considering that 87% of our energy consumption (a number believed to increase considerably by 2020) relies very heavily on fossil fuels. The global demand for fossil fuel-derived energy sums to 1,066 barrels of oil, 108,000 cubic meters of natural gas and 250 tonnes of coal per second as mentioned in **Chapter 1.3.1** [113]. Currently, it is estimated that coal reserves might cover the present world demand for over 110 years, compared to oil and natural gas, which will be depleted at this rate in 52.5 and 54.1 years, respectively, in the best case scenario [113]. These facts give the scientific community very limited time to develop and optimise sustainable technologies that will allow for production of renewable energy at an ever growing rate.

Functionalisation of semiconductor electrode materials, such as Si, with natural light harvesting proteins such as PSI complex is a particularly attractive concept, as such biohybrid solar technology utilises the combination of relatively cheap and stable semiconducting material, such as Si that absorbs the visible part of the electromagnetic spectrum, together with the highly efficient light-harvesting/charge separating natural pigment/protein complex that operates with the internal quantum yield close to unity [240]. However, the efficiency of the biohybrid PSI-based photoelectrodes is still limited to values below 1% mainly due to the recombination of photo-excited electron-hole pairs at the interface of the electrode modules, rather than being limited by the PSI photochemical activity itself. Other obstacles to obtain high power conversion efficiency of PSI-based biophotoelectrodes are poor electronic contact between the photoactive module and the electrode, insufficient and heterogeneous PSI loading onto the electrode and instability of the biological modules. Nevertheless, it has been recently shown that high energy photoactivated electrons that are generated in PSI upon light absorption can be recovered in artificial devices, even faster than in natural photosynthesis

itself [241], highlighting the great potential of PSI-based biohybrid solar technology once it is optimised.

Previously, metal electrodes have commonly been used in PSI-based photobioelectrodes [235–237]. Nonetheless, application of semiconducting electrode materials allowed for a significant improvement of photocurrent and photovoltage outputs [128,129,139,221,242]. In particular, *p*-doped Si was found to be an excellent platform for electron donation to the photo-oxidised P700 reaction centre [222,234] due to well matched valence and conduction bands for silicon (0.5 V and -0.6 V vs NHE respectively) and the P700 primary electron donor and F_B iron-sulphur cluster (terminal electron acceptor) of PSI (0.43 V and -0.58 V vs. NHE (or SHE), respectively) [234].

Due to the recent and substantial advancements in Si technology, it is possible to shift the Fermi level of silicon by introducing impurities. It is now well established that one can in fact control and enhance the electron flow through the biohybrid system by changing the doping type and doping density of Si biophotoelectrodes [234]. The optimised system allows for electrons to flow in a single direction, from Si substrate to the protein, and finally to a redox mediator, or ideally in the solid state to the counter electrode, to minimise energy losses due to the diffusional character mediator-based electron transfer (MET) [227]. Such a technology might in principle allow for construction of highly efficient thin-film Si-based biophotoelectrodes which would allow desirable electron-transfer efficiency at the all-solid-state interface, short-cutting electron transfer and minimising energy losses by otherwise energy consuming processes such as diffusion-based electron transfer in solution [227]. This way, it is hypothesised that the Shockley-Queisser limit might be finally breached when employed in conjunction with solar thermophotovoltaic converting (STPV) technology, envisaging solar-to-electric efficiencies greater than 32% for thin-film Si-based solar cells [123,232].

As mentioned in the previous chapter, there is no risk of Si shortage in any foreseeable future as it is the second most abundant and evenly distributed element in the earth's crust [113]. Importantly, it is now well established that in the hypothetical scenario where silicon PV technologies provide 100% of the world's electricity supply by 2030, the required Si production growth rate would fall within the range of the historical range recorded over the last four decades [113]. Moreover, the same applies to Au, which not only is essential for electrical contacts, but as a matter of fact is considered the most critical material in PV panels [118].

The main results described in this chapter are the construction of a novel type of all-solid-state mediatorless *p*-doped Si-based biophotoelectrodes containing both the substrate (Si) either with or without biological conductive layer of cyt c_{553} and ultimately, a photoelectroactive module of the robust extremophilic PSI-LHCI complex. The prototypes of such a biophotovoltaic devices described in this chapter provide the foundation for the green technology based on biophotoelectrodes that in long-run may be optimised to the competencies and efficiencies that would warrant implementation on the commercial scale. Moreover, it is demonstrated here, that the 19AA linker cyt c_{553} variant, used as a biological conductive interface between the *p*-doped Si substrate and PSI-LHCI photoactive module (see **Figures 101** and **102**), biopassivates the Si surface, as described in **Chapter 4.5**. As a result, introduction of the 19AA linker variant of cyt in the full PSI-LHCI-based biophotovoltaic device results in a 333 μV increment of the open-circuit potential (V_{oc}) upon illumination compared to the device comprised of PSI-LHCI/Si devoid of any cyt c_{553} conductive layer.

4.6.2 Immobilisation of PSI-LHCI complex on a *p*-doped silicon substrate (third (III) generation biophotovoltaic devices)

The optimisation of the construction of PSI-LHCI/*p*-doped Si biophotovoltaic devices was based on minimisation of the native oxide build-up and avoidance of improper electrical contact formation. The abovementioned were avoided thanks to the technical and engineering expertise provided in the Department of Optoelectronics of the Institute of Electronic Materials Technology (ITME, Warsaw, Poland) led by Head Eng. Marian Teodorczyk. **Figure 94** displays a flow-chart elucidating the main steps in the construction of these novel mediatorless all-solid-state biophotodevices.

Figure 95 displays the representation of the PSI-LHCI/Si nanodevice, with thickness of each layer indicated. The thickness of the consecutive layers was estimated *via* sputtering detection.

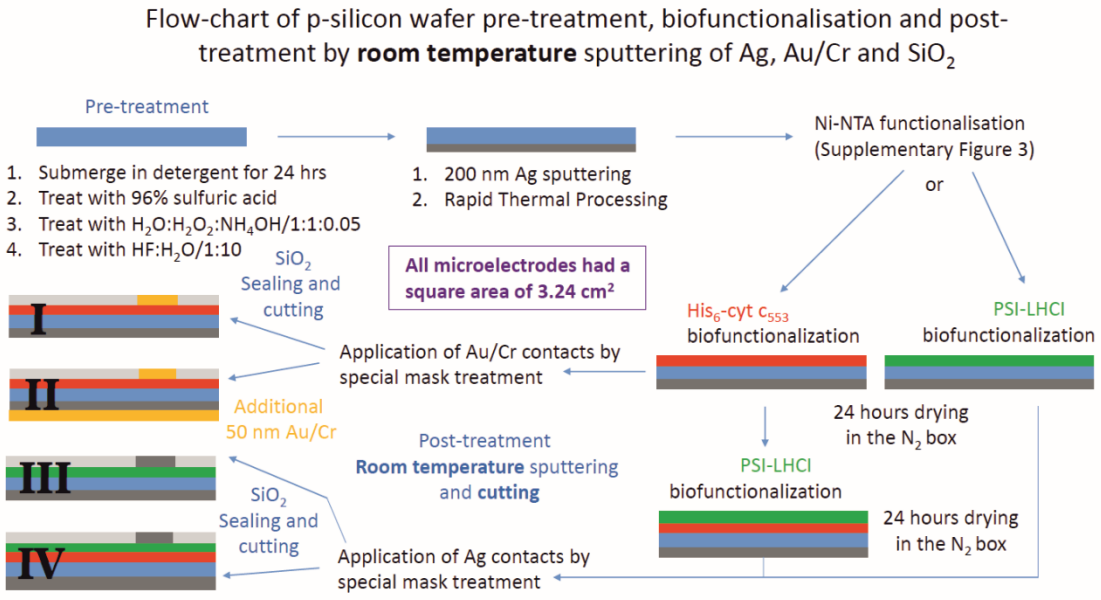

Figure 94

Flow-chart depicting preparation of all-solid-state PSI-LHCI/cyt *c*$_{553}$/*p*-doped Si biophotovoltaic devices. For a detailed protocol of Ni-NTA synthesis on Si refer to **Figure 34**. Roman numbers correspond to the consecutive generations of the biophotovoltaic devices prepared in this study. Four generations of the devices were constructed, as described in **Chapters 4.5** and **4.6**.

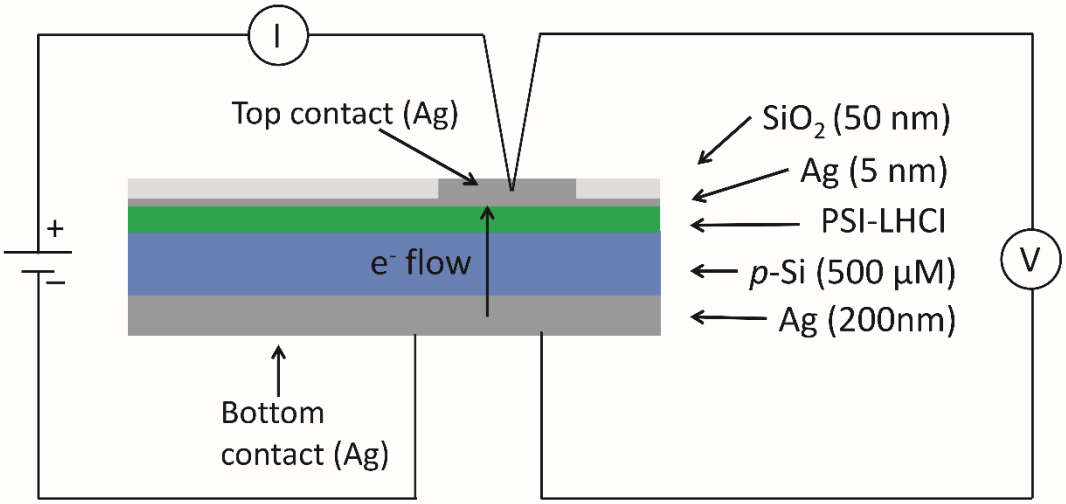

Figure 95

Diagrammatic representation of the PSI-LHCI/*p*-doped Si nanodevice (third (III) generation biophotovoltaic device). The thickness of each layer is indicated on the right and was estimated by sputtering detection. The components are not to scale. All Si layers were functionalised and contained a Ni-NTA SAM, as displayed in **Figure 94.**

Upon photoelectrochemical characterisation of the constructed devices, large variability was observed within many devices. This is due to several reasons. Firstly, *p*-doped Si is a considerably defective material. For doping Si to the required levels for the generation of the material with the desired Fermi level shift (in the case of the present study to a doping density of 2.13 x 10^{19}-1.3 x 10^{20} cm^{-3}), boron was introduced into the Si block before cutting the block into the standard wafer sizes. Wafers constituted a circle with a 100-mm diameter and a thickness of 500 µm. Usually, this process introduces significant defects into the nanostructure of Si (as evidenced by **Panel A** of **Figure 91** in **Chapter 4.5,** also pers. comm. by Grzegorz Gawlik, ITME, Warsaw, Poland).

Other reasons for variation may include unequal distribution of SAM functionalisation and uneven protein dispersion and biofunctionalization. It was noted also that even after rapid thermal processing of the bottom silver contact, the contact could be easily detached if handled

too harshly. As is noted in the literature [128,222,233,234,243], this variability from device to device seems to be commonplace in these novel types of all-solid-state mediatorless nanodevices [128,222,234]. Consequently, it was observed that nanodevices which displayed a notoriously anomalous or aberrant appearance in the bottom Ag contact displayed large variability in terms of the *J*-*V* data obtained.

As a starting point of PV performance characterisation, the changes in the open circuit potential (V_{oc}) were measured upon illumination of the constructed devices. The V_{oc} parameter represents the difference of electrical potential between two terminals of a device when disconnected from any external circuit (see **Figure 95** for a schematic of the circuit of the device employed for the all-solid-state photoelectrochemical characterisation). **Figure 96** displays the results of V_{oc} measurements obtained when this routine parametrisation was done with three independent devices, whereby the only difference between each set of devices was the presence of the PSI-LHCI layer. More than an order of magnitude increase in V_{oc} was observed for the PSI-LHCI-functionalised devices which display in average 1,300 µV increase of V_{oc} in comparison to the 100 µV increase for the bare *p*-doped Si SAM control. It must be mentioned that an anomalous behaviour was observed for one the *p*-doped Si SAM electrodes devoid of PSI-LHCI, where a V_{oc} change of 800 µV was detected. As the other two devices displayed identical photoelectrochemical behaviour, this anomaly is attributed to the aberrant quality of the Ag contacts observed in this device, which is believed to be the main reason for the inconsistent behaviour observed for several devices constructed in this study.

For the next step of PV characterisation, photocurrents were measured by photochronoamperometry to determine whether there was a marked difference between the *p*-doped Si/SAM control and the PSI-LHCI-functionalised *p*-doped Si devices. As shown in **Figure 97**, *p*-doped Si/SAM device produced on average residual current densities of 6 µA cm^{-2}. In contrast, when two independent PSI-LHCI/*p*-doped Si devices where tested, photocurrents of 104-234 µA cm^{-2} were detected, being the highest photocurrent densities reported to date for mediatorless all-solid-sate PSI-LHCI-functionalised nanodevices, when an overpotential of -250 mV and the same illumination conditions were applied [128,222,233,243] (see **Figure 98**).

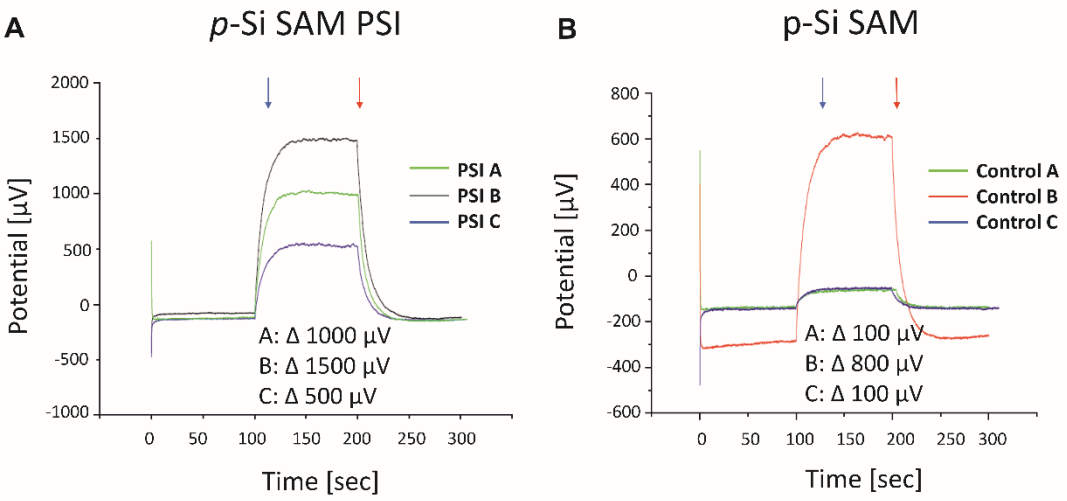

Figure 96

Open circuit potential (V_{oc}) measurement of illuminated PSI-LHCI/*p*-doped Si nanodevices. Upon illumination with white light of 100 mW cm^{-2} (2,200 µmoles photons m^{-2} s^{-1}), PSI-LHCI-functionalised *p*-doped Si devices (**Panel A**) display on average more than one order of magnitude increase in V_{oc} parameter compared to the *p*-doped Si/SAM control (**Panel B**), confirming that PSI-LHCI functionalisation is instrumental for the incrementation of V_{oc} upon illumination. Blue and red arrows symbolise light on and off, respectively. Potential values (µV) on the *y*-axis have been rescaled for clarity.

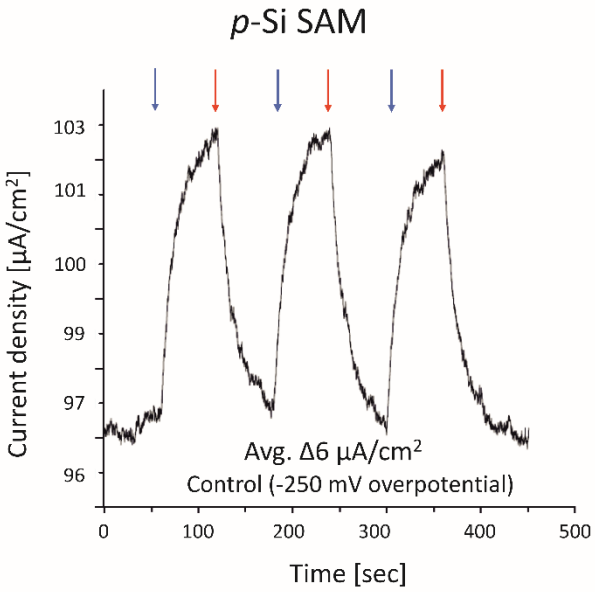

Figure 97

Representative photocurrent generation within *p*-doped Si/SAM control. An overpotential of -250 mV was applied in the circuit to feed electrons into the system. Blue and red arrows indicate light on and off, respectively. Note that the Si substrate produces residual photocurrents. Current density values on the *y*-axis have been rescaled for clarity.

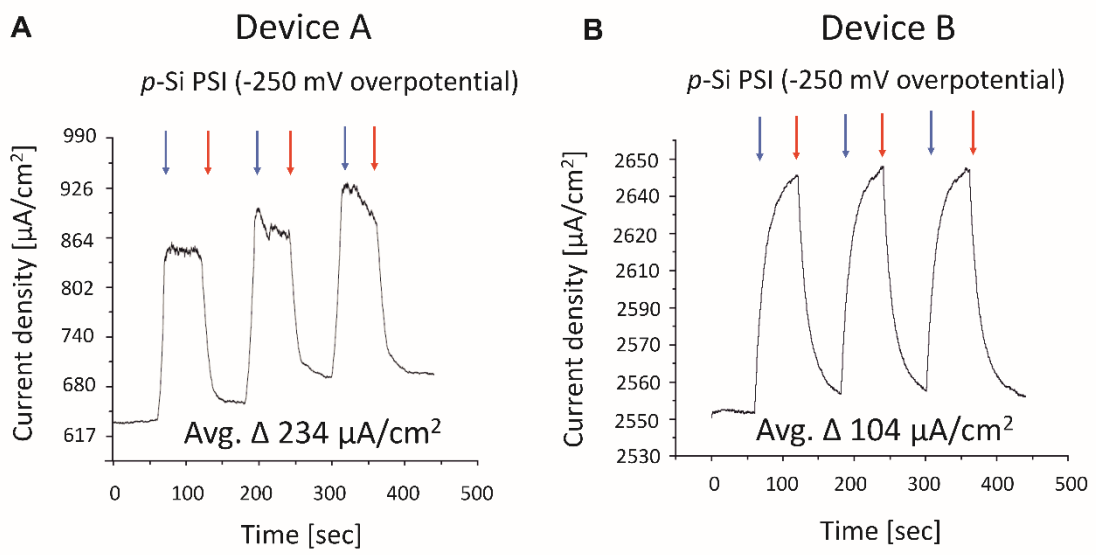

Figure 98

Photocurrent generation within two representative PSI-LHCI/*p*-doped Si devices. Panel A: A representative PSI-LHCI device characterised by photochronoamperometry. Panel B: A representative PSI-LHCI device characterised by photochronoamperometry. An overpotential of -250 mV was applied to the circuit to feed electrons into the system. Although both devices displayed large variability, reproducible photocurrent densities were detected upon standard illumination, ranging from 104-234 µA cm^{-2}. Blue and red arrows symbolise light on and off, respectively. Current density values on the *y*-axis have been rescaled for clarity. The shape of the photoresponsive curves was noted to vary from device to device, and could be attributed to imperfections in the construction of the device, unequal protein distribution or limited electron dispatchability.

4.6.3 Construction and photovoltaic characterisation of all-solid-state PSI-LHCI/cyt c_{553}/*p*-doped silicon devices (fourth (IV) generation biophotovoltaic devices)

Ultimately, it was important to determine whether incorporation of the cyt c_{553} linker variants (see **Chapters 4.2** and **4.5**) between the *p*-doped Si substrate and PSI-LHCI photoactive layer would influence DET, as measured by a marked increase in the generated photocurrents and the V_{oc} parameter in the presence of the cyt c_{553} conductive layer within the devices. In this case, the V_{oc} parameter would shine more light into the kinetics and competence of DET because it represents the difference of electrical potential between two terminals of a device when disconnected from any external circuit, and hence it is directly proportional to the kinetics of the unidirectional electron flow from the bottom Ag to the top Ag contact *via p*-Si/cyt c_{553}/PSI-LHCI layers (see **Figure 99** for a schematic representation of the full PSI-LHCI/cyt c_{553}-based biophotovoltaic device).

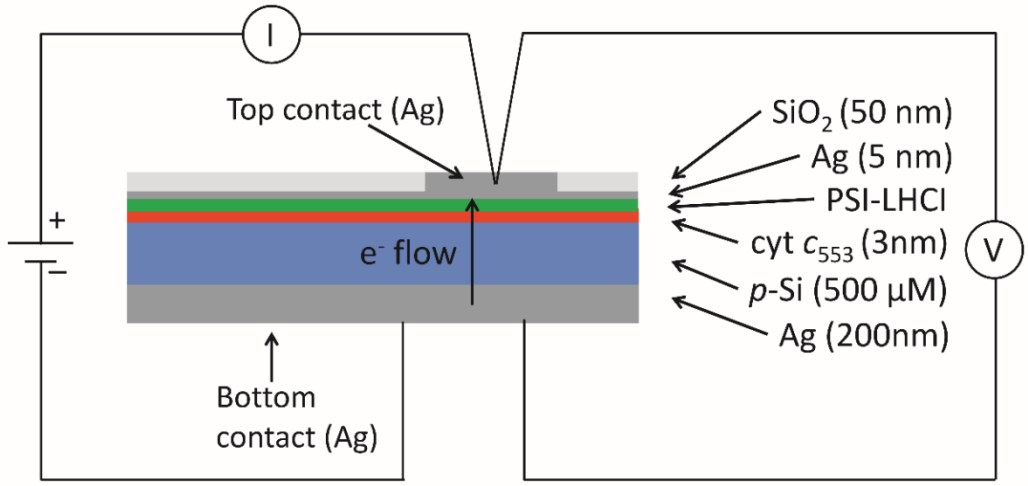

Figure 99

Diagrammatic representation of the PSI-LHCI/cyt c_{553}/*p*-doped Si nanodevice (fourth (IV) generation biophotovoltaic devices). The thickness of each layer indicated on the right was estimated by sputtering detection. The components are not to scale. All Si layer was consecutively functionalised with SAM, cyt c_{553} variant and PSI-LHCI (see **Figure 94**).

The open circuit potential measurements within the all-solid-state PSI-LHCI/cyt c_{553}/*p*-doped Si biophotovoltaic devices showed that introduction of the 19AA cyt c_{553} linker variant increased V_{oc} by 333 µV compared to the PSI-LHCI/*p*-doped Si sample (see **Figures 100** and **101**), most likely due to efficient biopassivation of the *p*-doped Si surface by this cyt c_{553} variant (see **Chapter 4.5**). It must be noted that it was not possible to assess the degree of biopassivation of the device which incorporated the 10AA linker variant. As observed in **Figure 100**, this type of device displays a ΔV_{oc} of 350 µV, however, with an SD value of nearly 200%, this device was excluded from further analyses. Such an aberrant behaviour was most likely due to severe defects in the Ag bottom contact in two out of the three 10AA devices employed for the PV assessment.

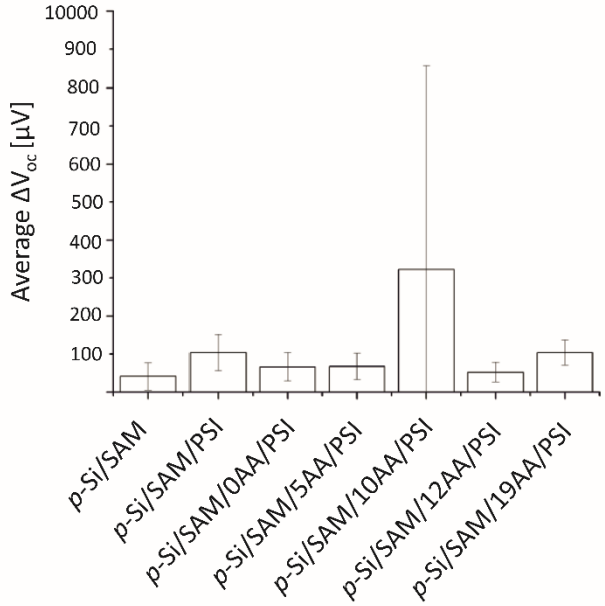

Figure 100

Average change (Δ) in open-circuit potential (V_{oc}) for all the different types of PSI-LHCI/cyt c_{553}/*p*-doped Si devices constructed in this study. The V_{oc} data (SD ± 100 μV for all the variants except for the 10AA linker variant) was averaged from three independent measurements from three devices for each class of the device. Note that a significant aberration is observed for the 10AA linker variant electrode due to notorious defect of two out of three devices incorporating this cyt c_{553} variant. Therefore, no conclusions could be reached for this class of the devices. The sample termed *p*-Si/SAM corresponds to the control with no biological modules. Average ΔV_{oc} values (μV) on the y-axis have been rescaled for clarity.

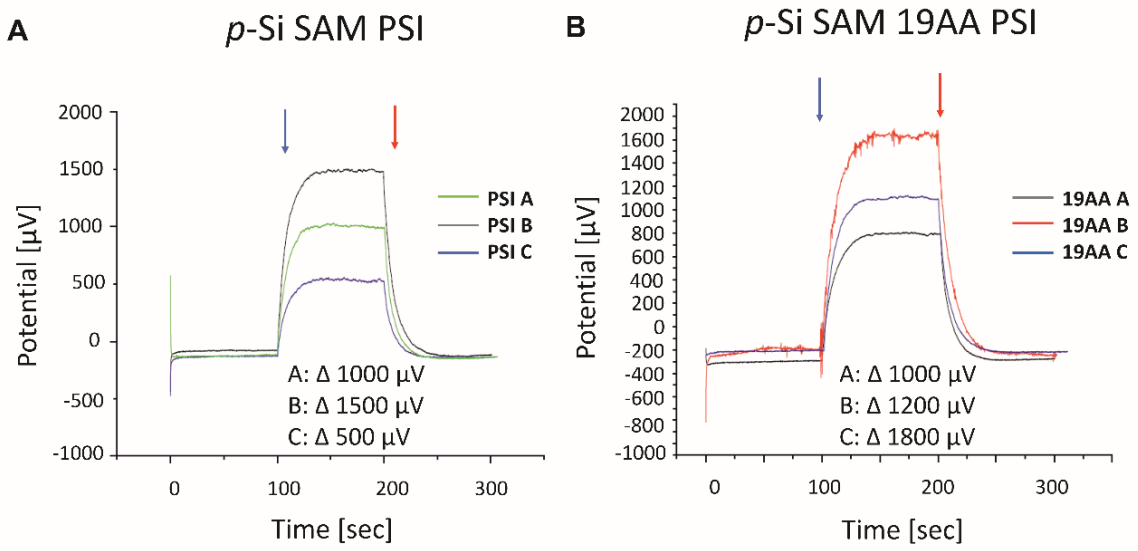

Figure 101

Photochronoamperometric determination of open-circuit potential (V_{oc}) within PSI-LHCI/*p*-doped Si (Panel A) and PSI-LHCI/19AA cyt c_{553}/*p*-doped Si biophotovoltaic devices (Panel B). After averaging the three independent devices, an increase in 333 µV is observed for the 19AA cyt variant-containing biophotoelectrode (**Panel B**) compared to the biophotoelectrode containing the PSI-LHCI alone (**Panel A**). The average V_{oc} increment for the biophotoelelctrode containing PSI-LHCI sample is 1,000 µV (shown in **Panel A**), while the average V_{oc} increment for the biophotoelectrode containing PSI-LHCI in addition to the 19AA linker variant is 1,333 µV (shown in **Panel B**). Blue and red arrows symbolise light on and off, respectively. Potential (µV) values on the *y*-axis have been rescaled for the ease of ΔV_{oc} estimation.

Measurements of the photocurrents in all the (IV) generation devices exhibited a large degree of variability. This was also the case for photochronoamperometric curves, most likely due to the faulty Ag back contacts, as mentioned earlier. It was noted that the devices which contained higher quality Ag back contacts displayed much clearer and cleaner photochronoamperometric signatures, such as those shown in **Panel A** of **Figure 102**. Unfortunately, most of the 19AA cyt variant-containing PSI devices contained rather damaged Ag back contacts (as shown by the V_{oc} measurements), rendering many devices impossible to analyse. Nevertheless, three independent devices of this class proved to be suitable for the measurement of photocurrents. **Figure 102** displays photocurrent generation within two

distinct *p*-doped Si/PSI-LHCI and *p*-doped Si/19AA cyt c_{553}/PSI-LHCI devices. The latter device displayed a much poorer quality of the photochronoamperometric curves compared to the *p*-doped Si/PSI-LHCI sample, due to the suboptimal Ag contacts which were easily dislodged even upon delicate manipulation. Despite the variability of the observed photocurrents, reasonably reproducible photocurrent densities were generated upon illumination, ranging from 104-234 µA cm^{-2} for the PSI-LHCI-containing nanodevices devoid of cyt c_{553}, compared to 70-147 µA cm^{-2} for the nanodevices that contained 19AA cyt variant between the *p*-doped Si and PSI-LHCI layer, when an overpotential of -250 mM was applied.

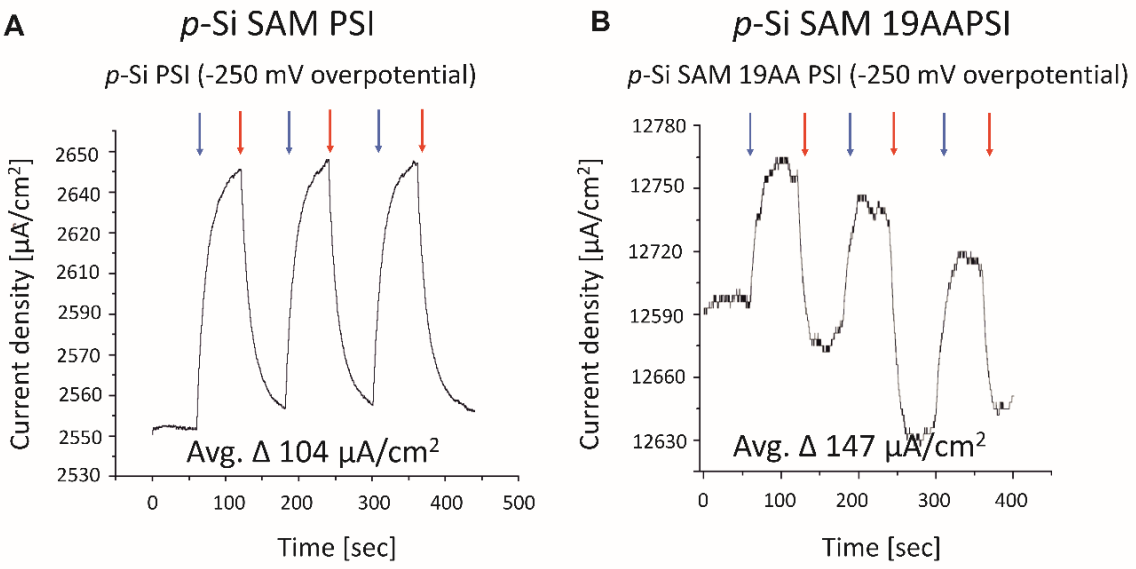

Figure 102

Photochronoamperometric measurements of photocurrents generated within two selected PSI-LHCI/*p*-doped Si and PSI-LHCI/19AA cyt c_{553}/*p*-doped Si biophotovoltaic devices. An overpotential of -250 mV was applied to feed electrons into the circuit. Blue and red arrows symbolise light on and off, respectively. Current density values on the *y*-axis have been rescaled for clarity.

To finalise PV characterisation, the short circuit current (J_{sc}) of the best performing *p*-doped Si/PSI-LHCI and *p*-doped Si/19AA cyt c_{553}/PSI-LHCI devices was measured by photochronoamperometry. The J_{sc} value is regarded in the realm of photovoltaics as possibly one of the most important values of a solar cell, as it displays the photocurrent generated when

the voltage across the circuit of the cell equals 0. As observed in **Figure 103**, biopassivation of *p*-doped Si substrate by the 19AA linker cyt variant causes a 20-fold J_{sc} value increase compared to that of that of the PSI-LHCI/*p*-doped Si device devoid of cyt.

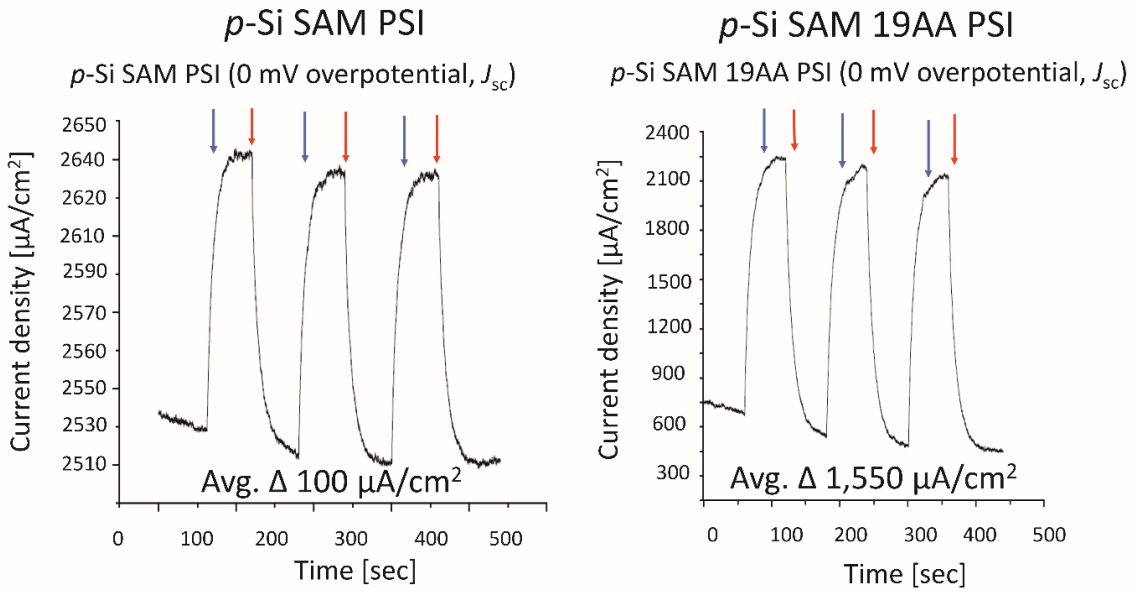

Figure 103

Photochronoamperometric determination of short circuit current (J_{sc}) within the best performing PSI-LHCI/*p*-doped Si and PSI-LHCI/19AA cyt c_{553}/*p*-doped Si biophotovoltaic devices. No overpotential was applied to determine J_{sc} parameter. Blue and red arrows symbolise light on and off, respectively. Current density values on the *y*-axis have been rescaled for clarity.

4.6.4 Concluding remarks

Two novel generation of nanodevices have been constructed which demonstrated that the presence of the 19AA linker enhances direct electron transfer between photoactivated *p*-doped Si and PSI-LHCI, in comparison to the devices with *p*-doped Si and PSI-LHCI alone, as proven by a marked V_{oc} enhancement of 333 µV in the presence of the 19AA cyt variant. Although a great degree of variation was observed in terms of the photochronoamperometric curves, the record photocurrent densities of 104-234 µA cm^{-2} were produced for PSI-containing devices devoid of cytochrome, being the highest reported to date for mediatorless all-solid-state PSI-LHCI-functionalised nanodevices, when an overpotential of -250 mV is applied [128,222,233,243]. In a similar device, featured by Jennings, Cliffel and colleagues, a

maximum photocurrent density of 127 μA cm^{-2} was reported when an overpotential was applied falling well in line with our results [222]. More recently, the same group featured a design with an polyaniline (PAni) polymer and a TiO_2 substrate when an overpotential was applied, reporting photocurrent densities of 72-100 μA cm^{-2}, also falling well in agreement with our results [128]. Due to the novelty and originality of our design, we could only find two reports in the literature which display a complete mediatorless setup, which, as aforementioned, produced photocurrents with similar values to ours [128,222]. We do not find it suitable or appropriate to compare our results with reports that employ in-solution mediators and/or electrolytes, as the photocurrent values reported barely exceed 15 μA cm^{-2} due to diffusion based energy loss [129,139,221,233,243,244]. Morevoer, we could clearly see the effect of cyt-evoked biopassivation of *p*-doped Si by comparing the measured the J_{sc} values for the best performing PSI-LHCI/*p*-doped Si and PSI-LHCI/19AA cyt c_{553}/*p*-doped Si devices. **Figure 103** shows that upon biopassivation, the J_{sc} current density is increased approximately 15-20 times in the biopassivated device compared to the device devoid of cyt c_{553}. Morevoer, this J_{sc} current density value (1,550 μA cm^{-2}) is the highest reported to date for any mediatorless all-solid-state PSI-LHCI containing device [128,222].

Although the results presented in this chapter are very promising, further optimisation of the device construction is required, e.g., optimisation of PSI-LHCI layer thickness and importantly, Ag contact construction and adhesion, to improve the reproducibility of photocurrent generation in the PSI/cyt-containing devices, which would aid the rigorous photoelectrochemical/photovoltaic assessment of the produced biovotovoltaic devices. Nonetheless, sealing the biological modules, such as extremophilic PSI-LHCI and cyt c_{553} proteins, with a thin layer of SiO_2 seems to aid tremendously in stabilisation of the modules and encapsulation of these robust biological modules. Furthermore, it should be noted that the photovoltaic/photoelectrochemical assessment of these devices was performed six months after construction of the devices, attesting once again to the unprecedented robustness of the photosynthetic biological modules of *C. merolae*. Additionally, these biological modules seem to be stable despite the rather aggressive chemical treatment during their incorporation into the biophotovoltaic devices (see Matarials and Methods). Therefore, the biological components employed in this study hold a great promise for construction of these all-solid-state mediatorless nanodevices with even higher efficiencies than those reported here (see **Table 23**).

Chapter 5 Discussion and future outlook

The soluble electron carrier responsible for transfer of electrons from cytochrome b_6f complex to photooxidised PSI-LHCI in *Cyanidioschyzon merolae* is cyt c_{553}. Once the electron carried by cyt c_{553} is used to reduce photooxidised $P700^+$ reaction centre, this complex undergoes a subsequent photo-event leading to the formation of its characteristic photoexcited state $P700^*$. The electron is then ejected from the primary electron donor and transferred *via* a highly organised chain of redox cofactors down the energy gradient to the terminal [4Fe-4S] cluster, F_B. The formation of $P700^*$ species occurs at unparalleled, almost 100% quantum efficiency, and the main limiting step is the re-oxidisation and re-reduction of P700 by cyt c_{553}. This important aspect of the primary events of photosynthesis, along with the essential bioenergetic properties of the redox cofactors involved in the electron transfer (respective E_m values of all redox transfer cofactors, including the haem mid-point potential of cyt c_{553}) prompted the working hypothesis of this PhD work, that the presence of cyt c_{553} in novel nanoarchitectured biosolar cells and solar-to-fuel devices, as well as plasmonic nanoconstructs would play a critical role in enhancing the energy transfer at the interface between the electrode/plasmonic nanostructure surface and the PSI photoelectroactive modules. Understanding the intricacies of electron transfer within the interfaces of specifically structured bionanodevices which incorporate nature's most efficient photoconverter known to mankind, namely the PSI complex, remains the major challenge in biosolar research, and this PhD work set out to address this important issue.

Purification of highly homogeneous PSI-LHCI sample devoid of peripheral light harvesting antenna for PSII, phycobilisomes (PBSs), was proven to be a non-trivial task, as described in detail in **Chapter 4.1**. As evidenced by **Figure 41**, after the multistep purification no detectable functionally-coupled PBSs remained present in the purified PSI-LHCI sample used in this study for construction of various configurations of solar-converting bionanodevices. These results contrast with the work of Hippler and colleagues, who detected a small pool of PBSs that seemed to be energetically coupled with the PSI-LHCI complex from *C. merolae* [97]. The present study showed that a small amount of allophycocyanin and phycocyanin were still present in the final PSI-LHCI sample, albeit most likely as an impurity, as it did not interact functionally with the PSI-LHCI RC, as shown by steady state 77K emission and excitation spectroscopy analyses (**Figures 41** and **42**). One of the reasons which could explain this discrepancy is the fact that Hippler and colleagues employed a different

purification strategy. As mentioned in **Chapter 4.1.3**, the purification strategy differed in that in our case, the PSI and PSII complexes were separated first through a two-step AEC protocol followed by sucrose gradient fractionation rather than starting from sucrose gradient fractionation followed by an AEC step as reported by Hippler and colleagues [97]. Moreovoer, there AEC step was based on a $MgSO_4$ gradient for elution of the PSI-LHCI supercomplex in contrast to NaCl employed in this study, which has a much higher ionic strength than $MgSO_4$. Moreover, Hippler and colleagues purified a subpool of the PSI-LHCI [97] complex from low light conditions, in contrast to medium light conditions used in the present study. Our single particle analysis of the *C. merolae* PSI-LHCI complex (data not shown) has shown the existence of the additional protein density in the LHCI complex, corresponding to the additional Lhcr subunits over and above the 4 Lhca subunits of the LHCI complex identified in the crystal structure of higher plant PSI-LHCI complex [3,64,65].

As discussed in **Chapter 1.2.3.2**, higher plant LHCI contains over 100 molecules of pigments including Chl*a*, Chl*b*, carotenoids (*β*-carotenes, violaxanthin and lutein) [245]. In red algae, the LHCI complex is composed of a varying number of the Lhcr subunits whose genes are encoded in the chloroplast genome [87]. It is now well established that phototrophs are able to remodel their antenna as a photoprotective adaptation to different light conditions [24,81,246]. Interestingly, *C. merolae* PSI-LHCI complex undergoes remodelling of its LHCI antenna under varying light conditions [91], as one of the mechanisms underlying its high robustness in high light. However, the precise molecular mechanisms underlying the photoprotection of the *C. merolae* PSI-LHCI complex are beyond the scope of this PhD thesis.

The highly stringent purification methodology was developed in the present work which yielded large amounts of highly active PSI-LHCI supercomplex which was subsequently used for the *in vitro* hydrogen production studies (**Chapter 4.3**), construction of novel AgNW plasmomic nanodevices (**Chapter 4.4**) and engineering of the various classes of biophotoelectrodes (**Chapter 4.6**). A more stringent purification procedure which was developed after the completion of this PhD study yields the PSI-LHCI samples completely devoid of PBSs [91], however, for the purposes of this project, the level of purity of this complex following the procedure developed in this study was sufficient. Additionally, the purification procedure optimised in this study was suitable for rapid production of mg amounts of highly active and stable PSI-LHCI complex, with yields ranging from 10% to 27.5% (see **Figures 35** and **36**) [91]. This was deemed advantageous as many optimisation protocols

(particularly for **Chapters 4.3**, **4.4** and **4.6**) required considerable amounts of PSI-LHCI (for instance, the functionalisation of the biophotoelectrodes required 500 µg Chl*a* per *p*-Si wafer).

Another protein used in this study was cyt c_{553}. This protein was produced in mg amounts and was successfully incorporatred in the bioelectrodes, using five different cyt c_{553} variants differing in the respective orientation and distance of the haem group with respect to the electrode surface. To this end, a relatively rapid and robust overexpression system was developed to produce redox active, homologous cyt c_{553} variants (**Chapter 4.2**). The *E. coli*-based overexpression system presented here is, to the best of our knowledge, the most robust expression system for these *c*-type class-I photosynthetic cytochromes [153,170,178–181]. With yields in the range of 12.5-25 mg of pure redox active cyt c_{553} protein per 1 L of *E. coli* cell culture, a reasonably low number of preparations were sufficient for the production of all the devices produced in this PhD project.

Once the optimisation of the purification protocol for both biological components of the biophotovoltaic devices was completed (see **Chapters 4.1** and **4.2**), the PSI-LHCI photoactive module was employed for construction of novel biophotoelectrodes, in a series of configurations which led to understanding of how the cyt c_{553} and PSI-LHCI complexes interact *ex vivo* (**Chapters 4.3**, **4.4** and **4.6**) during conversion of solar energy into photocurrents or molecular hydrogen. They also showed that by building a specific and highly ordered nanoarchitecture of both complexes on plasmonic nanostructures, such as AgNWs, it was possible to enhance the specific plasmonic interactions between the plasmonic surface of the nanowires and PSI-LHCI fluorophores, in the presence of cyt c_{553} (**Chapter 4.4)**.

The present work provides the strongest evidence that cyt c_{553} enhances energy transfer to PSI-LHCI in an *ex vivo* configuration, as shown by fluorescence enhancement observed for PSI-LHCI/cyt c_{553}/AgNWs nanoconstructs (**Chapter 4.4**, **Table 21, Figures 82-85**). Moreover, such plasmonic interactions have led to substantial extension of the absorption cross-section of the PSI-LHCI supercomplex, as evidenced by fluorescence enhancement following excitation of the PSI-LHCI/cyt c_{553}/AgNWs nanostructure at 535 nm, the wavelength that is normally poorly absorbed by the PSI-LHCI complex (**Table 21** and **Figure 84**). This phenomenon was not observed in the absence of cyt c_{553}, indicating that the presence of the native electron donor not only orients the PSI-LHCI fluorophore properly with its donor side towards the plasmonic nanostructure, but it also ensures that the plasmonic interactions are very specific and involve the discrete Chl subpools which are normally 'blind' (**Figures 80-85** and **Table 21**, **Chapter 4.4**). Consequently, highly oriented nanoarchitecture of PSI-

LHCI/cyt c_{553}/AgNWs displayed for the first time specific plasmonic interactions that led to improvement of the light harvesting functionality of PSI-LHCI. This discovery, described in **Chapter 4.4,** is important for developing a rational approach to constructing viable and highly efficient biosolar cells and solar-to-fuel devices. Furthermore, no fluorescence quenching was observed for such PSI-LHCI/cyt c_{553}/AgNWs nanostructures, which is normally not the case for these novel type of plasmonic devices [247–249]. This property is not desirable, as fluorescence quenching results in energy loss.

A possible explanation could be, that in a spatially highly organised configuration, i.e., whereby PSI-LHCI complexes are oriented uniformly on AgNWs by cyt c_{553}, plasmon-resonance energy transfer (PRET) and fluorescence-resonance energy transfer (FRET) events dominate, having the packets of energy move unidirectionally towards the tips of the wires. This could explain why such high values of emission were observed at the tips of the AgNWs upon bioconjugation with cyt c_{553} and PSI-LHCI. The specific nanoarrangement of PSI-LHCI by means of its domain-specific intermolecular interaction with cyt c_{553} lends itself to the construction of a super macromolecular-PSI-LHCI-complex in the shape of nanowires, which could in principle explain such pronounced emission intensity at the tips of the wires. Nonetheless, given the remarkable plasmon enhancement of fluorescence phenomena observed in such highly organised nanoarchitectures of PSI-LHCI, this novel bioengineering approach provides a possible alternative route to outperform current photoconverting platforms employed in solar-to-electric and solar-to-fuel nanodevices.

As discussed by Wang and colleagues [216], artificially structured plasmonic materials are versatile in light harvesting and energy conversion. Employing a simple and scalable design of near-percolating silver nanostructures, Wang and colleagues [216] elegantly demonstrated that the light-harvesting efficiency of Chls can be drastically enhanced by tuning the plasmon frequency of the constituent silver nanoparticles (or nanoarchitecture, in this case silver films) to coincide with the maximal photon flux of sunlight. They demonstrate that the photon upconversion efficiency was readily enhanced by more than a factor of twenty. Their findings suggest that Chls can serve as the molecular building blocks for ultra-high-efficiency light harvesting and solar energy converting nanoconstructs. Although in our findings (**Chapter 4.4**) we did not calculate photon upconversion efficiency, we observed very significant (almost by a factor of 50, see **Table 21**) fluorescence enhancement factors at the tip of AgNWs bioconjugated with cyt c_{553} and PSI-LHCI, demonstrating that organised, energetically compatible supramolecular emission is the key to improving efficient photonic

absorption and emission for viable future artificial leaves. Indeed, Friebe and colleagues have recently demonstrated that deposition of purple bacterial reaction centre and its associated light harvesting complex (RC-LH1) on two different types of nanosctructured silver yielded very high photocurrents even at relatively low fluorescence enhancement factor of 2.5 [207].

In the context of the results presented in **Chapter 4.4**, it is desirable to employ highly robust PSI-LHCI from extremophilic eukaryotes due to the inherent high photochemical activity of this photoconverter (**Chapter 4.1, Figure 42**) and the very reasonable fluorescence enhancement factors obtained upon plasmonic interaction (**Chapter 4.4, Table 21**). As it is well established that the plasmonic properties of metallic nanostructures can be tuned depending on the size and shape of the metallic nanostructure, one could envisage the system where the ideal nanostructure is designed, produced and employed with PSI-LHCI and cyt c_{553} in such a fashion such that the distance between PSI-LHCI and the nanostructure is optimised, while the distance between adjacent PSI-LHCI complexes is also optimised (which incidentally is the case here for AgNW) resulting in the scenario where the fluorescence enhancement factor is maximised.

Perhaps the strongest evidence of cyt c_{553}'s importance as electron transfer cofactor between an arbitrary sacrificial electron source and P700 is the fact that, as expected, in the absence of cyt c_{553} there is no *in vitro* H_2 production, when PSI-LHCI interacts with the proton reducing catalysts (PRCs), as shown in **Chapter 4.3** (**Figure 75**). This was demonstrated before [130,140,192,195] for cyanobacterial PSI/cyt c_6/PRCs reconstitution assays, and the present study supports this observation. The importance of these experiments is evident, as molecular hydrogen, will most likely become the fuel of the future [113] (section **4.3.4** of **Chapter 4.3** is highly recommended). Although the hydrogen-based economy seems nowadays an idealistic dream, scientifically it is important to state that molecular hydrogen is in fact the most energy dense fuel known to mankind after uranium, thorium, plutonium and tritium (specifically hydrogen gas compressed at 700 bar, which has an energy density of 1,555 Wh L^{-1} or a specific energy of 39,443 Wh kg^{-1}) [182]. Although the results presented here are preliminary, they hold the great potential for scaling up H_2 production using cheap, self-renewing and non-toxic biological photoelectroactive components, such as PSI, acting in tandem with novel PRCs to yield this clean solar fuel. As reported by Gross and colleagues [250], after prolonged illumination most DuBois-type Ni catalysts, such as those used in this study, suffer from photobleaching and ultimately undergo photodegradation. Therefore, finding alternative routes to stabilise these PRCs is highly desirable. The work presented in

Chapter 4.3 shows that PSI-LHCI/PRC hybrid systems are highly photostable, as they produce hydrogen with TOF values that were 3-fold and 16.6-fold higher than those published for cyanobacterial PSI/PRC hybrid systems employing cobaloxime [130] and a similar Ni mononuclear PRC [196], respectively. In contrast to the work published by Utschig and colleagues [130,192,195], these hydrogen production rates were obtained under intense white light illumination (8,130 μE m^{-2} s^{-1}). Although it was not possible to record the real-time hydrogen production data due to technical obstacles and only hydrogen yields after 16 h of continuous illumination were assessed, it is believed that the hydrogen evolution proceeded until the complete exhaustion of the electron donor, ascorbate.

Investigation of the process of electron transfer at the interface between the *p*-doped Si surface and immobilised His_6-tagged cyt c_{553} revealed that incorporation of this electroactive protein at the electrode surface results in considerable lowering of dark saturation currents (**Figure 92** and **Table 22**, **Chapter 4.5**). These type of currents, quantified by the recombination parameter (J_0), reflect the degree of semiconductor surface charge recombination, which is the intrinsic property of each type of semiconductor material [158]. Results in **Chapter 4.5** show that the length of the peptide linker engineered within the cyt c_{553} structure play a significant role in modulating the dark saturation currents of the bioelectrodes, whereby longer linkers result in lower dark saturation currents, whereas shorter linkers result in the largest, compared to the non-biofunctionalised control (**Table 22, Chapter 4.5**). As suggested by Amdursky and colleagues [251,252], this could be attributed to the ability of the haem group to relax electronically upon excitation from dark saturation inherent electrons at the interface. As shorter, more rigid linkers are likely to place the haem group closer to the *p*-Si surface (as evidenced by our 2D thermodynamic maps, see **Figure 90, Panels A** and **B**), there is a very low probability of the haem group relaxing electronically and hence, higher J_0 recombination currents are observed (**Figures 92** and **93, Table 22, Chapter 4.5**). On the other hand, longer, more flexible linkers allow larger structural flexibility of the haem group with respect to the *p*-Si surface, resulting in the higher probability of haem relaxation and significantly lowering the surface charge recombination (7.5 x 10^{-3} mA cm^{-2}, see **Table 22**), resulting in considerably lower J_0 values (**Figure 92, Chapter 4.5**). This hypothesis is also supported by the bioinformatic analysis of the Gibbs free energy distribution (see **Figures 89** and **90**) which shows that longer linkers have higher degrees of flexibility and result in transitory states where the haem group is placed at a further distance with respect to the surface of the *p*-Si electrode.

This mechanistic hypothesis could explain the significant differences in J_0 values depending on the cyt c_{553} variant used in this study. Furthermore, this study suggests that the ideal geometry for electron transfer from the *p*-doped Si surface to the haem group is that of parallel plane configuration, i.e., when the haem group is in parallel configuration with respect to the surface of the *p*-doped Si. Interestingly, the 0AA linker variant of cyt c_{553} introduces an aberrant behaviour when immobilised on the Si surface, yielding a J_0 value either very close to the non-functionalised control or significantly lower (see **Table 22**). Such anomalous behaviour of this class of biolelectrodes can be explained by the severe geometrical restriction imposed on the haem group by the lack of any peptide linker, whereby the haem might be either in perpendicular or parallel orientation with respect to the Si surface. Interestingly, the Gibbs free energy mapping supports this hypothesis, as clearly two distinct populations of thermodynamically feasible conformations of the immobilised 0AA linker cyt *c* variant can be distinguished (**Figure 90, Panel A, Chapter 4.5**). As the 19AA linker variant is the only one that possesses sufficient flexibility such as to allow a more favourable parallel alignment with the Si surface (see **Figure 92** and **Table 22, Chapter 4.5**), it would explain why these two ($0AA^b$ and the 19AA variant) possess reasonably similar J_0 values (2.8×10^{-3} and 7.5×10^{-3} mA cm^{-2}, respectively).

In order to verify whether the cyt c_{553} linker variants genetically engineered in this study would exert the same effect in the complete PSI-LHCI-containing biophotovoltaic devices, five types of PSI-LHCI/cyt c_{553}/Si biophotoelectrodes were constructed which incorporated a thin layer of PSI-LHCI on top of a cyt c_{553} variant layer (**Chapter 4.6, Figure 94**). Moreover, two controls composed of Si/PSI-LHCI and Si with Ni-NTA SAM were used as the reference devices to assess the effect of incorporation of cyt c_{553} variants on the overall electron transfer in the all-solid-state biophotovoltaic devices prepared in this study. The open-circuit potential analyses showed that the 19AA linker variant enhanced direct electron transfer within the devices, as evidenced by a 333 µV increase of V_{oc} upon illumination compared to the PSI-LHCI/*p*-doped Si electrode devoid of cytochrome. This is the most significant result of the PV analysis, as for the open-circuit potential measurements no external bias is applied, thus, only electrons responsible for incrementing the potential are those which are photo-generated, as discussed by Jennings and colleagues [243]. Therefore, by biopassivating the *p*-doped Si surface with the 19AA cyt linker variant the direct electron transfer was improved, as measured by the V_{oc} potential increase compared to the electrode with PSI-LHCI alone (**Figure 101**, **Chapter 4.6**).

The results of **Chapter 4.6** go well in agreement with those presented in **Chapter 4.5**, whereby three independent experimental approaches demonstrated that the 19AA linker variant of cyt c_{553} is the best biopassivator of all the cyt c_{553} linker variants genetically engineered in this study. Subsequently, these results were confirmed in a fully operational all-solid-state mediatorless artificial leaf composed of *p*-doped Si, 19AA cyt c_{553} variant, and the robust red algal PSI-LHCI complex. Although the devices presented a great degree of variability in terms of their PV performance due to imperfections in the Ag bottom contacts along with significant defects present in the *p*-doped Si, as evidenced by SEM imaging (**Figure 91, Chapter 4.5**), the data obtained in this study was obtained from three independent nanodevices that were constructed in an identical fashion. Furthermore, after application of an overpotential of -250 mV photocurrent densities were generated in the range of 104-234 μA cm^{-2}, placing them among the highest photocurrents reported to date for all-solid-state mediatorless PSI-LHCI-based nanodevices (**Figure 98**) [128,222,233,243]. Moreover, the PSI-LHCI/19AA cyt/*p*-doped Si devices display the highest short circuit current density (J_{sc}) reported to date for any PSI functionalised all-solid-state mediatorless device [128,222], a spectacular 1,550 μA cm^{-2}. It is impoprtant to clarify that the the short circuit current is the current across the solar cell when the voltage across the solar cell is zero (**Figure 98**).

Table 23 summarizes the performance of selected devices featured in this work compared to the most similar prototypes, namely those from Jennings, Cliffel and colleagues [128,222]. Biopassivation of *p*-doped Si substrate by the 19AA linker cyt variant enhances the external power conversion efficiency (η) of the device by 20-fold compared to the PSI/*p*-doped Si devices without cyt. The biopassivation effect exerted by 19AA cyt variant was also demonstrated by over 15-fold increase in the short circuit current (J_{sc}), when both types of the biophotovoltaic devices are compared (**Figure 103**). Perhaps one of the reasons why our power conversion effiency values are so low compared to those of Jennings, Cliffel and colleagues [128,222] is non-homogeneous PSI-LHCI loading on top of the cyt c_{553} layer (in case of the 19AA functionalised device) or on top of the *p*-Si surface (in the case of the device devoid of cyt c_{553}). This could be the case as it is difficult to control the PSI-LHCI orientation within such devices. Specifically, P700 should be oriented towards the *p*-Si surface or the cyt c_{553} haem for efficient cathodic photocurrent production. Furthermore, a homogeneous monolayer dispersion is challenging to achieve when employing vaccum-assisted spin coating. To overcome this, more sophisticated PSI-LHCI sealing techniques should be employed, such as confined-plume chemical deposition (CPCD) to obtain highly nanostructured PSI-LHCI/*p*-

Si or PSI-LHCI/cyt c_{553}/*p*-Si layers. An alternative technique could be to employ a redox active nanostructuring polymer as the interface between the substrate and PSI, such as PAni [128] or improve the direct electron transfer from the F_B cluster on the reducing side of PSI by application of ZnO layer [223]. Nonetheless, the fill factor (FF) values obtained in this study are comparable to those of the similar type all-solid-state mediatorless biophotovoltaic devices based on PSI (see **Table 23**). The FF parameter is important, as in conjunction with V_{oc} and J_{sc} parameters, it determines the maximum power output of a solar cell.

Table 23

Comparison of PV performance of all-solid-state mediatorless PSI/*p*-doped Si biophotovoltaic devices

Device configuration	J_{sc} **[μA · cm^{-2}]**	V_{oc} **[V]**	***FF***	η **[%]**	**References**
p-Si/19AA/PSI	1,550*	0.001333*	0.3[1]	0.0006[1]	this work
p-Si/PSI	100*	0.001*	0.3[1]	0.00003[1]	this work
p-Si/PSI/ZnO/ITO	127	0.214	0.28	0.0077	[222]
PAni/PSI/TiO_2/SnO_2	72	0.299	0.42	0.0091	[128]

J_{sc}; short circuit current, the current density when the voltage across the device is 0 V (**Figure 103**)
V_{oc}; open circuit voltage or open circuit potential (the photovoltage generated when no bias is present across the circuit) (**Figure 101**)
FF; fill factor
η [%]; external power conversion efficiency of the biophotovoltaic device
The performance of the listed solid state biosolar cells was evaluated at standard white light illumination of 100 mW cm^{-2} (AM 1.5) (See **Chapter 3.2.9.4**)
* values were estimated for selected electrodes with the best performance. As mentioned in **Chapter 4.6**, significant variability was observed between devices due to fragile construction.
[1]Calculation of fill factor and efficiency was performed with the open circuit voltage for the estimated values presented in the table assuming an ideality factor of 1 (n = 1) and a temperature of 300 K, as specified in **Chapter 3.2.9.4.**

Although mediatorless all-solid-state biophotovoltaic devices carry a number of advantages over mediated ones, including minimisation of charge recombination at the interfaces, eliminating toxicity of external mediators, avoidance of corrosion of metal electrodes, avoidance of mass transfer limitations, and avoidance of device failure caused by leaks [128,222,233,234,243], they also present certain challenges mainly due to limited stability of redox active species upon illumination, poor protein loading and non-uniform

orientation of the photoactive proteins with respect to the electrode substrate. A semi-solid-state/solution-based system would potentially allow for more flexibility of the haem groups in the cyt c_{553} variants depending on the peptide linker used. Ultimately, this could result in more efficient electron transfer from the haem groups to $P700^+$ but could also be energetically costly, as electron/hole pairs could recombine in solution, and mass transfer could dominate the mode of electron transfer in such devices [238].

In the work presented by Beam and colleagues [222], the biophotovoltaic device composed of *p*-Si, spinach PSI-LHCI, ZnO and indium tin oxide (ITO) exhibited a photocurrent density shift of 5 µA cm^{-2} when illuminated in a photo-electrochemical cell configuration with the electrolyte. In contrast, when the device was characterised in the all-solid-sate mediatorless mode, it displayed a photocurrent density shift of 15 µA cm^{-2}. That is an increase of 10 µA cm^{-2}, a rather significant gain in photocurrent density and a very clear example as to why the mediatorless all-solid-state configuration is more advantageous over the electrolyte/mediator photo-electrochemical cell configuration, which, as evidenced above, is energetically expensive and limiting in terms of competent electron transfer. The all-solid-state nanodevice presented in this study which incorporated the cyt c_{553} 19AA linker variant as the biopassivator of the semiconductor may hold the key to solving the problem of electron dispatchability at the interface between the semiconductor photo-active substrate (in this case *p*-doped Si) and PSI-LHCI, the latter serving as the photoactive module of the device.

In brief, it is shown by construction of three independent devices, i.e., (i) PSI-LHCI/cyt c_{553} AgNWs, (ii) hydrogen reconstitution assays, (iii) Ag/*p*-doped Si/cyt c_{553}/PSI-LHCI/Ag all-solid-state mediatorless biophotoelectrodes, that cyt c_{553} is not only essential for electron donation to P700, but actually critical for competent energy transfer between plasmonic nanoarchitectures and semiconducting substrates, leading to ameliorated electron transfer between the Si substrate and cyt, and lowering of the surface charge recombination events within the Si bioelectrodes. Importantly, a high degree of specific orientation of PSI-LHCI complex on cyt c_{553}/AgNWs leads to an improved absorption cross-section of the PSI-LHCI complex. Significantly, enhanced open-circuit potential increments when in the presence of the 19AA linker variant as a redox active solid-state mediator evidence and confirm biopassivation by this particular cyt c_{553} linker variant at the all-solid-state interface. Moreover, in the absence of cyt c_{553} hydrogen production *in vitro* reconstitution assays do not produce hydrogen (see **Figure 75**, **Chapter 4.3**), attesting once again to the criticial role that

cyt c_{553} plays in mediating electron transfer to P700, whether in solution or at the all-solid-state interface.

This study culminated with the purification, isolation and characterisation of PSI-LHCI of sufficient quality and quantity for employment in semi-solid-state, *in vitro* hydrogen production assays and all-solid-state set-ups. It produced a sufficiently robust cyt c_{553} *E. coli* based overexpression system (as a matter of fact the most robust reported to date) [153,170,178–181] such that sufficient amounts of five different variants of redox active, fully-operational cyt c_{553} were successfully isolated, purified and characterised.

As Si photovoltaics is expected to dominate the clean energy market by 2030 [113], the results of this study greatly support this technology and open it to "green' approaches. Nevertheless, considerable efforts will be necessary to overcome the main bottlenecks that hamper improvement of power conversion efficiencies of Si/PSI-based biophotovoltaics. First and foremost, overcoming the technical challenges associated with the construction of the Si biophotovoltaic devices is of paramount importance. The main factors responsible for lowering the overall performance of such devices are related to Si doping, contact adhesion, contact construction, and homogeneous doping. Another important technical challenge is homogenous (photo)electroactive protein loading and stability. In order to improve the latter aspect, electrospray should be employed in conjunction with spin coating, this way, homogenenous protein deposition in entire areas of the semiconductor can be ensured. The latter should be confirmed with subsequent profilometry analysis. Once all these aspects are optimised, the electron dispatchability issue should be addressed. As emphasised in this work, a novel type of biological, robust redox active all-solid-state mediator is proposed by employment of a variant of cytochrome c_{553}. This, in conjunction with improvement of material quality (either by improving doping technology or by more advanced Si processing techniques) should advance and ultimately optimise competent electron dispatchability.

This work shows that for improvement of direct electron transfer and overall power conversion efficiency of the all-solid-state mediatorless devices biopassivation with redox active cyt c can be successfully applied. The performance of such devices may be further improved by application of plasmonic photo-converting biohybrids with well-defined architecture of the biological photoconverter, such as PSI-LHCI used in this study, so that the light harvesting properties of the latter are maximised. In addition, application of solar thermophotovoltaic converting (STPV) technology to miminise energy losses by dissipation and maximise energy re-adsorption by means of an optical filter and a thermal emitter could

also be advantageous for PV performance improvement. These technologies, together with other developments in the field, shall culminate with breaching the Shockley–Queisser limit and subsequent achievement of spectacular and unanticipated solar-to-electric efficiencies, concluding in a cost-effective, clean, scalable, non-toxic technology that will prove viable.

In an even more ideal, yet quite plausible configuration, PSI-based biophotovoltaic device could be linked to photostable robust proton-reducing catalysts, such as those used in this study, that would work in conjunction with PSI to produce hydrogen in a prolonged, and perhaps even intermittent fashion at equatorial illumination intensities. Four important factors are considered in the pursuit for the 'ideal' artificial leaf: (1), power conversion efficiency; (2), robustness; (3), scalability; and (4), cost-effectiveness. The main challenge to date is the efficient production and proper interfacing of all the required components of a robust, scalable, cost-effective and most importantly, an efficient artificial photosynthetic device capable of producing fuel from water upon solar illumination [9]. Redox compatibility and efficient energy transfer seem to embody the main bottleneck. Therefore, a thorough characterisation of new materials and stringent selection of appropriate working conditions is of paramount importance [253]. Furthermore, the spatial organisation of the building modules chosen for a particular solar fuel system may have a significant impact on the overall power conversion efficiency due to the potential losses associated with chemical transport processes or parasitic electrical resistances inherent to certain solar-to-fuel device geometries [253]. An additional limitation arises from the physical combination of all the components into a fully operational water-splitting/fuel producing device. A proper example is the assembly and construction of a half-cell photoelectrode. The most efficient catalysts do not always produce the most efficient assemblies when placed on the most efficient light absorbing materials [253]. As mentioned previously, scalability and cost-effectiveness seem to be currently the most limiting factors in the field [9]. The term "scalability" is often mistakenly equated to the employment of earth-abundant materials for the construction of scalable, cost-effective artificial photosynthetic devices. This is certainly not the case. Other important factors must be taken into consideration, most pointedly the relationship between elemental abundance, capital and raw materials costs [9,253].

Currently, great efforts are undertaken in the PV field to optimise hydrogen storage, transport and safety, but once this technology is optimised, we shall finally achieve the holy grail of sustainability, and at long last, our quest for the ultimate sustainability of energy consumption and production, shall conclude. The Oxford dictionary defines the word 'quest'

as “a long or arduous search for something.” We do not have to look very far to learn what is left to be learnt to complete successfully a quest for the sustainable energy production. As evidenced by this PhD thesis, nature can teach us a great deal, and it is possible to use nature for the service of humanity. Nature, as it always has, and always will, holds within the bowels of its molecular machinery, the answer.

Chapter 6 Summary

6.1 Summary

In the quest for a viable, scalable, non-toxic and cost-effective artificial leaf incorporating nature's most efficient photoconverter, i.e., PSI, one must overcome the challenges presented by our current lack of knowledge regarding the intricacies of electron transfer within the modules of the bioelectrodes and at the interfaces within. In this study, it is demonstrated by three independent approaches, i.e., (*i*), construction of PSI-LHCI/cyt c_{553} AgNWs; (*ii*), photo-driven *in vitro* hydrogen production assays, and (*iii*), construction of Ag/*p*-doped Si/cyt c_{553}/PSI-LHCI/Ag all-solid-state mediatorless biophotovoltaic devices, that by employing the PSI-LHCI photoconverter together with its native electron donor, cyt c_{553}, significantly improved energy and electron transfer is achieved within such novel devices.

The specific nanoarchitectures described in this study involved orienting the robust extremophilic PSI-LHCI complex within a highly ordered architecture, i.e., with its donor side towards the semiconductor substrate or a specific plasmon-generating nanoconstruct of silver nanowires. To this end, cyt c_{533} was used as it specifically interacted with the domain of PSI-LHCI in the vicinity of the P700 primary electron donor. This 'orienting' molecular approach allowed for the energy packets (in the form of surface plasmons) to migrate more efficiently to the specific subpools of fluorophores present in the PSI-LHCI structure, or transfer electrons at a sufficient kinetics to drive the catalytic reduction of protons into molecular hydrogen by proton reducing catalysts upon their adsorption onto the acceptor side of PSI-LHCI complex. Moreover, in an all-solid-state configuration, application of a cyt c_{553} 19AA peptide linker variant facilitated competent electron transfer to P700, as evidenced by an open-circuit potential increase of 333 μV, as well 15-fold increase of the short circuit current upon illumination compared to a non-functionalised control. These results are consistent with minimisation of the J_0 recombination parameter recorded for the *p*-doped Si electrode which incorporated 19AA cyt c_{553} linker variant on its surface.

This PhD thesis is a testament to the fact that we still have a great deal to learn from Nature. Understanding the electron transfer modes and kinetics at the interfaces of biophotoelectrodes is important, as such knowledge will ultimately allow for the development of rational design of viable solar cells and solar-to-fuel nanodevices. The incessant and indiscriminate consumption of billions of years worth of photosynthesis (by burining fossil

fuels) will only last a couple of decades, and after that is up to us to find a way to harness and convert solar energy into clean carbon-neutral solar fuels, such as hydrogen. The results presented in this PhD thesis demonstrate that extraction of two natural components from the extremophilic photosynthetic apparatus and their subsequent employment in a number of rationally designed, highly ordered nanoarchitectures may provide an attractive green alternative to solar energy conversion into photocurrent and solar fuel, such as molecular hydrogen. Although the experimental platforms developed in this study are currently at the laboratory benchtop scale and require further optimisation, their possible scaling up and commercialisation seem to be on a good track to realisation.

As mentioned in the preface of this thesis:

"Nature has a great deal to teach us, and as this thesis shows, we do not need to circumvent nature to improve it. On the contrary, we need to learn, use and exploit nature for the service of the society. If we want to improve nature, we should understand how it works. Most importantly, we should understand the intricate molecular processes that exist in natural photosynthetic systems to be able to exploit the newly discovered or improved functionalities of photosynthetic complexes upon their nanostructuring within cheap and scalable solar energy-converting devices."

Julian David Janna Olmos

6.2 Podsumowanie

Optymalizacja procesów transferu energii i transferu elektronowego w biofotowoltaicznych nanourządzeniach zawierających fotosystem I oraz cytochrom c_{553} z ekstremofilnego krasnorostu *Cyanidioschyzon merolae*

Wobec zmniejszających się globalnie dostępnych zasobów paliw kopalnych i rosnącego zapotrzebowania na energię, konieczność opracowania wydajnych zielonych technologii pozwalających na konwersję praktycznie niewyczerpywalnej energii słonecznej w elektryczność i neutralne paliwa jest niepodważalna. Jednym z głównych wyzwań technologii biofotowoltaicznych, w których stosuje się wysokowydajne i aktywne fotochemicznie kompleksy białkowo-pigmentowe jako moduły konwertujące energię słoneczną, jest zwiększenie wydajności kwantowej urządzeń biofotowoltaicznych. W tym celu, jednym z najważniejszych zadań badawczych jest minimalizacja procesów rekombinacji ładunku w obrębie biologicznych i syntetycznych modułów, jak również interfejsu biofotoelektrod. Dodatkowym wyzwaniem jest zwiększenie stabilności i homogenności upakowania biofotoaktywnych komponentów.

W ramach niniejszej rozprawy doktorskiej opracowano nowatorską technologię polegającą na zastosowaniu wysokostabilnej naturalnej makromolekularnej maszyny konwertującej energię słoneczną, fotosystemu I (PSI) oraz naturalnego donora elektronów dla tego kompleksu, cytochromu c_{553} (cyt c_{553}), wyizolowanych z ekstremofilnego krasnorostu *Cyanidioschyzon merolae*, do konstrukcji trzech typów nanourządzeń biofotowoltaicznych: (*1*), biofotoogniw w stałej konfiguracji (*ang.*, all-solid-state), zawierających domieszkowany pozytywnie półprzewodnikowy substrat krzemowy (ang., *p*-doped Si) wraz z warstwami fotoaktywnego kompleksu PSI i cyt c_{553}; *(2)*, plazmonowych srebrnych bionanodrutów (AgNWs), funkcjonalizowanych wysokouporządkowaną nanoarchitekturą monowarstw PSI i cyt c_{553}, oraz (*3*), systemu fotokatalitycznej produkcji wodoru cząsteczkowego *in vitro* z zastosowaniem kompleksów hybrydowych PSI wraz z syntetycznymi katalizatorami redukcji protonów (*ang*., proton reducing catalysts, PRC).

Funkcjonalizacja elektrody *p*-Si wariantem cytochromu c_{553}, charakteryzującym się największym stopniem swobody orientacji grupy hemowej w stosunku powierzchni elektrody krzemowej, pozwoliła na efektywną biopasywację tego półprzewodnikowego substratu poprzez minimalizację parametru rekombinacji ładunku powierzchniowego J_0, co z kolei pozwoliło na zwiększenie parametru V_{oc} o 333 µV w biofotoogniwach PSI/cyt c_{553}/*p*-Si, w

porównaniu do kontroli zawierającej PSI/*p*-Si, a pozbawionej cyt c_{553}. Uzyskano fotoprądy w stałych biofotoogniwach PSI/*p*-Si w zakresie 104-234 µA cm^{-2} (przy nadpotencjale -0.25 V), co należy do jednych z najwyższych wartości fotoprądów generowanych przez stałe biofotoogniwa z PSI, w podobnych warunkach pomiarowych. Jednocześnie wydajność konwersji energii słonecznej w fotoogniwach typu PSI-LHCI/cyt c_{553}/*p*-Si była 20-krotnie wyższa, w obecności wariantu cyt c_{553} 19AA, zastosowanego w tych urządzeniech jako biologiczna warstwa biopasywacji substratu krzemowego oraz warstwa kondukcyjna pomiędzy substratem a PSI. Tym samym wykazano, że ów wariant może być zastosowany w urządzeniach biofotowoltaicznych do zwiększenia transferu elektronowego pomiędzy substratem a PSI.

W równoległym i komplementarnym kierunku badań, zastosowanie równomiernej i specyficznie ukierunkowanej nanoarchitektury fotoaktywnej warstwy PSI na plazmonowych nanostrukturach metalicznych AgNWs, sfunkcjonalizowanych uprzednio cyt c_{553}, pozwoliło na znaczące zwiększenie efektywnej absorpcji PSI, w zakresie spektralnym, w którym PSI jest nieaktywny *in vivo*, poprzez aktywację specyficznej puli tzw. czerwonych cząsteczek chlorofilu w obrębie fluoroforów PSI. Tym samym, pokazano, że oddziaływania plazmonowe mogą być efektywnie zastosowane nie tylko do zwiększenia całkowitej absorpcji fotoaktywnych kompleksów białkowych, ale również do aktywacji spektralnej specyficznych pigmentów, wyłącznie w obrębie wysokouporządkowanej i zorientowanej nanoarchitektury tych fotokompleksów na nanokonstruktach plazmonowych. Powyższe nowatorskie podejście badawcze może być w przyszłości zastosowane do konstrukcji nowej generacji urządzeń biofotowoltaicznych o zwiększonej wydajności konwersji energii słonecznej.

Optymalizacja biofotokatalitycznej produkcji wodoru cząsteczkowego z zastosowaniem systemów hybrydowych z PSI i PRC, opartych na kobaloksymie i niklowym katalizatorze mononuklearnym typu DuBois, precypitowanych na powierzchni PSI w roztworze wodnym, pozwoliła na osiągnięcie aktywności wydzielania wodoru odpowiednio, 521 moli H_2 (mol PSI)$^{-1}$ min^{-1} oraz 729 moli H_2 (mol PSI)$^{-1}$ min^{-1}, przewyższając tym samym 3-17-krotnie aktywność wydzielania wodoru w podobnych systemach biohybrydowych i warunkach pomiarowych.

6.3 Conclusiones (en castellano)

En la cruzada por una hoja artificial viable, realizable, ecológica, económica y factible, incorporando el foto-convertidor más eficiente de la naturaleza (el fotosistema I), uno debe superar los obstáculos presentados por la falta de conocimiento en relación con los detalles complicados e intricados con respecto a la transferencia electrónica entre los módulos de bioelectrodos biotecnológicos y particularmente entre sus interfaces. En este estudio se demuestra por tres técnicas independientes que la incorporación del donador de electrones biológico del fotosistema I, el citocromo c_{553}, culmina en transferencia electrónica competente por inyección dirigida a la pareja de clorofilas especializada del centro reactivo del fotosistema I gracias a una nano-geometría ultra-específica. La nano-arquitectura específica descrita en este estudio exigió la orientación del fotosistema I de una manera altamente organizada i.e., con su pareja de clorofilas especializadas dirigida hacia el material semiconductor o en una nano-arquitectura especializada sobre nanocables de Plata. Con este fin, el citocromo c_{553} fue utilizado ya que este tiene una interacción muy específica con el fotosistema I, particularmente con la pareja de clorofilas especializada (P700), la cual es responsable de la separación de carga y de recivir electrones por parte del citocromo c_{553}. Esta estrategia de 'orientación natural' permitió que los paquetes de energía (en la forma de plasmones de superficie) viajaran más eficientemente hacia los fluoroforos del fotosistema I, y también ha culminado en la transferencia de electrones en tal competencia que ha permitido la reducción de protones en hidrogeno molecular por medio de una catálisis dirigida gracias a compuestos adsorbidos en la vecindad del ultimo centro cuaternario de hierro [4Fe-4Fe] (conocido como F_B) del fotosistema I. Complementariamente, en una configuración del estado sólido completo, un variante especifico del citocromo c_{553}, (el variante de 19 amino ácidos descrito en esta tesis) ha demostrado transferencia electrónica super-competente a P700 evidenciado por un incremento de 333 µV cuando el biofotoelectrodo solar construido es iluminado comparado con un biofotoelectrodo idéntico simplemente que no contiene este citocromo y solo el fotosistema I en interface con la silicona. Los resultados demuestran sin duda alguna una reducción considerable de recombinación de carga en la interface de biofotoelectrodos de silicona tipo *p* que incorporan específicamente este variante del citocromo en la superficie del material semiconductor.

Esta disertación doctoral es un testimonio del hecho que aún tenemos mucho que aprender de la naturaleza. Entender los mecanismos de transferencia electrónica y cinética en las interfaces de biofotoelectrodos es de suma importancia ya que este conocimiento

últimamente nos permitirá desarrollar racionalmente un diseño de células solares viable en adición de nano y macro-maquinas que culminen en una eficiencia de conversión solar-a-combustible razonable, viable y comercializable. Nuestra devastación incesante, indiscriminada y agresiva de billones de años de fotosíntesis (en la forma de combustibles fósiles) solo aguantará un par de décadas, en el mejor de los casos, y después de que los combustibles fósiles se agoten es nuestra obligación encontrar la forma de utilizar la luz solar para convertirla en combustibles solares libres de carbón, como por ejemplo, el hidrogeno molecular. Los resultados presentados en esta disertación doctoral demuestran que la extracción de dos componentes naturales del aparato fotosintético de una micro-alga extremofílica acidofílica y su apropiada utilización en un número de nano-arquitecturas altamente organizadas, diseñadas racionalmente, que incluyen en su diseño un material semiconductor ideal para células solares, la silicona tipo *p*, además de la producción *in vitro* de hidrogeno donde el fotosistema I funciona sincronizado con compuestos catalíticos que reducen protones, o con materiales que emiten plasmones de superficie, como por ejemplo nano-cables de Plata, resultan en conversión foto-eléctrica competente, últimamente mejorando las características foto-físicas del fotosistema I o resultando en la producción sostenida de hidrogeno cuando este mismo foto-convertidor es utilizado con su donante natural de electrones, el citocromo c_{553}. Aunque las plataformas experimentales desarrolladas en este estudio solo se encuentran a escala de laboratorio al día de hoy, y sin duda alguna requieren de mucha más optimización, su posible comercialización e industrialización parecen estar en un buen camino hacia la ejecución.

Julián David Janna Olmos

6.4 Special notes from the author

At thirty years of age, and after many personal circumstances over the last seven years, I have come to the realisation of several momentous things. First and foremost, a PhD is a very tough lesson of endurance, fortitude and resolve. Without any of the latter it would be impossible for any doctoral candidate to accomplish their doctorate in full. I cannot deny that it had always been my dream to become a doctor of science. Today, observing and understanding that all my dreams are coming true, I feel that nothing can stop me, and that nothing can get on the way of my success. But most importantly, I have come to the realisation of a critical golden principle. Family is the one and only true wealth in this life. Being away from my family all these years has made me appreciate them more than I ever thought I could, and has made me realise that nothing can buy family love, nothing is more valuable than family and that nothing compares to true family love. Just as my dreams are coming true as I finish writing this thesis, I have faith and strong believe that very soon I shall be reunited with my family, and that very soon, we should all rejoice together to celebrate the love and trust that we so very much profess to each other. Faith has driven me through all these years of hard indefatigable and relentless work, and faith, only through true, passionate and everlasting faith, I will find the means to finally see my family again, and to feel once again the incredible and indescribably happiness and joy of being reunited with those that I always have and always will love.

Julian David Janna Olmos

6.5 Notas especiales del autor (en castellano)

A los 30 años de edad, y después de muchas circunstancias personales durante mis últimos siete años, he alcanzado finalmente el entendimiento de muchos temas transcendentales. Lo primero y lo más importante es que, un doctorado es una lección muy dura de perseverancia, determinación, paciencia y fortaleza. Sin ninguna de estas cuatro cualidades hubiera sido posible doctorarme. No puedo negar que siempre ha sido mi sueño convertirme en un doctor de ciencia. Hoy, observando y concibiendo que todos mis sueños se están haciendo realidad, siento que nada puede detenerme, y que nada se puede interponerse en mi camino al éxito. Pero lo más importante de todo, es que he llegado al entendimiento de un principio dorado. La familia es la única y verdadera riqueza en esta vida. Estar lejos de mi familia todos estos años me ha hecho apreciarlos mucho más de lo que yo pensé sería posible, y me ha hecho darme cuenta que nada puede comprar el amor de una familia. Nada es más precioso que la familia y nada puede compararse al verdadero amor familiar. Así como mis sueños se hacen realidad al terminar de escribir mi disertación doctoral, tengo muchísima fe y creo fuertemente que muy pronto podre estar reunido con mi familia un vez más, y, que muy pronto, junto con mi familia, celebraré el amor y la confianza que mutuamente nos profesamos con pasión. La fe me ha estimulado todos estos años de dedicación y trabajo arduo, duro e incesante, y solo por medio de una fe verdadera, eterna y apasionada, encontraré la forma de volver a estar reunido con mi familia un vez más, para sentir ese sentimiento de alegría tan inenarrable y tan intenso. Por fín, después de tantos años, podre sentir ese sentimiento de estar junto aquellos que amo y que siempre amaré, pese a las circunstancias, el tiempo, o la distancia.

Julian David Janna Olmos

Chapter 7

Appendices and supplementary information

7.1 Equations

$CO_2 + H_2O \rightarrow (CH_2O)_x + O_2$ (**Eq. 1**)

$ATP + H_2O \rightarrow ADP + P_i$ (-31 kJ mol^{-1}) (**Eq. 2**)

P_i + glucose → glucose-6-P + H_2O (+ 14 kJ mol^{-1}) (**Eq. 3**)

glucose + phosphate → glucose-6-P (-17 kJ mol^{-1}) (**Eq. 4**)

$2H_2O + 2NADP^+ + 3ADP \rightarrow 3P_iO_2 + 2NADPH + 3ATP$ (**Eq. 5**)

where P_i is a free phosphate ion that is negatively charged

$2H_2O \rightarrow O_2 + 4H^+ + 4e^-$ (**Eq. 6**)

$\Delta G^0 (PA \blacktriangleright P^+A^-) = q_e [E_m (P^+/P) - E_m (A/A^-)]$ (**Eq. 7**)

$J = J_0 ^{(qV/enkT) -1}$ [158] (**Eq. 8**)

$FF = (V_{oc} - \ln(V_{oc} + 0.72))/V_{oc} + 1$ (**Eq. 9**)

$\eta = (V_{oc} \cdot J_{sc} \cdot FF)/P_{in}$ (**Eq. 10**)

7.2 Plasmid maps

7.2.1 pET28b-(+)

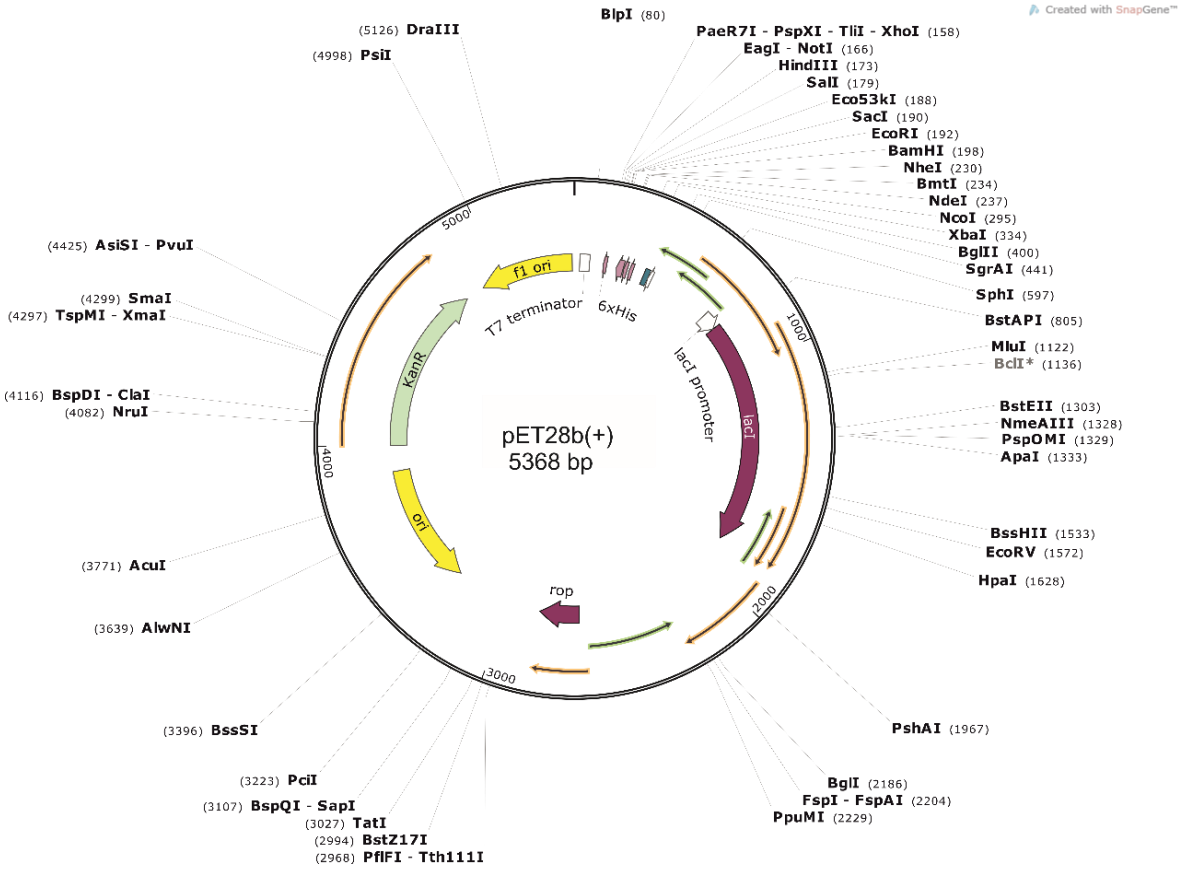

7.2.1 pBAD/HisA map

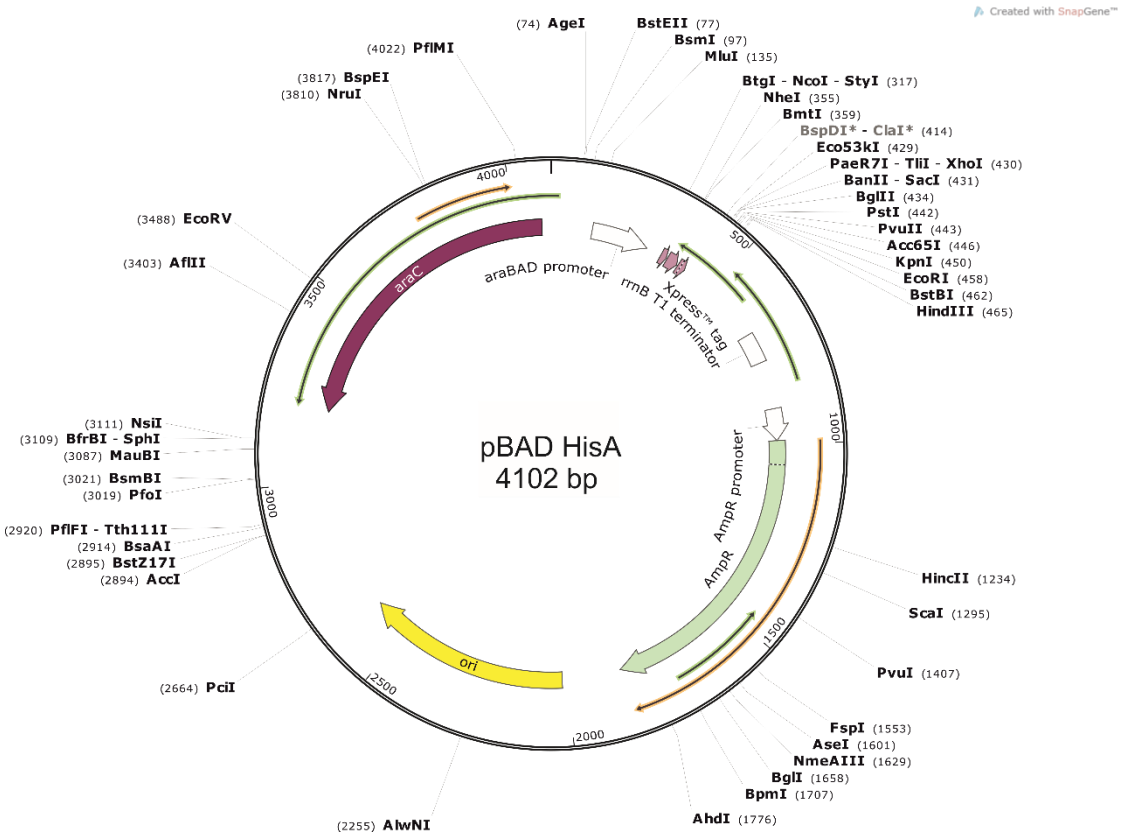

7.2.3 pEC86 map

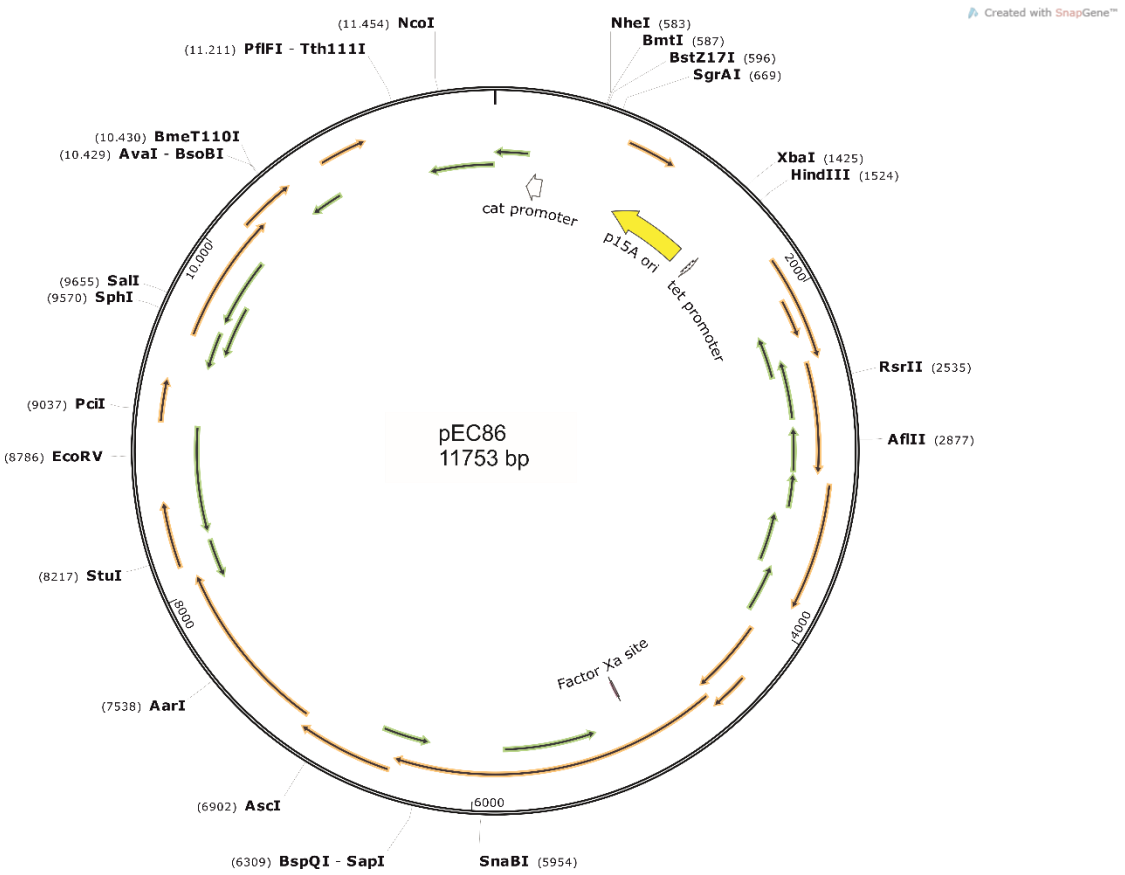

7.2.4 pET28b-(+) 0 AA map

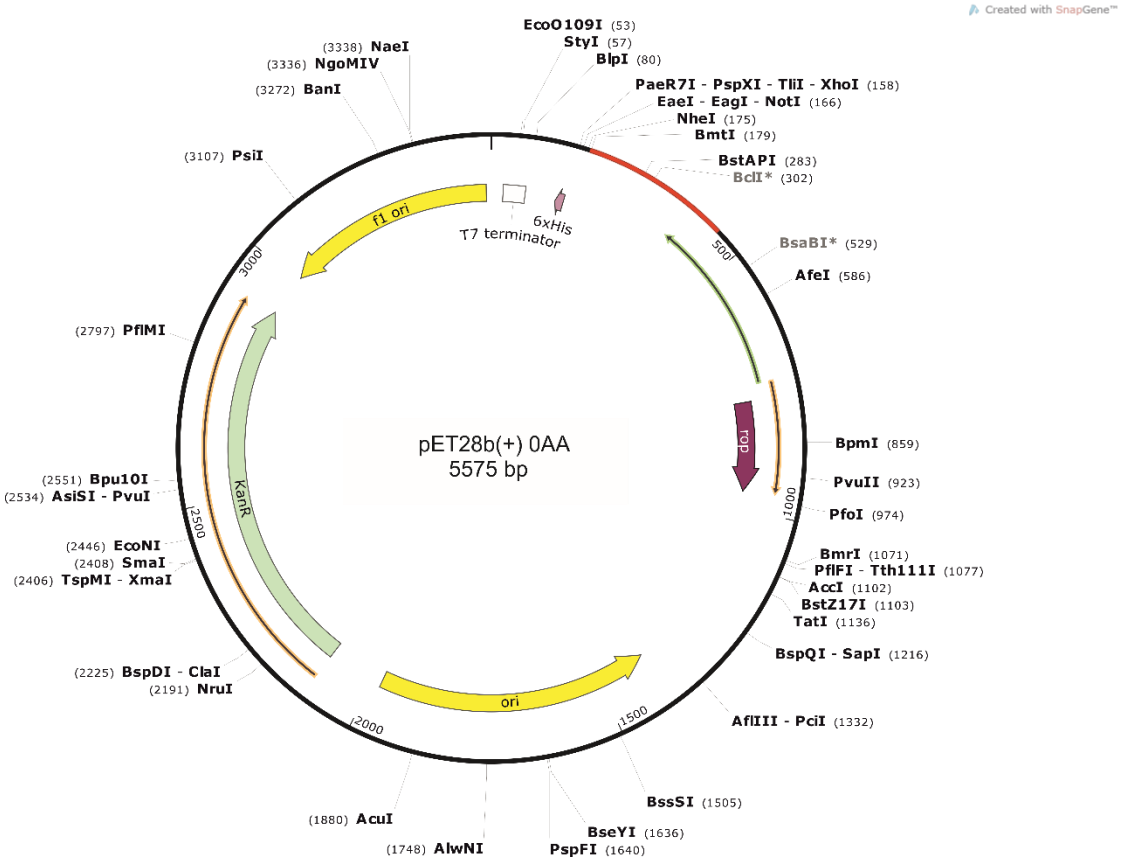

7.2.5 pET28b-(+) 5 AA map

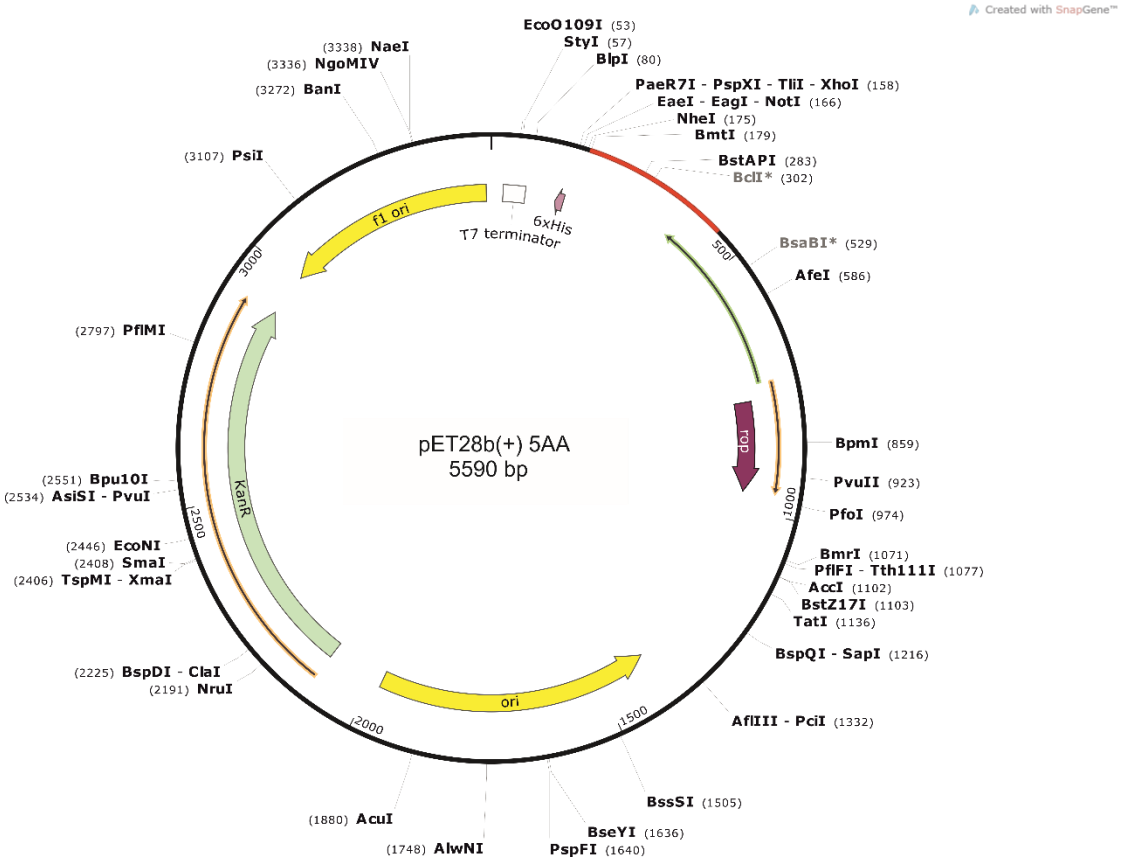

7.2.6 pET28b-(+) 10 AA map

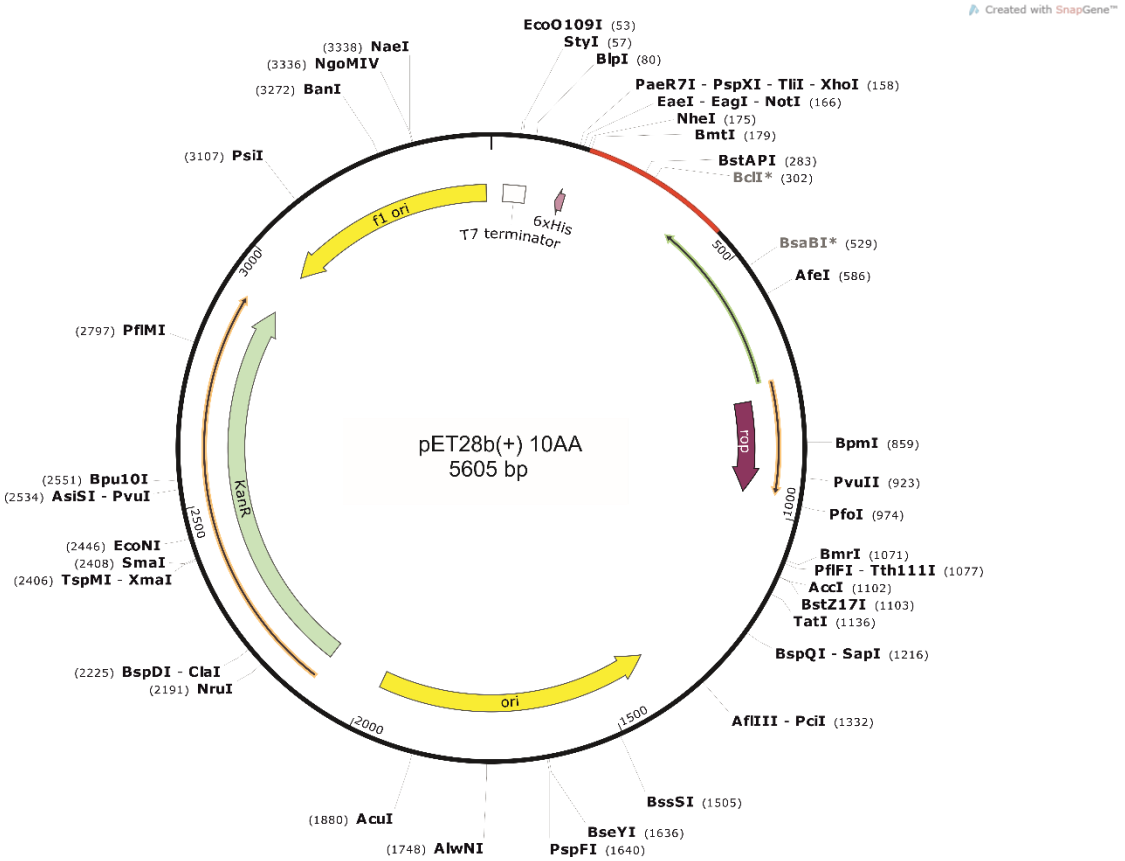

7.2.7 pET28b-(+) 12 AA map

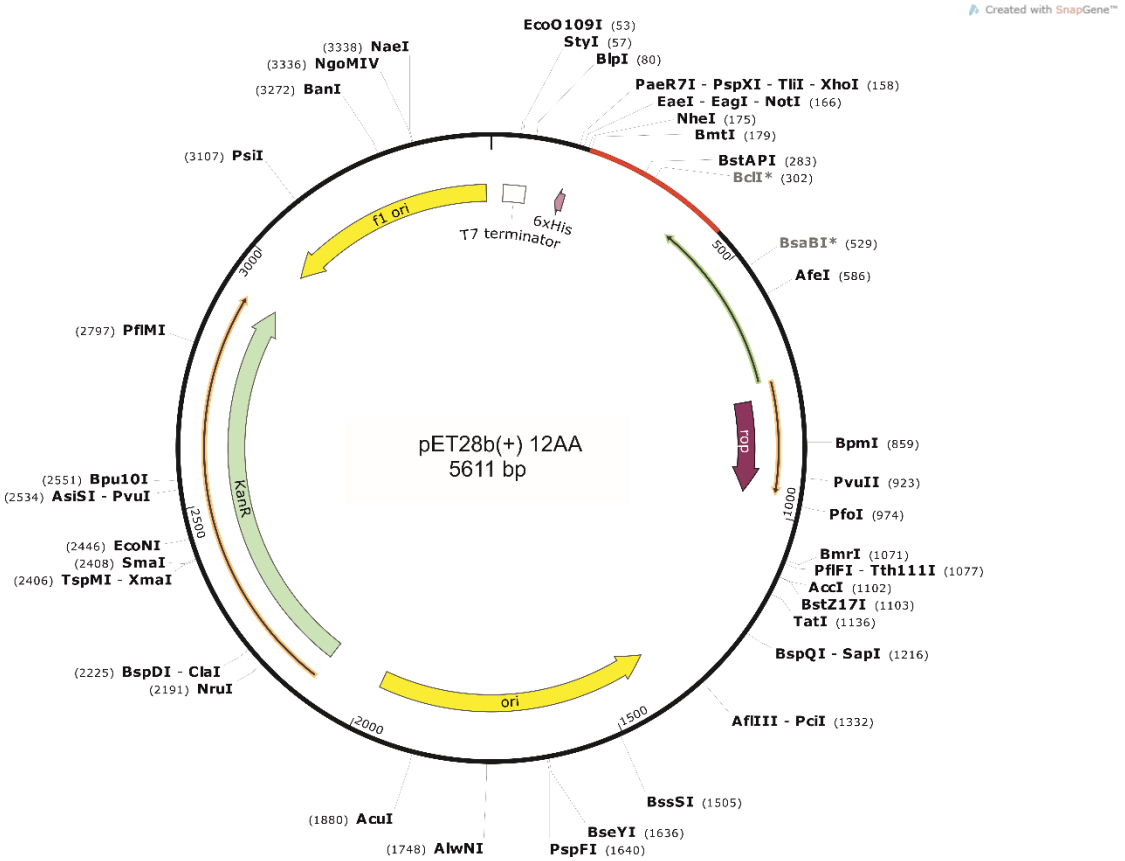

7.2.8 pET28b-(+) 19 AA map

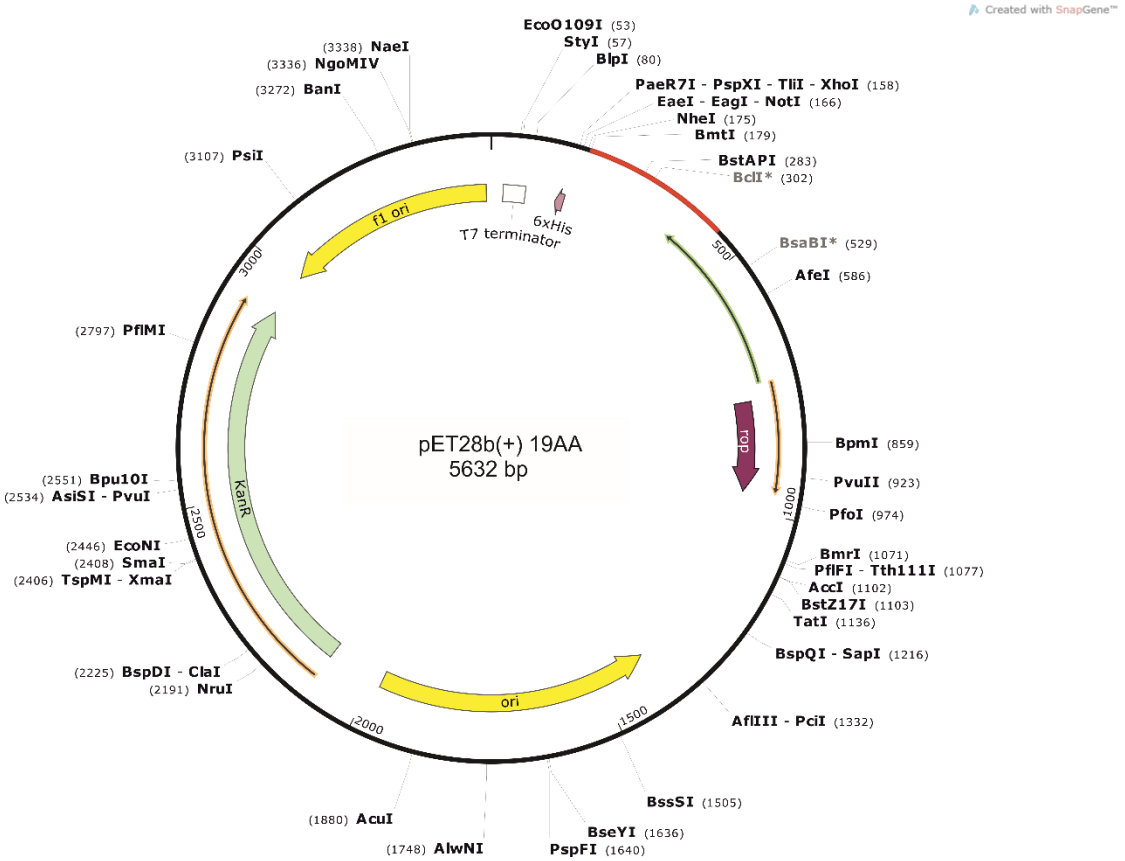

7.2.9 pBAD/HisA 0 AA map

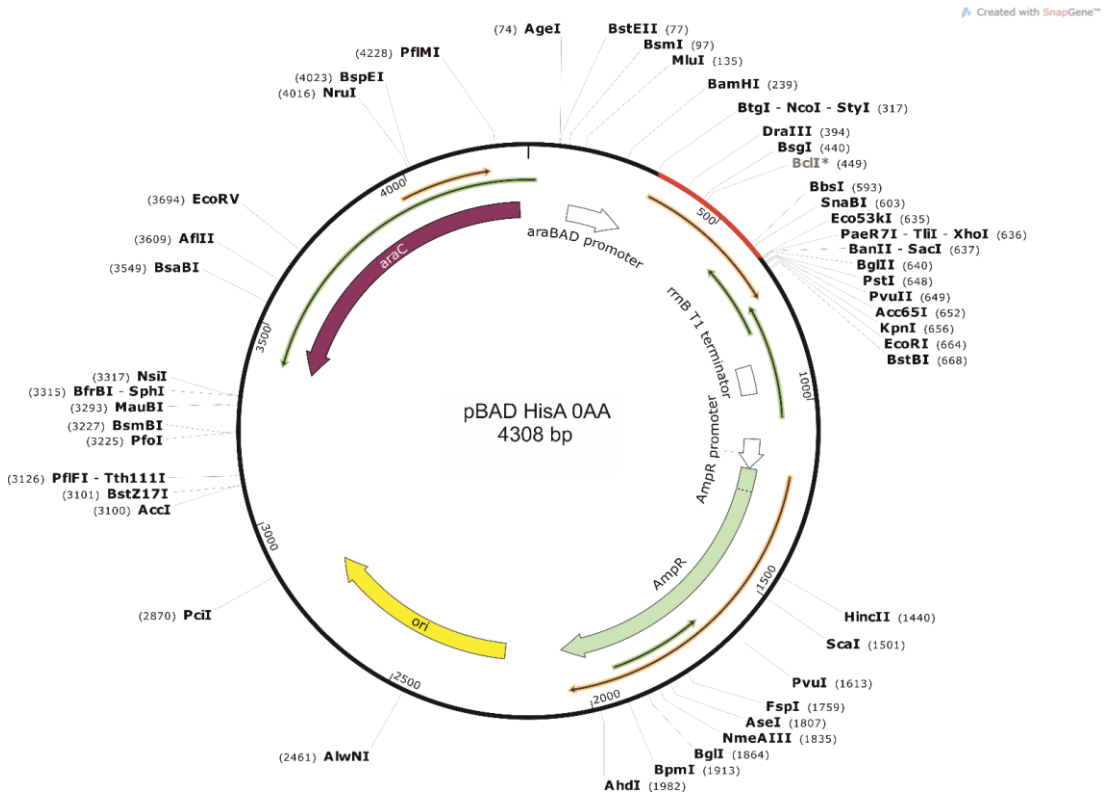

7.2.10 pBAD/HisA 5 AA map

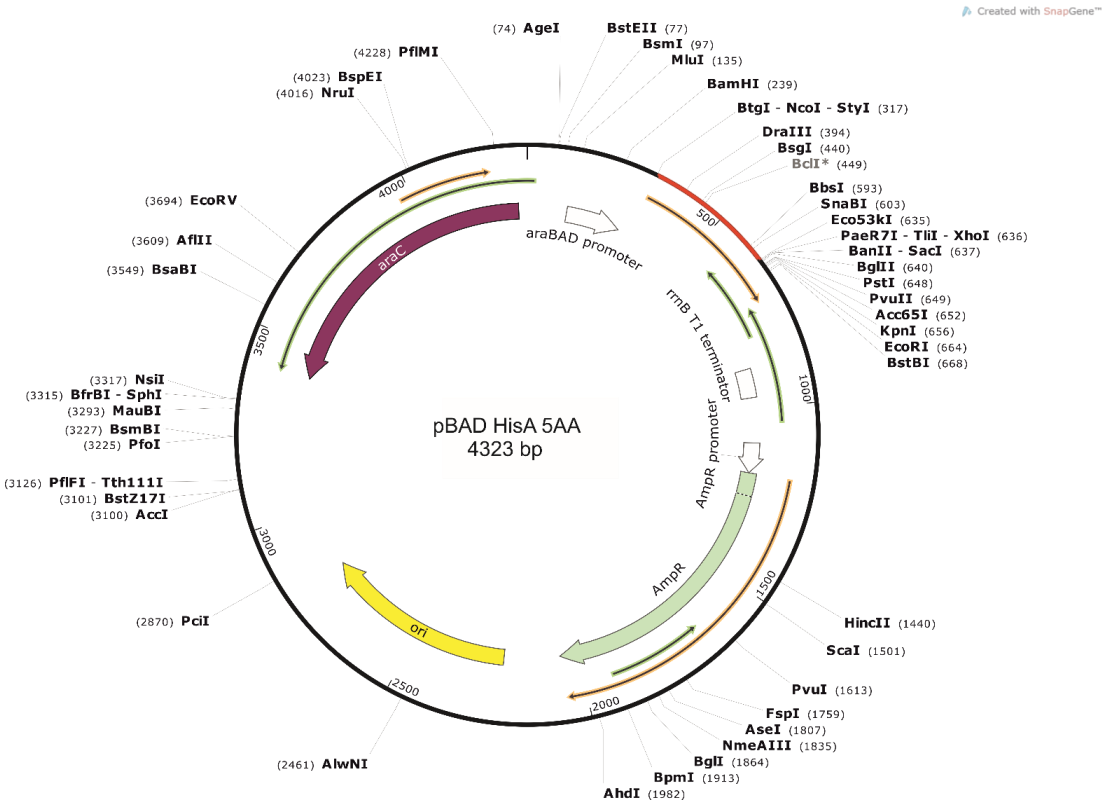

7.2.11 pBAD/HisA 10 AA map

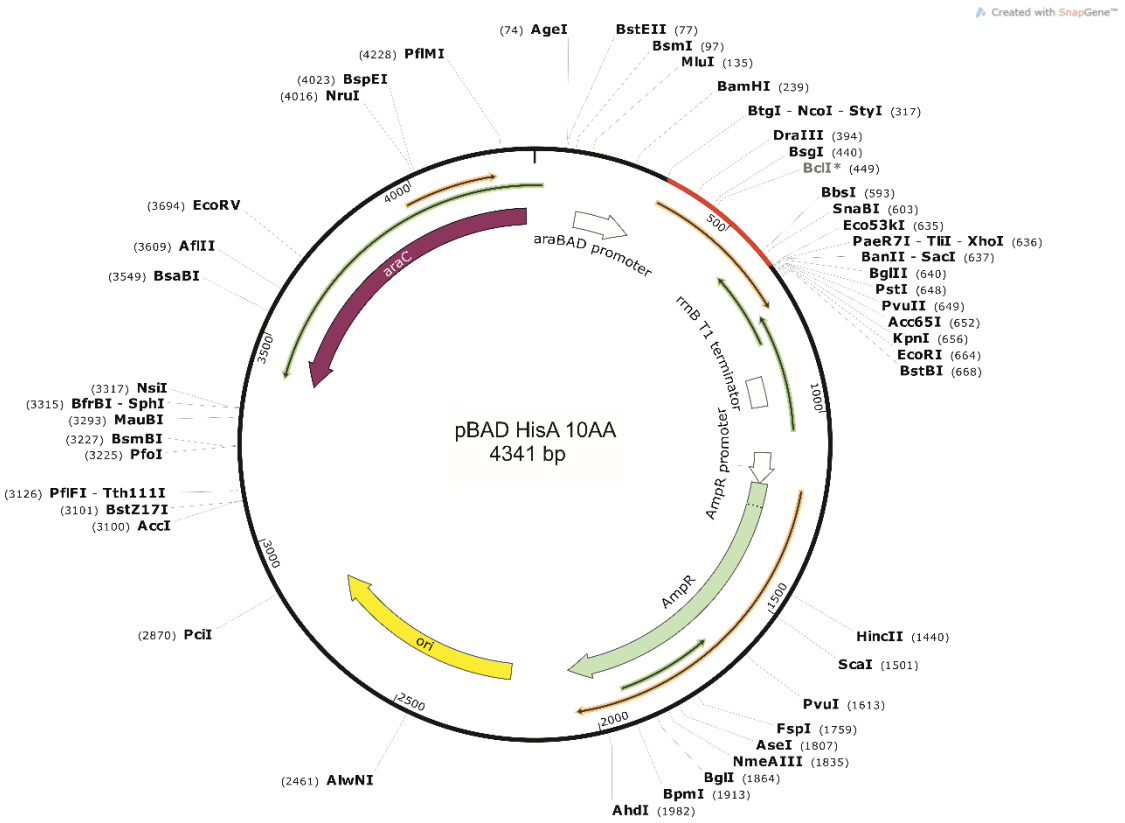

7.2.12 pBAD/HisA 12 AA map

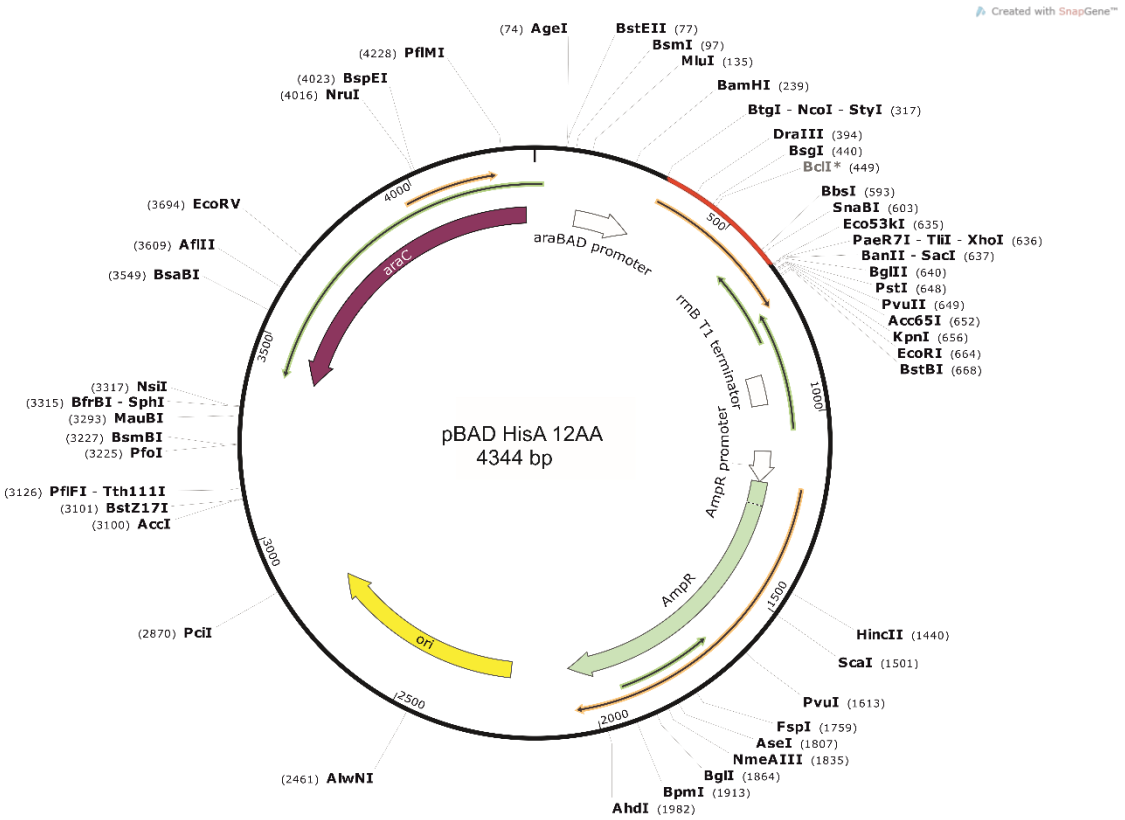

7.2.13 pBAD/HisA 19 AA map

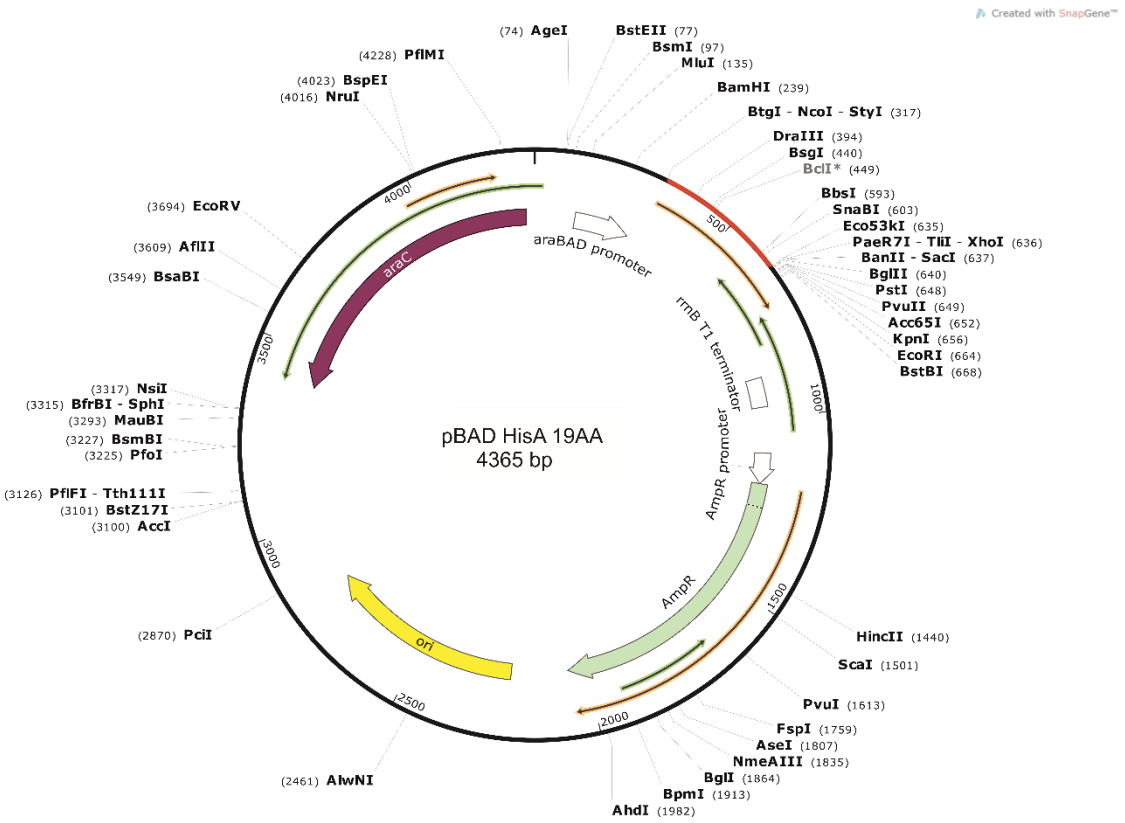

7.3 Supplementary Figures

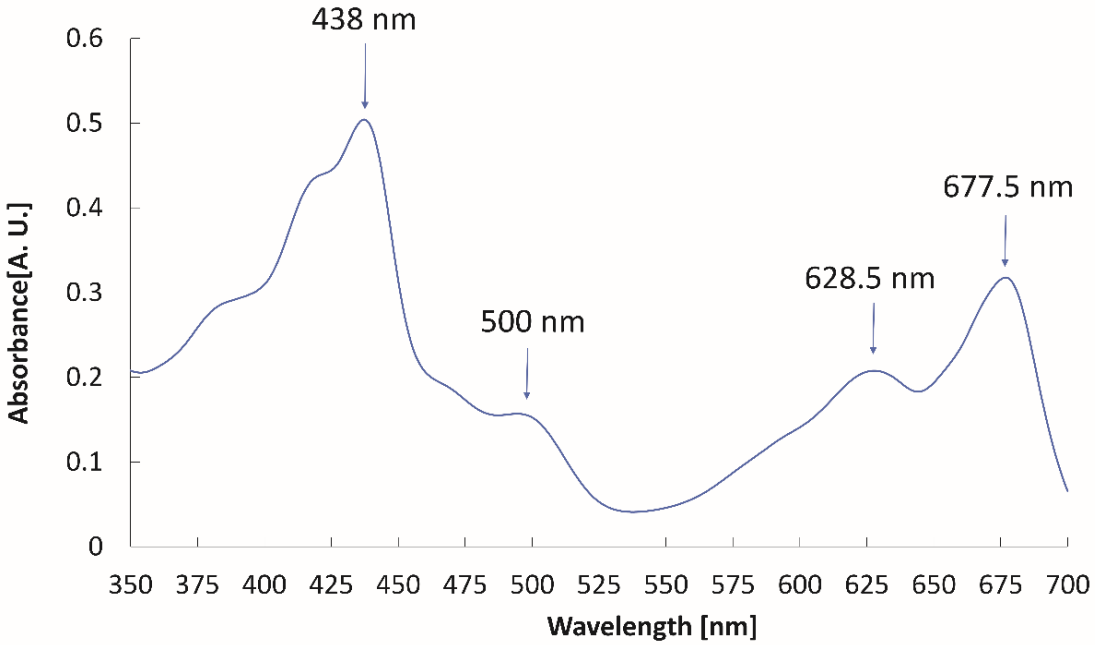

Supplementary Figure 1. Representative RT absorbance spectrum of PSI-LHCI phycobilisome-contaminated simple. Normally, an increase in absorbance was observed at 628.5 nm and a blue shift of the Chl*a* peak from 680 nm to 677.5 nm was observed for PSI-LHCI samples with a considerable contamination of PBSs. Moreover, as the amount of PBS contamination increased, a larger blue shift from 630 nm to 628.5 nm was observed. These PBSs-containing samples were deemed unsuitable for biotechnological applications and required much more extensive purification steps, as shown in **Chapter 4.1** and discussed in detail in **Chapters 3.2.3.3, 3.2.3.4** and **3.2.3.5**.

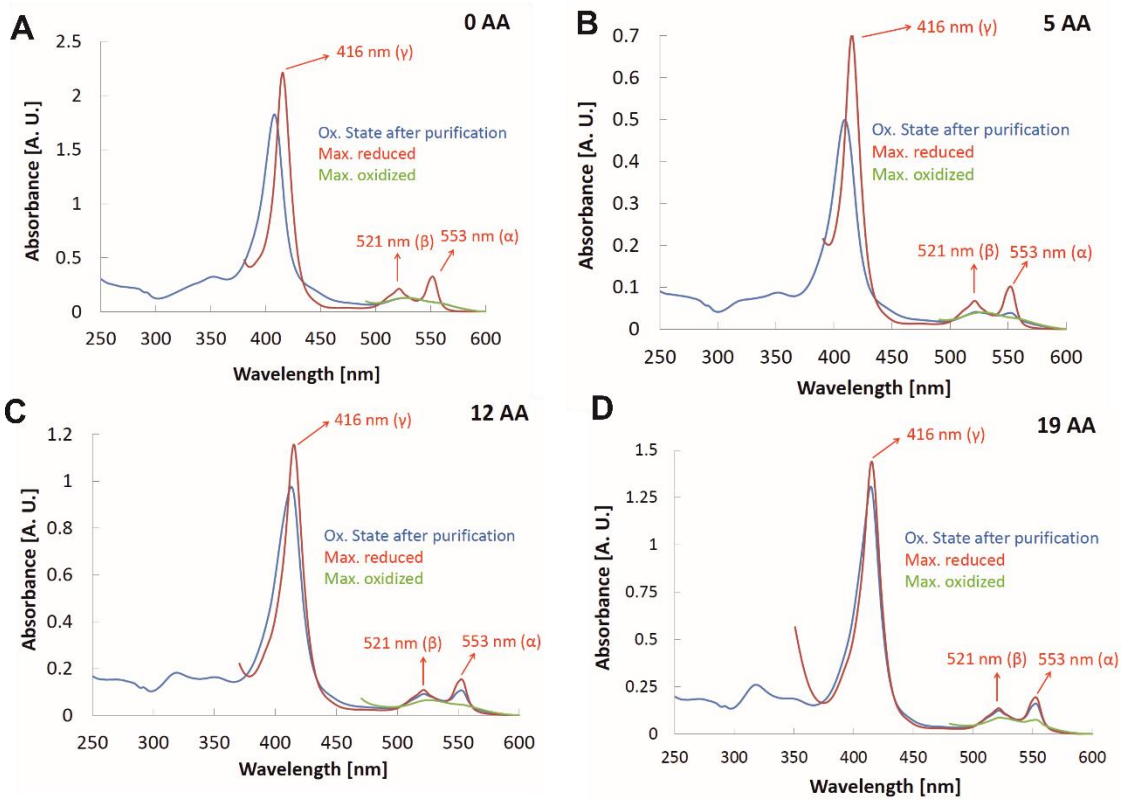

Supplementary Figure 2. Redox difference absorption spectra of the cyt c_{553} linker peptide variants used in this study (excluding the 10AA linker variant). Presence of α, β and γ peaks and their full redox reversibility indicate that all the cyt *c* proteins are active in electron transfer. All the variants possess identical redox difference spectra. The spectra also indicate appropriate haem group maturation, incorporation and full reversibility of the redox reaction. Spectra for fully oxidised (max. oxidised, displayed in green) species had to be cut off above unreliable absorbance values as excess FeCN had to be titrated depending on the amount of cyt c_{553} present to achieve the maximally oxidised species of the redox active protein. In the same fashion, spectra of fully reduced species were truncated below 370 nm, as the sodium dithionite maxima overshadows the cyt c_{553}-specific peaks. Absorbance values on the *y*-axis were re-scaled for clarity and to display equal spectral intensity on the four panels.

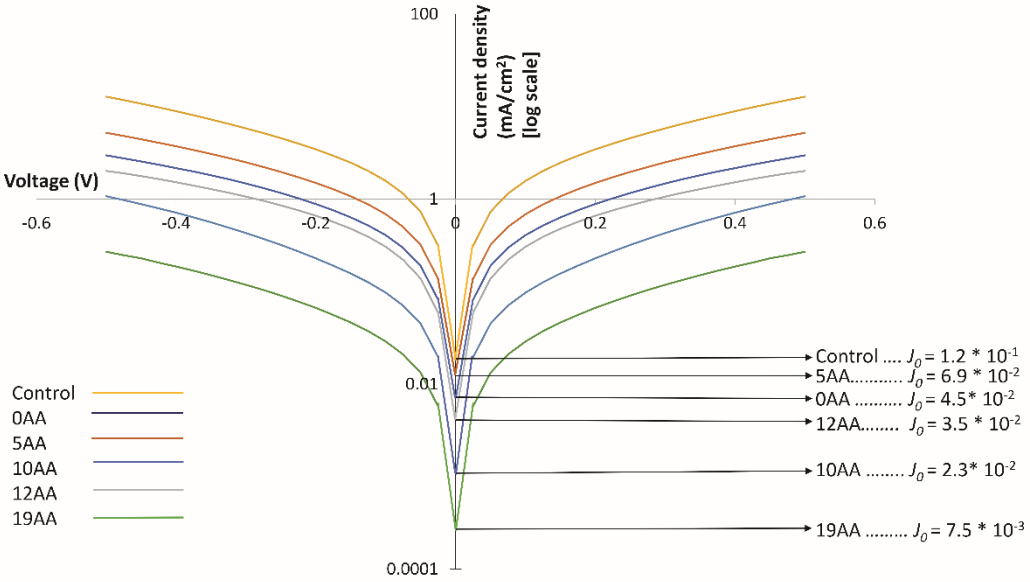

Supplementary Figure 3. Dark *J-V* characterisation of cytochrome c_{553}/*p*-doped silicon bioelectrodes. Dark current density *J* (mA cm^{-2}) was measured for all the devices, as shown in **Figure 91**. Semi-logarithmic representation of the measured *J-V* values allows for estimation of the J_0 recombination parameter which corresponds to the *y*-intercept and is calculated according to **Eq. 8**.

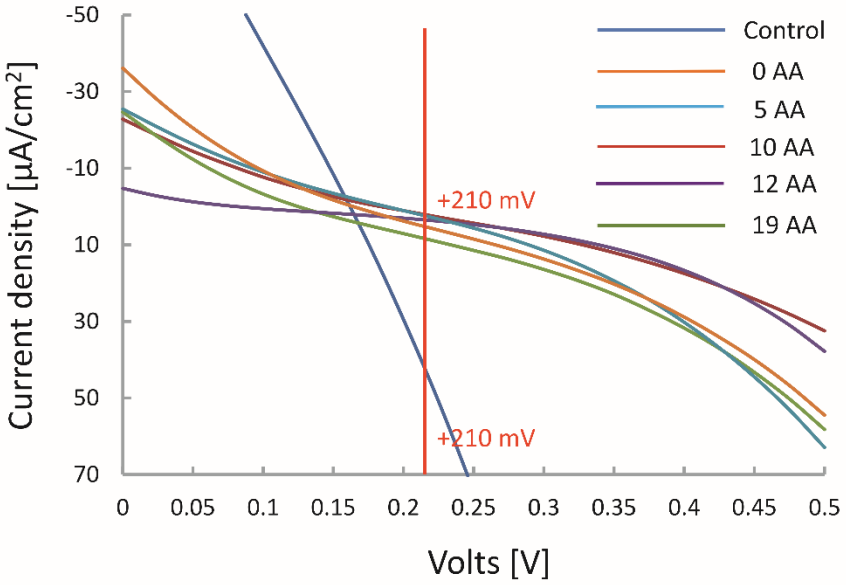

Supplementary Figure 4. PV determination of cyt c_{553} mid-point potential. The potential was estimated at the mid-point when the tangent line of the photovoltaic curves, generated upon illumination with standard AM 1.5 light (1 kW m^{-2}), stopped decreasing and before it started to increase again. As eternal illumination produced severe Auger recombination, current density values on the *y*-axis were drastically decreased and had to be re-scaled for clarity. Note the discrepant behaviour of the *p*-Si SAM control on its own, confirming the strong redox interaction between cyt c_{553} and *p*-Si.

References

1. Liu C, Colón BC, Ziesack M, Silver PA, Nocera DG: Water splitting–biosynthetic system with CO_2 reduction efficiencies exceeding photosynthesis. *Science (80)*, 2016, 352:1210–1213.
2. Barber J: Photosynthetic energy conversion: natural and artificial. *Chem. Soc. Rev.* 2009, 38:185–96.
3. Qin X, Suga M, Kuang T, Shen J-R: Structural basis for energy transfer pathways in the plant PSI-LHCI supercomplex. *Science (80)*, 2015, 348:989–995.
4. Williams PJLB, Laurens LML: Microalgae as biodiesel & biomass feedstocks: Review & analysis of the biochemistry, energetics & economics. *Energy Environ. Sci.* 2010, 3:554.
5. Janna Olmos JD, Kargul J: Oxygenic photosynthesis: Translation to solar fuel technologies. *Acta Soc. Bot. Pol.* 2014, 83:423–440.
6. Kargul J, Barber J: Structure and function of bacterial photosynthetic reaction centres. In *Molecular Solar Fuels*. Edited by Thomas J Wydrzynski WH. 2011:107–142.
7. Cogdell RJ, Gardiner AT, Hashimoto H, Brotosudarmo THP: A comparative look at the first few milliseconds of the light reactions of photosynthesis. *Photochem. Photobiol. Sci.* 2008, 7:1150–8.
8. Collins AM, Wen. J, Blankenship RE: Photosynthetic light-harvesting complexes. In *Molecular Solar Fuels*. . 2011:85–106.
9. Janna Olmos JD, Kargul J: A quest for the artificial leaf. *Int. J. Biochem. Cell Biol.* 2015, 66:37–44.
10. Suga M, Akita F, Hirata K, Ueno G, Murakami H, Nakajima Y, Shimizu T, Yamashita K, Yamamoto M, Ago H, et al.: Native structure of photosystem II at 1.95 Å resolution viewed by femtosecond X-ray pulses. *Nature* 2014, 517:99–103.
11. Hasan SS, Proctor EA, Yamashita E, Dokholyan N V., Cramer WA: Traffic within the cytochrome b_6f lipoprotein complex: Gating of the quinone portal. *Biophys. J.* 2014, 107:1620–1628.
12. Kerfeld CA, Anwar HP, Interrante R, Merchant S, Yeates TO: The structure of chloroplast cytochrome c_6 at 1.9 Å resolution: evidence for functional oligomerization. *J. Mol. Biol.* 1995, 250:627–47.
13. Yamaoka A, Ozawa Y, Ueno Y, Endo T, Morimoto Y, Urushiyama A, Ohmori D, Imai T: *Cyanidioschyzon merolae* ferredoxin: a high resolution crystal structure analysis and its thermal stability. *FEBS Lett* 2011, 585:1299–1302.
14. Bruns CM, Karplus P a: Refined crystal structure of spinach ferredoxin reductase at 1.7 Å resolution: oxidized, reduced and 2'-phospho-5'-AMP bound states. *J. Mol. Biol.* 1995, 247:125–145.
15. Allen JF: Cyclic, pseudocyclic and noncyclic photophosphorylation: New links in the chain. *Trends Plant Sci.* 2003, 8:15–19.
16. Asada K: The water-water cycle in chloroplasts: Scavenging of active oxygens and dissipation of excess photons. *Annu. Rev. Plant Physiol. Plant Mol. Biol.* 1999, 50:601–

639.

17. Shikanai T: Cyclic electron transport around photosystem I: Genetic approaches. *Annu. Rev. Plant Biol.* 2007, 58:199–217.

18. Yamori W, Shikanai T: Physiological functions of cyclic electron transport around photosystem I in sustaining photosynthesis and plant growth. *Annu. Rev. Plant Biol.* 2016, 67:81–106.

19. Falkowski PG, Fujita Y, Ley A, Mauzerall D: Evidence for cyclic electron flow around photosystem II in *Chlorella pyrenoidosa*. *Plant Physiol.* 1986, 81:310–312.

20. Miyake C, Yonekura K, Kobayashi Y, Yokota A: Cyclic electron flow within PSII functions in intact chloroplasts from spinach leaves. *Plant Cell Physiol.* 2002, 43:951–957.

21. Prasil O, Kolber Z, Berry J, Falkowski PG: Cyclic electron flow around photosystem II *in vivo*. *Photosynth. Res.* 1996, 48:395–410.

22. Minagawa J, Tokutsu R: Dynamic regulation of photosynthesis in *Chlamydomonas reinhardtii*. *Plant J.* 2015, 82:413–428.

23. Iwai M, Takizawa K, Tokutsu R, Okamuro A, Takahashi Y, Minagawa J: Isolation of the elusive supercomplex that drives cyclic electron flow in photosynthesis. *Nature* 2010, 464:1210–1213.

24. Drop B, Yadav KNS, Boekema EJ, Croce R: Consequences of state transitions on the structural and functional organization of Photosystem I in the green alga *Chlamydomonas reinhardtii*. *Plant J.* 2014, 78:181–191.

25. Senge MO, Ryan AA, Letchford KA, MacGowan SA, Mielke T: Chlorophylls, symmetry, chirality, and photosynthesis. *Symmetry (Basel).* 2014, 6:781–843.

26. Yano J, Yachandra VK: Where water is oxidized to dioxygen: Structure of the photosynthetic Mn_4Ca cluster from X-ray spectroscopy. *Inorg. Chem.* 2008, 47:1711–1726.

27. Yano J, Kern J, Irrgang K-D, Latimer MJ, Bergmann U, Glatzel P, Pushkar Y, Biesiadka J, Loll B, Sauer K, *et al.*: X-ray damage to the Mn_4Ca complex in single crystals of photosystem II: a case study for metalloprotein crystallography. *Proc. Natl. Acad. Sci. U. S. A.* 2005, 102:12047–52.

28. Yano J, Yano J, Kern J, Kern J, Sauer K, Sauer K, Latimer MJ, Latimer MJ, Pushkar Y, *et al.*: Where water is oxidized to dioxygen: structure of the photosynthetic Mn_4Ca cluster. *Science* 2006, 314:821–5.

29. Yano J, Pushkar Y, Glatzel P, Lewis A, Sauer K, Messinger J, Bergmann U, Yachandra V: High-resolution Mn EXAFS of the oxygen-evolving complex in photosystem II: Structural implications for the Mn_4Ca cluster. *J. Am. Chem. Soc.* 2005, 127:14974–14975.

30. Nelson N, Yocum CF: Structure and function of photosystems I and II. *Annu. Rev. Plant Biol.* 2006, 57:521–565.

31. Kamiya N, Shen J-R: Crystal structure of oxygen-evolving photosystem II from *Thermosynechococcus vulcanus* at 3.7-Å resolution. *Proc. Natl. Acad. Sci. U. S. A.* 2003, 100:98–103.

32. Minagawa J, Takahashi Y: Structure, function and assembly of photosystem II and its

light-harvesting proteins. *Photosynth. Res.* 2004, 82:241–63.

33. Umena Y, Kawakami K, Shen J-R, Kamiya N: Crystal structure of oxygen-evolving photosystem II at a resolution of 1.9 Å. *Nature* 2011, 473:55–60.

34. Dau H, Haumann M: The manganese complex of photosystem II in its reaction cycle-Basic framework and possible realization at the atomic level. *Coord. Chem. Rev.* 2008, 252:273–295.

35. Dau H, Grundmeier A, Loja P, Haumann M: On the structure of the manganese complex of photosystem II: extended-range EXAFS data and specific atomic-resolution models for four S-states. *Philos. Trans. R. Soc. Lond. B. Biol. Sci.* 2008, 363:1237-43–4.

36. Glöckner C, Kern J, Broser M, Zouni A, Yachandra V, Yano J: Structural changes of the oxygen-evolving complex in photosystem II during the catalytic cycle. *J. Biol. Chem.* 2013, 288:22607–20.

37. Kuhl H, Rögner M, Van Breemen JFL, Boekema EJ: Localization of cyanobacterial photosystem II donor-side subunits by electron microscopy and the supramolecular organization of photosystem II in the thylakoid membrane. *Eur. J. Biochem.* 1999, 266:453–459.

38. Duan L, Wang L, Li F, Li F, Sun L: Highly efficient bioinspired molecular Ru water oxidation catalysts with negatively charged backbone ligands. *Acc. Chem. Res.* 2015, 48:2084–2096.

39. Duan L, Bozoglian F, Mandal S, Stewart B, Privalov T, Llobet A, Sun L: A molecular ruthenium catalyst with water-oxidation activity comparable to that of photosystem II. *Nat. Chem.* 2012, 4:418–423.

40. Duan L, Fischer A, Xu Y, Sun L: Isolated seven-coordinate Ru(IV) dimer complex with [HOHOH]- bridging ligand as an intermediate for catalytic water oxidation. *J. Am. Chem. Soc.* 2009, 131:10397–10399.

41. Ago H, Adachi H, Umena Y, Tashiro T, Kawakami K, Tian NKL, Han G, Kuang T, Liu Z, Wang F, et al.: Novel features of eukaryotic photosystem II revealed by its crystal structure analysis from a red alga. *J. Biol. Chem.* 2016, 291:5676–5687.

42. Krupnik T, Kotabová E, Van Bezouwen LS, Mazur R, Garstka M, Nixon PJ, Barber J, Kaňa R, Boekema EJ, Kargul J: A reaction center-dependent photoprotection mechanism in a highly robust photosystem II from an extremophilic red alga, *Cyanidioschyzon merolae*. *J. Biol. Chem.* 2013, 288:23529–23542.

43. Berry EA, Guergova-Kuras M, Huang L, Crofts AR: Structure and function of cytochrome *bc* complexes. *Annu. Rev. Biochem.* 2000, 69:1005–1075.

44. Cramer WA, Zhang H, Yan J, Kurisu G, Smith JL: Transmembrane traffic in the cytochrome b_6f complex. *Annu. Rev. Biochem.* 2006, 75:769–790.

45. Crofts AR: The cytochrome bc_1 complex: function in the context of structure. *Annu. Rev. Physiol.* 2004, 66:689–733.

46. Hasan SS, Yamashita E, Ryan CM, Whitelegge JP, Cramer WA: Conservation of lipid functions in cytochrome *bc* complexes. *J. Mol. Biol.* 2011, 414:145–162.

47. Hasan SS, Yamashita E, Baniulis D, Cramer WA: Quinone-dependent proton transfer pathways in the photosynthetic cytochrome b_6f complex. *Proc. Natl. Acad. Sci. U. S.*

A. 2013, 110:4297–302.

48. Hasan SS, Cramer WA: Internal lipid architecture of the hetero-oligomeric cytochrome b_6f complex. *Structure* 2014, 22:1008–1015.

49. Stroebel D, Choquet Y, Popot J-L, Picot D: An atypical haem in the cytochrome b_6f complex. *Nature* 2003, 426:413–418.

50. Yamashita E, Zhang H, Cramer WA: Structure of the cytochrome b_6f complex: Quinone analogue inhibitors as ligands of heme *cn*. *J. Mol. Biol.* 2007, 370:39–52.

51. Zhang H, Whitelegge JP, Cramer WA: Ferredoxin:$NADP^+$ Oxidoreductase is a subunit of the chloroplast cytochrome b_6f complex. *J. Biol. Chem.* 2001, 276:38159–38165.

52. Burrows PA, Sazanov LA, Svab Z, Maliga P, Nixon PJ: Identification of a functional respiratory complex in chloroplasts through analysis of tobacco mutants containing disrupted plastid ndh genes. *EMBO J.* 1998, 17:868–876.

53. Lavergne J: Membrane potential-dependent reduction of cytochrome b_6 in an algal mutant lacking photosystem I centers. *BBA - Bioenerg.* 1983, 725:25–33.

54. Joliot P, Joliot A: The low-potential electron-transfer chain in the cytochrome *bf* complex. *BBA - Bioenerg.* 1988, 933:319–333.

55. Depège N, Bellafiore S, Rochaix J-D: Role of chloroplast protein kinase Stt7 in LHCII phosphorylation and state transition in *Chlamydomonas*. *Science* 2003, 299:1572–1575.

56. Wollman FA: State transitions reveal the dynamics and flexibility of the photosynthetic apparatus. *EMBO J.* 2001, 20:3623–3630.

57. Chauvet A, Agarwal R, Al Haddad A, van Mourik F, Cramer WA: Photo-induced oxidation of the uniquely liganded heme *f* in the cytochrome b_6f complex of oxygenic photosynthesis. *Phys. Chem. Chem. Phys.* 2016, 18:12983–12991.

58. Lange C, Nett JH, Trumpower BL, Hunte C: Specific roles of protein-phospholipid interactions in the yeast cytochrome bc_1 complex structure. *EMBO J.* 2001, 20:6591–6600.

59. Nelson N: Plant photosystem I - The most efficient nano-photochemical machine. *J. Nanosci. Nanotechnol.* 2009, 9:1709–1713.

60. Scholes GD, Fleming GR, Olaya-Castro A, van Grondelle R: Lessons from nature about solar light harvesting. *Nat. Chem.* 2011, 3:763–74.

61. Mazor Y, Borovikova A, Nelson N: The structure of plant photosystem I super-complex at 2.8 Å resolution. *Elife* 2015, 4:1–18.

62. Jordan P, Fromme P, Witt HT, Klukas O, Saenger W, Krauss N: Three-dimensional structure of cyanobacterial photosystem I at 2.5 Å resolution. *Nature* 2001, 411:909–917.

63. Scheller HV, Jensen PE, Haldrup A, Lunde C, Knoetzel J: Role of subunits in eukaryotic photosystem I. *Biochim. Biophys. Acta - Bioenerg.* 2001, 1507:41–60.

64. Amunts A, Toporik H, Borovikova A, Nelson N: Structure determination and improved model of plant photosystem I. *J. Biol. Chem.* 2010, 285:3478–86.

65. Ben-Shem A, Frolow F, Nelson N: Crystal structure of plant photosystem I. *Nature* 2003, 426:630–635.

66. Kargul J, Janna Olmos JD, Krupnik T: Structure and function of photosystem I and its application in biomimetic solar-to-fuel systems. *J. Plant Physiol.* 2012, 169:1639–1653.

67. Santabarbara S, Kuprov I, Fairclough W V., Purton S, Hore PJ, Heathcote P, Evans MCW: Bidirectional electron transfer in photosystem I: Determination of two distances between $P700^+$ and $A1^-$ in spin-correlated radical pairs. *Biochemistry* 2005, 44:2119–2128.

68. Santabarbara S, Galuppini L, Casazza AP: Bidirectional electron transfer in the reaction centre of photosystem I. *J. Integr. Plant Biol.* 2010, 52:735–749.

69. Guergova-Kuras M, Boudreaux B, Joliot A, Joliot P, Redding K: Evidence for two active branches for electron transfer in photosystem I. *Proc. Natl. Acad. Sci. U. S. A.* 2001, 98:4437–42.

70. Santabarbara S, Zucchelli G: Comparative kinetic and energetic modelling of phyllosemiquinone oxidation in photosystem I. *Phys. Chem. Chem. Phys.* 2016, 18:9687–9701.

71. Allen JP, Feher G, Yeates TO, Komiya H, Rees DC: Structure of the reaction center from *Rhodobacter sphaeroides* R-26: the cofactors. *Proc. Natl. Acad. Sci. U. S. A.* 1987, 84:5730–5734.

72. Deisenhofer J, Epp O, Sinning I, Michel H: Crystallographic refinement at 2.3 Å resolution and refined model of the photosynthetic reaction centre from *Rhodopseudomonas viridis*. *J. Mol. Biol.* 1995, 246:429–57.

73. Watanabe T, Kobayashi M, Hongu A, Nakazato M, Hiyama T, Murata N: Evidence that a chlorophyll *a* dimer constitutes the photochemical reaction centre (P700) in photosynthetic apparatus. *FEBS Lett.* 1985, 191:252–256.

74. Makita H, Hastings G: Directionality of electron transfer in cyanobacterial photosystem I at 298 and 77 K. *FEBS Lett.* 2015, 589:1412–1417.

75. Brettel K, Leibl W: Electron transfer in photosystem I. *Biochim. Biophys. Acta - Bioenerg.* 2001, 1507:100–114.

76. Renaud N, Powell D, Zarea M, Movaghar B, Wasielewski MR, Ratner MA: Quantum interferences and electron transfer in photosystem I. *J. Phys. Chem. A* 2013, 117:5899–5908.

77. Wientjes E, Croce R: The light-harvesting complexes of higher-plant photosystem I: Lhca1/4 and Lhca2/3 form two red-emitting heterodimers. *Biochem. J.* 2011, 433:477–485.

78. Gobets B, Van Grondelle R: Energy transfer and trapping in photosystem I. *Biochim. Biophys. Acta - Bioenerg.* 2001, 1507:80–99.

79. Morosinotto T, Mozzo M, Bassi R, Croce R: Pigment-pigment interactions in Lhca4 antenna complex of higher plants photosystem I. *J. Biol. Chem.* 2005, 280:20612–20619.

80. Mozzo M, Morosinotto T, Bassi R, Croce R: Probing the structure of Lhca3 by mutation analysis. *Biochim. Biophys. Acta - Bioenerg.* 2006, 1757:1607–1613.

81. Croce R, Van Amerongen H: Light-harvesting in photosystem I. *Photosynth. Res.* 2013, 116:153–166.

82. Fiedor L, Kania A, Myśliwa-Kurdziel B, Orzeł Ł, Stochel G: Understanding chlorophylls: Central magnesium ion and phytyl as structural determinants. *Biochim. Biophys. Acta - Bioenerg.* 2008, 1777:1491–1500.

83. De Luca P, Taddei R, Varano L: *Cyanidioschyzon merolae*: a new alga of thermal acidic environments. *Webbia* 1978, 33:37–44.

84. Ferris MJ, Sheehan KB, Kühl M, Cooksey K, Wigglesworth-Cooksey B, Harvey R, Henson JM: Algal species and light microenvironment in a low-pH, geothermal microbial mat community. *Appl. Environ. Microbiol.* 2005, 71:7164–7171.

85. Mitchell P: Coupling of phosphorylation to electron and hydrogen transfer by a chemi-osmotic type of mechanism. *Nature* 1961, 191:144–148.

86. Kuroiwa T, Kuroiwa H, Sakai a, Takahashi H, Toda K, Itoh R: The division apparatus of plastids and mitochondria. *Int. Rev. Cytol.* 1998, 181:1–41.

87. Matsuzaki M, Misumi O, Shin-I T, Maruyama S, Takahara M, Miyagishima S-Y, Mori T, Nishida K, Yagisawa F, Nishida K, et al.: Genome sequence of the ultrasmall unicellular red alga *Cyanidioschyzon merolae* 10D. *Nature* 2004, 428:653–657.

88. Minoda A, Sakagami R, Yagisawa F, Kuroiwa T, Tanaka K: Improvement of culture conditions and evidence for nuclear transformation by homologous recombination in a red alga, *Cyanidioschyzon merolae* 10D. *Plant Cell Physiol.* 2004, 45:667–671.

89. Barbier G, Oesterhelt C, Larson MD, Halgren RG, Wilkerson C, Garavito RM, Benning C, Weber APM: Genome Analysis. *Plant Physiol.* 2005, 137:460–474.

90. Kobayashi Y, Ohnuma M, Tanaka K, Ha- M: The basics of cultivation and molecular genetic analysis of the unicellular red alga *Cyanidioschyzon merolae*. *Cell* 2010, 20:53–61.

91. Haniewicz P, Janna Olmos JD: Molecular mechanisms of photoprotection in the highly robust photosystem I and its associated light harvesting antenna supercomplex from an extremophilic red alga *Cyanidioschyzon merolae*. *In preparation.*

92. Krulwich T a, Sachs G, Padan E: Molecular aspects of bacterial pH sensing and homeostasis. *Nat. Rev. Microbiol.* 2011, 9:330–43.

93. Arteni AA, Nowaczyk M, Lax J, Kouřil R, Rögner M, Boekema EJ: Single particle electron microscopy in combination with mass spectrometry to investigate novel complexes of membrane proteins. *J. Struct. Biol.* 2005, 149:325–331.

94. Vanselow C, Weber APM, Krause K, Fromme P: Genetic analysis of the photosystem I subunits from the red alga, *Galdieria sulphuraria*. *Biochim. Biophys. Acta - Bioenerg.* 2009, 1787:46–59.

95. Jensen PE, Bassi R, Boekema EJ, Dekker JP, Jansson S, Leister D, Robinson C, Scheller HV: Structure, function and regulation of plant photosystem I. *Biochim. Biophys. Acta - Bioenerg.* 2007, 1767:335–352.

96. Tan S, Ducret A, Aebersold R, Gantt E: Red algal LHC I genes have similarities with both Chl a/b- and a/c-binding proteins: A 21 kDa polypeptide encoded by LhcaR2 is one of the six LHCI polypeptides. *Photosynth. Res.* 1997, 53:129–140.

97. Busch A, Nield J, Hippler M: The composition and structure of photosystem I-associated antenna from *Cyanidioschyzon merolae*. *Plant J.* 2010, 62:886–897.

98. Thangaraj B, Jolley CC, Sarrou I, Bultema JB, Greyslak J, Whitelegge JP, Lin S, Kouřil

R, Subramanyam R, Boekema EJ, et al.: Efficient light harvesting in a dark, hot, acidic environment: The structure and function of PSI-LHCI from *Galdieria sulphuraria*. *Biophys. J.* 2011, 100:135–143.

99. Busch A, Hippler M: The structure and function of eukaryotic photosystem I. *Biochim. Biophys. Acta - Bioenerg.* 2011, 1807:864–877.

100. Merchant S, Bogorad L: Regulation by copper of the expression of plastocyanin and cytochrome c_{552} in *Chlamydomonas reinhardi*. *Mol. Cell. Biol.* 1986, 6:462–9.

101. Merchant S, Bogorad L: The Cu (II) -repressible plastidic cytochrome *c*. *J. Biol. Chem.* 1987, 262:9062–9067.

102. Yamada S, Park S-Y, Shimizu H, Koshizuka Y, Kadokura K, Satoh T, Suruga K, Ogawa M, Isogai Y, Nishio T, et al.: Structure of cytochrome c_6 from the red alga *Porphyra yezoensis* at 1.57 Å resolution. *Acta Crystallogr. Sect. D Biol. Crystallogr.* 2000, 56:1577–1582.

103. Redinbo MR, Cascio D, Choukair MK, Rice D, Merchant S, Yeates TO: The 1.5-Å crystal structure of plastocyanin from the green alga *Chlamydomonas reinhardtii*. *Biochemistry* 1993, 32:10560–10567.

104. Beißinger M, Sticht H, Sutter M, Ejchart A, Haehnel W, Rösch P, Ro P: Solution structure of cytochrome c_6 from the thermophilic cyanobacterium *Synechococcus elongatus*. *EMBO J.* 1998, 17:27–36.

105. Kerfeld CA, Krogmann DW: Photosynthetic cytochromes *c* in cyanobacteria, algae, and plants. *Annu. Rev. Plant Physiol. Plant Mol. Biol.* 1998, 49:397–425.

106. Ambler RP: Sequence variablility in bacterial cytochromes *c*. *Biochim. Biophys. Acta* 1991, 1058:42–47.

107. Allen JWA, Daltrop O, Stevens JM, Ferguson SJ: C-type cytochromes: diverse structures and biogenesis systems pose evolutionary problems. *Philos. Trans. R. Soc. Lond. B. Biol. Sci.* 2003, 358:255–66.

108. Hill KL, Li HH, Singer J, Merchant S: Isolation and structural characterization of the *Chlamydomonas reinhardtii* gene for cytochrome c_6: Analysis of the kinetics and metal specificity of its copper-responsive expression. *J. Biol. Chem.* 1991, 266:15060–15067.

109. Howe G, Merchant S: Maturation of thylakoid lumen proteins proceeds post-translationally through an intermediate *in vivo*. *Proc Natl Acad Sci U S A* 1993, 90:1862–1866.

110. del Campo EM: Post-transcriptional control of chloroplast gene expression. *Gene Regul. Syst. Bio.* 2009, 3:31–47.

111. Sjuts I, Soll J, Bölter B: Import of soluble proteins into chloroplasts and potential regulatory mechanisms. *Front. Plant Sci.* 2017, 8:1–15.

112. Bruce BD: The paradox of plastid transit peptides: Conservation of function despite divergence in primary structure. *Biochim. Biophys. Acta - Mol. Cell Res.* 2001, 1541:2–21.

113. Armaroli N, Balzani V: Solar electricity and solar fuels: Status and perspectives in the context of the energy transition. *Chem. - A Eur. J.* 2016, 22:32–57.

114. Turan B, Becker J, Urbain F, Finger F, Rau U, Haas S: Upscaling of integrated photoelectrochemical water-splitting devices to large areas. *Nat. Commun.* 2016,

7:12681.

115. Hanak JJ: Monolithic solar cell panel of amorphous silicon. *Sol. Energy* 1979, 23:145–147.

116. Nakano S, Matsuoka T, Kiyama S, Kawata H, Nakamura N, Nakashima Y, Tsuda S, Nishiwaki H, Ohnishi M, Nagaoka I, et al.: Laser patterning method for integrated type a-Si solar cell submodules. *Jpn. J. Appl. Phys.* 1986, 25:1936–1943.

117. Haas S, Gordijn A, Stiebig H: High speed laser processing for monolithical series connection of silicon thin-film modules. *Prog. Photovoltaics Res. Appl.* 2008, 16:195–203.

118. Kavlak G, McNerney J, Jaffe RL, Trancik JE: Metal production requirements for rapid photovoltaics deployment. *Energy Environ. Sci.* 2015, 8:1651–1659.

119. Green MA, Emery K, Hishikawa Y, Warta W, Dunlop ED: Solar cell efficiency tables (Version 45). *Prog. Photovoltaics Res. Appl.* 2015, 23:1–9.

120. Shockley W, Queisser HJ: Detailed balance limit of efficiency of *p-n* junction solar cells. *J. Appl. Phys.* 1961, 32:510–519.

121. Rühle S: Tabulated values of the Shockley-Queisser limit for single junction solar cells. *Sol. Energy* 2016, 130:139–147.

122. De Vos A: Detailed balance limit of the efficiency of tandem solar cells. *J. Phys. D. Appl. Phys.* 1980, 13:839–846.

123. Bierman DM, Lenert A, Chan WR, Bhatia B, Celanović I, Soljačić M, Wang EN: Enhanced photovoltaic energy conversion using thermally based spectral shaping. *Nat. Energy* 2016, 1:16068.

124. Chan WR, Bermel P, Pilawa-Podgurski RCN, Marton CH, Jensen KF, Senkevich JJ, Joannopoulos JD, Soljacic M, Celanovic I: Toward high-energy-density, high-efficiency, and moderate-temperature chip-scale thermophotovoltaics. *Proc. Natl. Acad. Sci. U. S. A.* 2013, 110:5309–14.

125. Datas A, Chubb DL, Veeraragavan A: Steady state analysis of a storage integrated solar thermophotovoltaic (SISTPV) system. *Sol. Energy* 2013, 96:33–45.

126. Bensaid S, Centi G, Garrone E, Perathoner S, Saracco G: Towards artificial leaves for solar hydrogen and fuels from carbon dioxide. *Chem. Sus. Chem.* 2012, 5:500–521.

127. Lewis NS: Progress towards a synergistically integrated, scalable solar fuels generator. *Nanotechnol. Deliv. Promise Vol. 2* 2016, 2:3–22.

128. Gizzie E a., Scott Niezgoda J, Robinson MT, Harris AG, Kane Jennings G, Rosenthal SJ, Cliffel DE: Photosystem I-polyaniline/TiO_2 solid-state solar cells: simple devices for biohybrid solar energy conversion. *Energy Environ. Sci.* 2015, 8:3572–3576.

129. Gordiichuk PI, Wetzelaer GJAH, Rimmerman D, Gruszka A, De Vries JW, Saller M, Gautier DA, Catarci S, Pesce D, Richter S, et al.: Solid-state biophotovoltaic cells containing photosystem I. *Adv. Mater.* 2014, 26:4863–4869.

130. Utschig LM, Silver SC, Mulfort KL, Tiede DM: Nature-driven photochemistry for catalytic solar hydrogen production: A photosystem I - transition metal catalyst hybrid. *J. Am. Chem. Soc.* 2011, 133:16334–16337.

131. Qian DJ, Liu AR, Nakamura C, Wenk SO, Miyake J: Photoinduced hydrogen evolution

in an artificial system containing photosystem I, hydrogenase, methyl viologen and mercaptoacetic acid. *Chinese Chem. Lett.* 2008, 19:607–610.

132. Evans BR, O'Neill HM, Hutchens SA, Bruce BD, Greenbaum E: Enhanced photocatalytic hydrogen evolution by covalent attachment of plastocyanin to photosystem I. *Nano Lett.* 2004, 4:1815–1819.

133. Lubner CE, Applegate A. M, Knorzer P, Ganago A., Bryant D A., Happe T, Golbeck JH: Solar hydrogen-producing bionanodevice outperforms natural photosynthesis. *Proc. Natl. Acad. Sci.* 2011, 108:20988–20991.

134. Grimme RA, Lubner CE, Golbeck JH: Maximizing H_2 production in photosystem I/dithiol molecular wire/platinum nanoparticle bioconjugates. *Dalt. Trans.* 2009, 0:10106–10113.

135. Krassen H, Schwarze A, Friedrich B, Ataka K, Lenz O, Heberle J: Photosynthetic hydrogen production by a hybrid complex of photosystem I and [NiFe]-hydrogenase. *ACS Nano* 2009, 3:4055–4061.

136. Bora DK, Braun A, Constable EC: "In rust we trust". Hematite – the prospective inorganic backbone for artificial photosynthesis. *Energy Environ. Sci.* 2013, 6:407–425.

137. Bora DK, Braun A, Erni R, Müller U, Döbeli M, Constable EC: Hematite-NiO/α-$Ni(OH)_2$ heterostructure photoanodes with high electrocatalytic current density and charge storage capacity. *Phys. Chem. Chem. Phys.* 2013, 15:12648–59.

138. Gajda-Schrantz K, Tymen S, Boudoire F, Toth R, Bora DK, Calvet W, Grätzel M, Constable EC, Braun A, Grätzel M, et al.: Formation of an electron hole doped film in the α-Fe_2O_3 photoanode upon electrochemical oxidation. *Phys. Chem. Chem. Phys.* 2013, 15:1443–1451.

139. Ocakoglu K, Krupnik T, Van Den Bosch B, Harputlu E, Gullo MP, Olmos JDJ, Yildirimcan S, Gupta RK, Yakuphanoglu F, Barbieri A, et al.: Photosystem I-based biophotovoltaics on nanostructured hematite. *Adv. Funct. Mater.* 2014, 24:7467–7477.

140. Iwuchukwu IJ, Vaughn M, Myers N, O'Neill H, Frymier P, Bruce BD: Self-organized photosynthetic nanoparticle for cell-free hydrogen production. *Nat. Nanotechnol.* 2010, 5:73–79.

141. Graetzel M, Janssen RAJ, Mitzi DB, Sargent EH: Materials interface engineering for solution-processed photovoltaics. *Nature* 2012, 488:304–12.

142. Jingshan L, Jeong-Hyeok I, Mayer MT, Schreier M, Nazeeruddfn MK, Nam-Gyu P, Tilley SD, Hong Jin F, Gratzel M: Water photolysis at 12.3% efficiency via perovskite photovoltaics and Earth-abundant catalysts. *Science (80)*, 2014, 345:1593–1596.

143. Reece SY, Hamel J., Sung K, Jarvi TD, Esswein. J, Pijpers JJH, Nocera DG: Wireless Solar Water Splitting Using Silicon-Based Semiconductors and Earth-Abundant Catalysts. *Science (80)*, 2011, 334:645–648.

144. Sun J, Zhang J, Zhang M, Antonietti M, Fu X, Wang X: Bioinspired hollow semiconductor nanospheres as photosynthetic nanoparticles. *Nat. Commun.* 2012, 3:1139.

145. Castenholz RW: Culturing methods for cyanobacteria. *Methods Enzymol.* 1988, 167:68–93.

146. Bertani G: Studies on lysogenesis. I. The mode of phage liberation by lysogenic *Escherichia coli*. *J. Bacteriol.* 1951, 62:293–300.

147. Schagger H: Tricine-SDS-PAGE. *Nat.Protoc.* 2006, 1:16–22.

148. Bradford MM: A rapid and sensitive method for the quantitation of microgram quantities of protein utilizing the principle of protein-dye binding. *Anal. Biochem.* 1976, 72:248–254.

149. Szalkowski M, Janna Olmos JD, Buczyńska D, Maćkowski S, Kowalska D, Kargul J: Plasmon-induced absorption of blind chlorophylls in photosynthetic proteins assembled on silver nanowires. *Under review*.

150. Helm ML, Stewart MP, Bullock RM, DuBois MR, DuBois DL: A Synthetic nickel electrocatalyst with a turnover frequency above 100,000 s^{-1} for H_2 production. *Science*, 2011, 333:863–866.

151. Kargul J, Nield J, Barber J: Three-dimensional reconstruction of a light-harvesting complex I-photosystem I (LHCI-PSI) supercomplex from the green alga *Chlamydomonas reinhardtii*: Insights into light harvesting for PSI. *J. Biol. Chem.* 2003, 278:16135–16141.

152. Porra RJ, Thompson W, Kriedemann PE: Determination of accurate extinction coefficients and simultaneous-equations for assaying chlorophyll-*a* and chlorophyll-*b* extracted with 4 different solvents - Verification of the concentration of chlorophyll standards by atomic-absorption spectroscopy. *Biochim. Biophys. Acta* 1989, 975:384–394.

153. Díaz A, Navarro F, Hervás M, Navarro JA, Chávez S, Florencio FJ, De la Rosa MA: Cloning and correct expression in *E. coli* of the *petJ* gene encoding cytochrome c_6 from *Synechocystis* 6803. *FEBS Lett.* 1994, 347:173–177.

154. Vernon LP, Cardon S: Direct spectrophotometric measurement of photosystem I and photosystem II activities of photosynthetic membrane preparations from *Cyanophora paradoxa*, *Phormidium laminosum*, and spinach. *Plant Physiol.* 1982, 70:442–445.

155. Allakhverdiev SI, Sakamoto A, Nishiyama Y, Inaba M, Murata N: Ionic and osmotic effects of NaCl-induced inactivation of photosystems I and II in *Synechococcus sp. Plant Physiol.* 2000, 123:1047–1056.

156. Chen S, Kimura K: Synthesis of thiolate-stabilized platinum nanoparticles in protolytic solvents as isolable colloids. *J. Phys. Chem. B* 2001, 105:5397–5403.

157. Maury P, Escalante M, Péter M, Reinhoudt DN, Subramaniam V, Huskens J: Creating nanopatterns of His-tagged proteins on surfaces by nanoimprint lithography using specific Ni-NTA-histidine interactions. *Small* 2007, 3:1584–1592.

158. Cuevas A: The recombination parameter J_0. *Energy Procedia* 2014, 55:53–62.

159. Nozaki H, Matsuzaki M, Takahara M, Misumi O, Kuroiwa H, Hasegawa M, Shin-i T, Kohara Y, Ogasawara N, Kuroiwa T: The phylogenetic position of red algae revealed by multiple nuclear genes from mitochondria-containing eukaryotes and an alternative hypothesis on the origin of plastids. *J. Mol. Evol.* 2003, 56:485–497.

160. Hoffman R and ZD: Red algae in the genomic age. *Red Algae Genomic Age* 2010, 13:45–60.

161. Ohta H, Suzuki T, Ueno M, Okumura A, Yoshihara S, Shen JR, Enami I: Extrinsic

proteins of photosystem II: An intermediate member of the PsbQ protein family in red algal PS II. *Eur. J. Biochem.* 2003, 270:4156–4163.

162. Bertini I, Cavallaro G, Rosato A: Cytochrome *c*: Occurrence and functions. *Chem. Rev.* 2006, 106:90–115.

163. Hannibal L, Tomasina F, Capdevila DA, Demicheli V, Tórtora V, Alvarez-Paggi D, Jemmerson R, Murgida DH, Radi R: Alternative Conformations of cytochrome *c*: Structure, function, and detection. *Biochemistry* 2016, 55:407–428.

164. Dickerson RE, Takano T, Eisenberg D, Kallai OB, Samson L, Cooper A, Margoliash E: Ferricytochrome *c*. I. General features of the horse and bonito proteins at 2.8 Å resolution. *J. Biol. Chem.* 1971, 246:1511–1535.

165. Swanson R, Trus BL, Mandel N, Mandel G, Kallai OB, Dickerson RE: Tuna cytochrome *c* at 2.0 Å resolution. I. Ferricytochrome structure analysis. *J. Biol. Chem.* 1977, 252:759–775.

166. Takano T: Redox conformation changes in refined tuna cytochrome *c*. 1980, 77:6371–6375.

167. Sites JBCA: Crystallization of of tuna ferricytochrome *c* at low ionic strength. 1990, 265:4177–4180.

168. Sugimura Y, Yoshizaki F, Katagiri J, Horiuchi C: Studies on algal cytochromes. I. Purification and properties of cytochrome b_{561} from *Enteromorpha prolifera*. *J. Biochem.* 1980, 87:541–7.

169. Sugimura Y, Hosoya K, Yoshizaki F, Shimokoriyama M: Studies on algal cytochromes. V. Purification and characterization c_{552} from a red alga, *Polysiphonia urceolata*. *J. Biochem.* 1984, 96:1681–1687.

170. Białek W, Krzywda S, Jaskolski M, Szczepaniak A: Atomic-resolution structure of reduced cyanobacterial cytochrome c_6 with an unusual sequence insertion. *FEBS J.* 2009, 276:4426–4436.

171. Laskowski RA: PDBsum new things. *Nucleic Acids Res.* 2009, 37:D355–D359.

172. Fischer F, Künzler P, Ritz D, Hennecke H, Fischer F, Ku P, Institut M: *Escherichia coli* genes required for cytochrome *c* maturation. These include: *Escherichia coli* genes required for cytochrome *c* maturation. *J. Bacteriol.* 1995, 177:4321–4326.

173. Allen JWA, Tomlinson EJ, Hong L, Ferguson SJ: The *Escherichia coli* cytochrome *c* maturation (Ccm) system does not detectably attach heme to single cysteine variants of an apocytochrome *c*. *J. Biol. Chem.* 2002, 277:33559–33563.

174. Jarvis P, Robinson C: Mechanisms of protein import and routing in chloroplasts. *Curr. Biol.* 2004, 14:1064–1077.

175. Harris EH, Boynton JE, Gillham NW: Chloroplast ribosomes and protein synthesis. *Microbiol. Rev.* 1994, 58:700–754.

176. Sanders C, Turkarslan S, Lee DW, Daldal F: Cytochrome *c* biogenesis: The Ccm system. *Trends Microbiol.* 2010, 18:266–274.

177. Barlow DJ, Thornton JM: Helix geometry in proteins. *J. Mol. Biol.* 1988, 201:601–619.

178. Arslan E, Schulz H, Zufferey R, Kunzler P, Thony-Meyer L: Overproduction of the *Bradyrhizobium japonicum c*-type cytochrome subunits of the cbb_3 oxidase in

Escherichia coli. *Biochem. Biophys. Res. Commun.* 1998, 251:744–747.

179. Kan SBJ, Lewis RD, Chen K, Arnold FH: Directed evolution of cytochrome *c* for carbon–silicon bond formation: Bringing silicon to life. *Science (80)*, 2016, 354:1048–1051.

180. Watkins DW, Armstrong CT, Beesley JL, Marsh JE, Jenkins JMX, Sessions RB, Mann S, Ross Anderson JL: A suite of de novo *c*-type cytochromes for functional oxidoreductase engineering. *Biochim. Biophys. Acta - Bioenerg.* 2016, 1857:493–502.

181. Białek W, Nelson M, Tamiola K, Kallas T, Szczepaniak A: Deeply branching c_6-like cytochromes of cyanobacteria. *Biochemistry* 2008, 47:5515–5522.

182. Töpler J: Hydrogen as energy-storage-medium and fuel. *Renew. Energy Environ. Sustain.* 2016, 1:31.

183. Detz RJ, Sakai K, Spiccia L, Brudvig GW, Sun L, Reek JNH: Towards a bioinspired-systems approach for solar fuel devices. *Chempluschem* 2016, 81:1024–1027.

184. Kemppainen E, Bodin A, Sebok B, Pedersen T, Seger B, Mei B, Bae D, Vesborg PCK, Halme J, Hansen O, et al.: Scalability and feasibility of photoelectrochemical H_2 evolution: the ultimate limit of Pt nanoparticle as an HER catalyst. *Energy Environ. Sci.* 2015, 8:2991–2999.

185. Zeng M, Li Y: Recent advances in heterogeneous electrocatalysts for the hydrogen evolution reaction. *J. Mater. Chem. A* 2015, 3:14942–14962.

186. Thoi VS, Sun Y, Long JR, Chang CJ: Complexes of earth-abundant metals for catalytic electrochemical hydrogen generation under aqueous conditions. *Chem. Soc. Rev.* 2013, 42:2388–2400.

187. Schilter D, Camara JM, Huynh MT, Hammes-Schiffer S, Rauchfuss TB: Hydrogenase enzymes and their synthetic models: The role of metal hydrides. *Chem. Rev.* 2016, 116:8693–8749.

188. Becker R, Amirjalayer S, Li P, Woutersen S, Reek JNH: An iron-iron hydrogenase mimic with appended electron reservoir for efficient proton reduction in aqueous media. *Sci. Adv.* 2016, 2:e1501014 (1-9).

189. Dutta A, DuBois DL, Roberts JAS, Shaw WJ: Amino acid modified Ni catalyst exhibits reversible H_2 oxidation/production over a broad pH range at elevated temperatures. *Proc. Natl. Acad. Sci.* 2014, 111:16286–16291.

190. Martini LA, Moore GF, Milot RL, Cai LZ, Sheehan SW, Schmuttenmaer CA, Brudvig GW, Crabtree RH: Modular assembly of high-potential zinc porphyrin photosensitizers attached to TiO_2 with a series of anchoring groups. *J. Phys. Chem. C* 2013, 117:14526–14533.

191. Van Den Bosch B, Rombouts JA, Orru RVA, Reek JNH, Detz RJ: Nickel-based dye-sensitized photocathode: Towards proton reduction using a molecular nickel catalyst and an organic dye. *ChemCatChem* 2016, 8:1392–1398.

192. Utschig LM, Dimitrijevic NM, Poluektov OG, Chemerisov SD, Mulfort KL, Tiede DM: Photocatalytic hydrogen production from noncovalent biohybrid photosystem I/Pt nanoparticle complexes. *J. Phys. Chem. Lett.* 2011, 2:236–241.

193. Bakac A, Brynildson ME, Espenson JH: Characterization of the structure, properties, and reactivity of a cobalt(II) macrocyclic complex. *Inorg. Chem. Am. Chem. Soc.* 1986,

25:4108–4114.

194. Razavet M, Artero V, Fontecave M, Fourier J, Cb D, Bat K, Cedex G: Proton electroreduction catalyzed by cobaloximes : Functional models for hydrogenases. *Inorg. Chem. Am. Chem. Soc.* 2005, 44:4786–4795.

195. Silver SC, Niklas J, Du P, Poluektov OG, Tiede DM, Utschig LM: Protein delivery of a Ni catalyst to photosystem I for light–driven hydrogen production. *J. Am. Chem. Soc.* 2013, 210:1–9.

196. Rongé J, Bosserez T, Martel D, Nervi C, Boarino L, Taulelle F, Decher G, Bordiga S, Martens JA: Monolithic cells for solar fuels. *Chem. Soc. Rev.* 2014, 43:7963–81.

197. Kumari S, White RT, Kumar B, Spurgeon JM: Solar hydrogen production from seawater vapor electrolysis. *Energy Environ. Sci.* 2016, 9:1725–1733.

198. Ebbesen SD, Jensen SH, Hauch A, Mogensen MB: High temperature electrolysis in alkaline cells, solid proton conducting cells, and solid oxide cells. *Chem. Rev.* 2014, 114:10697–10734.

199. Wang M, Wang Z, Gong X, Guo Z: The intensification technologies to water electrolysis for hydrogen production. *Renew. Sustain. Energy Rev.* 2014, 29:573–588.

200. Rongé J, Bosserez T, Huguenin L, Dumortier M, Haussener S, Johan A. Martens: Solar hydrogen reaching maturity. *OGST - Rev. d'IFP Energies Nouv.* 2014, 70:863–876.

201. Gahleitner G: Hydrogen from renewable electricity: An international review of power-to-gas pilot plants for stationary applications. *Int. J. Hydrogen Energy* 2013, 38:2039–2061.

202. Graetz J: New approaches to hydrogen storage. *Chem. Soc. Rev.* 2009, 38:73–82.

203. Szalkowski M, Ashraf KU, Lokstein H, Mackowski S, Cogdell RJ, Kowalska D: Silver island film substrates for ultrasensitive fluorescence detection of (bio)molecules. *Photosynth. Res.* 2016, 127:103–108.

204. Czechowski N, Lokstein H, Kowalska D, Ashraf K, Cogdell RJ, Mackowski S: Large plasmonic fluorescence enhancement of cyanobacterial photosystem I coupled to silver island films. *Appl. Phys. Lett.* 2014, 105.

205. Wientjes E, Renger J, Curto AG, Cogdell R, van Hulst NF: Strong antenna-enhanced fluorescence of a single light-harvesting complex shows photon antibunching. *Nat. Commun.* 2014, 5:4236.

206. Linic S, Christopher P, Ingram DB: Plasmonic-metal nanostructures for efficient conversion of solar to chemical energy. *Nat. Mater.* 2011, 10:911–921.

207. Friebe VM, Delgado JD, Swainsbury DJK, Gruber JM, Chanaewa A, Van Grondelle R, Von Hauff E, Millo D, Jones MR, Frese RN: Plasmon-enhanced photocurrent of photosynthetic pigment proteins on nanoporous silver. *Adv. Funct. Mater.* 2016, 26:285–292.

208. Mackowski S: Hybrid nanostructures for efficient light harvesting. *J. Phys. Condens. Matter* 2010, 22:193102.

209. Lakowicz JR: Radiative decay engineering: biophysical and biomedical applications. *Anal. Biochem.* 2001, 298:1–24.

210. Lee JS, Shevchenko E V., Talapin D V.: Au-PbS core-shell nanocrystals: Plasmonic

absorption enhancement and electrical doping *via* intra-particle charge transfer. *J. Am. Chem. Soc.* 2008, 130:9673–9675.

211. Bharadwaj P, Novotny L: Spectral dependence of single molecule fluorescence enhancement. *Opt. Express* 2007, 15:14266–14274.

212. Schmidt MK, Mackowski S: Theoretical studies of excitation dynamics in a peridinin-chlorophyll-protein coupled to a metallic nanoparticle. *Cent. Eur. J. Phys.* 2011, 9:562–569.

213. Schmidt MK, Mackowski S, Aizpurua J: Control of single emitter radiation by polarization- and position-dependent activation of dark antenna modes. *Opt. Lett.* 2012, 37:1017–9.

214. Lal S, Hafner JH, Halas NJ, Link S, Nordlander P: Noble metal nanowires : From plasmon waveguides to passive and active devices. *Acc. Chem. Res.* 2012, 45:1887–1895.

215. Xu X, Cheng C, Zhang Y, Lei H, Li B: Dual focused coherent beams for three-dimensional optical trapping and continuous rotation of metallic nanostructures. *Sci. Rep.* 2016, 6:29449 (1-12).

216. Wang Y-L, Nan F, Liu X-L, Zhou L, Peng X-N, Zhou Z-K, Yu Y, Hao Z-H, Wu Y, Zhang W, et al.: Plasmon-enhanced light harvesting of chlorophylls on near-percolating silver films *via* one-photon anti-Stokes upconversion. *Sci. Rep.* 2013, 3:1861 (1-7).

217. Ritchie RH: Plasma losses by fast electrons in thin films. *Phys. Rev.* 1957, 106:874–881.

218. Ozbay E: Plasmonics: merging photonics and electronics at nanoscale dimensions. *Science* 2006, 311:189–93.

219. Hippler M, Drepper F, Farah J, Rochaix J-D: Fast electron transfer from cytochrome c_6 and plastocyanin to photosystem I of *Chlamydomonas reinhardii*. *Biochemistry* 1997, 36:6343–6349.

220. Döscher H, Young JL, Geisz JF, Turner JA, Deutsch TG: Solar-to-hydrogen efficiency: shining light on photoelectrochemical device performance. *Energy Environ. Sci.* 2016, 9:74–80.

221. Mershin A, Matsumoto K, Kaiser L, Yu D, Vaughn M, Nazeeruddin MK, Bruce BD, Graetzel M, Zhang S: Self-assembled photosystem-I biophotovoltaics on nanostructured TiO_2 and ZnO. *Sci. Rep.* 2012, 2:234.

222. Beam JC, LeBlanc G, Gizzie EA, Ivanov BL, Needell DR, Shearer MJ, Jennings GK, Lukehart CM, Cliffel DE: Construction of a semiconductor-biological interface for solar energy conversion: *p*-doped silicon/photosystem I/zinc oxide. *Langmuir* 2015, 31:10002–10007.

223. Zhu Q, Chen J, Xu M, Tian S, Pan H, Qian J, Zhou X: Microsphere assembly of rutile TiO_2 hierarchically hyperbranched nanorods: CdS sensitization and photovoltaic properties. *Solid State Sci.* 2011, 13:1299–1303.

224. Zhao F, Conzuelo F, Hartmann V, Li H, Nowaczyk MM, Plumeré N, Rögner M, Schuhmann W: Light induced H_2 evolution from a biophotocathode based on photosystem I-Pt nanoparticles complexes integrated in solvated redox polymers films. *J. Phys. Chem. B* 2015, 119:13726–13731.

225. Su F, Lu J, Tian Y, Ma X, Gong J: Branched TiO_2 nanoarrays sensitized with CdS quantum dots for highly efficient photoelectrochemical water splitting. *Phys. Chem. Chem. Phys.* 2013, 15:12026–32.

226. Wittenberg G, Sheffler W, Darchi D, Baker D, Noy D: Accelerated electron transport from photosystem I to redox partners by covalently linked ferredoxin. *Phys. Chem. Chem. Phys.* 2013, 15:19608–14.

227. Janna Olmos JD, Becquet P, Gront D, Dąbrowski A, Gawlik G, Teodorczyk M, Kargul J: Biopassivation of *p*-doped silicon with cytochrome c_{553} leads to minimisation of charge recombination and leakage current at the semiconductor surface. *Under review*.

228. Tian J, Zhang Q, Uchaker E, Gao R, Qu X, Zhang S, Cao G: Architectured ZnO photoelectrode for high efficiency quantum dot sensitized solar cells. *Energy Environ. Sci.* 2013, 6:3542.

229. Tian J, Gao R, Zhang Q, Zhang S, Li Y, Lan J, Qu X, Cao G: Enhanced performance of CdS / CdSe quantum dot cosensitized solar cells *via* homogeneous distribution of quantum dots in TiO_2 film. *J. Phys. Chem. C* 2012, 116:18655–18662.

230. Liu D, Wei Z, Shen Y, Sajjad SD, Hao Y, Liu F: Ultra-long electron lifetime induced efficient solar energy storage by an all-vanadium photoelectrochemical storage cell using methanesulfonic acid. *J. Mater. Chem. A* 2015, 3:20322–20329.

231. Savin H, Repo P, von Gastrow G, Ortega P, Calle E, Garín M, Alcubilla R: Black silicon solar cells with interdigitated back-contacts achieve 22.1% efficiency. *Nat. Nanotechnol.* 2015, 10:1–6.

232. Yoshikawa K, Kawasaki H, Yoshida W, Irie T, Konishi K, Nakano K, Uto T, Adachi D, Kanematsu M, Uzu H, et al.: Silicon heterojunction solar cell with interdigitated back contacts for a photoconversion efficiency over 26%. *Nat. Energy* 2017, 2:17032.

233. Ciesielski PN, Cliffel DE, Jennings GK: Kinetic model of the photocatalytic effect of a photosystem I monolayer on a planar electrode surface. *J. Phys. Chem. A* 2011, 115:3326–3334.

234. Leblanc G, Chen G, Gizzie EA, Jennings GK, Cliffel DE: Enhanced photocurrents of photosystem I films on *p*-doped silicon. *Adv. Mater.* 2012, 24:5959–5962.

235. Kamran M, Delgado JD, Friebe V, Aartsma TJ, Frese RN: Photosynthetic protein complexes as bio-photovoltaic building blocks retaining A high internal quantum efficiency. *Biomacromolecules* 2014, 15:2833–2838.

236. Ihssen J, Braun A, Faccio G, Gajda-Schrantz K, Thony-Meyer L: Light harvesting proteins for solar fuel generation in bioengineered photoelectrochemical cells. *Curr. Protein Pept. Sci.* 2014, 15:374–384.

237. Yehezkeli O, Tel-Vered R, Michaeli D, Willner I, Nechushtai R: Photosynthetic reaction center-functionalized electrodes for photo-bioelectrochemical cells. *Photosynth. Res.* 2014, 120:71–85.

238. Lewis NS, Wrighton MS: Electrochemical reduction of horse heart ferricytochrome *c* at chemicaily derivatized electrodes. *Science (80),* 1981, 211:944–947.

239. Metropolis N, Rosenbluth AW, Rosenbluth MN, Teller AH, Teller E: Equation of state calculations by fast computing machines. *J. Chem. Phys.* 1953, 21:1087–1092.

240. Hogewoning SW, Wientjes E, Douwstra P, Trouwborst G, van Ieperen W, Croce R,

Harbinson J: Photosynthetic quantum yield dynamics: From photosystems to leaves. *Plant Cell* 2012, 24:1921–1935.

241. Kothe T, Poeller S, Zhao F, Fortgang P, Roegner M, Schuhmann W, Plumere N: Engineered electron-transfer chain in photosystem I based photocathodes outperforms electron-transfer rates in natural photosynthesis. *Chem. - A Eur. J.* 2014, 20:11029–11034.

242. Shah VB, Henson WR, Chadha TS, Lakin G, Liu H, Blankenship RE, Biswas P: Linker-free deposition and adhesion of photosystem I onto nanostructured TiO_2 for biohybrid photoelectrochemical cells. *Langmuir* 2015, 31:1675–1682.

243. Ciesielski PN, Hijazi FM, Scott AM, Faulkner CJ, Beard L, Emmett K, Rosenthal SJ, Cliffel D, Kane Jennings G: Photosystem I - based biohybrid photoelectrochemical cells. *Bioresour. Technol.* 2010, 101:3047–3053.

244. Yu D, Wang M, Zhu G, Ge B, Liu S, Huang F: Enhanced photocurrent production by bio-dyes of photosynthetic macromolecules on designed TiO_2 film. *Sci. Rep.* 2015, 5:9375–9384.

245. Klimmek F, Ganeteg U, Ihalainen JA, Van Roon H, Jensen PE, Scheller H V., Dekker JP, Jansson S: Structure of the higher plant light harvesting complex I: *In vivo* characterization and structural interdependence of the Lhca proteins. *Biochemistry* 2005, 44:3065–3073.

246. Croce R, Morosinotto T, Castelletti S, Breton J, Bassi R: The Lhca antenna complexes of higher plants photosystem I. *Biochim. Biophys. Acta - Bioenerg.* 2002, 1556:29–40.

247. Sugawa K, Tamura T, Tahara H, Yamaguchi D, Akiyama T, Otsuki J, Kusaka Y, Fukuda N, Ushijima H: Metal-enhanced fluorescence platforms based on plasmonic ordered copper arrays: Wavelength dependence of quenching and enhancement effects. *ACS Nano* 2013, 7:9997–10010.

248. Szmacinski H, Ray K, Lakowicz JR: Effect of plasmonic nanostructures and nanofilms on fluorescence resonance energy transfer. *J. Biophotonics* 2009, 2:243–252.

249. Feng AL, You ML, Tian L, Singamaneni S, Liu M, Duan Z, Lu TJ, Xu F, Lin M: Distance-dependent plasmon-enhanced fluorescence of upconversion nanoparticles using polyelectrolyte multilayers as tunable spacers. *Sci. Rep.* 2015, 5:7779.

250. Gross MA, Reynal A, Durrant JR, Reisner E: Versatile photocatalytic systems for H_2 generation in water based on an efficient DuBois-type nickel catalyst. *J. Am. Chem. Soc.* 2014, 136:356–366.

251. Amdursky N, Ferber D, Bortolotti CA, Dolgikh D a, Chertkova R V, Pecht I, Sheves M, Cahen D: Solid-state electron transport *via* cytochrome *c* depends on electronic coupling to electrodes and across the protein. *Proc. Natl. Acad. Sci.* 2014, 111:5556–5561.

252. Amdursky N, Pecht I, Sheves M, Cahen D: Electron transport *via* cytochrome *c* on Si-H surfaces: Roles of Fe and heme. *J. Am. Chem. Soc.* 2013, 135:6300–6306.

253. McKone JR, Lewis NS, Gray HB: Will solar-driven water-splitting devices see the light of day? *Chem. Mater.* 2014, 26:407–414.